Chapter 5: Information from Paleoclimate Archives

Coordinating Lead Authors: Valérie Masson-Delmotte (France), Michael Schulz (Germany)

Lead Authors: Ayako Abe-Ouchi (Japan), Juerg Beer (Switzerland), Andrey Ganopolski (Germany), Jesus Fidel González Rouco (Spain), Eystein Jansen (Norway), Kurt Lambeck (Australia), Juerg Luterbacher (Germany), Tim Naish (New Zealand), Timothy Osborn (UK), Bette Otto-Bliesner (USA), Terrence Quinn (USA), Rengaswamy Ramesh (India), Maisa Rojas (Chile), XueMei Shao (China), Axel Timmermann (USA)

Contributing Authors: Kevin Anchukaitis (USA), Patrick J. Bartlein (USA), Gerardo Benito (Spain), Peter Clark (USA), Thomas Crowley (USA), Patrick De Deckker (Australia), Barbara Delmonte (Italy), Pedro DiNezio (USA), Trond Dokken (Norway), Harry J. Dowsett, R. Lawrence Edwards (USA), Hubertus Fischer (Switzerland), Dominik Fleitmann (UK), Claus Fröhlich (Switzerland), Aline Govin (Germany), Alan Haywood (UK), Chris Hollis (New Zealand), Ben Horton (USA), Robert Kopp(USA), Amaelle Landais (France), Camille Li (Norway), Dan Lunt (UK), Natalie Mahowald (USA), Shayne McGregor (USA), Jerry X. Mitrovica (USA), Anders Moberg (Sweden), Daniel R. Muhs (USA), Stefan Mulitza (Germany), Frédéric Parrenin (France), Paul Pearson (UK), Alan Robock (USA), Eelco Rohling (UK), Ulrich Salzmann (UK), Joel Savarino (France), Jason Smerdon (USA), Olga Solomina (Russia), Pavel Tarasov (Germany), Claire Waelbroeck (France), Dieter Wolf-Gladrow (Germany), Yusuke Yokoyama (Japan), Masakazu Yoshimori (Japan), James Zachos (USA), Dan Zwartz (New Zealand)

Review Editors: Anil K. Gupta (India), Fatemeh Rahimzadeh (Iran), Dominique Raynaud (France), Heinz Wanner (Switzerland)

Date of Draft: 5 October 2012

Notes: TSU Compiled Version

Table of Contents

Executive Summary

Greenhouse-Gas Variations and Past Climate Responses

Present-day concentrations of atmospheric greenhouse gases (CO_2, CH_4, and N_2O) exceed the range of variability recorded in ice core records during past 800,000 years. Past changes in atmospheric greenhouse-gas concentrations can be determined with *high confidence* from polar ice cores. New data extend the AR4 statement that present-day concentrations *likely* exceed the natural range of variability back to 800,000 years ago. [5.2.2]

Reconstructions from high-CO_2 climates provide further evidence for coupling between atmospheric CO_2 concentration and global mean temperature. During the middle Pliocene (3.3–3.0 Ma, million years ago), atmospheric CO_2 concentrations between 330 ppm and 420 ppm (*medium confidence*) were associated with global mean surface temperatures approximately 2–3.5°C (*low to medium confidence*) warmer than for pre-industrial climate [5.3.1]. During the Early Eocene (52–48 Ma), atmospheric CO_2 concentration likely reached ~1000 ppm and was associated with global mean surface temperatures 8–14°C (low confidence) warmer than for pre-industrial conditions. [5.3.1]

Proxy information has strengthened the notion of amplified temperature response in the Arctic. For high CO_2 climates such as the middle Pliocene and low CO_2 climates such as the Last Glacial Maximum, temperature reconstructions show polar amplification for the Arctic (*high confidence*). Available simulations from coupled climate models underestimate the strength of this amplification with respect to proxy-based reconstructions, although the reason for this underestimation is unclear. [Box 5.2]

Changes in atmospheric CO_2 concentration play an important role in glacial-interglacial cycles (*high confidence*). While orbital forcing is the primary driver of glacial cycles, climate-ice sheet models of different complexities as well as reconstructions show that the internal feedback of CO_2 accounts for a significant fraction of glacial-interglacial climate variability. Since AR4, leads and lags between temperature and CO_2 have been revised. New Antarctic data and dating methods depict simultaneous increases in Antarctic temperature and CO_2 during the last glacial termination, preceding Northern Hemisphere warming due to the bipolar seesaw (*high confidence*). [5.3.2]

New estimates of Charney climate sensitivity using climate reconstructions and simulations for the Last Glacial Maximum (LGM) indicate that values below 1.4°C or above 6°C are very unlikely. This range is also supported by evidence for the last 65 million years. However, asymmetries associated for example with cloud feedbacks, suggest that sensitivity estimates for colder climate conditions are not directly applicable to warmer climate conditions (*low confidence*). [5.3.3]

Climate Change and Sea Level Variations

There is *high confidence* that global mean sea level was above modern levels during some of the warm intervals of the mid-Pliocene, implying reduced volume of polar ice sheets. The best estimates from various methods imply that sea level was ~10 m (±10 m) above present during the warmest periods of the Pliocene (*medium confidence*). We have low confidence in estimates suggesting that sea level was more than 20 m above present. Direct geological evidence, supported by ice sheet simulations, suggests that most of the variation in ice volume occurred in the Greenland and West Antarctic ice sheets while the East Antarctic ice sheet was only slightly reduced compared to today. [5.6.1]

The Greenland and West Antarctic ice sheets have retreated during periods of the past few million years that were warmer than today. It is *likely* that the Greenland ice sheet was strongly reduced and the West Antarctic ice sheet was absent during warm periods of the middle Pliocene when CO_2 concentrations were in the range 330–420 ppm [5.3; 5.6.1]. Ice sheet model simulation suggests that West Antarctic ice sheet is very sensitive to subsurface southern ocean warming and imply with *low confidence* that a large part of the West Antarctic ice sheet may eventually retreat if the atmospheric CO_2 concentration stays above approximately 400 ppm for several millennia. [5.8]

There is *high confidence* that during the last interglacial period, global mean sea level was between 6 and 10 m higher than present. Global-mean annual temperature change for this period can only be estimated with *medium confidence*. Data syntheses suggest maximum global warmth of 1–2°C above pre-industrial temperatures, with larger Arctic and Antarctic warming. Climate models simulate no significant global-average temperature change, but produce Arctic warming in response to orbital forcing. There is *medium confidence* that globally the oceans were not significantly warmer than present, precluding a significant contribution from thermal expansion. New Greenland ice core data can only be reconciled with ice-sheet simulations that show limited Greenland ice-sheet retreat (< 2 m sea level equivalent; *medium confidence*), implying a larger contribution from the West and/or East Antarctic ice sheets than previously estimated. [5.3.4; 5.6.2]

The rate of current global mean sea level change is unusually high in the context of the past millennium [*medium confidence*]. For the last few thousand years, oscillations in sea level on centennial to millennial timescales are unlikely [*medium confidence*] to have exceeded 25 cm. [5.6.3]

Hemispheric and Regional Climate Variations

20th century warming has reversed long-term cooling trends in mid-to-high latitudes of the Northern Hemisphere. Continental-scale temperature reconstructions reveal long-term trends throughout the last 2000 years, which are attributed to orbital forcing (*high confidence*). [5.5.1]

Summer sea ice cover between 8 ka and 6.5 ka was reduced compared to late 20th Century levels both in the Arctic Ocean and along East Greenland. There is *medium confidence* that the modern ice loss and increase of sea surface temperatures in the Arctic are anomalous in the perspective of at least the last two millennia. [5.5.2]

The current near-global recession of glacier length is unusual in the context of the last 2 millennia [*medium confidence*] and consistent with reconstructed surface-temperature anomalies. Retreating glaciers are still larger now than in the early-to-mid Holocene in most regions (*high confidence*). [5.5.3]

For average annual Northern Hemisphere temperatures, there is *medium confidence* that 1981–2010 CE was the warmest 30-year period of the last 1300 years and it is *very likely* that it was the warmest of the last 800 years. This is supported by multiple reconstructions using a variety of proxy data and statistical methods. Before 1200 CE there is only *medium evidence* and *medium agreement* because there are fewer independent reconstructions, they rely on fewer proxy records, and the published uncertainty ranges may underestimate the true uncertainty. Simulations forced by natural and anthropogenic radiative changes during the last millennium are consistent with reconstructions of Northern Hemisphere temperature, within the broad uncertainty ranges (*high confidence*). [5.3.5]

In contrast to the late 20th century there is *high confidence* that the Medieval Climate Anomaly was not characterized by a pattern of higher temperatures that were consistent across seasons and regions. Internal variability as well as solar and volcanic forcing may have significantly influenced the patterns of temperature difference between the Medieval Climate Anomaly and the Little Ice Age. Uncertainties in forcings and reconstructed temperatures limit the value of comparisons between model results and reconstructions. [5.3.5.3, 5.5.1]

In most regions, proxy information from the last millennium provides evidence of megadroughts of greater magnitude and longer duration than observed during the 20th century. There is *high confidence* that during the LIA more megadroughts occurred in Asia and wetter conditions prevailed in the South American monsoon region compared to the Medieval Climate Anomaly and 20th century [5.5.4 and 5.5.5].

Paleoflood discharges larger than recorded during the 20th century are reconstructed for the past centuries in northern and central Europe, western Mediterranean region, and eastern Asia (*high confidence*). In some regions (e.g., Near East, India, central North America) modern large floods are comparable or surpass in magnitude and/or frequency historical floods. [5.5.5].

Confidence in the link between changes in North-Atlantic climate and low-latitude hydroclimate has increased since AR4. Based on evidence from reconstructions supported by modelling experiments, it is *very likely* that North Atlantic cooling during glacial stadials in combination with a weakening of the Atlantic meridional overturning circulation caused southward shifts of the Atlantic intertropical convergence zone and affected global monsoon systems, causing droughts in some regions and wet phases in others. [5.7]

Past Changes in Climate Modes

A new reconstruction from the equatorial Pacific and modelling experiments show high levels of variability in El Niño-Southern Oscillation (ENSO) behaviour throughout the entire Holocene. This weakens the evidence assessed in AR4 for reduced ENSO variance during the early-to-mid Holocene. [5.4]

Changes in total solar irradiance have no discernible effect on ENSO variance while volcanic aerosol forcing has a weak effect on ENSO statistics. Multidecadal changes in ENSO variance over the last 500 years are unrelated (*high confidence*) to solar variability at timescales from decades to centuries. ENSO reconstructions suggest with *medium confidence* an increased likelihood in the occurrence of El Niño events in the two years following a major volcanic eruption. [5.4]

Late 20th century North Atlantic Oscillation (NAO) behavior is not unusual in the context of the last 500 years. Decadal periods of persistent positive NAO, similar to those observed from the late 1960s to the mid-1990s are not unprecedented (*high confidence*) in the context of reconstructed NAO state during at least the past 500 years. [5.4]

5.1 Introduction

This chapter assesses the information on past climate obtained prior to the instrumental period. The information is based on documentary and proxy data from various paleoclimatic archives as well as modeling past climate changes. The information updates Chapter 6 of AR4 of the IPCC Working Group 1.

Paleoclimate data provide quantitative information on the Earth-system response to various natural climate forcings (solar, volcanic and orbital), which acted in the past and will affect future climate evolution. Paleoclimate information allows the study of Earth-system feedbacks (Box 5.1), which operate on timescales longer than a few centuries and cannot be evaluated from short instrumental records. Past climate changes also document transitions between different climate states, including abrupt events which occurred on timescales of decades to a few centuries.

Major progress since AR4 includes the acquisition of new and more precise information from paleoclimate archives, the synthesis of regional information, as well as transient and more comprehensive modelling of past climate responses to forcings. This chapter assesses the understanding of past climate variations, using paleoclimate reconstructions as well as climate models of varying complexity, while the model evaluation based on paleoclimate information is covered in Chapter 9. Additional paleoclimate perspectives are included in Chapters 6, 10, 13 and 14.

The chapter is organized by going from changes in atmospheric composition and external climate forcings, including solar and volcanic activity (Section 5.2, FAQ 5.1), to global and hemispheric responses (Section 5.3). Several open debates are covered, including the evolution of surface temperatures during the past 2000 years (Section 5.3.5), the temporal relationship between atmospheric CO_2 content and temperature during glacial-to-interglacial transitions (so-called terminations; [Section 5.3.2]) and paleoclimate constraints on climate sensitivity (Section 5.3.3).

After evaluating the evidence for past changes in climate modes of variability (Section 5.4), a specific focus is given to regional changes in temperature, cryosphere and hydroclimate during the current interglacial period (Section 5.5). Sections on sea level change (Section 5.6, FAQ 5.2), abrupt climate changes (Section 5.7) and illustrations of irreversibility and recovery time scales (Section 5.8), conclude the chapter. The relationships between ice sheets, sea level, atmospheric CO_2 concentration and climate are addressed in several sections (Sections 5.3.1, 5.5, and 5.8.1), while polar amplification is addressed in Box 5.2.

The content of this chapter is limited to topics for which significant new information has emerged since AR4. This includes revised proxy-based estimates of the atmospheric CO_2 content during the past ~65 million years (Section 5.2.2), and magnitudes of sea level variations during interglacial periods (Section 5.6.2). Information from glacial climates has only been reported when the underlying processes are of direct relevance for an assessment of the projected climate change. The impact of past climate changes on biological systems and past civilizations are not covered as these topics are beyond the scope of Working Group I.

Additional information to this chapter is available in Appendix 5.A. Processed data underlying the figures will be finally archived in the PANGAEA database (www.pangaea.de) while model output from the Paleoclimate Modelling Intercomparison Project (PMIP) is available from: pmip3.lsce.ipsl.fr/wiki/doku.php/pmip3:database:access.

In all sections, information is structured by going from past to present, and radiocarbon-based ages are quoted as the published calibrated ages.

5.2 Radiative Forcings and Radiative Perturbations from Earth System Feedbacks

5.2.1 External Forcings

5.2.1.1 Orbital Forcing

Orbital forcing is well-known from precise astronomical calculations for the past and future. Changes in Earth's astronomical parameters – eccentricity, longitude of perihelion (precession), and axial tilt (obliquity) (Berger and Loutre, 1991; Laskar et al., 2004) predominantly affect the seasonal and latitudinal distribution and magnitude of solar energy received at the top of the atmosphere (Jansen et al., 2007) and the durations and intensities of local seasons (Huybers, 2006; Timm et al., 2008). Obliquity also modulates the annual insolation, with opposite effects at high and low latitudes. The term "orbital forcing" is used for the astronomical forcing originating from changes in Earth´s orbital parameters as well as changes in its axial tilt. Orbital forcing is considered the pacemaker of transitions between glacials and interglacials and vice versa (high confidence), although there is no consensus on exactly how it influences changes in ice-sheet mass (Section 5.3.2). The different periodicities of the orbital parameters make each glacial and interglacial period unique in its orbital configuration (e.g., Yin and Berger, 2010). Orbitally-induced insolation variations over the last millennium (Schmidt et al., 2011) have also been invoked for explaining millennial trends (Wanner et al., 2008).

5.2.1.2 Solar Forcing

A new lower absolute value for Total Solar Irradiance (TSI) of 1360.8 ± 0.5 W m^{-2} (Kopp and Lean, 2011) was determined during the 2008 solar minimum, which is less than the previous estimate of 1365.5 W m^{-2} used in some model runs and in Figure 5.1 (see also Chapter 8, Section 8.3.1.1.1). The effect of this difference implies 1.2 W m^{-2} lower solar energy input for the global radiative energy budget (e.g., Loeb et al., 2009). However, the lower TSI value does not affect the TSI long-term variations and thus this result is not expected to be very significant for simulated climate changes. Since AR4, solar irradiance models (e.g., Wenzler et al., 2005) have been improved to explain the instrumental records of total and spectral (wavelength dependent) solar irradiance (SSI). Typical changes measured over an 11-year solar cycle are 0.1% for TSI and several percent for the ultra-violet (UV) part of SSI (see Section 8.3). Changes in TSI directly impact the Earth's surface, whereas changes in SSI primarily affect the stratosphere, but can influence the tropospheric circulation through dynamical coupling (Gray et al., 2010). Most models attribute all TSI and SSI changes exclusively to magnetic phenomena on the solar surface (sunspots, faculae, magnetic network), neglecting any potential internal phenomena such as changes in energy transport. These models can successfully reproduce the measured TSI changes between 1978 and 2003 (Balmaceda et al., 2007; Crouch et al., 2008), but not necessarily the last minimum of 2008 (Krivova et al., 2011). The basic concept of these models is to divide the solar surface into different magnetic features each with a specific radiative flux. Sunspots are dark features that reduce irradiance; faculae and the magnetic network are bright features enhancing irradiance. The contrasting dark and bright solar features provide a higher TSI value during solar cycle maximum and at most wavelengths, but some wavelengths may be out of phase with the solar cycle (Cahalan et al., 2010; Haigh et al., 2010; Harder et al., 2009). TSI and SSI are calculated by adding the radiative fluxes of all features plus the contribution from the magnetically inactive surface. This approach requires detailed information of all the magnetic features and their temporal changes (Krivova and Solanki, 2008; Wenzler et al., 2006) (see also Section 8.3).

The extension of TSI and SSI into pre-satellite times poses two main challenges. First, the satellite period (since 1978 CE) used to calibrate the models does not show any significant multi-decadal trend. Second, detailed information about the various magnetic features is no longer available and must be deduced from proxies such as sunspots for the last 400 years and cosmogenic radionuclides (^{10}Be and ^{14}C) for the past millennia. Since all reconstructions rely ultimately on the same data (sunspots and cosmogenic radionuclides), but differ in the details of the applied models, the reconstructions agree rather well in their shape, but differ in their amplitude (Figure 5.1b) (Krivova et al., 2011; Lean et al., 2011; Schrijver et al., 2011; Wang et al., 2005) (see Section 8.3.1). ^{10}Be and ^{14}C records reflect not only solar activity, but also the geomagnetic field intensity and effects of their respective geochemical cycles (Pedro et al., 2011; Steinhilber et al., 2012). Correcting for these non-solar components increases the uncertainty of the reconstructions (grey band in Figure 5.1c).

TSI reconstructions are characterized by distinct grand solar minima lasting 50–100 years (e.g. the Maunder Minimum, 1645–1715 CE) that are superimposed upon long-term changes. Spectral analysis of TSI reveals periodicities of 87, 104, 150, 208, 350, 510, ~980, and ~2200 years (Stuiver and Braziunas, 1993) but varying amplitudes (Steinhilber et al., 2009; Vieira et al., 2011). Most recent reconstructions show a considerably smaller difference (<0.1%) in TSI between the averaged instrumental period and the Maunder

minimum (1645–1715 CE) when the Sun was very quiet, compared to the often used reconstruction of Lean et al., (1995b) (0.24%). The effect of solar forcing on climate during the last millennium is assessed in (Section 5.3.5).

Note that the current state of understanding the effects of galactic cosmic rays on clouds is discussed in Section 8.3.1.5 and not in this chapter.

[INSERT FIGURE 5.1 HERE]

Figure 5.1: a) Two reconstructions of volcanic forcing for the past 1000 years derived from ice core sulfate and used for PMIP3-CMIP5 (Coupled Model Intercomparison Project) simulations (Schmidt et al., 2011). GRA: (Gao et al., 2008); CEA: (Crowley and Unterman, submitted; Crowley and Hyde, 2008; Timmreck et al., 2009). Volcanic sulfate peaks identified from their isotopic composition as originating from the stratosphere (Cole-Dai et al., 2009) are indicated by squares (green: Greenland; brown: Antarctica) (Baroni et al., 2008). b) TSI reconstructions back to 1000 CE. Proxies of solar activity (e.g., sunspots, ^{10}Be) are used to estimate the parameters of the models or directly TSI. All records except LBB (Lean et al., 1995b) have been used for PMIP3-CMIP5 simulations (Schmidt et al., 2011). DB: (Delaygue and Bard, 2011); MEA: (Muscheler et al., 2007); SBF: (Steinhilber et al., 2009); WLS: (Wang et al., 2005); VSK: (Vieira et al., 2011). Before 1600 CE, the 11-year cycle has been added artificially to the original data. c) TSI reconstruction (100-year low-pass filtered; grey shading: 1 standard deviation uncertainty range) for the past 9300 years (Steinhilber et al., 2009). The reconstruction is based on ^{10}Be and calibrated using the relationship between instrumental data of the open magnetic field, which modulates the production of ^{10}Be and TSI for the past 4 solar minima. d) Wavelet analysis (Torrence and Compo, 1998) of TSI showing the existence of several preferred periodicities (87, 104, 150, 208, 350, 510, ~980, ~2200 years) with varying amplitudes.

5.2.1.3 Volcanic Forcing

Volcanic activity affects global climate through the radiative impacts of atmospheric sulphate aerosols injected in the stratosphere by volcanic eruptions (see Chapters 2, 7, 8, 10 and 11). Quantifying pre-satellite volcanic forcing is important for historical and last millennium climate simulations, climate-sensitivity estimates and detection and attribution studies. Reconstructions of past volcanic forcing are based on chemical records from multiple ice cores from Greenland and Antarctica, combined with atmospheric modelling of aerosol distribution and optical depth.

Since AR4, two new reconstructions of spatial distribution of volcanic aerosol optical depth have been produced from polar ice cores, spanning the past 1500 years (Gao et al., 2008; Gao et al., 2006) and 1200 years (Crowley and Unterman, submitted; Crowley and Hyde, 2008) (Figure 5.1a). The timing and relative magnitude of large stratospheric volcanic aerosol injections is generally consistent amongst these and earlier studies (Jansen et al., 2007) for the last 700 years; the 1783 CE Laki (Iceland) eruption being a notable exception. The recurrence time of past large volcanic aerosol injections (eruptions with radiative forcing >1 W m^{-2}) is 35 ± 28 (1 standard deviation; Gao et al., 2008) and 39 ± 33 years (Crowley and Unterman, submitted), with only 2–3 periods of 100 years without such eruptions since 850 CE.

Hegerl et al (2006) estimated the uncertainty of the radiative forcing for a given volcanic event to be ~50%. Differences between reconstructions (Figure 5.1a) arise from the selection of different data; their scaling to observations of volcanic aerosol radiative forcing; the identification of the type of injection (tropical vs. high latitude, tropospheric vs. stratospheric); the methods to estimate spatial distributions of optical depths, including atmospheric lifetime (Kravitz and Robock, 2011); the parameterization of scavenging processes for large events (e.g., Kuwae, 1453 CE) (Timmreck et al., 2009). Key limitations are associated with ice core age scales, proxy types (e.g., sulphate flux or electrical conductivity), identification of volcanic events and spatio-temporal variability in deposition patterns (Moore et al., 2012).

A new independent methodology has recently been developed to distinguish between tropospheric and stratospheric volcanic aerosol deposits, based on the specific sulphur isotopic composition caused by mass-independent fractionation during photochemical reactions above the ozone layer (Baroni et al., 2007). The stratospheric character of several large eruptions has started to be assessed from Greenland and/or Antarctic ice core sulphur isotope data (Baroni et al., 2008; Cole-Dai et al., 2009) with a debate on data interpretation for the Laki event (Lanciki et al., 2012; Schmidt et al., submitted) (Figure 5.1a).

The use of different volcanic forcing reconstructions in pre-Coupled Model Intercomparison Project (CMIP) 5 (see AR4 Chapter 6) and PMIP3/CMIP5 last millennium simulations (Schmidt et al., 2011), together with the methods used to implement these volcanic indices with different representations of aerosols in climate models is a source of uncertainty in model inter-comparisons. The impact of volcanic forcing on last millennium climate is assessed in Sections 5.3, 5.4 and 5.5 and in Chapter 10, Section 10.7.

5.2.2 Radiative Perturbations from Greenhouse Gases and Dust

5.2.2.1 Atmospheric Concentrations of CO_2, CH_4 and N_2O from Ice Cores

Air enclosed in polar ice provides a direct, albeit low-pass filtered (Joos and Spahni, 2008; Köhler et al., 2011), record of past atmospheric GHG (greenhouse gas) concentrations complementing instrumental data (see Chapter 2). Since AR4, new and higher resolved records of CO_2, CH_4 and N_2O variations were obtained (Ahn and Brook, 2008; Bereiter et al., 2012; Loulergue et al., 2008; Lüthi et al., 2008; MacFarling Meure et al., 2006; Mischler et al., 2009; Schilt et al., 2010). Centennial variations of up to 10 ppm CO_2, 40 ppb CH_4 and 10 ppb N_2O occur throughout the late Holocene (see Chapter 6, Section 6.2.3 and Figure 6.6). Existing long-term records have been extended from 650 ka to 800 ka (Figures 5.2, 5.3) (Loulergue et al., 2008; Lüthi et al., 2008; Schilt et al., 2010), showing lower than pre-industrial (280 ppm) CO_2 concentration during pre-420 ka interglacial periods. The long CO_2 record reveals subtle long-term (>200 thousand year [kyr]) trends in addition to glacial interglacial variations (Lüthi et al., 2008).

The GHG concentrations stay within well-defined natural limits with maximum interglacial concentrations of about 300 ppm, 800 ppb, and 300 ppb for CO_2, CH_4 and N_2O, respectively, and minimum glacial concentrations of about 172 ppm, 350 ppb, and 200 ppb. The occurrence of a peak similar in size and duration to the anthropogenic rise can be excluded to have occurred during the last 22,000 yr for CO_2 and CH_4 and during the last 16,000 yr for N_2O with very high confidence, even after taking the low-pass filter of the ice core gas archive into account (Joos and Spahni, 2008). The same holds true for rates of change. Observed rates were not encountered during these time intervals and, with medium confidence, also not during the last 800 kyr.

By combining different ice cores, stacked CO_2, CH_4, and N_2O records at centennial to millennial resolution were compiled for the last glacial cycle (Schilt et al., 2010). Significant centennial variations in CH_4 and N_2O during the last glacial are linked to Northern Hemisphere (NH) rapid climate changes, while millennial CO_2 changes are connected to their Southern Hemisphere (SH) bipolar seesaw counterpart (Ahn and Brook, 2008; Bereiter et al., 2012; Capron et al., 2010b; Grachev et al., 2009; Loulergue et al., 2008; Lüthi et al., 2008; Schilt et al., 2010).

New records of $\delta^{13}C$ of atmospheric CO_2 provide important constraints on the sources and processes involved in past GHG changes, which are assessed in Chapter 6 (Sections 6.2.2 and 6.2.3). Significant $\delta^{13}CO_2$ drops during the onset of the last two terminations are suggested to reflect upwelling of old, carbon-enriched deep water contributing to the concurrent CO_2 increase (Lourantou et al., 2010a; Lourantou et al., 2010b; Schmitt et al., 2012). The small late Holocene $\delta^{13}CO_2$ decrease suggests that the multi-millennial CO_2 increase of 20 ppm can be explained by carbonate compensation and coral reef formation (Elsig et al., 2009). The open debate on the relative importance of ocean processes, land use changes, peat uptake (Yu et al., 2010) as drivers of Holocene CO_2 is also addressed in Chapter 6 (Section 6.2.3).

For CH_4, the inter-hemispheric gradient as well as carbon and hydrogen isotopes support the role of changes in boreal and tropical wetlands in explaining most of the observed long-term and centennial pre-industrial changes (Bock et al., 2010; Fischer et al., 2008; Petrenko et al., 2009; Sowers, 2006; Sowers, 2010). These CH_4 stable isotope data rule out, with high confidence, marine clathrate destabilization as a major driver of glacial-interglacial CH_4 variations. The relative importance of anthropogenic (agricultural) versus natural (wetland, biomass burning) causes for the CH_4 increase during the second half of the Holocene remains disputed (Ruddiman et al., 2011; Singarayer et al., 2011) and is assessed in Chapter 6 (Section 6.2.3).

Finally, multiple, consistent ice core CO_2 and CH_4 isotope data show with very high confidence the anthropogenic origin of ongoing changes, since two centuries (Ferretti et al., 2005; Francey et al., 1999; Mischler et al., 2009), further supporting earlier IPCC assessments.

5.2.2.2 Atmospheric CO_2 Concentrations from Geological Proxy Data

Geological proxies provide indirect information on atmospheric CO_2 concentration for time intervals older than covered by ice-core records (see Section 5.2.2.1). Since AR4, the four primary proxy methods have undergone further development (Appendix 5.A, Table 5.A.1). A reassessment of biological respiration and carbonate formation has reduced CO_2 estimates from fossil soils by ~50% (Breecker et al., 2010). Bayesian statistical techniques for calibrating leaf stomatal density reconstructions produce consistently higher CO_2 estimates (Beerling et al., 2009), resulting in more convergence between estimates from the two terrestrial proxies. Recent CO_2 reconstructions using the boron isotope proxy utilise a corrected isotopic fractionation factor in foraminifera (Klochko et al., 2006), and an improved understanding of the evolution of seawater boron isotopes and alkalinity (Foster, 2008). Quantification of the phytoplankton cell-size effects on carbon isotope fractionation has also improved the consistency of the alkenone method (Henderiks and Pagani, 2007). These proxies have also been applied more widely and at higher resolution to a range geological records, resulting in an increased number of atmospheric CO_2 estimates since 65 Ma (Beerling and Royer, 2011). While there is improved consensus between the proxy CO_2 estimates, a significant degree of variation between the different techniques remains. All four techniques have been included in the assessment, as at present, there is insufficient knowledge to discriminate between different proxy estimates on the basis of confidence.

In the time interval between 65 and 45 Ma, the boron isotope proxy estimates span a range of 300 ppm to 3000 ppm, and estimates based on leaf stomatal density values are below 1000 ppm. An independent thermodynamic constraint on Early Eocene atmospheric CO_2 concentration is provided by the occurrence of the sodium carbonate mineral, nahcolite, in about 50-Myr old lake sediments in the Green River Basin, USA (Lowenstein and Demicco, 2006). Nahcolite precipitates in association with halite at the sediment-water interface only at CO_2 levels >1125 ppm, which is inconsistent with lower estimates from stomata and paleosols. While the reconstructions indicate a general decrease in CO_2 concentrations over the past ~ 50 Ma (Figure 5.2), the large scatter of proxy data does not allow for a firm assessment of such trend. For the "Early Eocene Climatic Optimum" (EECO; 54–48 Ma) paleo-CO_2 concentrations stayed likely above the pre-industrial level and below ~2000 ppm with a most likely value of ~1000 ppm (Figure 5.2).

New CO_2 reconstructions based on marine proxies undertaken for the Pliocene (~5.3–2.6 Ma) have produced consistent estimates mostly in the range 330 ppm to 420 ppm (Bartoli et al., 2011; Pagani et al., 2010; Seki et al., 2010). There is high confidence that CO_2 levels were above pre-industrial interglacial concentration (~280 ppm), but did not exceed ~500 ppm. Additional confidence can be placed on the boron- and alkenone-based CO_2 reconstructions for the Pliocene, because of the agreement between the two proxies, and that a boron-derived dataset for the last 2 Myr agrees within error (± 25 ppm) with the ice core record (Hönisch et al., 2009).

[INSERT FIGURE 5.2 HERE]

Figure 5.2: (Top) Radiative forcings and perturbations and orbital-scale Earth system responses 3.6 Ma to present. Reconstructed dust mass accumulation rate from the Atlantic sector of the Southern Ocean (red) (Martinez-Garcia et al., 2011). Sea level curve (purple) is the stacked benthic oxygen isotope proxy for ice volume and ocean temperature (Lisiecki and Raymo, 2005) calibrated to global average eustatic sea level (Miller et al., 2012; Naish and Wilson, 2009). Also shown are global eustatic sea level reconstructions for the last 500 kyr based on sea level calibration of the $\delta^{18}O$ curve using dated coral shorelines (grey line; Waelbroeck et al., 2002) and weighted mean estimates (2 standard deviation uncertainty) for far-field reconstructions of eustatic peaks during mid-Pliocene interglaciations (red dots; Miller et al., 2012). The dashed horizontal line represents modern sea level. Tropical sea surface temperature (black line) based on a stack of 4 alkenone-based SST reconstructions (Herbert et al., 2010). Atmospheric CO_2 measured from EPICA Dome C ice core (blue line; Lüthi et al., 2008), and estimates of CO_2 from boron $\delta^{11}B$ isotopes in foraminifera in marine sediments (blue triangles; Hönisch et al., 2009; Seki et al., 2010), and phytoplankton alkenone-derived carbon isotope proxies (red diamonds; Pagani et al., 2010; Seki et al., 2010), plotted with 2 standard deviation uncertainty. Present (2012 CE) and pre-industrial CO_2 concentrations are indicated with long-dashed and short-dashed grey lines, respectively. (Bottom) Concentration of atmospheric CO_2 for the last 65 Myr is reconstructed from marine and terrestrial proxies and complied by Beerling and Royer (2011; additional boron CO_2 proxy data from Pearson and Palmer (2000) are also included). Individual proxy methods are colour-coded. Errors represent reported uncertainties (plotted with 2 standard deviation uncertainty; see also Table 5.1 for assessment of confidence of proxies). Most of the data points for CO_2 proxies are based on duplicate and multiple analyses. The blue line is a kernel regression through all the data points with a bandwidth of 8 Myr prior to 30 Ma, and 1 Myr to present. The blue shading is a 1 standard

deviation. Uncertainty band constructed using block bootstrap resampling (Mudelsee et al., submitted). Shaded grey vertical band highlights global warmth during the Pliocene (~5–2.7 Ma; about +2–3°C global mean; see also Box 5.2 Figure 1). The red box labelled MPWP represents the Mid Pliocene Warm Period from 3.3–3 Ma)

5.2.2.3 Past Changes in Mineral Dust Aerosol (MDA) Concentrations

AR4 assessed the importance of the MDA radiative perturbation at the Last Glacial Maximum (LGM, centered on 21 thousand years ago [ka]), with implications for estimating climate sensitivity. Since AR4, new records of past MDA deposition have been obtained.

A MDA-flux reconstruction from the Southern Ocean imply reduced dust generation and transportation during the Early Pliocene, with dust mass accumulation rates at or below Holocene levels and the first significant rise around 2.7 Ma (Figure 5.2), coincident with the intensification of glaciation in the Northern Hemisphere (Martinez-Garcia et al., 2011).

In central Antarctica, MDA fluxes are systematically higher by a factor of ~30 during glacial compared to interglacial periods (Fischer et al., 2007; Lambert et al., 2008; Petit and Delmonte, 2009). This is due to enhanced dust production in southern South America and Australia (De Deckker et al., 2010; Gabrielli et al., 2010; Wegner et al., 2012), and to atmospheric MDA lifetime change (Petit and Delmonte, 2009). MDA flux records from marine sediments from the Atlantic sector of the Southern Ocean (Martinez-Garcia et al., 2011) show a glacial/interglacial decline of only a factor of 5 and may serve as first-order estimate for the changes in Patagonian dust source strength (Martinez-Garcia et al., 2011). Equatorial Pacific glacial-interglacial MDA fluxes co-vary with Antarctic records, but with a factor of 3–4 between interglacial and glacial periods (Winckler et al., 2008), attributed to enhanced dust production from Asian and northern South American sources in glacial times (Maher et al., 2010).

In Greenland ice cores, dust concentrations are higher by 1 to 2 orders of magnitude during cold (glacial and stadial) compared to warm (interglacial and interstadial) periods. This is mainly due to changes in the dust sources for Greenland (Asian desert areas), atmospheric lifetime and transportation of MDA (Fischer et al., 2007). A strong coherence is observed between dust in Greenland ice cores and aeolian deposition in European loess formations (Antoine et al., 2009).

These spatial and temporal fluctuations in atmospheric MDA concentrations make it difficult to assess the global radiative forcing linked with past MDA changes. Global data synthesis is so far only available for the LGM, showing 2–4 times more dust deposition than today (Derbyshire, 2003; Maher et al., 2010). Estimates of global mean LGM dust radiative forcing vary from –3 W m^{-2} to +0.1 W m^{-2}, due to uncertainties in radiative properties ; the best estimate value however remains at –1 W m^{-2} as in AR4 (Claquin et al., 2003; Mahowald et al., 2011; Mahowald et al., 2006; Patadia et al., 2009; Takemura et al., 2009; Yue et al., 2010).

[START BOX 5.1 HERE]

Box 5.1: Earth-System Feedbacks and their Role in Climate Change

The response of the Earth system to perturbations is determined by the adjustment time (inertia) of individual components of the Earth system and by feedbacks within and between these components (some of which are represented in Box 5.1, Figure 1). An initial response is amplified if positive feedbacks dominate, but damped if negative feedbacks are stronger. The time-evolution of the response to a temporary perturbation, such as a radiative forcing anomaly, is governed by the magnitude and timescale of these processes. The Earth system may then return to its initial state on a timescale controlled by its inertia and by the relative strength of negative and positive feedbacks. Alternatively, the changes may be irreversible (Section 5.8) if the temporary perturbation/forcing drives the Earth system to a new (quasi)-equilibrium state in which it remains for a very long time, even after the removal of the initial perturbation/forcing. In this case one would observe hysteresis behaviour. The presence of multiple equilibria is closely linked to the existence of nonlinear feedbacks and bifurcations. A third type of response is the excitation of oscillatory behaviour, which may result from a combination of positive and delayed negative feedbacks. To quantify the climate response to external radiative perturbations/forcings for different climate background conditions, two different concepts of equilibrium climate sensitivity have been introduced (see Chapter 1):

- The *Charney climate sensitivity* (CCS) (Hansen et al., 1985; Hansen et al., 2008; Schneider von Deimling et al., 2006a) characterizes the equilibrium climate response of the Earth system to radiative perturbations, allowing for fast feedbacks between atmosphere, ocean, sea ice and land, but assuming the stationarity of Earth system components, such as the carbon cycle, ice sheets and vegetation. This concept was adopted in TAR and AR4. Most recent AR5 updates on the probability distribution of the present-day Charney climate sensitivity can be found in Chapter 12.

- In contrast, the *Earth-system climate sensitivity* (ESCS) (Hansen et al., 2008; Lunt et al., 2010) quantifies the global mean surface temperature response to radiative perturbations, accounting for other Earth System feedbacks, involving ice sheets, vegetation and the carbon cycle which often respond on timescales of hundreds to thousands of years and beyond.

To estimate the CCS from the difference between glacial and interglacial climate states, greenhouse gas, orbital, ice-sheet albedo and other processes causing radiative perturbations (e.g., linked with vegetation or dust) have to be considered. However, following the ESCS concept, greenhouse gas variations and ice-sheet albedo changes have to be treated as feedbacks, rather than as forcings. Both feedbacks operate overall as positive feedbacks and hence increase the ESCS relative to estimates of the CCS. While CCS and ESCS can be readily calculated from radiative perturbation experiments conducted with climate and Earth-System models, the applicability of these equilibrium concepts to paleo proxy data is less straightforward. On timescales of 10^4–10^5 years the Earth system is continuously forced by orbitally-induced variations in the distribution of solar radiation. As a result, the slow components of the Earth system, that have similar response timescales (10^3–10^5 years), such as ice sheets and the global carbon cycle, may in fact never be in equilibrium with the continuously varying external forcings. The implications of this potential non-equilibrium behaviour are far reaching and concern in particular estimates of ESCS. For instance, as a result of lower pre-industrial orbital eccentricity compared to the LGM, the global mean annual orbital forcing difference between these states amounts to about –0.014 W m^{-2}. Wrongly applying the ESCS concept and falsely assuming that the LGM was in equilibrium with the orbital forcing, one would obtain a very large and negative ESCS value, which is highly unrealistic. Moreover, the existence of multiple equilibria, irreversible responses and bifurcations in the Earth system can lead to widely different estimates of the ESCS and estimates that would differ depending on whether the system moves from cold to warm or from warm to cold conditions.

To further document the complexities resulting from the interactions of fast and slow components in the Earth system and the associated new modelling challenges, we focus on the above-mentioned example of climate-ice-sheet feedbacks. Ice sheets have played an essential role in Earth's climate history. They interact with the atmosphere, the ocean, the lithosphere and the surrounding vegetation (see Box 5.1, Figure 1). Ice sheets form when snow accumulation exceeds summer melting. Expansion of an ice sheet replaces previously vegetated areas, with relatively low albedo, by higher-albedo ice, leading to major changes in surface albedo and heat balance, and changing the mass balance of the ice sheet. As ice sheets grow in height and area, surface temperatures drop as a result of the lapse rate effect, but also snow accumulation decreases because colder air holds less moisture (inset in Box 5.1, Figure 1, shows typical vertical profiles of temperature and humidity). This so-called elevation-desert effect (Oerlemans, 1980) is an important negative feedback for ice-sheets and limits their growth under cold conditions. Ice sheets also affect the atmospheric stationary wave structure and associated regional patterns of temperature and snowfall (e.g.,, Roe and Lindzen, 2001). The enormous weight of mature ice sheets causes a depression of the underlying bedrock, a drop in ice sheet height and hence a warming of its surface as a result of the lapse rate effect. The lithospheric adjustment has been shown to play an important role in delaying the ice sheet response to orbital forcing (van den Berg et al., 2008). Higher ice sheets can be associated with enhanced calving at their margins, because the ice flow will be accelerated directly by increased surface slopes and indirectly by lubrication at the base of the ice sheet. Calving, basal lubrication and other forms of thermo-mechanical coupling may have played important roles in accelerating glacial terminations, and hence in contributing to the temporal saw-tooth structure of glacial cycles (Figure 5.3). Other important dynamical processes are ice-sheet/ice shelf ocean instabilities, which may have caused past variations of the West Antarctic ice-sheet (Pollard and DeConto, 2009) and Laurentide ice sheet (Alvarez-Solas et al 2010). Quantifying the magnitudes of these feedbacks relative to each other and for different past climate periods requires concerted

modelling efforts, using a range of Earth-System models in combination with the analysis of quantitative reconstructions of past climate variations and present-day process studies.

Major uncertainties remain in our understanding of Earth-System feedbacks and how they contribute to climate dynamics and ESCS. Whereas the initial response to anthropogenic greenhouse warming of some Earth system components such as ice-sheets can be quite fast (order 10–100 years), their long-term adjustment to the ongoing warming will exceed human lifetimes. Hence the evolution of the Greenland and Antarctica ice-sheets for the next centuries will not be in equilibrium with the current radiative perturbations. This also implies that current climate change is very likely to affect the ice-sheets for centuries with chances of threshold behaviour, as discussed for Greenland (Robinson et al., 2012) and the West-Antarctic ice-sheet (Kopp et al., 2009; Kriegler et al., 2009).

[**INSERT BOX 5.1, FIGURE 1 HERE**]

Box 5.1, Figure 1: Schematic illustration of multiple interactions between ice sheets, solid Earth, and climate system which can drive internal variability and affect the coupled ice sheet–climate response to external forcings on timescales of hours to millions of years.

[END BOX 5.1 HERE]

5.3 Earth System Responses and Feedbacks at Global and Hemispheric Scales

This section updates the information available since AR4 on changes in surface temperature on million-year to orbital timescales and for the last 2000 years. New information on changes of the monsoon systems and atmospheric circulation on glacial-interglacial timescales is also assessed.

5.3.1 High CO_2 Worlds and Temperature

Cenozoic (last 65 Ma) geological archives provide examples of natural climate states globally warmer than the present, some of which are associated with atmospheric CO_2 concentrations above pre-industrial levels. The relationship between times of global warmth and high CO_2 during the Cenozoic is far from straightforward, and is complicated by factors such tectonics and the evolution of biological systems, which play an important role in the carbon cycle (e.g., Zachos et al., 2008). Although new reconstructions of deep ocean temperatures from benthic $\delta^{18}O$ records have been compiled since AR4 (e.g.,Cramer et al., 2011), low confidence remains in the precise relationship between CO_2 and deep-ocean temperature (e.g., Beerling and Royer, 2011).

Since AR4 there are now sufficient proxy and model data from two warm periods in the Cenozoic to enable an assessment of forcing, feedbacks and the surface temperature response (e.g., Dowsett et al., 2012; Lunt et al., 2012). These are the "mid-Pliocene warm period" (MPWP; 3.3–3.0 Ma) and the Early Eocene climatic optimum. Reconstructions of surface temperatures based on proxy data remain challenged by: (i) the limited number and uneven geographical distribution of sites, (ii) seasonal and latitudinal biases and (iii), the validity of assumptions required by each proxy method (assessed in Appendix 5.A, Table 5.A.2). There is also a lack of consistency in the way uncertainties are reported for proxy climate estimates. In most cases error bars represent the analytical and calibration error. In some compilations qualitative confidence assessments are reported to account for the quality of the age control, number of samples, fossil preservation and abundance, performance of the proxy method utilized, and agreement of multiple proxy estimates (e.g., Dowsett et al., 2012; MARGO Project Members, 2009).

Glacial-interglacial cycles inferred from Pliocene benthic $\delta^{18}O$ records imply moderate fluctuations in global ice volume paced by the 41 kyr obliquity cycle (Lisiecki and Raymo, 2005; Naish et al., 2009a). This orbital variability is also evident in a tropical Pacific sea surface temperature (SST) (Herbert et al., 2010) and Southern Ocean mineral dust aerosol records (Martinez-Garcia et al., 2011), and indicate a close coupling between temperature, atmospheric circulation and ice volume during MPWP (Figure 5.2). Model-data comparisons (see also Box 5.2, Figure 1) provide high confidence that mean surface temperature was warmer than pre-industrial for the average interglacial climate state during the MPWP (Dowsett et al., 2012; Haywood et al., submitted; Salzmann et al., submitted). Estimated global mean SST was +1.7°C (without given uncertainty) above the 1901–1920 CE mean (Lunt et al., 2010), based on a synthesis of 84 SST

estimates. GCMs agree with this SST anomaly (to within ± 0.5°C), and produce a range of global mean surface air temperature anomalies of 1.9–3.5°C (Haywood submitted). The MPWP represents the last time atmospheric CO_2 concentrations were in the range 330–420 ppm (Section 5.2.2.2). Weakened meridional temperature gradients are shown by all GCM simulations, and have significant implications for the stability of polar ice sheets and sea level (see Section 5.6). Vegetation reconstructions (Salzmann et al., 2008) imply that the global extent of arid deserts decreased, and forests replaced tundra in the Northern Hemisphere, and GCMs predict an enhanced hydrological cycle, but with large regional differences in total precipitation between individual models (Haywood et al., submitted). The East Asian Summer Monsoon, as well as other monsoon systems, may have been enhanced (e.g., Wan et al., 2010), and there is high confidence from models of increased precipitation in the tropics during this time (Haywood et al., submitted).

The EECO represents the last time atmospheric CO_2 concentrations may have reached a level of ~1000 ppm (Section 5.2.2.2). However, unlike the MPWP, there were no substantial polar ice sheets, and climatic boundary conditions including oceanic and continental configurations, vegetation type and distribution were significantly different from today. Proxy temperature estimates are few and of limited geographical distribution. Therefore, while there is reasonably close agreement between proxy and model surface air temperature (SAT) reconstructions (within 2 standard deviations) for the EECO (Hollis et al., submitted; Huber and Caballero, 2011; Lunt et al., 2012), medium confidence is placed on the global mean surface temperature anomaly estimate of +8°C to +14°C (Box 5.2, Figure 1).

Climate reconstructions for the warm periods of the Cenozoic also provide an opportunity to assess the long-term climate sensitivity, or "Earth-system climate sensitivity" (ESCS) (Box 5.1). The limited number of paleo-data and models for MPWP, which take into account slow feedbacks such as ice sheets and the carbon cycle, imply with medium confidence ESCS may be up to 2 times the Charney Climate sensitivity (CCS) (Haywood et al., submitted; Lunt et al., 2010; Pagani et al., 2010). However, if the slow amplifying feedbacks associated with ice sheets and CO_2 are included in the forcing term then estimates of "paleo-sensitivity" approximate the CCS from models (PALAEOSENS Project Members, accepted).

Complications arise estimating climate sensitivity from transient radiative perturbations further back in the Cenozoic, due to long-term changes in the Earth system which change the background climate state. An example is the pronounced transient global warming and carbon-cycle perturbation during the Paleocene-Eocene Thermal Maximum, which punctuated an already warm climate state at the beginning of the EECO. Uncertainties on both global temperature and CO_2 reconstruction preclude deriving robust quantitative estimates of CCS or ESCS from the available proxy data (DeConto et al., 2012).

[START BOX 5.2 HERE]

Box 5.2: Polar Amplification

Polar amplification occurs when surface temperature change in high latitudes exceeds the global average temperature change in response to climate forcings. Robust evidence for polar amplification in either one or both hemispheres has been found in climate model experiments of past and future climate change, paleo-climate data and recent instrumental temperature records. The relative strength of internal climate feedbacks (Box 5.1) determines the transient and equilibrium response to external forcings. The specific mix of these feedbacks is very much dependent on the region under consideration.

In the Arctic Ocean, the sea ice/ocean albedo surface feedback plays an important role (Curry et al., 1995; Serreze and Barry, 2011). With retreating sea ice, surface albedo decreases, air temperatures increase and the ocean can absorb more heat. The resulting ocean warming contributes to further sea ice melting. The sea ice ocean surface albedo feedback can exhibit threshold behaviour when temperatures cross the freezing point of sea ice. This may also translate into a strong seasonality of the response characteristics. Other feedbacks, including water vapour and cloud feedbacks have been suggested as important amplifiers of Arctic Ocean climate change (Abbot and Tziperman, 2008, 2009; Graversen and Wang, 2009; Lu and Cai, 2009; Screen and Simmonds, 2010; Vavrus, 2004). In continental Arctic regions with seasonal snow-cover, changes in radiative forcing can heavily influence the snow cover (Ghatak et al., 2010), and thus the surface albedo. Other positive feedbacks operating on timescales of decades and centuries in continental high latitude regions are associated with surface vegetation changes (Bhatt et al., 2010) and thawing permafrost (e.g.,

Walter et al., 2006). On glacial/interglacial timescales the very slow ice-sheet-albedo response to external forcings (see Box 5.1) is an important contributor to polar-amplification in the Northern Hemisphere.

An amplified response of Southern Ocean air temperatures to radiative perturbations also emerges from the sea ice albedo feedback. However, in contrast to the Arctic Ocean, which in parts is highly stratified, mixed layer depths in the Southern Ocean typically exceed several hundreds of meters which allows the ocean to take up vast amounts of heat (Gregory, 2000) and damp the sea-surface temperature response to external forcing. This process is likely to affect the transient SST response for instance to rapid atmospheric CO_2 changes and requires a much longer equilibration time than in other areas of the world ocean. In the context of greenhouse warming, one, hence, expects an asymmetric warming between Arctic and Southern Ocean, with the former responding quicker to the current and projected changes in greenhouse gasses than the latter. Above the Antarctic ice-sheet, however, surface-air temperature can respond quickly to radiative perturbations.

Box 5.2, Figure 1 illustrates the polar amplification effect for three different periods of Earth's climate history: (i) the Early Eocene Climatic Optimum, EECO (54–48Ma), (ii) the Mid-Pliocene Warm Period, MPWP (3.3–3 Ma) and (iii) the Last Glacial Maximum, LGM (~21 ka). When comparing proxy data or model simulations for the three different periods, one has to note that these past climate states also corresponded to very different boundary conditions and forcings.

As a result of uncertainties in estimates of forcings and boundary conditions, proxy data interpretations and calibrations, and possible model deficiencies, mismatches between model simulations and proxy reconstructions are to be expected in the comparison shown in Box 5.2, Figure 1. In spite of this, all three timeslices reveal, albeit for different reasons, robust Arctic and Antarctic surface air temperature amplification of up to 2 times the global mean. The absence (EECO), or presence (LGM) of massive extratropical ice-sheets is likely to affect the zonally averaged surface temperatures due to the lapse-rate effect (see Box 5.1), hence contributing to the polar amplification.

Transient polar amplification as recorded in historical instrumental data and as projected by AOGCMs for the 21st century involves different mechanisms than for the "equilibrium" past states featured in Box 5.2, Figure 1. Instrumental temperature records show that the Arctic north of 60° latitude has warmed at a rate of 1.36°C per century since 1875, approximately twice as strong as the global average (Bekryaev et al., 2010), with an even stronger rate of warming of 1.35°C during the last decade (2000–2010). These warming trends can be attributed (Gillett et al., 2008) to a large extent to anthropogenic factors (see AR5 Chapter 10). Available observations (Chylek et al., 2009; Polyakov et al., 2010; Screen and Simmonds, 2010; Semenov et al., 2010; Serreze et al., 2009; Spielhagen et al., 2011) further confirm that the strongest recent warming occurs in autumn and winter, strongly linking Arctic amplification to feedbacks associated with the seasonal reduction in sea ice extent and duration, as well as the insulating effect of sea ice in winter (e.g., Serreze and Barry, 2011; Serreze et al., 2009; Soden et al., 2008). For future model projections, following the RCP4.5 scenario, annual mean Arctic (70^oN–90^oN) warming is expected to exceed the global average 2.7-fold for the period 2081–2100 compared to 1986–2005 (see Chapter 12).

Currently there is no compelling observational evidence for a robust CO_2-induced polar amplification in Antarctica. Whereas the Antarctic Peninsula is experiencing one of the strongest regional warming trends (0.5°C decade^{-1} over the past 50 years), almost twice that of the global mean temperature, zonal mean Antarctic surface warming has been modest at 0.1°C per decade over the same time period (O'Donnell et al., 2010; Steig et al., 2009). West Antarctic Ice Sheet (WAIS) Divide borehole measurements indicate warming of 0.8°C per decade during the last two decades (Orsi et al., 2012), but it remains unclear if this trend represents long term polar amplification, or is within the range of regional decadal variability (see also AR5 Chapter 2). Polar amplification in the Southern Ocean and Antarctica is virtually absent in the transient CMIP5 RCP4.5 future simulations (see Chapter 12).

The magnitude of polar amplification is of concern due to its impacts on ice sheet stability and sea level (see Sections 5.6, 5.8.1 and Chapter 13) and for the carbon cycle feedbacks such as those linked with permafrost melting (see Chapter 6).

[INSERT BOX 5.2, FIGURE 1 HERE]

Box 5.2, Figure 1: Data and multi model mean (MMM) comparisons of a) SST, b) zonally-averaged MMM SST gradient and proxy SST, c) zonally averaged MMM surface air temperature (SAT) gradient and proxy SAT, and d) SAT anomalies for the Early Eocene Climatic Optimum (EECO, top row), the mid-Pliocene warm period (MPWP, middle row) and the LGM (bottom row). Model temperature anomalies are calculated relative to the pre-industrial value of each model in the ensemble prior to calculating the MMM anomaly (a, d; colour shading). Zonal MMM gradients (b, c) are plotted with a shaded band indicating 2 standard deviation uncertainty. Site specific temperature anomalies estimated from proxy data are calculated relative to present site temperatures and are plotted (a, d) using the same colour scale as the model data, and a circle size scaled to estimates of confidence. In the zonal plots (b, c) the proxy data anomalies are shown with error bars indicating 2 standard deviation uncertainty. Proxy data compilations for the LGM are from MARGO Project Members (2009) and Bartlein et al., (2011), for the MPWP are from Dowsett et al., (2012) and Salzmann et al., (2008), and for the EECO are from Hollis et al., (submitted) and Lunt et al., (2012). Model ensemble simulations for the LGM are after (Harrison et al., submitted), for the Pliocene are from Haywood et al., (submitted), and for the EECO are after Lunt et al., (2012).

[END BOX 5.2 HERE]

5.3.2 Glacial-Interglacial Dynamics

5.3.2.1 Role of CO_2 in Glacial Cycles

Numerous paleoclimate records demonstrate that climate variability increased considerably around 2.7 Ma after the onset of glacial cycles with timescales close to the periods of Earth's orbital variations (approx. 21, 41 and 100 kyr) (Jansen et al., 2007). Recent modelling work provides strong support for the notion that variations in Earth's orbital parameters are one of the key factors in generating long-term variability of Earth's climate. In particular, simulations with GCMs (Carlson et al., 2012; Herrington and Poulsen, 2012) support the principal conjecture of the Milankovitch theory that a reduction in northern hemisphere summer insolation produces sufficient cooling to initiate ice sheet growth. Since orbital forcing can be accurately determined for the future (Berger and Loutre, 1991), efforts can be made to predict the onset of the next glacial period. However, the glaciation threshold depends not only on insolation but also on atmospheric CO_2 content (Archer and Ganopolski, 2005). Models of different complexity have been used to investigate the response to orbital forcing in the future for a range of atmospheric CO_2 levels. These results show consistently that a glacial inception is unlikely to happen within the next approximate 50 kyr if either atmospheric CO_2 concentrations remain above 300 ppm or cumulative carbon emissions exceed 1000 PgC (Archer and Ganopolski, 2005; Cochelin et al., 2006; Loutre and Berger, 2000). Only if atmospheric CO_2 content were below the pre-industrial level, would a glaciation be possible within the next several thousand years (Cochelin et al., 2006; Kutzbach et al., 2011; Loutre and Berger, 2000; Tzedakis et al., 2012; Vettoretti and Peltier, 2011). Even for the RCP 2.6 scenario, atmospheric CO_2 concentrations will exceed 300 ppm until the year 3000 CE (see Chapter 12). Based on our understanding of glacial inceptions during the late Quaternary, it seems therefore very unlikely that orbital forcing on its own would trigger a glacial inception before the end of the next millennium.

Comprehensive understanding of the dynamics of glacial cycles, especially its strongly nonlinear aspects, remains a scientific challenge. In particular, the mechanisms of abrupt glacial terminations after long periods of ice sheet build-up are still not well understood. New paleoclimate records document that all recent glacial terminations occurred during periods of high summer insolation in the northern hemisphere (Cheng et al., 2009; Kawamura et al., 2007). Climate-ice sheet models with varying degrees of complexity and forced by orbital variations and reconstructed atmospheric CO_2 concentrations simulate ice volume variations and other climate characteristics during the last and several previous glacial cycles consistent with paleoclimate records (Abe-Ouchi et al., 2007; Bonelli et al., 2009; Ganopolski et al., 2010) (see Figure 5.3).

There is high confidence that orbital forcing is the only external driver of glacial cycles. However, atmospheric CO_2 content plays an important role as internal feedback. Orbital-scale variability in CO_2 concentrations over the last several hundred thousand years covary (Figure 5.3) with proxy climate records including reconstructions of global ice-volume (Lisiecki and Raymo, 2005), climatic conditions in central Asia (Prokopenko et al., 2006), tropical (Herbert et al., 2010) and Southern Ocean SST (Lang and Wolff, 2011; Pahnke et al., 2003; Parrenin et al., submitted), deep ocean temperature (Elderfield et al., 2010), biogeochemical conditions in the North Pacific (Jaccard et al., 2010), and deep ocean ventilation (Lisiecki et al., 2008). Such close linkages between CO_2 concentration and climate variability are consistent with

modelling results suggesting with high confidence that glacial-interglacial variations of CO_2 and other greenhouse gases explain a considerable fraction of glacial-interglacial climate variability in regions not directly affected by the Northern Hemisphere continental ice sheets (Shakun et al., 2012; Timmermann et al., 2009).

[INSERT FIGURE 5.3 HERE]

Figure 5.3: Orbital parameters and proxy records over the past 800 kyr. (a) Eccentricity, (b) obliquity, (c) precessional parameter (Berger and Loutre, 1991), (d) atmospheric concentration of CO_2 from Antarctic ice cores (Ahn and Brook, 2008; Lüthi et al., 2008; Petit et al., 1999; Siegenthaler et al., 2005), (e) tropical SST stack (Herbert et al., 2010), (f) Antarctic temperature stack based on up to seven different ice cores (Blunier and Brook, 2001; EPICA Community Members, 2006; Jouzel et al., 2007; Petit et al., 1999; Stenni et al., 2011; Watanabe et al., 2003), (g) stack of benthic $\delta^{18}O$, a proxy for global ice volume and deep ocean temperature (Lisiecki and Raymo, 2005), (h) reconstructed sea level (Waelbroeck et al., 2002). Solid lines represent orbital forcing and proxy records, dashed lines depict results of simulations with climate and climate-ice sheet models forced by variations of the orbital parameters and the atmospheric concentrations of the major greenhouse gases. Short dashed line: CLIMBER-2 (Ganopolski and Calov, 2011), long dashed line: IcIES (Abe-Ouchi et al., 2007), dotted line: Bern3D (Ritz et al., 2011). Note the change of the age-axis scale at 140 ka.

Continental temperatures in Antarctica are governed by a number of processes, including the dominant CO_2 radiative effect, orbital forcing and changes in ice-sheet height. Previous reconstructions indicated a lead of Antarctic temperature over CO_2 concentration during previous glacial terminations by 800 ± 600 years (Caillon et al., 2003; Monnin et al., 2001; Appendix 5.A, Table 5.A.3). Recently an improved estimate of gas ice-ice age differences in different ensembles of Antarctic ice cores suggested that earlier studies likely overestimated this lead. For the last glacial termination the most recent estimate is indistinguishable from zero (Parrenin et al., submitted; Pedro et al., 2012).

Large-scale reconstructions of Southern Hemisphere climate change (Shakun et al., 2012) for the last glacial termination document a lead of Southern Hemisphere averaged temperature over Northern Hemisphere temperature. This lead can be explained by the bipolar thermal seesaw concept (Stocker and Johnsen, 2003) (see also Section 5.7) related to changes in the interhemispheric ocean heat transport caused by weakening of the AMOC during glacial termination (Ganopolski and Roche, 2009). Southern Hemisphere warming prior to Northern Hemisphere warming can also be explained by the fast sea ice response to changes in austral spring insolation (Stott et al., 2007; Timmermann et al., 2009). According to these mechanisms, southern temperature lead over Northern Hemisphere neither contradicts the northern hemisphere forcing of deglacial ice volume changes (high confidence), nor the important role of CO_2 in generating glacial-interglacial temperature variations due to the greenhouse effect.

5.3.2.2 Extratropical Atmospheric Circulation Changes

It has been suggested that the strength and position of Southern Hemisphere westerlies exerts an important control on the portioning of CO_2 between ocean and atmosphere via changes in upwelling intensity in the Southern Ocean (Toggweiler et al., 2006). Accordingly, southward shift and intensification of the Southern Hemisphere westerlies during a glacial termination are considered to enhance upwelling of carbon-rich waters over the Southern Ocean. This mechanism provides a positive feedback to the climate-carbon system during glaical terminations (see Chapter 6). However, the actual state of the Southern Hemisphere westerlies under LGM conditions remains debated. Proxy records indicate consistently an intensification and/or southward shift of the westerly belt through the last glacial termination, which extended into the late Holocene (Anderson et al., 2009; Bard and Rickaby, 2009; Beal et al., 2011; De Deckker et al., 2012; Fletcher and Moreno, 2011; Sikes et al., 2009), albeit with regional and seasonal complexity (Lamy et al., 2010; Shulmeister et al., 2004) . Contrary to the paleo-proxy interpretations, climate model experiments using LGM boundary conditions do not present an unequivocal picture. Only some models show small equatorward shifts or weakening of the southern hemisphere westerlies since the LGM (Chavaillaz et al., submitted; Rojas et al., 2009). Overall, while there is medium confidence in direction and magnitude of reconstructed changes in the Southern Hemisphere westerlies, only low confidence exists with regard to the modelled changes in Southern Hemisphere westerlies.

Based on a range of independent model experiments, there is high confidence that the paths of Northern Hemisphere westerlies was orographically steered by the glacial ice-sheets over North America and Eurasia

(Eisenman et al., 2009; Justino et al., 2005; Li and Battisti, 2008; Pausata et al., 2011b) (see also Section 5.4.2).

5.3.2.3 Monsoon Systems

On glacial-interglacial timescales, most monsoon systems have been found to respond to orbital forcing and in particular to precession (Figure 5.4). Speleothem data from southeastern China (Wang et al., 2008) and northern Borneo (Meckler et al., 2012) document hydrological changes that are dominated by eccentricity-modulated precessional cycles, whereas monsoon proxies from regions closer to the major Northern Hemispheric ice sheets, such as Northern Africa, the Arabian Peninsula and Arabian Sea also exhibit high variance on glacial-interglacial timescales and reflect glacial inceptions and rapid terminations (Bar-Matthews et al., 2003; Schulz et al., 1998; Weldeab et al., 2007) (Figure 5.4), partly as a result of remote atmospheric influences from the Northern Hemisphere ice sheets (Qiuzhen et al., 2008; Timm et al., 2010). Notably, the weaker interglacial amplitudes prior to the Mid-Brunhes event (430 ka), recorded for instance in marine benthic oxygen isotopes, atmospheric CO_2 concentration, water isotopes in Antarctic ice cores and warm pool SST, and, are not captured in a speleothem record from Marine Isotopic Stage (MIS) 13 from Borneo, indicating limited impacts of glacial-interglacial changes in atmospheric composition or ice volume, relative to the orbital forcing (Meckler et al., 2012). On glacial-interglacial timescales, increasing (decreasing) boreal (austral) summer insolation leads to an out of phase interhemispheric change, with overall drying in Southern Hemispheric summer monsoon systems and an increased hydrological cycle in the Northern Hemisphere tropics (Figure 5.4a,d,g). Qualitatively similar out-of-phase interhemispheric responses to insolation forcing have also been documented in coupled time-slice and transient GCM simulations (Braconnot et al., 2008; Kutzbach et al., 2008) (Figure 5.4), thereby providing high confidence in the large-scale orbital control mechanism of interhemispheric rainfall variability and its representation in models. Across longitudes, the response of precipitation may, however, be different for the same orbital forcing. For instance drier conditions occurred during the mid-Holocene over central North America (Diffenbaugh et al., 2006) and wetter conditions in northern Africa (Hély et al., 2009; Liu et al., 2007b; Tierney et al., 2011), as well as east-west shifts of precipitation in South America (Cruz et al., 2009).

[INSERT FIGURE 5.4 HERE]

Figure 5.4: Interhemispheric response of monsoon systems to orbital forcing, AMOC changes, and radiative forcing since 850 CE: a. boreal summer insolation changes at 20°N (black) (W m $^{-2}$), austral summer insolation changes at 20°S (blue); b. Temperature changes in Greenland (°C) reconstructed from NGRIP ice core on SS09 timescale (Huber et al., 2006), location indicated by black circle in c; c. Location of proxy records displayed in relation to the global monsoon regions (Wang and Ding, 2008) North American Monsoon (NAMM), South American Monsoon (SAMM), NAFM (North African Monsoon), SAFM (South African Monsoon), IM (Indian Monsoon), EAM (East Asian Monsoon), WNPM (Western North Pacific Monsoon), AUM (Australian Monsoon). d. Reconstructed (purple) standardized negative $\delta^{18}O$ anomaly in East Asian Summer Monsoon region derived from Hulu cave (Wang et al., 2001) and Sanbao cave speleothem records, China (Wang et al., 2008) and simulated standardized multi-model average (black) of annual mean rainfall anomalies averaged over region 108°E–123°E and 25°N–40°N using the transient runs conducted with LOVECLIM (Timm et al., 2008), FAMOUS (Smith and Gregory, 2012), and the HadCM3 snapshot simulations (Singarayer and Valdes, 2010); e. $\delta^{18}O$ from Xiaobailong cave, China (Cai et al., 2010); f. standardized negative $\delta^{18}O$ anomalies (purple) in Huangye (Tan et al., 2011) and Wanxian Caves (Zhang et al., 2008), China, and simulated standardized annual mean and 30-year low pass filtered rainfall anomalies (black) in region 100°E –110°E, 20°N–35°N, ensemble averaged over the Last Millennium experiments conducted with CCSM4, ECHO-G, MPI-ESM, CSIRO-MARK3, MIROC, HADCM3; g. standardized negative $\delta^{18}O$ anomaly (blue) from Botuvera speleothem, Brazil (e.g., Cruz et al., 2009) and simulated standardized multi-model average (black) of annual mean rainfall anomalies averaged over region 45°W–60°W and 35°S–15°S using same experiments as in panel d; h. standardized negative $\delta^{18}O$ anomaly (brown) from Pacupahuain cave, Peru (Kanner et al., 2012); i. standardized $\delta^{18}O$ anomalies (blue) from Cascayunga Cave, Peru (Reuter et al., 2009) and Pumacocha Lake, Peru (Bird et al., 2011) and simulated standardized annual mean and 30-year low-pass filtered rainfall anomalies (black) in region 76°W–70°W, 15.7°S–8°S, ensemble averaged over the Last Millennium experiments from f.

5.3.3 Glacial Climate Sensitivity

The LGM is characterized by large response to relatively well defined radiative perturbations (Braconnot et al., 2012b; Section 5.2), allowing the use of LGM data and simulations to estimate climate sensitivity. Numerous new temperature reconstructions have been completed since AR4. Proxies used in glacial climate reconstructions include pollen data (Bartlein et al., 2011), isotope-based temperature proxies in ice cores, and

ocean circulation, temperature and salinity proxies from marine sediment cores (Butzin et al., 2005; Tagliabue et al., 2009). The MARGO reconstruction (MARGO Project Members, 2009), the most recent synthesis of the LGM SST, employed multiple proxy approaches to revise and refine previous synthesis efforts such as CLIMAP (CLIMAP Project Members, 1976, 1981) and GLAMAP (Sarnthein et al., 2003a; Sarnthein et al., 2003b). Annual mean cooling is largest (up to –10ºC relative to 20th century) in the mid-latitude North Atlantic with the western Mediterranean also cooling significantly (−6ºC). Seasonally ice free conditions were documented, however, in the northeastern North Atlantic and in the eastern Nordic Seas, in contrast to the widely used CLIMAP reconstruction which suggested perennial sea ice for these areas. Proxy-based reconstruction of the polar front in the Southern Ocean indicates a northward shift in position to 45ºS, associated with a 2–6ºC cooling during glacial austral summer relative to the 20th century. Reconstruction of annual mean SST in the inner tropics (15ºS–15ºN) indicates cooling relative to the 20th century of 2.9 ± 1.3ºC in the Atlantic, 1.4 ± 0.7ºC in the Indian, and 1.2 ± 1.1ºC in the Pacific. There is, however, substantial longitudinal variability and the uncertainty remains as to the interpretation of proxies such as biased sensitivity of proxies to a particular season (Leduc et al., 2010). About 1.5 ± 1.2ºC tropical (30ºS–30ºN) mean SST cooling suggested by the new MARGO reconstruction is smaller than the estimate of about 2.7 ± 0.5ºC cooling (Ballantyne et al., 2005) referenced in AR4. Uncertainties with depth calibration of some proxies may also have underestimated LGM cooling in the tropics (Telford et al., submitted). There are, however, many records in the western and eastern tropical Pacific that shows as much as 2–3ºC cooling relative to the preindustrial period (de Garidel-Thoron et al., 2007; Koutavas and Sachs, 2008; Lea et al., 2000; Lea et al., 2006; Leduc et al., 2007; Linsley et al., 2010; Pahnke et al., 2007; Steinke et al., 2008; Stott et al., 2007), collectively pointing that large uncertainty still remains. A recent pollen-based synthesis of terrestrial climates during the LGM (Bartlein et al., 2011) generally show year-round cooling in most regions, with a few, so far unexplained, deviations in Alaska and in Africa. Isotopic analysis in ice cores indicates a decrease of about 7–10°C in Antarctica relative to the preindustrial period (Stenni et al., 2010; Uemura et al., 2012), with essentially no change in the estimate since AR4. These LGM temperature reconstructions of incomplete spatial coverage are used as constraints to estimate global mean temperature with climate models. While studies using single intermediate complexity model suggested a wide range of global mean cooling (Holden et al., 2010b; Schmittner et al., 2011; Schneider von Deimling et al., 2006a), the most recent study combining proxy data with multiple GCMs yields 3.9 ± 0.8°C (95% confidence interval) global cooling (Annan and Hargreaves, submitted).

GCMs reproduce the direction and large-scale patterns of reconstructed SST during the LGM (Figure 5.5c), but tend to underestimate the magnitude of regional changes, most notably the longitudinal variations of tropical SST (Otto-Bliesner et al., 2009). Since AR4, questions were raised regarding temperature simulation of East Antarctica, concerning potential overestimation of ice sheet elevation, an important boundary condition to the models (Masson-Delmotte et al., 2008). New ice sheet reconstructions based on several different methods (Lambeck et al., 2010a; Tarasov and Peltier, 2007) were introduced for PMIP3 climate model simulations, and the simulated temperature changes are shown to be mostly consistent with the reconstructions (Figure 5.5e). As in AR4, Greenland temperature change in LGM is underestimated by PMIP3 model simulations which show only about 7°C–15°C cooling relative to the preindustrial period. While it is possible that this failure reflects model deficiencies, other possibilities also remain that the peak cooling in Greenland does not represent the LGM period and/or climate forcing such as mineral dust (see Section 5.2.2.3) is missing or underestimated (Lambert et al., submitted).

Temperature change recorded in proxies results from various feedback processes (see Box 5.1), and the forcing (e.g., atmospheric CO_2 content) typically varies before equilibrium of the whole system (e.g., land ice) is reached. Nevertheless, the CCS is estimated or constrained from paleoclimate archives by explicitly counting the slow components of the processes as forcing, rather than as feedbacks (PALAEOSENS Project Members, accepted). This is achieved in three fundamentally different ways (Edwards et al., 2007; see also Chapters 9 and 10). Firstly, climate sensitivity may be estimated by scaling temperature change in the past with the radiative forcing difference of the past and $2 \times CO_2$. The results are subject to uncertainties in the estimate of global mean temperature based on proxy records of incomplete spatial coverage (Köhler et al., 2010; MARGO Project Members, 2009). In this approach, an important assumption is made that the climate response to a certain amount of radiative forcing is the same even under different types of forcing (e.g., CO_2 or ice sheet) and climate states (e.g., warm or cold). Modelling studies have shown, however, that this is not necessarily the case due to the difference in cloud feedback (Crucifix, 2006; Hargreaves et al., 2007; Yoshimori et al., 2011; Figure 5.4b). This is confirmed in Figure 5.5b which shows different shortwave

cloud feedback strengths between LGM and projections in PMIP3/CMIP5 simulations. Correlation between simulated global LGM cooling and projected warming is weak (Figure 5.5a), and therefore the linear scaling of the global LGM temperature change may introduce errors into the climate sensitivity estimate. Secondly, an ensemble of LGM simulations is carried out using a single climate model in which each ensemble member typically differs in model parameters and the ensemble covers a range of climate sensitivity (Annan et al., 2005; Holden et al., 2010b; Schmittner et al., 2011; Schneider von Deimling et al., 2006a). Model parameters are then constrained by reconstructed LGM climate, and probability distribution of climate sensitivity is generated. While intermediate complexity models are often used in order to attain sufficiently large ensemble size, studies with GCMs point out the potential importance of asymmetric response between warming and cooling through the cloud feedback not included in many intermediate complexity models. Thirdly, multiple GCM simulations are compared to proxy data (Otto-Bliesner et al., 2009), and performance of the models and indirectly their climate sensitivity are assessed (Braconnot et al., 2012b). Dust and vegetation changes are in many cases not included in these model simulations and consequently there is also an uncertainty in their radiative forcing estimate (Lambert et al., submitted). While the definitive conclusion remains to be drawn, some studies have suggested that both processes generally amplify the initial temperature change (Lambert et al., 2008; Maher et al., 2010; Mahowald et al., 2006; McGee et al., 2010; Takemura et al., 2009; Winckler et al., 2008; see Section 5.2.2.3). Simulated LGM cooling is therefore likely underestimated in the absence of these two effects, and needs to be taken into account in assessing the climate sensitivity.

CCS is constrained by considering regional climate change in the past (Hargreaves et al., 2007), and it is estimated to lie very likely between 1.4 and 6°C (Annan and Hargreaves, 2006; Holden et al., 2010b; Köhler et al., 2010; MARGO Project Members, 2009; Schmittner et al., 2011; Schneider von Deimling et al., 2006a) although with remaining uncertainties it is not possible to establish tighter bounds using only data from past climates colder than today. This range is also supported by the estimate of 1.5°C–5.2°C (95% confidence interval) for the CCS based on the past 65 Myr of climate records (PALAEOSENS Project Members, accepted).

[INSERT FIGURE 5.5 HERE]

Figure 5.5: a) Relation between equilibrium climate sensitivity estimated from 2 × CO_2 or abrupt 4 × CO_2 experiments and that estimated from LGM simulations. Climate sensitivity of PMIP2 AOGCMs was taken from Crucifix (2006) and that of CMIP5/PMIP3 models was taken from Andrews et al., (2012) and Brady et al., (submitted). Climate sensitivity based on LGM simulations were derived by multiplying the ratio of radiative forcing between 2 × CO_2 and LGM (ΔF_{ratio}). ΔF_{ratio} for three PMIP2 models (CCSM3, HadCM, CM4) were taken from Crucifix (2006), and it was taken from Yoshimori et al., (2009) for MI3. Its range, –0.80 to –0.56, with a mean of –0.67 was used for CMIP5/PMIP3 models. Horizontal bars represent 90% confidence interval for the estimated climate sensitivity based on glacial climates in literatures: "S06a", "M09", "H10", "K10" and "S11" denote Schneider von Deimling et al., (2006a), MARGO Project Members (2009), Holden et al., (2010a), Köhler et al., (2010), and Schmittner et al., (2011), respectively. Vertical bars represent 90% confidence interval for LGM global mean temperature change in literatures multiplied by the mean of ΔF_{ratio}. "S06b" and "A12" denote Schneider von Deimling et al., (2006b) and Annan and Hargreaves (submitted), respectively. Also plotted is a one-to-one line; b) Strength of individual feedbacks for the CMIP5/PMIP3 abrupt4 × CO_2 (131–150 years) and LGM (stable states) experiments following the method in Yoshimori et al., (2011). "WV+LR", "A", "CSW", "CLW" denote water vapour plus lapse-rate, surface albedo, shortwave cloud, and longwave cloud feedbacks, respectively. "All" denotes the sum of all feedbacks except for the Planck response. Feedback parameter here is defined as the change in net radiation at the top of the atmosphere due to the change in individual fields such as water vapour, and it is normalized by the global mean surface air temperature change. Climate sensitivity depends on forcings, feedbacks and ocean heat uptake. Positive (negative) value indicates that the feedback amplifies (suppresses) the initial temperature response; c) Relation between models' climate sensitivity and LGM tropical SST change from today; d) Same as in c but for tropical surface air temperature over land; and e) Same as in c but for surface air temperature in East Antarctica. Gray shadings in c-e are 90% confidence intervals for temperature reconstructions from Annan and Hargreaves (submitted) and a range for East Antarctica based on reconstructions from stable isotopes from several ice cores (Dome F, Vostok, EDC and EDML) from Stenni et al., (2010) and Uemura et al., (2012). Pink shading in c represents estimates by Ballantyne et al., (2005) with ±1 standard deviation. "HadCM", "CM4", "MI3", "CGCM3", "MPESM", "CM5A", and "MIESM" denote "HadCM3", "IPSL-CM4", "MIROC3.2", "MRI-CGCM3", "MPI-ESM-P", "IPSL-CM5A-LR", and "MIROC-ESM", respectively.

5.3.4 Interglacial Periods

Interglacial climate allow the current changes to be studied in the perspective of natural climate variability and understand feedbacks determining responses to orbital forcing. The current interglacial, the Holocene, extending from 11.7 ka to the present, is the most extensively studied (Section 5.5).

The Last Interglaciation (LIG, approximately 130–116 ka; Section 5.6.2) (Stirling et al., 1998), occurred largely at greenhouse gas concentration characteristic of the pre-industrial Holocene (Figure 5.3). It experienced stronger orbital forcing than the Holocene with the additive effects of large obliquity and eccentricity (Figure 5.3), resulting in strong positive insolation anomalies during boreal summer in the NH and austral spring in the SH. Quantitative data syntheses allow estimating maximum annual warmth around the globe for the LIG (McKay et al., 2011; Turney and Jones, 2010) (Figure 5.6). These estimates assumed that the warmest phases were globally synchronous. However, warming in the Southern Ocean and over Antarctica led peak warmth in the North Atlantic and Nordic Seas by 3–5 kyr (Bauch et al., 2011; Jouzel et al., 2007; Masson-Delmotte et al., 2010b). If available, uncertainties of reconstructed climate parameters differ significantly between reconstruction methods and regions, especially due to seasonal effects (e.g., McKay et al., 2011; Tarasov et al., 2011; Velichko et al., 2008). A robust feature of transient LIG model simulations is peak Northern Hemisphere summer warmth early in the LIG (~130–125 ka) in line with orbital forcing (Bakker, submitted) with regional evolution dependent on the assumptions of NH ice sheets and melt in individual simulations (Bakker, submitted; Sánchez Goñi et al., 2012; Swingedouw et al., 2009).

Large polar warming during the LIG has implications for the stability of the polar ice sheets (Sections 5.6 and 5.8). The Greenland NGRIP and NEEM ice-core stable isotope records indicate precipitation-weighted annual warming of 5–8°C (Dahl-Jensen et al., submitted; Masson-Delmotte et al., 2011). Evidence, though fragmentary, also indicates seasonally open water off northern Greenland and in the central Arctic at some time during the LIG (Adler et al., 2009; Nørgaard-Pedersen et al., 2007), which could be important for explaining the Greenland isotope record (Sime et al., submitted). East Antarctica ice cores record early LIG warming, possibly more than 5°C warmer than present (Jouzel et al., 2007; Sime et al., 2009; Stenni et al., 2010). Ocean-atmosphere coupled simulations underestimate the magnitude of polar ice-sheet warming, particularly for Antarctica (Lunt, submitted; Otto-Bliesner et al., submitted; Overpeck et al., 2006) (Figure 5.6). Indirect feedbacks to a bipolar seesaw response to persistent iceberg melting at high northern latitudes (Ganopolski and Roche, 2009; Govin et al., 2012) and/or disintegration of the West Antarctic Ice Sheet (Holden et al., 2010b) may be needed for the LIG Antarctic warming.

Considering age-scale and proxy-calibration uncertainties, the global mean annual surface temperature change for the LIG can only be estimated with medium confidence. Based on data syntheses of peak warmth, global mean annual surface temperature ranges from about 1°C to 2°C warmer than pre-industrial (Otto-Bliesner et al., submitted; Turney and Jones, 2010). In response to orbital forcing, PMIP2 and PMIP3 models simulate an insignificant global mean annual surface temperature change, ranging from –0.2°C to +0.2°C (Lunt, submitted). The models underestimate regional warming (Figure 5.6) possibly due to representation of ice sheets, vegetation, sea ice, and cloud processes in models (Born et al., 2010; Fischer and Jungclaus, 2010; Holden et al., 2010b; Kim et al., 2010; Masson-Delmotte et al., 2011; Schurgers et al., 2007). Peak LIG SST warming is estimated with medium confidence to be 0.7°C ± 0.6°C (McKay et al., 2011) with models giving more confidence to the lower bound (Figure 5.6) (Otto-Bliesner et al., submitted). The data suggests a strong land-ocean response to the forcing with peak LIG terrestrial warming estimated to be about 1.5°C. Model results give terrestrial warming of 0.9°C–1.1°C when sampled at the data locations but only 0°C–0.3°C when averaged over the full model grids, pointing to difficulties in estimating global mean annual surface temperature with current data coverage (Otto-Bliesner et al., submitted).

Several recent compilations from marine, ice and terrestrial archives, with updated age models, have provided an expanded view of the overall geographical patterns and strengths of earlier interglacials of the last 800 kyr, though not on the temporal phasing because of the quality of the age controls (Jouzel et al., 2007; Lang and Wolff, 2011; Rohling et al., 2012). There is currently no consensus on whether interglacials changed in strength after the mid-Brunhes event ~430 ka. EPICA Dome C Antarctic ice cores record warmer temperatures and higher CO_2 after the mid-Brunhes event (Masson-Delmotte et al., 2010a), and marine records of deep-water temperatures are characterized by generally warmer values during post- mid-Brunhes event interglacials than earlier interglacials (Lang and Wolff, 2011). In contrast, weaker earlier interglacials (430–800 ka) are not observed in some terrestrial archives from Eurasia (Candy et al., 2010; Prokopenko et al., 2002) or hydroclimate proxies of the western North Pacific monsoon (Section 5.3.2.3). Consistent with

this regional variability, recent modelling proposes that GHG changes (Section 5.3.2) play a dominant role in explaining the global and southern high latitude mean annual surface temperature variations, while seasonal insolation changes from orbital forcing and associated feedbacks of vegetation and sea ice explain northern high-latitude mean annual surface temperature (Yin and Berger, 2012). The warmest and coolest interglacials occur when GHGs and insolation reinforce each other (Herold et al., submitted; Yin and Berger, 2012; Yin and Berger, 2010). Regionally, over the last 2.8 Myr, there is evidence for significantly higher Arctic amplification compared to the present and last interglacials (Melles et al., 2012).

[INSERT FIGURE 5.6 HERE]

Figure 5.6: Changes in surface temperature for the Last Interglacial as reconstructed from data and simulated by an ensemble of climate model experiments in response to orbital forcing. Top left: Proxy data syntheses of annual surface temperature anomalies as published by Turney and Jones (2010) and McKay et al., (2011) . McKay et al., calculated an annual anomaly for each record as the average SST of the 5-kyr period centered on the warmest temperature between 135 ka and 118 ka and then subtracting the average SST of the late Holocene (5 ka to 0 ka). Turney and Jones calculated the annual temperature anomalies relative to 1961–1990 CE by averaging the LIG temperature estimates across the isotopic plateau in the marine and ice records and the period of maximum warmth in the terrestrial records (assuming globally synchronous terrestrial warmth). Top right: Proxy records of zonal mean anomalies of SST from Turney and Jones (annual) and McKay et al., (annual and seasonal) and terrestrial surface temperature from Turney and Jones (annual) and compiled from published literature by Tarasov and Müller (seasonal). SST anomalies larger than 6°C (two annual in Nordic Sea, two annual in Southern Ocean, one annual in eastern tropical Pacific) and terrestrial anomalies larger than 10°C (four annual in Siberia, one DJF each in Siberia and Finland) or less than –6°C (two DJF in France) are not included in zonal averages. Bottom left: Multi-model average of annual surface air temperature anomalies simulated for the Last Interglacial computed with respect the pre-industrial control simulations. The results for the Last Interglacial are obtained from 18 simulations for 125–130ka conducted by 12 modeling groups (CCSM3_Bremen, CCSM3_LLN, CCSM3_NCAR, CLIMBER_LSCE, COSMOS_AWI, ECHAM5_ZMAW, HadCM3_Bristol, IPSL_LSCE, KCM_Kiehl, LOVECLIM_Amsterdam, LOVECLIM_LLN, and MIROC_Tokyo). Bottom right: Zonal mean anomalies of SST and terrestrial surface temperature from the multi-model mean for annual, June-July-August and December-January-February. Gray-shaded bands indicate the 2 standard deviation uncertainties of the annual mean anomalies.

5.3.5 Temperature Variations During the Last 2000 Years

Research on hemispheric and global temperatures is important to improve understanding of climate responses to external forcings. Expanded proxy data networks and better understanding of existing and newly developed reconstruction methods have supported a more complete characterization of the spatiotemporal distribution of surface temperature changes (Section 5.3.5.1) and their associated uncertainties (Section 5.3.5.2) during the last 2000 years, as well as more extensive comparisons with GCM simulations (Section 5.3.5.3).

5.3.5.1 Recent Warming in the Context of New Reconstructions

Since AR4, reconstructions using new statistical methods and additional proxy data have been published (Figure 5.7; Table 5.1; Appendix 5.A.1). This evidence, particularly in the NH, endorses the notion of a generally warm period during the so-called Medieval Climate Anomaly (MCA; Glossary), followed by the colder Little Ice Age (LIA; Glossary) that lasted from the middle centuries of the millennium to the rise in global temperatures that began in the late 19th century. The timing and spatial structure of the MCA and LIA are not well defined (see Box 6.4 in AR4 and Diaz et al., 2011), with different records exhibiting warm and cold conditions at different times for different regions. In some places we consider averages over the time intervals 950–1250 CE and 1400–1700 CE as representative of the MCA and LIA, although timings may differ between published records, particularly at regional scales (Section 5.5).

Published reconstructions and their error estimates provide multiple lines of evidence (using different statistical methods or different compilations of proxy records; Appendix 5.A.1) to indicate, with high confidence, that modern (the last 30- or 50-year mean) NH temperatures very likely exceeded those from any previous 30- or 50-year mean in the last 800 years (Table 5.1). The timing of warm and cold periods is mostly consistent across reconstructions (in some cases this is because they use similar proxy compilations) but the magnitude of the changes is clearly sensitive to the statistical method and to the target domain (land or land and sea; the full hemisphere or only the extra-tropics; Figure 5.7a). Even accounting for these

uncertainties, almost all reconstructions agree that each 30-year (50-year) period from 1200 CE to present was very likely colder in the NH than the 1981–2010 CE (1961–2010 CE) instrumental temperature.

The NH temperature reconstructions that reach back to 800 CE or earlier suggest that this assessment might be extended back 1200 years or more, particularly when comparing the last 30 years that encompass the strongest recent warming (Table 5.1 and Figure 5.7a). However, some reconstructions use proxy records that may not fully resolve past variations on timescales as short as 30 years while comparison of 50-year means identifies more reconstructions for which it is ambiguous if modern temperatures were higher than those reconstructed during 800–1200 CE. Furthermore, they rely on fewer proxy records before 1200 CE, yielding less independence among the reconstructions while making them more susceptible to errors in individual proxy records, and the published uncertainty ranges do not include all sources of error (Section 5.3.5.2) and do not correspond exactly to the 30- and 50-year timescales considered in Table 5.1. Nevertheless, evidence for warmth in recent decades (Chapter 2) is more seasonally and geographically extensive than the evidence for Medieval warmth, providing medium confidence that 1961–2010 CE and 1981–2010 CE were the warmest 50- and 30-year periods in the last 1300 years.

An increasing number of proxy records and regional reconstructions are being developed for the SH (Section 5.5), but relatively few reconstructions of SH or global mean temperatures have been published (Figure 5.7b and c). These few indicate that the last decades are relatively warm for the SH and at global scales (Table 5.1), but there is only limited evidence and therefore low confidence that the recent warming has exceeded the range of reconstructed temperatures over the last 4 centuries.

[INSERT FIGURE 5.7 HERE]

Figure 5.7: Reconstructed (a) Northern and (b) Southern Hemisphere, and (c) global annual temperatures during the last 2000 years. Individual reconstructions (see Appendix 5.A.1 for further information about each one) are shown as indicated in the legends, grouped by colour according to their spatial representation (red: land-only all latitudes; orange: land-only extra-tropical latitudes; light blue: land and sea extra-tropical latitudes; dark blue: land and sea all latitudes) and instrumental temperatures shown in black (HadCRUT3 land and sea, and CRUTEM3 land-only). All series represent anomalies (°C) from the 1881–1980 CE mean (horizontal dashed line) and have been smoothed with a filter that reduces variations on timescales less than ~50 years.

Table 5.1: Comparison of recent hemispheric and global temperature estimates (reconstructions and instrumental data) with earlier reconstructed values, using published uncertainty ranges to assess likelihood of unusual warmth.

	Region:	NH															SH			Global		
	Domain:	Land and Sea				Land								Extratropics			Land			Land		
	Season:	Ann				Ann								Ann			Ann			Ann		
	Study:	1	2	3	4	5	6	7	8	9	10	11	12	13	14	15	8	7	12	8	11	12
50-year	1600–1899	■	☒	☒	■	■	☒	■	☒	■	■	■	■	■	■	■	■	■	■	■	■	■
	1400–1899	■	☒	☒	☒	■	☒	■	☒	■	■			■	■	■	■	■		■		
	1200–1899	■	☒	☒	☒	■	⊡	■	☒	■	■			■	☒	■	■	☒		■		
	1000–1899	☒	☒	⊡	☒	☒	⊡	■	□	■	☒			☒	☒	☒	■	☒		■		
	800–1899	☒	⊡	□		☒	□	■	□	■				☒	☒		⊡	☒		■		
	600–1899	☒	⊡	□		☒	□	■	□					☒	☒		⊡	☒		■		
	400–1899	☒	⊡			☒	□	☒	□					☒			□					
	200–1899	☒				☒	□	☒						☒			□					
	1–1899	☒				☒								☒								
30-year	1600–1899	■	☒	☒	■	■	■	■	☒	■	■	■	■		■	■	■	■	■	■	■	■
	1400–1899	■	☒	☒	☒	■	☒	■	☒	■	■				■	■	■	■		■		
	1200–1899	■	☒	☒	☒	■	☒	■	☒	■	■				■	■	■	☒		■		
	1000–1899	☒	☒	☒	☒	☒	☒	■	⊡	■	☒				■	☒	■	☒		■		
	800–1899	☒	☒	⊡		☒	□	■	⊡	■					■		☒	☒		■		
	600–1899	☒	☒	⊡		☒	□	■	⊡						■		☒	☒		■		

		1	2	3	4	5	6	7	8	9	10	11	12	13	14	15
	400–1899	☒	☒			☒	☐	☒	⊡						☒	
	200–1899	☒				☒	☐	☒							☒	
	1–1899	☒				☒										

Notes:
Symbols indicate the likelihood (based on the published multi-decadal uncertainty ranges) that each 30- or 50-year mean of the reconstructed temperature during the indicated period was colder than the warmest 30- or 50-year mean after 1900. A reconstructed mean temperature X is considered to be likely (very likely) colder than a modern temperature Y if $X+aE < Y$, where E is the reconstruction standard error and a = 0.42 (1.29).
⊡ indicates the reconstructed temperatures were likely colder than the 1981–2010 or 1961–2010 mean instrumental temperature;
☒ indicates that this is very likely, while
■ extends this to also very likely colder than the warmest 30- or 50-year mean of the post-1900 reconstruction (which is typically not as warm as the end of the instrumental record);
☐ means that at least one 30- or 50-year reconstructed mean is about as likely colder as warmer than the 1981–2010 or 1961–2010 mean instrumental temperature;
no symbol is given where the reconstruction does not fully cover the indicated period.
Further information for each study is given in Appendix 5.A, Table 5.A.4.
1 = Moberg et al., (2005);
2 = EIV_HADCRUT Mann et al., (2008);
3 = Mann et al., (2009);
4 = Ammann and Wahl (2007) with Mann et al., (1999) error estimates;
5 = Ljungqvist (2010);
6 = Loehle and McCulloch (2008);
7 = CPS_CRUTEM Mann et al., (2008);
8 = EIV_CRUTEM Mann et al., (2008);
9 = D'Arrigo et al., (2006);
10 = Juckes et al., (2007);
11 = Pollack and Smerdon (2004);
12 = Leclercq and Oerlemans (2012);
13 = Christiansen and Ljungqvist (2012) for 50-year timescale only;
14 = Hegerl et al., (2007); 15 = Frank et al., (2007).

5.3.5.2 *Reconstruction Methods, Limitations and Uncertainties*

Reconstructing NH, SH or global-mean temperature variations over the last 2000 years remains a challenge due to limitations of spatial sampling, uncertainties in individual proxy records and challenges associated with the statistical methods used to calibrate and integrate multi-proxy information (Frank et al., 2010a; Hughes and Ammann, 2009; Jones et al., 2009). Since AR4, important new assessments of the statistical methods used to reconstruct either global/hemispheric temperature averages or spatial fields of past temperature anomalies have been published. The former include approaches for simple compositing and scaling of local or regional proxy records into global and hemispheric averages using uniform or proxy-dependent weighting (Christiansen and Ljungqvist, 2012; Hegerl et al., 2007; Juckes et al., 2007; Mann et al., 2008). The latter correspond to improvements in climate field reconstruction methods (Mann et al., 2009; Smerdon et al., 2011) that apply temporal and spatial relationships between instrumental and proxy records to the pre-instrumental period. New developments for both reconstruction approaches include implementations of Bayesian inference (Li et al., 2010a; McShane and Wyner, 2011; Tingley and Huybers, 2010; Werner et al., in press). In particular, Bayesian hierarchical methods enable a more explicit representation of the underlying processes that relate proxy (and instrumental) records to climate, allowing a more systematic treatment of the multiple uncertainties that affect the climate reconstruction process. This is done by specifying simple parametric forms for the proxy-temperature relationships that are then used to estimate a probability distribution of the reconstructed temperature evolution that is compatible with the available data (Tingley et al., 2012).

An improved understanding of potential uncertainties and biases associated with reconstruction methods has been achieved, particularly by using millennial GCM simulations as a surrogate reality in which pseudo-proxy records are created and reconstruction methods are replicated and tested (Smerdon, 2012). A key finding is that the methods used for many published reconstructions can underestimate the amplitude of the low-frequency variability (Christiansen et al., 2009; Lee et al., 2008; Smerdon et al., 2010). The magnitude

of this amplitude attenuation in real-world reconstructions is uncertain but for affected methods the problem will be larger: (i) for cases with weaker correlation between instrumental temperatures and proxies (Christiansen et al., 2009; Lee et al., 2008; Smerdon et al., 2011); (ii) if errors in the proxy data are not incorporated correctly (Ammann et al., 2010; Hegerl et al., 2007); or (iii) if the data are detrended in the calibration phase (Christiansen et al., 2009; Lee et al., 2008). The 20th-century trends in proxies may contain relevant temperature information (Ammann and Wahl, 2007), however calibration with detrended or undetrended data has been an issue of debate (Mann et al., 2007; von Storch et al., 2006; Wahl et al., 2006) because 20th century proxy trends can be induced by other (non-temperature) climate and non-climatic influences (Gagen et al., 2011; Jones et al., 2009). Recent developments mitigate the loss of low-frequency variance in global and hemispheric reconstructions by increasing the correlation between proxies and temperature through temporal smoothing (Lee et al., 2008) or by correctly assigning part or all of the temperature-proxy error to the proxy data (Hegerl et al., 2007; Juckes et al., 2007; Mann et al., 2008). Pseudoproxy experiments have shown that a particular local calibration method (Christiansen, 2011; Christiansen and Ljungqvist, 2012; Hegerl et al., 2007) can also avoid attenuation of low-frequency variability, though it is debated whether it might instead inflate the variability and thus constitute an upper bound for low-frequency variability (Moberg, 2012).

The fundamental limitations for deriving past temperature variability at global/hemispheric scales are the relatively short instrumental period and the number, geographical distribution, reliability and climate signal of proxy records (Jones et al., 2009). The database of high-resolution proxies has been expanded since AR4 (Mann et al., 2008; Neukom and Gergis, 2011; PAGES 2k Consortium, submitted; Wahl et al., 2010) but data are still sparse in the tropics, SH and over the oceans (see new developments in Section 5.5). The short instrumental period and the paucity of proxy data in specific regions may preclude obtaining accurate estimates of the covariance of temperature and proxy records (Juckes et al., 2007), impacting the selection and weighting of proxy records in global/hemispheric reconstructions (Bürger, 2007; Osborn and Briffa, 2007) and resulting in regional errors in climate field reconstructions (Smerdon et al., 2011)

Two further sources of uncertainty have been partially considered in the published literature. First, some studies have used multiple statistical models (Mann et al., 2008) or generated ensembles of reconstructions by sampling parameter space (Frank et al., 2010b), but this type of structural and parameter uncertainty needs further consideration (Christiansen et al., 2009; Smerdon et al., 2011). Second, other climate and non-climate influences on a proxy can lead to non-stationarity through time in proxy–temperature relationships, a prominent example being the divergence between some tree-ring width and density chronologies and instrumental temperatures during the last decades of the 20th century (Briffa et al., 1998). This phenomenon does not affect all tree-ring records (Esper and Frank, 2009; Wilson et al., 2007) while other studies (Büntgen et al., 2008; Esper et al., 2010) found no clear divergence in many hundreds of tree-ring chronologies with careful selection of sites and consideration of standardization methods, calibration uncertainties and instrumental data quality, indicating that divergence may be an artefact of particular methods (Briffa and Melvin, 2011) rather than an inherent problem of tree-ring chronologies. In cases that do show divergence, a number of factors may be responsible, such as direct temperature or drought stress on trees, delayed snowmelt, changes in seasonality and reductions in solar radiation (D'Arrigo et al., 2008; Lloyd and Bunn, 2007; Porter and Pisaric, 2011). The ability of tree-ring proxies to fully respond to volcano-induced cooling has recently been questioned (Mann et al., 2012), though the proposed explanation has little support from either tree-ring data or tree-growth models (Anchukaitis et al., submitted; Esper et al., submitted).

The above limitations and uncertainties indicate that published error estimates likely underestimate the true uncertainty of large-scale temperature reconstructions (see Section 5.3.5.1), fostering continued debate about the ability of proxies to provide useful climate information (e.g., McShane and Wyner, 2011 and associating comments and rejoinder). Future improvements in proxy availability, development of new proxy sources, understanding of proxy-climate relationships and new statistical methods allowing for a better treatment of processes will contribute to better characterized uncertainties and improved knowledge of temperature variations during the last 2 ka (Hughes and Ammann, 2009; Tingley et al., 2012).

5.3.5.3 Comparing Reconstructions and Simulations

The number of GCM simulations of the last millennium has increased since AR4 (Fernández-Donado et al., submitted), complemented by the PMIP3/CMIP5 standardized experiments (Schmidt et al., 2011). The simulations have used different estimates of natural and anthropogenic forcings (Appendix 5.A, Table 5.A.5). In particular, the PMIP3/CMIP5 simulations are driven by TSI that has smaller long term changes (Section 5.2.1; Figure 5.1b): increases between the Maunder Minimum and the late 20th century ≤0.10 % (Schmidt et al., 2011), while previous simulations use increases between 0.23% and 0.29% (Fernández-Donado et al., submitted). Simulated NH temperatures lie mostly within the uncertainties of the available reconstructions during the last millennium (Figure 5.8a). While this is illustrative of the agreement between GCMs and reconstructions, it is not very discriminating because models with different climate sensitivities are consistent with the reconstructions when internal variability and uncertainties in the forcings and reconstructions are taken into account.

Paleodata have also been assimilated into climate model experiments (see Sections 5.5 and 10.7) by either nudging simulations to follow local or regional proxy-based reconstructions (Widmann et al., 2010) or by selecting simulations from decade-by-decade ensembles to obtain the closest match to reconstructed climate patterns (Goosse et al., 2012a). The resulting simulations are constrained by the proxy data, the external forcings applied and the model dynamics and physics, and provide useful insight into the relative roles of internal variability and external forcing (Goosse et al., 2012b), as well as process-based understanding of mechanisms that may account for the spatial distribution of past climate anomalies (Crespin et al., 2009; Palastanga et al., 2011).

Figure 5.8b-d provides additional tests of model-data agreement by compositing the temperature response to a number of distinct forcing events. The models simulate a significant NH cooling in response to individual volcanic events (Figure 5.8b; peaks between 0.09°C and 0.38°C depending on model) that lasts 3 to 5 years; reconstructions with annual resolution also show cooling on average (0.05°C to 0.30°C). Despite the overlapping ranges, it is likely that the models have a stronger response than the reconstructions because the reconstructions mostly represent land temperatures, while the simulated values shown here are an average over land and sea. Such differences could arise from deficiencies in the models, in the volcanic forcing (omitting faster fallout of larger particles, Timmreck et al., (2009), or injection of stratospheric water vapour, Joshi and Jones (2009)) or in the temperature reconstructions (see Section 5.3.5.2, but note that Brohan et al., (submitted) find that some climate models simulate greater cooling following the major 1809 and 1815 eruptions than is apparent in early instrumental data). Since many reconstructions do not have annual resolution, similar composites (Figure 5.8c) are formed to show the response to changes in multi-decadal volcanic forcings (representing clusters of eruptions). Both the simulated and reconstructed responses are significant and comparable in magnitude, although simulations show a faster recovery after peak negative forcing (<5 years). Solar forcing estimated over the last millennium shows weaker variations than volcanic forcing (Figure 5.8d, Section 5.2), even at multidecadal timescales. Compositing the response to these weaker multi-decadal fluctuations in solar irradiance shows cooling in simulations and reconstructions of NH temperature between 0.0°C and 0.2°C or 0.0°C and 0.1°C, respectively. In both cases, the cooling may be partly a response to concurrent variations in volcanic forcing (green line in Figure 5.8d).

Other measures of the amplitude of NH temperature variations during the last millennium are the temperature differences between the MCA and the LIA (Figures 5.8e, 5.9a–c) and between the LIA and the 20th century (Figures 5.8f, 5.9g–i). Despite the close correspondence between the multi-model and multi-reconstruction means, the range of individual results is very wide (NH mean temperature differences from less than 0.1°C to more than 0.8°C; see Chapters 9 and 10 for a comparison of reconstructed and simulated variability across various frequency ranges). The warming from the LIA to the present in these simulations covers a similar wide range as the reconstructed warming, with no clear difference between runs with weaker or stronger solar forcing (Figure 5.8f; Section 10.7.2.2). The difference between the MCA and LIA temperatures, however, has a smaller range for the model simulations than the reconstructions, and the simulations with weaker solar forcing lie within the lower half of the reconstructed range of temperature changes (Figure 5.8e). Recent studies (e.g., Bothe et al., submitted) have assessed the consistency of model simulations at regional to global scales and (Hind and Moberg, submitted) found closer data-model agreement for simulations with 0.1% TSI increase than 0.24% TSI increase, but they note that the result is sensitive to the reconstruction uncertainty and the climate sensitivity of the model. Simulations with an Earth system model of intermediate complexity using a much stronger solar forcing (0.44% TSI increase from

Maunder Minimum to present, Shapiro et al., (in press) appear to be incompatible with temperature reconstructions (Feulner, 2011).

The spatial distributions of simulated and reconstructed (Ljungqvist et al., 2012; Mann et al., 2009) temperature changes between the MCA, LIA and present are shown in Figure 5.9. Simulated changes tend to be larger, particularly with stronger TSI forcing, over the continents and ice/snow-covered regions, showing polar amplification (Box 5.2). The largest simulated and reconstructed changes are between the LIA and present, and reconstructions (Figure 5.9i) indicate widespread warming except for negative anomalies in the North Atlantic Ocean, south of Greenland. Models also simulate overall warming between the MCA and present (Figure 5.9d,e), whereas the reconstructions indicate regional cooling (in the North Atlantic, southwestern North America, and the mid-latitudes of the Pacific Ocean). This not surprising, because greater regional variability is expected in the reconstructions compared with the mean of an ensemble of model simulations. Reconstructed changes for such areas with few or no proxy data should also be interpreted with caution (Smerdon et al., 2011). The reconstructed MCA-LIA temperature differences (Figure 5.9c) indicate higher medieval temperatures over the Northern Hemisphere continents in agreement with simulations (Figure 5.9a,b) under stronger TSI changes. For weaker TSI changes model results are similar, but inter-model differences are more sensitive to internal variability. This pattern of change has been shown in proxy assimilation experiments to be compatible with a direct response to a relatively weak solar forcing and internal variability changes suggesting a positive Northern Annular Mode phase and northward shift of the Kuroshio and Gulf Stream currents (Goosse et al., 2012b). For the tropical regions, an enhanced zonal gradient produced by either a warmer Indian Ocean (Graham et al., 2011) or a cooler eastern Pacific have been invoked as possible mechanism that could explain many of the large scale anomalies during the MCA. A cooler eastern Pacific, referred to as a La Niña-like background state, is reconstructed for the MCA in comparison to the LIA (Figure 5.9c), albeit not reproduced by model simulations (Figure 5.9a,b). The existence of a warmer pool in the Indian ocean (Graham et al., 2011) or a La Niña-like state during the MCA (Mann et al., 2009; Seager et al., 2007) is uncertain, but if confirmed could be either a response to external forcing or part of a climate reorganization associated with internal variability, neither of which are reproduced by the currently available simulations (Figure 5.9a,b; see Sections 5.5.1, and 5.4.1).

[INSERT FIGURE 5.8 HERE]

Figure 5.8: Comparisons of simulated and reconstructed NH temperature changes. (a) Changes over the last millennium. (b) Response to individual volcanic events. (c) Response to multi-decadal periods of volcanic activity. (d) Response to multi-decadal variations in solar activity. (e) Mean change from MCA to LIA. (f) Mean change from 20th century to LIA. Note that some reconstructions represent a smaller spatial domain than the full NH or a specific season, while annual temperatures for the full NH mean are shown for the simulations. (a) Simulations shown by coloured lines (thick lines: multi-model-mean; thin lines: multi-model 90% range; red/blue lines: models forced by stronger/weaker solar variability, though other forcings and model sensitivities also differ between the red and blue groups); overlap of reconstructed temperatures shown by grey shading; all data are expressed as anomalies from their 1500–1850 CE mean and smoothed. Superposed composites (time segments from selected periods positioned so that the years with peak negative forcing are aligned) of the forcing and temperature response to (b) the 13 strongest individual volcanic forcing events after 1400 CE (the data shown are not smoothed); (c) multi-decadal changes in volcanic activity; (d) multi-decadal changes in solar irradiance. Upper panels show the volcanic or solar forcing for the individual selected periods together with the composite mean (thick); in (d), the composite mean of the volcanic forcing (green) during the solar composite is also shown. Lower panels show the NH temperature composite means and 90% range of spread between simulations (red line, pink shading) or reconstructions (grey line and shading), with overlap indicated by darker shading. Mean NH temperature difference between (e) MCA (950–1250 CE) and LIA (1400–1700 CE) and (f) 20th century (1900-2000) and LIA, from reconstructions (grey), multi-reconstruction mean and range (dark grey), multi-model mean and range (brown), and simulations (red/blue for models forced by stronger/weaker solar variability). Where an ensemble of simulations is available from one model, the ensemble mean is shown in solid and the individual ensemble members by open circles. Results are sorted into ascending order and labelled. Reconstructions, models and further details are given in Appendix 5.A.1 and Appendix 5.A.2.

[INSERT FIGURE 5.9 HERE]

Figure 5.9: Simulated and reconstructed temperature changes for key periods in the last millennium. Annual temperature differences for: (a) to (c) MCA (950–1250 CE) minus LIA (1400–1700 CE); (d) to (f) present (1950–2000 CE) minus MCA; (g) to (i) present minus LIA. Model temperature differences (left and middle columns) are average temperature changes in the ensemble of available model simulations of the last millennium (see Appendix 5.A.2), grouped into those using stronger solar forcing changes (TSI change from the LMM to present >0.23 %; left column) and those weaker changes (TSI change from the LMM to present < 0.1%; middle column). Right column shows differences in the Mann et al., (2009) field reconstruction, and in (c), dots represent proxy anomalies from Ljungqvist et

al., (2012) scaled by 0.5 for display purposes. Unhatched grid-cells indicate significant differences (<0.05 level) in reconstructed fields (right) or that ≥80% of the simulations agreed in showing significant changes of the same sign (left and middle). For simulations starting after 950 CE, the period 1000–1250 was used to estimate MCA values. Grid-cells outside the domain of the Mann et al., (2009) reconstruction are shaded grey in the model panels to enable easier comparison, though contours illustrate model output over the complete global domain. Simulations have been weighted by the number of experiments used from each model: BCC-csm1-1 (1), CSM1.4 (1), CCSM3 (5), CSIRO-mk3L-1-2 (7), ECHAM5-MPIOM (8), MPI-ESM-P (1), ECHO-G (3), FGOALS-gl (1), GISS-E2-R (4), HadCM3 (2), IPSLCM4 (1).

5.4 Modes of Climate Variability

Since AR4, new proxies and model simulations have provided new insights into forced and unforced past variability of the El Niño-Southern Oscillation (ENSO), the northern annular modes (NAO/NAM), the Southern Annular Mode (SAM) and longer term variability associated with the Atlantic Multidecadal Oscillation (AMO) (see Chapter 14 for definitions and illustrations). This section is organized from low to high latitudes and from interannual to decadal-scale modes of variability.

5.4.1 Tropical Modes

Changes in the statistics of interannual variability associated with ENSO have been studied in response to changes in climatic boundary conditions and external forcings using GCMs and climate reconstructions from historical and proxy records (corals, tree rings, oxygen isotopes in trees, ice cores and marine and lake sediment cores). During warm intervals of the Pliocene, climate conditions in the equatorial Pacific were characterized by weaker zonal (Wara et al., 2005) and meridional (Steph et al., 2010) SST gradients, consistent with the absence of an eastern equatorial cold tongue. Although this state is sometimes referred to as a “permanent El Niño” (Fedorov et al., 2006), proxy records sensitive to interannual surface climate variations (Scroxton et al., 2011; Watanabe et al., 2011), supported by GCM simulations (Haywood et al., 2007) indicate with medium confidence that in spite of climate background conditions being considerably different from today’s (cf. Section 5.3.1), interannual ENSO variability continued to operate during the Pliocene.

Climate model runs for LGM boundary conditions simulate wide ranges of ENSO behaviour with little consistency (Liu et al., 2007a; Zheng et al., 2008) (Figure 5.10). ENSO sensitive proxies for the LGM are currently too sparse (Wolff et al., 2011) to help constrain the simulated ENSO responses to LGM boundary conditions. GCM experiments indicate that a weakening of the Atlantic Meridional Overturning Circulation (AMOC), such as during Heinrich stadial 1 (about 18.5 ka to 14.8 ka) or the Younger Dryas (about 12.8 ka to 11.5 ka) induces an intensification of ENSO amplitude (high confidence), in qualitative agreement with sub-annually resolved fossil coral data from Tahiti (Felis et al., 2012) and some cases a reduction of the annual cycle in the eastern equatorial Pacific (Braconnot et al., 2012a; Merkel et al., 2010; Timmermann et al., 2007) (Figure 5.10).

AR4 (Chapter 6) reported that the early to mid-Holocene likely experienced weak ENSO variability. Previous evidence for a reduction of ENSO variability during the early to mid-Holocene (9 ka to 4 ka) is, however, controversial (Carre et al., 2005; Conroy et al., 2008; Dolan et al., 2011; Donders et al., 2008; Koutavas et al., 2006; Tudhope et al., 2001; Woodroffe et al., 2003). New sub-annually resolved coral records from the central Pacific ENSO-activity center covering the last ~7 ka (Cobb et al., submitted) provide no statistically significant difference between mid- and late Holocene ENSO variance, but exhibit large ranges of natural ENSO variations. The multimodel analysis of eleven GCM experiments under mid-Holocene conditions (Figure 5.10) reveals a small 8% reduction of ENSO amplitude but a large inter-model spread of ±15% with respect to the present-day amplitude. GCMs run under mid-Holocene conditions simulate with medium confidence a reduction in the strength of the annual cycle of eastern equatorial Pacific SST (Figure 5.10). The reason for this change remains unresolved.

Reconstructions of ENSO for the last millennium also document multidecadal to centennial variations of the amplitude of reconstructed interannual eastern equatorial Pacific SST anomalies (Li et al., 2011; McGregor et al., 2010; Wilson et al., 2010). Statistical efforts to determine ENSO variance changes in different annually–resolved ENSO proxies reveal with medium confidence extended periods of low ENSO activity during parts of the LIA (D'Arrigo et al., 2005; Fowler et al., 2012; Hereid et al., in press; McGregor et al., 2010) compared to the 20th century. A new compilation of fossil coral data from the central equatorial

Pacific further confirms higher ENSO variance during the 20th century, compared to the average variance during the last 7000 years (Cobb et al., submitted). Climate model simulations (Mann et al., 2005; Meehl et al., 2009) and proxy records from the eastern tropical Pacific suggest a possible effect of solar irradiance changes on the mean state of the tropical Pacific (Marchitto et al., 2010) (see also Sections 5.3.5, 5.5.10 and Figure 5.9). However, the reconstructed multidecadal variance changes of interannual ENSO variability are fully consistent with the notion of internal variability (McGregor et al., 2010; Russon et al., submitted) and are uncorrelated with variations in TSI. According to reconstructions of volcanic events (Section 5.2.1.3) and some ENSO proxies, a slightly increased probability exists (medium confidence) in the occurrence of El Niño events in the 2 years following major volcanic eruptions (Adams et al., 2003; McGregor et al., 2010; Wilson et al., 2010). Simplified intermediate complexity ENSO models are able to reproduce this behaviour (Emile-Geay et al., 2008; Mann et al., 2005), whereas GCM experiments show a more complex response with an initial cooling and a subsequent warming due to the recharge of heat into the equatorial thermocline (McGregor and Timmermann, 2010).

5.4.2 Extratropical Modes

LGM and Mid-Holocene northern annular modes were investigated in modelling studies. Robust evidence from climate model simulations under LGM conditions indicates a weakening of the Northern Annular Mode (NAM) variability, connected with stronger planetary wave activity (Lü et al., 2010). A significant but model-dependent distortion of the simulated LGM North Atlantic Oscillation (NAO) pattern may result from the strong topographic ice-sheet forcing (Handorf et al., 2009; Justino and Peltier, 2005; Pausata et al., 2009). A multimodel analysis of NAO behaviour during the mid-Holocene (6 ka) simulations (Gladstone et al., 2005) reveals an NAO mode, similar to its pre-industrial state, with a more positive NAO during the early Holocene (Rimbu et al., 2003) but no consistent change in its interannual variability. Robust proxy evidence to test these model-based results has not yet been established. Since AR4 only a few new cold season NAO reconstructions have been published. They are based on long instrumental pressure series (Cornes et al., 2012), a combination of instrumental and ship log-book data (Küttel et al., 2010) and proxy archives (Trouet et al., 2009). Whereas these and earlier NAO reconstructions (Cook et al., 2002; Luterbacher et al., 2002; Timm et al., 2004) differ in several aspects, they demonstrate with high confidence (taking into consideration associated reconstruction uncertainties) that the strong positive NAO phases within the early 20th century and the mid-1990s are not unusual in the context of the past half millennium. (Trouet et al., 2009) presented a winter NAO reconstruction that yielded a persistent positive phase during the MCA in contrast to higher frequency variability during the LIA. (Trouet et al., 2012) postulated that this MCA/LIA difference might be related to a weakening of the AMOC and a transition to more negative NAO conditions or through a shift to increased storminess over the North Atlantic linked to increased mid-latitude cyclogenesis. However, a recent pseudo-proxy-based assessment of low-frequency NAO behaviour (Lehner et al., 2012) infers weaknesses in the reconstruction method used by (Trouet et al., 2009). TSI-forced last millennium GCM simulations reveal no significant response of the NAO to solar forcing (Yiou et al., 2012), except for the GISS-ER coupled model which includes ozone photochemistry, extends into the middle atmosphere and exhibits a stronger NAO during MCA compared to the LIA (Mann et al., 2009).

Changes in the Southern Annular Mode (SAM) modulate the strength and position of the mean Southern Hemispheric westerlies (see Section 5.4.2.3), and leave an important signature on SH surface climate (Gillett et al., 2006). A first hemispheric-wide mid-latitude tree-ring based austral summer SAM reconstruction (Villalba et al., submitted) indicates with medium confidence that the 20th century trend in the strength of Southern Hemisphere westerlies may have been anomalous in the context of the last 600 years, thus supporting earlier South American proxy evidence (Holz and Veblen, 2011; Lara et al., 2008; Urrutia et al., 2011) and GCM (Wilmes et al., 2012) studies.

Large-scale SST variations are observed in the North Atlantic Ocean on multidecadal timescales. Most prominent is the basin-wide variation of the AMO, marked by alternation of warm and cold SST anomalies in the North Atlantic with a timescale of about 60–80 years (Delworth and Mann, 2000; Knight et al., 2005) (see also chapter 9,14). Due to the wide range of impacts outside the North Atlantic region, both marine (Black et al., 2007; Kilbourne et al., 2008; Saenger et al., 2009; Sicre et al., 2008) and terrestrial proxy archives (Gray et al., 2004; Shanahan et al., 2009) from different locations have been used to reconstruct the past evolution of the AMO. Whereas most of these records show a good correspondence with the instrumental data during the industrial period, there still exist uncertainties in the reconstructions prior to

1900 CE (Winter et al., 2011). Using 8000-year long proxy records, (Knudsen et al., 2011) concluded that the AMO is unrelated to TSI changes and can be explained in terms of internally generated ocean-atmosphere variability. However, GCM experiments (Ottera et al., 2010; Waple et al., 2002) using solar and/or volcanic forcing reconstructions indicate that external forcings may have played a role in driving or at least pacemaking AMO variations.

[INSERT FIGURE 5.10 HERE]

Figure 5.10: Relative changes in amplitude of the annual cycle of SST in Niño 3 region (average over 5°S–5°N and 150°W–90°W) (left) and changes in amplitude of interannual SST anomalies in the Niño 3.4 region (average over 5°S–5°N and 170°W–120°W) (right) simulated by an ensemble of climate model experiments in response to external forcing. Left: Multi-model average of relative changes (%) in amplitude of the mean seasonal cycle of Niño 3 SST for mid-Holocene and LGM time-slice experiments and for freshwater perturbation experiments (Hosing) that lead to a weakening of the AMOC by more than 50%. Bars encompass the 25 and 75 percentiles, with the red horizontal lines indicating the median in the respective multi-model ensemble, red crosses are values in the upper and lower quartile of the distribution; Right: same as left, but for the SST anomalies in the Niño 3.4 region, representing ENSO variability. The MH and LGM experiments were coordinated by the Paleoclimate Modelling Intercomparison Project Phase II (PMIP2) or III (PMIP3). The MH ensemble includes 4 experiments (6k) performed by models participating in PMIP2 (FGOALS1.0g, IPSL-CM4, MIROC3.2 medres, CCSM3.0) and *7* experiments (mid-Holocene) performed by models participating in PMIP3 (CCSM4.0, CSIRO-Mk3-6-0, HadGEM2-CC, HadGEM2-ES, MIROC-ESM, MPI-ESM-P, MRI-CGCM3). The LGM ensemble includes 5 experiments (21 ka) performed by models participating in PMIP2 (FGOALS1.0g, IPSL-CM4, MIROC3.2 medres, CCSM3.0, HadCM3) and 5 experiments (LGM) performed by models participating in PMIP3 (CCSM4, GISS-E2-R, IPSL-CM5A-LR, MIROC-ESM, and MPI-ESM-P). The changes in response to MH and LGM forcing are computed with respect the preindustrial control simulations coordinated by PMIP2 (0k experiment) and PMIP3 (piControl experiment). The results for Hosing are obtained from freshwater perturbation experiments conducted with CCSM2.0, CCSM3.0, HadCM3, ECHAM5-MPIOM, GFDL-CM2.1 (Timmermann et al., 2007), CSM1.4 (Bozbiyik et al., 2011) for pre-industrial or present-day conditions and with CCSM3 for glacial conditions (Merkel et al., 2010). The changes in response to fresh water forcing are computed with respect the portion of simulations when the AMOC is high.

5.5 Regional Changes during the Holocene

Emphasis is placed on regional changes that have emerged since AR4 from proxy records and climate simulations, including the global consistency of regional changes and their comparison with instrumental records.

5.5.1 Temperature

5.5.1.1 Northern Hemisphere Mid-to-High Latitudes

New studies confirm the surface-air temperature and SST distribution summarised in AR4 (Jansen et al., 2007). Most of the long-term Holocene climate trends were very likely influenced by orbital forcing orbital forcing (Section 5.2.1.1). Spatial variability in the temperature anomalies and the timing of the thermal maximum implicate indirect, atmospheric or oceanic circulation mediated responses as well as downwind effect from remaining ice sheets (e.g., Bartlein et al., 2011; Leduc et al., 2010; Renssen et al., 2012; Wanner et al., 2008). Model simulations and proxy data suggest that the highest early-to-mid Holocene North Atlantic and sub-Arctic SSTs were restricted to the stratified uppermost surface ocean layer, below which early Holocene temperatures were lower than late Holocene (Andersson et al., 2010; Hald et al., 2007).

Terrestrial early-to-mid Holocene summer-season temperatures warmer than today are ubiquitous in the mid to high latitude (Central and Northern Europe, Northern Asia and Northern North America), consistent with a direct response to local summer insolation, and there is also robust evidence for warmer mid-Holocene winters compared to the late 20th century (e.g., Bartlein et al., 2011; Wanner et al., 2008) (Figure 5.11). The PMIP2 and CMIP5/PMIP3 simulations for the mid-Holocene (6 ka) share similar large-scale seasonal changes (Figure 5.11), with significant summer warming compared to mid-20th century but large winter inter-model spread (Bartlein et al., 2011; Braconnot et al., 2007; Harrison et al., submitted). There is a general NH cooling after ca. 5 ka (Kobashi et al., 2011; Vinther et al., 2009; Wanner et al., 2008) and increased amplitude of millennial scale variability (Risebrobakken et al., 2011). The regional patterns of the Holocene SST cooling trend are well-simulated for the North Atlantic and western North Pacific oceans, but models generally show weaker Holocene SST trends than alkenone SST records (Lohmann et al., submitted).

This general cooling trend, consistent with orbital forcing, has been documented in the Arctic and Scandinavia over the last two millennia, until it was interrupted by the 20th century warming, (Esper et al., 2012b; Kaufman et al., 2009; Spielhagen et al., 2011). Marine proxy records of the last millennium indicate warm SSTs north of Iceland and the Norwegian Sea from 900 CE to 1400 CE, followed by a generally colder period that ended in the early 20th century. Modern SSTs may still be cooler than the warmest intervals of the 900–1400 CE period (Cunningham et al., submitted). Further north, in Fram Strait, modern SSTs of the advected Atlantic Water appear warmer than those reconstructed for any prior period of the last 2000 years (Spielhagen et al., 2011). Bonnet et al., (2010) analyzed dinocysts rather than foraminifera in the same sediment core (the two proxies reflect different water masses) and identified a cooling trend over the last 2000 years without a 20th century rise, and intervals at 100 CE and 600 CE warmer than during Medieval times. During medieval times (centred around 1000 CE), portions of the Arctic and sub-Arctic experienced periods warmer than any subsequent period except the last 50 years (Kaufman et al., 2009; Kobashi et al., 2010; Kobashi et al., 2011; Spielhagen et al., 2011; Vinther et al., 2010).

Focusing now on the last millennia, progress has been made to reconstruct surface air temperatures for different regions (Figure 5.12). For North America tree-ring data and lake sediment varve thickness records from the North American treeline (Alaska and northern Canada; McKay et al., 2008; Bird et al., 2009; D'Arrigo et al., 2009; Anchukaitis et al., 2012) suggest broad-scale common centennial and multidecadal climate variability during the last several centuries. Reconstructions document warming beginning in the late 19th century, an early 20th century period of warmer temperatures and the highest estimated temperature at the end of the 20th century. Summer mean temperatures reconstructed from lacustrine pollen records in Wisconsin lakes (Wahl et al., 2012) suggest a relatively warm period during ca. 1200–1500 CE which is not in phase with higher latitudes. The generally colder conditions until 1900 CE are in broad agreement with other pollen, tree ring and lake sediment evidence from northwest Canada, Canadian Rockies and Colorado (Loso, 2009; Luckman and Wilson, 2005; MacDonald et al., 2009; Salzer and Kipfmueller, 2005; Thomas and Briner, 2009). Pollen records (Viau et al., 2012) indicate that North American warmest month temperatures during 650–1050 CE and 1550–1850 CE were colder than the last decades especially over the eastern portions and boreal regions of the continent and likely also across the continent.

[INSERT FIGURE 5.11 HERE]

Figure 5.11: Model-data comparison of surface temperature anomalies for the mid-Holocene (6 ka). MTCO is the mean temperature of the coldest month; MTWA is the mean temperature of the warmest month. Top panels are pollen-based reconstructions of Bartlein et al., (2011). Middle panels are corresponding surface temperature anomalies simulated by the PMIP2 and PMIP3 models. Bottom panels contain boxplots for reconstructions (grey), for model ensembles (orange) and for the individual models interpolated to the locations of the reconstructions. The boxes are drawn using the 25th, 50th and 75th percentiles (bottom, middle and top of the box, respectively), and whiskers extend to the 5th and 95th percentiles of data or model results within each area. The northern extratropics are defined as 30-90ºN and the tropics as 30ºS-30ºN. Thirty-three models are assessed, PMIP2 OA: CCSM3, CSIRO-Mk3L-1.0, CSIRO-Mk3L-1.1, ECBILTCLIOVECODE, ECHAM5-MPIOM1, FGOALS-1.0g, FOAM, GISSmodelE, IPSL-CM4-V1-MR, MIROC3.2, MRI-CGCM2.3.4fa, MRI-CGCM2.3.4nfa, UBRIS-HadCM3M2; PMIP2 OAV: ECBILTCLIOVECODE, ECHAM53-MPIOM127-LPJ, FOAM, MRI-CGCM2.3.4fa, MRI-CGCM2.3.4nfa, UBRIS-HadCM3M2; CMIP5/PMIP3 OA: CCSM4, CNRM-CM5, CSIRO-Mk3-6-0, EC-EARTH-2-2, FGOALS-s2, FGOALS-g2, MPI-ESM-P, MRI-CGCM3, UNSW; CMIP5/PMIP3 BCC-CSM1.1, HadGEM2-CC, HadGEM2-ES, IPSL-CM5A-LR, MIROC-ESM.

Since AR4, several new temperature reconstructions have been produced for different parts of Europe. Tree ring-based summer temperatures reconstructions from different locations in northern Fennoscandia (Büntgen et al., 2011a; Esper et al., 2012a; Esper et al., 2012b; Helama et al., 2010; Linderholm et al., 2010; McCarroll et al., submitted; Melvin et al., accepted) reveal periods of alternating cooler and warmer summer temperatures over the last one-to-two millennia. The comparatively data-rich period around 1000 to 1100 CE in northern Fennoscandia indicates similar levels of summer warmth compared to those observed during the mid and late 20th century. Warmth is also indicated in Roman times (around the 1st century) but comparison with the present climate is uncertain due to limitations of tree-ring data to capture long-term temperature trends (Esper et al., 2012a).

In the Alpine region, millennium long tree ring records (Büntgen et al., 2006; Büntgen et al., 2005; Büntgen et al., 2011a; Corona et al., 2010; Corona et al., 2011; Nicolussi et al., 2009) and summer temperatures derived from chironomids from lake sediments (Larocque-Tobler et al., 2010; Larocque-Tobler et al., 2012;

Trachsel et al., 2012). (Millet et al., 2009) points to relatively warm conditions centred around 1000 CE and 1200 CE, though lower than the most recent decades (high confidence level). Büntgen et al., (2011a) and Stewart et al., (2011a) extended summer temperature reconstructions from different parts of the Alps back for 2500 years. They found multiple examples during Roman and earlier times as warm (or warmer) than most of the 20th century.

Reconstructions of European mean summer temperature for the last two millennia (PAGES 2k Consortium, submitted) identify a warm period centred around 1000 CE. Generally cooler summer conditions prevailed from the 13th to the 19th century with short relatively warm periods during the 15th and 18th centuries (Guiot et al., 2010). The decade 2001 to 2010 CE in European summer temperature stands substantially above any other 10 year summer period covering the past 2000 years (PAGES 2k Consortium, submitted) and the hot summers of 2003 CE and 2010 CE were likely the warmest for more than half a millennium (Barriopedro et al., 2011). Annual mean temperatures in Central Europe since 1988 were very likely the warmest since 1500 CE according to historical documentary evidence and long instrumental records (Dobrovolný et al., 2010).

Temperature reconstructions from Asian tree-ring records provide evidence for various regions (Western Himalayas, Tibetan Plateau, Tianshan Mountains and western High Asia) with warm conditions from the 11th to the 15th century, lower temperature afterwards and warming within the 20th century in the Western Himalaya (Esper et al., 2007a; Yadav et al., 2011; Zhang et al., 2009; Zhu et al., 2008). Late 20th century warmth in parts of China is likely unprecedented compared to the last 500 years; prior to this, 1000-year to 2000-year long cold and warm season temperature reconstructions (based on documentary evidence and natural proxies) consistently show warm conditions during the MCA but it is not clear whether they exceed modern temperatures because of the large uncertainties (Ge et al., 2006; Ge et al., 2010; Holmes et al., 2009; Wang et al., 2007; Yang et al., 2009; Zhang et al., 2009). However, the period between 900 CE and 1150 CE are characterized by low winter and summer mean temperature in the Aral Sea basin (Central Asia) based on high-resolution pollen analyses from sediment cores (Sorrel et al., 2007). In northeast China, an alkenone-based reconstruction indicated that the growing season temperature was about 1°C during the period 1260–1300 CE compared with the 20th century (Chu et al., 2011).

An unresolved topic is the decadal to centennial variability of the Atlantic meridional overturning circulation variability and its climate impacts. Surface Atlantic meridional overturning circulation dynamics likely amplified the relatively warm conditions during the MCA and the cooler conditions during the LIA within the North Atlantic sector (Wanamaker et al., 2012).

[INSERT FIGURE 5.12 HERE]

Figure 5.12: Regional temperature reconstructions and simulations over the past millennium (1001–1999 CE). Temperature anomalies are calculated with respect to the 1961–1990 CE reference period, for annual (ANN) or selected seasons (December to February [DJF], June to August [JJA] or September to February [SONDJF]) in regions indicated in the lower right panel. Reconstructions (PAGES 2k Consortium, submitted, thick black line) and simulated (coloured lines) temperature anomalies are for land only, with the exception of the Arctic and Australasian regions which combine land and ocean. Grey shading indicates uncertainty ranges of reconstructions, as defined for each region (PAGES 2k Consortium, submitted). Model results from Last Millennium simulations are displayed using dashed lines for pre-PMIP3 simulations and solid lines for CMIP5-PMIP3 simulations. Blue/green colours indicate simulations using low solar forcing (see Appendix 5.A, Table 5.A.5) and red/yellow indicate simulations using strong solar forcing (Appendix 5.A, Table 5.A.5). All model time series are smoothed with a 30-year moving average filter. Models used: Pre-PMIP3: ECHO-G (Gonzalez-Rouco et al., 2006), CCSM (Ammann et al., 2007), IPSL (Servonnat et al., 2010), CCSM-Bern (Hofer et al, 2011), ECHAM5/MPIOM (E1, E2) (Jungclaus et al., 2010), and CNRM (Swingedouw et al., 2011). CMIP5-PMIP3: CCSM4 (Landrum et al., submitted), GISS-E2-R (Schmidt et al., 2006), HadCM3 (Schurer et al., submitted), CSIRO-Mk3L-1-2 (Phipps et al., 2011), MPI-ESM-P (Raddatz et al., 2007), and BCC-CSM1-1 (Wu et al., submitted).

5.5.1.2 Tropics

This section focuses first on paleoceanographic records of SST trends, and on modelling results for mid-Holocene climate changes.

Holocene tropical SST trends are regionally heterogeneous and variable in magnitude. Alkenone records from the eastern tropical Pacific, western tropical Atlantic, and the Indonesian archipelago document a warming trend of ~0.5°C to 2°C from the early Holocene to present (Leduc et al., 2010), consistent with local insolation. In contrast, regional trends of planktonic foraminiferal Mg/Ca records are heterogeneous, and imply smaller magnitude SST changes (Leduc et al., 2010; Schneider et al., 2010). In the Indo-Pacific warm-pool region, different magnitudes of cooling trends are depicted by foraminiferal Mg/Ca records from species inhabiting the surface mixed layer (Linsley et al., 2010; Stott et al., 2004) or from thermocline-dwelling species. In summary, the tropical oceans are marked by a regional and variable response in surface temperatures over the Holocene.

The PMIP2 and CMIP5/PMIP3 simulations for the mid-Holocene simulate summer cooling and shorter growing season in the tropical monsoon regions of Africa and southeast Asia (Harrison et al., submitted) (Figure 5.11), attributed to increased cloudiness. In contrast, for the entire tropics (30°S to 30°N), both simulations and reconstructions show generally higher warm-season temperatures and lower cold-season temperatures than for the mid-20th century. Terrestrial reconstructions are strongly biased toward Africa and to some extent to southeast Asia (Figure 5.11), with no reconstructions available in the form of syntheses from South America and Australia. Data availability thus limits assessment of model performance for the latter regions.

5.5.1.3 Southern Hemisphere Mid to High Latitudes

In the high latitude Southern Ocean, Holocene SST trends follow the decrease in austral summer duration, with a cooling trend from the Early Holocene (Kaiser et al., 2008; Shevenell et al., 2011). As in the Northern Hemisphere near surface temperature variations strengthened after 5–4 ka with emergence of high-amplitude, millennial-to-centennial scale variations, particularly between 5 ka and 4 ka, possibly due to variations in the position and strength of the westerlies (Euler and Ninnemann, 2010; Moros et al., 2009; Shevenell et al., 2011). Indices for the position of Southern Ocean fronts and the strength and position of the westerlies diverge (Moros et al., 2009; e.g., Shevenell et al., 2011). For the mid-to-late Holocene, climate models of different complexity consistently show a poleward shift and intensification of the Southern Hemisphere westerlies in response to orbital forcing (Varma et al., 2012). However, magnitude, spatial pattern and seasonal response vary significantly among the models.

The Holocene land surface temperature history is difficult to assess. Individual reconstructions generally track the trends registered by Antarctic ice-core records through the glacial termination into the Holocene (Clark et al., 2012), and show smaller seasonal temperature anomalies for the mid Holocene than in the north.

Since AR4, syntheses of high-resolution records for the last 2000 years have been completed (Neukom and Gergis, 2011). Reconstructions include tree ring records from the subtropical and central Andes, northern and southern Patagonia, Tierra del Fuego, New Zealand and Tasmania (Boninsegna et al., 2009; Cook et al., 2006; Villalba et al., 2009), ice cores, lake sediments and documentary evidence from southern South America (Neukom et al., 2011; Prieto and García Herrera, 2009; Tierney et al., 2010; Vimeux et al., 2009; von Gunten et al., 2009), terrestrial and shallow marine geological records from eastern Antarctica (Verleyen et al., 2011), ice cores from East Antarctica (Goosse et al., accepted), boreholes from western Antarctica (Orsi et al., 2012) and coral records from the Indian and Pacific Oceans (Linsley et al., 2008; Lough, 2011; Zinke et al., 2009).

A multi-proxy reconstruction for southern South America (Neukom et al., 2011) displays austral summer temperatures between 900 CE and 1350 CE that are, with medium confidence, warmer than the 20th century climatology. A 1000-year temperature reconstruction for land and ocean representing Australasia provides evidence that summer temperatures in the post-1950 CE period were warmest in the last ~580 years (PAGES 2k Consortium, submitted). Prior to this, the reconstruction is based on only three or fewer proxy series and less confident conclusions can be supported.

5.5.1.4 Patterns of MCA-LIA Changes

Multiple lines of evidence suggest that the MCA was not characterized by a pattern of higher temperatures that were consistent across seasons and regions. Changes in the persistence or frequency of climate modes (Section 5.4) can generate climate reorganizations that would explain temperature anomalies over the past millennium. Specifically, changes in medieval climate has been argued to be a result of shifts in the dynamics of the Indo-Pacific and Atlantic basins. Several studies (Diaz et al., 2011; Graham et al., 2011; Graham et al., 2007; Mann et al., 2009; Seager et al., 2008) support medieval cooling related to a La Niña-like background state in the eastern equatorial Pacific (Sections 5.3.5.3 and 5.4.1, Figure 5.9) in combination with a positive mode of the AMO/NAO in the North Atlantic (Oglesby et al., 2012; Trouet et al., 2009, see Section 5.4.2). These changes have been made responsible for warm MCA summers and drought in North America (Seager et al, 2007; Wahl et al, 2012, Oglesby et al, 2012). Temperature anomalies in the Indo-Pacific regions have also been found to be consistent with SST proxy records (Oppo et al., 2009) and hydrological evidence from lakes in tropical East Africa (Tierney et al., 2010; Tierney et al., submitted). Enhanced NAO through SST changes (Graham et al., 2011) have also been argued to contribute to medieval warmer conditions in NW Europe (Trouet et al, 2009) and are consistent with model assimilation experiments (Goosse et al, 2012b).

5.5.2 Sea Ice

Since AR4 several new Holocene sea ice reconstructions for the Arctic and sub-Arctic have been published, resolving multi-decadal to century scale variability. Proxies of sea ice extent have been further developed from biomarkers in deep sea sediments (e.g., IP25, Belt et al., 2007; Müller et al., 2011) and from sea ice biota preserved in sediments (e.g., Justwan and Koç, 2008). Indirect information on sea ice conditions based on drift wood and beach erosion has also been compiled (Funder et al., 2011).In general, these sea ice reconstructions parallel regional SST, yet they display spatial heterogeneity, and differences between the methods, making it difficult to provide quantitative estimates of past sea ice extent.

Summer sea ice cover apparently was reduced compared to late 20th century levels both in the Arctic Ocean and along East Greenland between 8 ka and 6.5 ka (e.g., Funder et al., 2011; Moros et al., 2006; Polyak et al., 2010). The response of this sea ice cover to summer insolation warming was shown to be central for explaining the reconstructed warmer winter temperatures over the adjacent land (Otto et al., 2009; Zhang et al., 2010). During the last 6 kyr available records show a long-term trend of a more extensive Arctic sea ice cover driven by the orbital forcing, but punctuated by strong century- to millennial scale variability. Several sea ice proxies indicate relatively reduced sea ice cover 800 CE to 1200 CE in line with temperature proxies, with an increased sea ice cover in the LIA (see overview in Polyak et al., 2010). Proxy reconstructions also document the 20th century ice loss trend, which is also observed in historical sea ice data sets (Divine and Dick, 2006), with a decline since the late 19th century. There is medium confidence that the current ice loss and increasing SSTs in the Arctic are anomalous in the perspective of at least the last two millennia (England et al., 2008; Kaufman et al., 2009; Kinnard et al., 2008; Kinnard et al., 2011; Macias Fauria et al., 2010; Polyakov et al., 2010; Spielhagen et al., 2011).

Fewer high resolution records exist from the Southern Ocean. Data from the Indian Ocean sector of the Southern Ocean document an increasing sea ice trend during the Holocene, following the local orbital forcing, with a rather abrupt increase between 5 ka and 4 ka (Denis et al., 2010).

5.5.3 Glaciers

Reconstructions of glacier length variations provide important independent paleoclimatic information and place recent changes in cryosphere and climate into a longer context. Due to the timescale of glacier front responses, high frequency mass balance perturbations are filtered by glaciers and their length variations resolve only decadal to centennial scale climate variability. The key factors governing extra-tropical glacier growth and shrinkage are summer temperature and winter/annual precipitation (see Chapter 4). Glaciers in regions with high seasonal accumulation (e.g., Iceland, coastal Norway, New Zealand) and those located in the monsoon regions are particularly sensitive to the precipitation factor. Since AR4 new data have improved the accuracy of many regional Holocene glacial chronologies (e.g., Davis et al., 2009). Various techniques have been extensively applied to date moraines and have significantly improved many chronologies of glacier variations (Anderson et al., 2008; Hughes et al., 2012; Joerin et al., 2008; Jomelli et al., 2009; Licciardi et al., 2009; Menounos et al., 2009; Schaefer et al., 2009; Wiles et al., 2011; Yang et al., 2008).

Studies of sediments from glacier-fed lakes and marine deposits have allowed continuous reconstructions of glacier fluctuations (Bertrand et al., 2012; Bowerman and Clark, 2011; Briner et al., 2010; Larsen et al., 2011; Matthews and Dresser, 2008; Russell et al., 2009; Vasskog et al., 2012). New reconstructions of the history of ice-shelves and ice sheets/caps have also emerged (Antoniades et al., 2011; Hodgson, 2011; Kirshner et al., 2012; Simms et al., 2011; Smith et al., 2011).

New data confirm the general Holocene increase of glacier extent in the NH and its decrease in the SH over the Holocene period, consistent with the orbital derived trends of summer insolation and temperatures (see Section 5.5.1.1) in both hemispheres (Davis et al., 2009). Some exceptions exist, however, e.g., in the eastern Himalayas, where glaciers were most extensive in the early Holocene (Gayer et al., 2006; Seong et al., 2009). Model results (Rupper et al., 2009) indicate that this might be an effect of a decrease in summer temperatures as a dynamical response to orbital forcing. Due to remaining dating uncertainties, incompleteness and heterogeneity of most existing glacial chronologies it is difficult to compare glacier variations between regions at centennial and shorter time scales (Heyman et al., 2011; Kirkbride and Winkler, 2012). There are thus no conclusive results regarding potential interhemispheric synchronicity of submillennial scale glacier fluctuations during the Holocene (Jomelli et al., 2009; Licciardi et al., 2009; Schaefer et al., 2009; Wanner et al., 2011; Wanner et al., 2008; Winkler and Matthews, 2010). Documented asynchrony between Europe and New Zealand is likely a result of regional climate control rather than interhemispheric mechanisms (Putnam et al., in press).

Glacial chronologies for the last 2 kyr are better constrained by dating. The multi-centennial variability of glaciers in this period was suggested to be linked with variations in solar activity (Holzhauser et al., 2005; Wiles et al., 2008), volcanic forcing (Anderson et al., 2008), changes in North Atlantic circulation (Linderholm and Jansson, 2007; Marzeion and Nesje, 2012; Nesje, 2009).

Consistent with global warming, glaciers are currently retreating globally (Chapter 4) releasing organic remains and artefacts from previous warm periods with reduced glacier size (Agatova et al., 2012; Joerin et al., 2008; Nesje et al., 2011; Öberg and Kullman, 2011). There is high confidence that glaciers at times have been smaller than at present in several regions (the Alps, Scandinavia, North America, Altay in Central Asia), but the precise glacier extent in the previous warm periods is often difficult to assess. Although currently retreating, glaciers are still larger now than in previous Holocene warm periods in most regions, especially compared to the Early to Mid Holocene in the Northern Hemisphere. Most of these earlier minima can be attributed to high summer insolation in the Early to Mid Holocene (see Section 5.5.1.1). Altogether, the available data indicate a more heterogeneous and complex glacier response during the MCA than the uniform global glacier recession observed at present (Chapter 4). Some glaciers were smaller in the MCA than in the early 21st Century (western Antarctic Peninsula (Hall et al., 2010); southern Swiss Alps (Scapozza et al., 2010), however, prominent advances occurred within the MCA, at 1050 and 1150 CE, in the Alps (Holzhauser et al., 2005), Patagonia (Luckman and Villalba, 2001), New Zealand (Schaefer et al., 2009) and SE Tibet (Yang et al., 2008). Glaciers in western North America were similar in size in the MCA compared to the peak of the LIA. These advances were likely forced by increased winter precipitation due to prolonged La Niña-like conditions (Koch and Clague, 2011).

The available information indicates with medium confidence that the global recession of glacier length is unusual in the context of the last 2 kyr. This is consistent with reconstructed temperature anomalies (Sections 5.3.5 and 5.5.1.1).

5.5.4 Monsoon Systems and Convergence Zones

Since AR4, higher resolution hydroclimate reconstructions using speleothems (Asmerom et al., 2010; Berkelhammer et al., 2010; Hu et al., 2008; Kanner et al., 2012; Sinha et al., 2007; Stríkis et al., 2011; Wang et al., 2008), lake sediments (Shanahan et al., 2009; Stager et al., 2009; Wolff et al., 2011), marine sediments (Ponton et al., 2012; Tjallingii et al., 2008; Weldeab et al., 2006; Weldeab et al., 2007) and tree ring chronologies (Buckley et al., 2010; Cook et al., 2010b) have provided a more comprehensive view on the dynamics of monsoon systems on a variety of timescales. From water isotope enabled modelling experiments (e.g., Lewis et al., 2010; Pausata et al., 2011a) and evaluation of marine and terrestrial data (Clemens et al., 2010), East Asian monsoon speleothem $\delta^{18}O$ is suggested to be affected by large-scale moisture transport in addition to local precipitation.

This subsection focuses on internal and externally-driven variability of monsoon systems during the last millennium. The dynamics of abrupt monsoon changes associated with Dansgaard–Oeschger and Heinrich events (Figure 5.4 b, e, h) are further assessed in Section 5.7.1. Orbital-scale monsoon (Figure 5.4a, d, g) changes are evaluated in Section 5.3.2

On multi-decadal-to-centennial timescales, influences of North Atlantic multidecadal SST variations have been demonstrated for North and South African monsoon, Indian and East Asia summer monsoons (see Figure 5.4c), both using paleo-climate reconstructions (Feng and Hu, 2008; Shanahan et al., 2009) and climate model experiments (Lu et al., 2006; Luo et al., 2011; Wang et al., 2009; Zhang and Delworth, 2006). Some GCM simulations of the last millennium (Liu et al., 2009a) suggest that solar variability and volcanic forcing (Fan et al., 2009) may exert weak regional influences on monsoon systems (Figure 5.4f,i). Hydrological proxy data characterizing the intensity of the East Asian monsoon (South American monsoon) show increased (decreased) hydrological activity during the MCA as compared to the LIA (medium confidence) (Figure 5.4f,i), in accordance with proxy evidences suggesting a North Atlantic warming and a northward progression of the Atlantic Intertropical Convergence Zone (ITCZ) (Bird et al., 2011; Vuille et al., 2012; Zhang et al., 2008). These shifts were accompanied by the changing occurrence of megadroughts (high confidence) in parts of monsoon Asia (Buckley et al., 2010; Cook et al., 2010b) (Figure 5.13). A five-member multi-model ensemble mean of CMIP5/PMIP3 Last Millennium simulations exhibits decreased (increased) standardized monsoon rainfall accompanying periods of reduced shortwave radiative forcing in the East Asian (South American) monsoon regions (Figure 5.4). There is however a considerable inter-model spread in the simulated annual mean precipitation response to solar forcing with the multi-model mean explaining on average only ~25 ± 15% (1 standard deviation) of the variance of the individual model simulations. Lake sediment evidence from coastal eastern Africa suggests dry conditions in the latter MCA, a wet LIA, and return toward dry conditions in the 18th or early 19th century (Stager et al., 2005; Tierney et al., 2011; Verschuren et al., 2000; Verschuren et al., 2009; Wolff et al., 2011), qualitatively similar to the South American monsoon proxies in Figure 5.4i, whereas some inland and southern African lakes suggest dry spells during the LIA (Anchukaitis and Tierney, submitted; Garcin et al., 2007). An assessment of the response of monsoon systems to volcanic forcing using paleo-proxy data has revealed wetter conditions over Southeast Asia in the year of a major volcanic eruption and drier conditions in central Asia (Anchukaitis et al., 2010), in contrast to experiments with climate models (Brovkin et al., 2008; Fan et al., 2009; Oman et al., 2005; Schneider et al., 2009).

Extended intervals of monsoon failures and dry spells have been reconstructed for the last few millennia for West Africa (Shanahan et al., 2009; Wolff et al., 2011), northern Africa (Esper et al., 2007b; Touchan et al., 2008; Touchan et al., 2011), India and southeastern Asia (Berkelhammer et al., 2010; Buckley et al., 2010; Cook et al., 2010b; Zhang et al., 2008) and Australia (Mohtadi et al., 2011). Proxy data document that, as part of unforced natural variability, monsoon failures in some regions, such as the Sahel (Shanahan et al., 2009) can last for several decades, causing droughts that were much more extensive than those during the 20th century.

5.5.5 Megadroughts and Floods

Paleo-drought reconstructions provide estimates of the frequency, duration and severity of past dry periods. Megadroughts are typically whose cumulative severity or duration exceed observed drought, typically on decadal or multidecadal time scales (e.g., Herweijer et al., 2007; Seager et al., 2008; Stine, 1994; Woodhouse and Overpeck, 1998). As an example, Figure 5.13 presents drought (Palmer Drought Severity Index) occurrence, the duration, severity, and their frequency during the last millennium from North America using tree ring information (Cook et al., 2010a; Cook et al., 2010b). Longer and more severe droughts than today are seen in particularly during the MCA (Cook et al., 2010b; Meko et al., 2007). The period from the MCA to the LIA appears to coincide in North America with a shift towards overall wetter conditions in the middle of the 14th century (Chen et al., 2010; Cook et al., 2010a; Cook et al., 2010b). In contrast with evidence from the desert southwest US, new reconstructions from lake sediment $\delta^{18}O$ from the Pacific North West indicate exceptional wetness during the MCA and extended drought during the LIA (Steinman et al., 2012). Those opposite patterns are consistent with impacts of the El Niño Southern Oscillation (ENSO) and the Pacific Decadal Oscillation (PDO). Multiple lines of proxy evidence from tree-rings, lake sediments, and speleothems indicate that megadroughts are a feature of North American hydroclimate throughout the

Holocene (e.g., Asmerom et al., 2007; Ault et al., submitted; Cook et al., 2010a; Cook et al., 2010b; Newby et al., 2011; Oswald and Foster, 2011; Routson et al., 2011; Shuman et al., 2010; Shuman et al., 2009; Stambaugh et al., 2011; Woodhouse et al., 2010).

In Scandinavia, new tree-ring based reconstructions show a multi-centennial drought phase during medieval time (900–1350 CE). New tree ring reconstructions from southern-central (Wilson et al., 2012) and southeastern British Isles (Cooper et al., 2012) do not find multi-centennial drought during the medieval period, rather alternating multi-decade-long dry and wet periods. Wilson et al., (2012) reconstructed drier conditions between ~1300 CE and the early 16th century. Büntgen et al., (2011b) identified exceptionally dry conditions in central Europe from 200–350 CE and between 400 and 600 CE. Numerous tree-ring records from the eastern Mediterranean testify to the regular occurrence of late Holocene droughts there (e.g., Akkemik et al., 2008; Luterbacher et al., 2012; Nicault et al., 2008). In northern Africa, Esper et al., (2007b) and Touchan et al (2008; 2011) show severe drought events through the last millennium, particularly prior to 1300 CE, in the 1400s CE, between 1700 and 1900 CE, and in the most recent proxy and instrumental data. The wide spread medieval drought occurred also in synchrony with equatorial East Africa (Russell and Johnson, 2005; Russell and Johnson, 2007; Stager et al., 2005; Tierney et al., submitted; Verschuren et al., 2000). Chase et al., (2010) provides evidence for a dry late Holocene in southern Africa, but with generally drier conditions during the LIA compared to the MCA (900–1300 CE), potentially related to solar forcing.

Since AR4 an increasing number of proxies from multiple archives as well as documentary sources provide additional evidence for past drought in South America (Boninsegna et al., 2009; Prieto and García Herrera, 2009; Villalba et al., 2009). Using multiple proxies from southern South America, Boucher et al., (2011) inferred wetter conditions from 1000 CE to 1250 CE, followed by much drier conditions until 1400 CE and wetter conditions similar to present afterwards. For the South American Altiplano Morales et al., (2012) found drier conditions in the 14th, 16th, and 18th centuries, as well as a modern drying trend.

[INSERT FIGURE 5.13 HERE]

Figure 5.13: Severity, duration, and frequency of droughts in the Monsoon Asia (Cook et al., 2010b) and North American (Cook et al., 2004) Drought Atlases. The box in a) and d) indicates the region over which the tree ring reconstructed Palmer Drought Severity Index (PDSI) values have been averaged to form the regional mean time series shown in c) and f), respectively. Solid black lines in c) and f) are a 9 year Gaussian smooth on the annual data shown by the red and blue bars. The covariance of drought (PDSI < 0) duration and cumulative severity for each region is shown in panels b) and e) by the red circles (corresponding to the left x-axis), along with the respective marginal frequency histograms for each quantity. Not shown in b) is an outlier with an apparent duration of 24 years, corresponding to the 'Strange Parallels' drought identified in Cook et al., (2010b). Return intervals for droughts of given durations (shown as connected lines and their error bars and corresponding to the right x-axes in the same panels) are estimated as the mean interval between their occurrence, with the minimum and maximum reconstructed intervals indicated. No error bars are present if there is only a single observation of a drought of that duration. The period of analysis is restricted by the availability of tree-ring data to the period 1300 CE to 1989 CE for Monsoon Asia, following Cook et al., (2010), and from 800 CE to 1978 CE for North America, following Cook et al., (2004).

The SREX report (IPCC, 2012) concludes on the lack of a direct statistical link between anthropogenic climate change and trends in the magnitude/frequency of instrumentally recorded floods. Insight on past and current flood behaviour is provided from sedimentary, botanical and historical records (Baker, 2008; Brázdil et al., 2006; Brázdil et al., 2012). During the Late Holocene, flood records reveal strong decadal to secular variability and non-stationarity in flood frequency and preferential clustering of paleofloods which varied among regions (Benito et al., 2008; Ely et al., 1993; Glaser et al., 2010; Knox, 2000; Macklin et al., 2006; Piccarreta et al., 2011; Stewart et al., 2011b). Recent flooding frequencies are difficult to evaluate due to extensive river regulation (dams, dikes) and land-use changes. However current extreme rainfall conditions have been conducive to large floods despite of engineering works.

In mid-to-high latitude regions, the comparison of flood magnitudes along centennial records need to consider the role of snow melt and ice jams during cold periods. In southern Norway, high flood frequency at about 2300, 1200 and 200 years ago occurred in relation with the amount of solid winter precipitation and related spring/summer snowmelt (Støren et al., 2012). In parts of Europe, the contemporaneous flood magnitudes are not unusual within the context of the last 1000 years (e.g., Benito et al., 2011; Brázdil et al., 2012; Enzel et al., 1993; Greenbaum et al., 2000; Herget and Meurs, 2010; Mudelsee et al., 2003). The

highest peak flows in the modern instrumental record were exceeded by reconstructed flows during older historical periods for the rivers Rhine (Herget and Meurs, 2010; Wetter et al., 2011), Vltava (Brázdil et al., 2005), Tiber (Calenda et al., 2005), Llobregat (Thorndycraft and Benito, 2006), and Gardon (Sheffer et al., 2008).

Recent extreme floodings in the British Isles are not exceptional within the last centuries (Macdonald, 2007) (Figure 5.14i), and over millennia record floods tend to be clustered during wet periods such as 1100–1300 CE (Macklin et al., 2006). In Central Europe, long records of the Elbe and the Oder/Odra rivers showed a decrease in winter floods during the last 80 to 150 years, while summer floods indicate no significant trend (Mudelsee et al., 2003); Figure 5.14f-i). In the Alps, paleoflood records derived from lake sediments showed a higher flood frequency during cool and/or wet phases (Giguet-Covex et al., 2012; Stewart et al., 2011a; Wilhelm et al., 2012), a feature also found in Central Europe (Starkel et al., 2006). Documentary records from the Rhine in Basel (Switzerland) indicate that severe summer floods were particularly frequent between the mid-17th to the mid-18th century whereas extreme winter floods have not occurred since the late 19th century despite a significant increase in winter precipitation (Wetter et al., 2011).

In the Mediterranean region, increased flood frequency may have coincided either with relatively cool and/or wet climate conditions or during warm/dry periods; e.g., 4.8–4.4 ka, 960–790 CE (Benito et al., 2008; Luterbacher et al., 2012; Machado et al., 2011; Piccarreta et al., 2011; Thorndycraft and Benito, 2006) (Figure 5.14a-d). In the western Mediterranean region, the frequency of large floods (>50 year return period) has decreased since the late 19th century, whereas the extraordinary and ordinary floods increased over the 20th century (Figure 5.14a-c). There is high confidence that this decrease in frequency of large floods has also occurred in other rivers of central and north-western Europe (Figure 5.14f-i). Paleoflood records from Israel indicate an increase of large floods during wetter periods from 750CE to 1100 CE and after 1940 CE (Greenbaum et al., 2000; Greenbaum et al., 2006).

The severity of 20th century floods in eastern China was similar to earlier times. Since the mid-17th century, a trend towards larger floodings is reported (Zheng et al., 2006). For the Yellow River, Weihe and Qishuihe rivers, extraordinary paleoflood events occurred synchronously with severe droughts and dust falls coinciding with a monsoonal shift, the latest episode occurred at 3.1–3 ka (Huang et al., 2012; Zha et al., 2009). In contrast, in India, flood frequencies since 1950 CE are the largest for the last several hundred years for 8 rivers, interpreted as a strengthening of the monsoon conditions from the LIA (Kale, 2008).

In western North America, the increased frequency of high-magnitude palaeofloods coincide with periods of cool, wet climate, whereas warm intervals including the MCA, corresponded with significant decreases in the number of large floods (Ely et al., 1993). In this region, a positive relationship between the paleofloods and long-term variations in the frequency of El Niño events is evident at least over the last millennium (Ely, 1997). In the Great Plains of North America (at Black Hills of Southern Dakota) the frequency of large floods increases significantly around 850 CE with magnitudes roughly 2–3 times larger than those of the 1972 flood (Harden et al., 2011).

In the winter rainfall zone of southern Africa, the frequency of large floods decreased during warmer conditions (e.g., from 1425 CE to 1600 CE and after 1925 CE) and increased during wetter, colder conditions (Benito et al., 2011). Long-term paleoflood records of southern Africa indicate that the second half of the 20th century witnessed a reduction in the frequency of large floods coincident with a gradual warming and decreasing rainfall (Benito et al., 2011).

In conclusion, there is high confidence that the main driver for past flood frequency and magnitude variability is natural climate fluctuations. In general, paleoflood discharges larger than those recorded during the 20th century are documented, although in some regions (e.g., Near East, India, central North America) modern large floods are comparable or surpass in magnitude and/or frequency historical floods.

[INSERT FIGURE 5.14 HERE]

Figure 5.14: Flood frequency from palaeofloods, historical and instrumental records in selected European rivers. Depicted is the number of floods that exceeded a particular discharge threshold or flood level over periods of 20-years (bidecadal). Flood categories include large-catastrophic floods (CAT) associated with high flood discharge or severe damages, and extraordinary floods (EXT) causing inundation of the floodplain with moderate to minor damages. Legend at each panel indicates for each category the period of record in years, number of flood over the period, and the

average occurrence interval (in years). A: Tagus River combined paleoflood, historical and instrumental flood records from Aranjuez and Toledo with thresholds of 100–400 $m^3 s^{-1}$ (EXT) and >400 $m^3 s^{-1}$ (CAT) (data from (Benito et al., 2003; Benito et al., 2003b). B: Segura River Basin (SE Spain) documentary and instrumental records at Murcia (Barriendos and Rodrigo, 2006; Machado et al., 2011). C: Gardon River combined discharges from paleofloods at La Baume (Sheffer et al., 2008), documented floods (since the 15th century and historical and daily water stage readings at Anduze (1741–2005; (Neppel et al., 2010). Discharge thresholds referred to Anduze are 1000–3000 $m^3 s^{-1}$ (EXT), >3000 $m^3 s^{-1}$ (CAT). At least five floods larger than the 2002-flood (the largest in the gauged record) occurred in the period AD 1400–1800 (Sheffer et al., 2008). D: Tiber River floods in Rome from observed historical stages (since AD 1100; (Calenda et al., 2005; Camuffo and Enzi, 1996) and continuous stage readings (1870 to present) at the Ripetta landing (Calenda et al., 2005). Discharge thresholds set at 2300–2900 $m^3 s^{-1}$ (EXT) and >2900 $m^3 s^{-1}$ (CAT; >17 m stage at Ripetta). Recent flooding is difficult to evaluate in context due to river regulation structures. F: Vltava River combined documentary and instrumental flood record at Prague (Brázdil et al., 2005) discharge thresholds: CAT, flood index 2 and 3 or discharge >2900 $m^3 s^{-1}$; EXT flood index 1 or discharge 2000–2900 $m^3 s^{-1}$. G: Elbe River combined documentary and instrumental flood record (Mudelsee et al., 2003). Classes refer to Mudelsee et al., (2003) strong (EXT) and exceptionally strong (CAT) flooding. H: Oder River combined documentary and instrumental flood record (Mudelsee et al., 2003). I: River Ouse at York combined documentary and instrumental flood record (Macdonald and Black, 2010). Discharge thresholds for large floods was set at 500 $m^3 s^{-1}$ (CAT) and for ordinary floods at 350–500 $m^3 s^{-1}$ (EXT). The map shows the location of rivers used in the flood frequency plots.

5.6 Past Changes in Sea Level

This section discusses evidence for global mean sea level (GMSL) change from selected periods that are relevant for understanding the responsible processes during interglaciations or that are pertinent for testing climate and ice sheet models under different forcing conditions. The MPWP is selected for intervals of higher than present sea levels (Section 5.6.1), warmer temperatures (Section 5.3.1) and atmospheric CO_2 likely between pre-industrial and current levels (Section 5.2.2.2). Of the recent interglaciations with evidence for higher than present sea level, the last interglacial period, or LIG (MIS 5e) is most important because it has the best-preserved observational record against which sea level proxy indicators can be calibrated (Section 5.6.2) but we also discuss briefly the long MIS11 interglaciation (Section 5.6.2.5). For testing Glacio-Isostatic Adjustment (GIA) models, we discuss briefly the principal characteristics of Termination I including Melt Water Pulse-1A (Section 5.6.3). For the Holocene, the emphasis is on the last 6000 years when ice volumes stabilized near present-day values, providing the baseline for the discussion of anthropogenic contributions.

5.6.1 Mid-Pliocene

Estimates of peak sea levels during the MPWP based on a variety of geological records are consistent in suggesting higher-than-present sea levels, but they range widely (5–40 m) (Miller et al., 2012), and are each subject to large uncertainties. For example, coastal records (shorelines, continental margin sequences) are influenced by GIA (Raymo et al., 2011) and global mantle dynamic processes (Moucha et al., 2008; Müller et al., 2008). Both signals are large (5–30 m) and uncertain. To date their influence on Pliocene sea level estimates has not been robustly determined.

Benthic $\delta^{18}O$ records are better dated than many coastal records and provide a continuous time series, but the $\delta^{18}O$ signal reflects ice volume and temperature, with possible contribution from regional hydrographic variability. During the mid-Pliocene warm interval, the 0.1–0.25‰ anomaly recorded in the LR04 benthic $\delta^{18}O$ stack (Lisiecki and Raymo, 2005) would translate into ~12–31 m higher than present sea level, if it reflected only ice volume, or could be explained entirely by warmer deep-water temperatures (Dowsett et al., 2009) (See Appendix 5.A.3). Accounting for temperature and ice sheet components, existing studies conclude a higher-than-present sea level during mid-Pliocene warm periods with large uncertainties (±10 m) (Dwyer and Chandler, 2009; Miller et al., 2012; Naish and Wilson, 2009; Sosdian and Rosenthal, 2009).

Direct NH geological evidence based on the first appearance of ice-rafted debris across the entire North Atlantic indicates that continental ice sheets in North America and Eurasia did not develop until ~2.7 Ma (Kleiven et al., 2002), suggesting that earlier, mid-Pliocene high sea levels were only associated with loss from the Greenland ice sheet (GIS), the WAIS and EAIS. The sedimentary record indicates that the WAIS retreated periodically on orbital timescales during the warmest interglacial periods between 3.3 and 2.6 Ma (Naish et al., 2009a). Ross Sea SST are reconstructed to range from 2°C to 8°C (McKay et al., 2012), with values >5°C between 4.6–3.0 Ma being, according to one ice-sheet model, above the stability threshold for

ice shelves and marine portions of the WAIS and EAIS (Pollard and DeConto, 2009) (see also Section 5.8.1). A synthesis of the geological evidence from the coastal regions of the Transantarctic Mountains and Prydz Bay also supports coastal thinning and retreat of the EAIS between ~5–2.7 Ma (Barrett, in press). Ice-sheet models forced by Pliocene reconstructed climate variability are consistent in suggesting near-complete deglaciation of GIS (+7 m) and WAIS (+4 m) (Hill et al., 2010; Lunt et al., 2008; Pollard and DeConto, 2009), and one model identifies an orbitally driven response of the EAIS (+3 m) (Dolan et al., 2011), altogether corresponding to a sea level rise increase of 4 to 14 m.

In summary, there are multiple lines of evidence that global mean sea level during MPWP was higher than today, but low agreement on how high it reached. The most robust lines of evidence come from proximal sedimentary records that suggest periodic deglaciation of the WAIS (Naish et al., 2009a) and from ice-sheet models that suggest near-complete deglaciation of GIS, WAIS and some contribution from the EAIS. We have therefore medium confidence that sea level was 10 ± 10 m above present during the warmest periods of the Pliocene, with an uncertainty that brackets the range of most estimates from various methods. We have *low confidence* that sea level was more than 20 m above present.

5.6.2 Past Interglaciations

Records of past sea level can be found both in deep-sea cores foraminiferal $\delta^{18}O$ records and emergent shorelines. Particularly important issues with regard to the LIG are (i) its start and duration; (ii) the magnitude of its maximum rise; and (iii) possible variability within the interval. Deep-sea cores can constrain (ii) and possibly (iii). Emergent shorelines on tectonically active coasts can constrain (i) and (iii) and possibly (ii) if vertical tectonic rates are independently known; shorelines on tectonically stable coasts can constrain (i), (ii) and (iii). Here we emphasize the record from emergent shorelines that can be dated directly.

5.6.2.1 Start and Duration of the LIG

The timing of interglaciations (Appendix 5.A.3) is important for understanding lags between climate variations and the sea level response. Independent estimates of the start and duration of the LIG come from emergent coral-bearing reef terraces where ages from U-series consistent with an isotopically closed-system history have been generated. Appendix 5.A.3 provides an assessment of the underlying uncertainties. On tectonically stable islands of the western Atlantic Ocean, these LIG age ranges are: Bermuda, ~125–113 ka (Muhs et al., 2002a); Florida Keys, ~123–114 ka (Muhs et al., 2011); and Bahamas, ~129–115 ka (Thompson et al., 2011). From tectonically stable localities in the Pacific and Indian Oceans, the age ranges are: Australia, 127–116 ka (Stirling et al., 1998; Stirling et al., 1995); and Seychelles, ~129–123 ka (Israelson and Wohlfarth, 1999). On tectonically (or volcanically) rising coasts worldwide, the age ranges are: Barbados, 136–115 ka (Gallup et al., 2002; Speed and Cheng, 2004); Curaçao, ~126–118 ka (Muhs et al., 2012); Hawaii, 127–113 ka (Muhs et al., 2002a); New Guinea, ~136–116 ka (Stein et al., 1993); California and Baja California, ~123–114 ka (Muhs et al., 2002b).

5.6.2.2 Magnitude of LIG Sea Level Rise

Estimates of the magnitude of LIG sea level rise are preferably made from localities on tectonically stable coasts unless uplift rates can be independently determined or realistic error models can be placed on the uncertainties of these rates. Only two tectonically stable far-field areas have been studied, Australia and the Seychelles islands. At these sites, in contrast to sites near the former ice margins, the isostatic signals are less sensitive to the choice of parameters defining the Earth rheology and the ice sheets of both glaciations Lambeck et al., 2012). On the west coast of Australia, the highest LIG reef elevations are at +3.5 m and Dutton and Lambeck (2012) inferred a probable apparent paleo-sea level of +4.0 m relative to present. In the Seychelles, LIG coral reefs occur from 0 m to 6 m, but also possibly as high as ~9 m (Israelson and Wohlfarth, 1999 and references therein). Dutton and Lambeck (2012) examined outcrops on the Seychelles and estimated that water depths were only slightly higher than the maximum elevations of the corals themselves.

For the Caribbean and North Atlantic regions, the isostatic effects can be more important as well as more dependent on the choice of Earth- and ice-model parameters. Along the Yucatan coast of Mexico, LIG corals

with *Acropora palmata* occur as high as +6 m; this species lives only within the upper ~5 m of the water column. In the intermediate-field localities of the Bahamas and the Florida Keys, reefs occur as high as ~3 m (Bahamas) and ~5.3 m (Florida Keys); in both localities, water depths were likely at least ~3 m (Muhs et al., 2011; Thompson et al., 2011). If so, these observations imply LIG sea level at least as high as +6 m (Bahamas) and possibly as high as +8.3 m (Florida Keys). In the near field, the island of Bermuda has LIG coral-bearing marine conglomerates (Muhs et al., 2002a) that occur at elevations as low as ~1 m and as high as ~6 m (Harmon et al., 1983). All these estimates are of relative sea level, made without consideration of GIA effects.

Since AR4, two approaches have addressed GIA effects in order to infer LIG sea level from observations of coastal sites. Kopp et al., (2009) obtained a probabilistic estimate of GMSL based on a large and geographically broadly distributed database of LIG sea level indicators (Figure 5.15). Their analysis accounted for GIA effects as well as uncertainties in geochronology, the interpretation of sea level indicators, and regional tectonic uplift and subsidence. They concluded that GMSL was very likely +6.6 m (95% probability) and likely +8.0 m (67% probability), relative to present, and that it is unlikely to have exceeded +9.4 m (33% probability). The other approach, taken by Dutton and Lambeck (2012), used data from far-field sites that are tectonically stable. Their LIG estimate of +5.5 m to +9 m is consistent with the probabilistic estimates made by Kopp et al., (2009). We thus conclude that there is high confidence that during the LIG, GMSL was more than 6 m higher but less than 10 m above present-day level.

5.6.2.3 Evidence for LIG Sea Level Variability

There is medium confidence that local LIG sea levels experienced a metre-scale fluctuation sometime between 126 ka and 120 ka (Hearty et al., 2007; Kopp et al., 2009; Rohling et al., 2008a; Thompson and Goldstein, 2005; Thompson et al., 2011). Regional sea level variability and uncertainties in sea level proxies and their ages, however, cause considerable differences in the timing and amplitude of the reported fluctuation. Blanchon et al., (2009) inferred that there were two episodes of reef building on the Yucatan coast, one early in the LIG at a relative sea level of +3 m, followed by a later episode at +6 m. Chen et al., (1991) and Thompson et al., (2011) reported evidence for two episodes of reef building during the LIG in the Bahamas. Thompson et al., (2011) inferred a +4 m relative sea level at ~123 ka, followed by a fall to near present, and finally a rise to +6 m at ~119 ka. The higher estimate at the end of the interval may reflect GIA effects that result in a rise in relative sea level at these locations (Dutton and Lambeck, 2012). On the tectonically rising Huon Peninsula of New Guinea, there is an inference of two LIG reefs (VIIa and VIIb) with a lowering of sea level between the times of their formation, but there is currently no consensus about this interpretation (Stein et al., 1993). Schellmann and Radtke (2004) suggested that as many as three reef terraces formed during the LIG on Barbados but this is a tectonically uplifting island and the terraces may be the result of co-seismic displacement.

Based on a $\delta^{18}O$ record from the Red Sea, Rohling et al., (2008a) estimated LIG sea level peaks up to 10 m (±3 m at 1 standard deviation) above present, around a long-term mean of +6 m, with rates of rise estimated between 1.1 m per century and 2.6 m per century. However, the Red-Sea chronology was based on a short LIG duration of 124−119 ka, after Thompson and Goldstein (2005). The longer LIG duration of 130−116 ka indicated by the coral data (Section 5.6.2.1) reduces these rates of rise to 0.4−0.9 m per century, indicating low confidence in these estimates of interglacial sea level variability.

In their probabilistic assessment of LIG sea level, Kopp et al., (2009) concluded that, during the time interval over which GMSL was greater than –10 m, the 1000-year average rate of GMSL rise very likely exceeded 5.6 m kyr^{-1} (95% probability), likely exceeded 7.4 m kyr^{-1} (67% probability), and was unlikely to have exceeded 9.2 m kyr^{-1},. They noted that faster rates lasting less than a millennium could not be ruled out by their data. The most rapid change occurs during the early part of the LIG (Figure 5.15) when sea level may still be responding to the previous deglaciation. For the time interval in which GMSL was above present GMSL the maximum rate of GMSL rise very likely exceeded 2.0 m kyr^{-1} (95% probability), likely exceeded 4.1 m kyr^{-1} (67% probability), and was unlikely to have exceeded 5.8 m kyr^{-1} (33% probability), By having integrated a large number of observations within a probabilistic framework, these latter estimates from Kopp et al., (2009) provide the most robust evidence currently available for sea level oscillations during the LIG.

[INSERT FIGURE 5.15 HERE]

Figure 5.15: Sea level during the Last Interglaciation. (**a**) Proxy-derived estimate of global mean sea level anomaly (Kopp et al., (2009). Median (red line) and 16th and 84th percentiles (orange lines). Due to scale, only the 84th percentile is displayed prior to 130 ka. (**b**) Predicted sea levels for selected sites in the Caribbean and North Atlantic on the assumption that ice volumes during the interval from 129–116 ka are equal to those of today (Lambeck et al., 2012), displaying the spatial variability that can be expected across the region due to isostatic effects. The reference ice-volume model for the LIG interval (shaded), Earth rheology and ice sheet parameters are based on rebound analyses from different regions spanning the interval from Marine Isotope Stage 6 to the present (c.f. Lambeck et al., 2006).These predictions are strongly dependent on the ice load over North America, both, before and after the interglacial period, as well as on mantle rheology. Observations from these sites provide more information on ice histories than on global sea level function. (**c**) Same as (b) but for different sites along the Western Australia coast. The dependence on details of the ice sheet and on Earth-model parameters is less important at these sites than for those in (b). Thus data from these locations, assuming tectonic stability, is more appropriate for estimating LIG sea level. (**d**) Local LIG relative sea level reconstructions from Western Australia based on coral elevations (red) that pass diagenetic screening (Dutton and Lambeck, 2012). All results are for *in-situ* samples. Age error bars correspond to 2 standard deviation uncertainties. All elevations have been normalised to the upper growth limit of corals corresponding to mean low water spring or mean low sea level. The blue line indicates the simplest interpretation of local sea level consistent with reef stratigraphy and should be considered as lower limits by an amount indicated by the blue upper limit error bars. The differences from (a) in the timing of the start and end of the interglacial interval, as well as in the timing of the lowstand in the middle of the interval may be a consequence of different assumptions used in deriving the model ages. (**e**) The Western Australian reconstructed evidence (blue) from (d) compared with the model-predicted result (red) as in (c) for a reference site midway between the northern and southern most localities. The difference between the reconstructed and predicted functions provides an estimate of the global mean sea level (green). Uncertainties in this estimate include the observational uncertainties from (d) and the model uncertainties. Reference ice-volume model (shaded) as in (c). (**f**) Contribution of ice sheets to sea level change derived from transient ice sheet model simulations for the Greenland ice sheet (red, a: Quiquet et al., submitted; blue, b: Helsen et al., submitted; green, c: Abe-Ouchi et al., 2007 and Greve et al, 2011; pink, d:Robinson et al., 2011; light green, e: Stone et al., submitted, (a)–(e) correspond to the labels in Figure 5.16) and for the Antarctic ice sheet (black, f: Pollard and DeConto, 2009). (**g**) Central Greenland surface-air temperature anomalies for summer (June–August, JJA) used for ice sheet simulations displayed in panel (f) and in Figure 5.16. Anomalies in all panels are calculated relative to present.

5.6.2.4 Implications for Ice Sheet Loss during the LIG

The principal sources for the additional LIG meltwater are the GIS, WAIS and the low elevation, marine-based margins of the EAIS. Contributions from mountain glaciers are likely to have been small, an upper limit being ~0.6 ± 0.1 m if all present-day mountain glaciers melted (Radic and Hock, 2011). Likewise, ocean thermal expansion contributions are also likely to have been small, 0.4 ± 0.3 m (McKay et al., 2011). Sedimentological evidence indicates that southern Greenland was not ice-free during the LIG (Colville et al., 2011). Since AR4, the evidence for LIG ice layers in Greenland ice cores, which was ambiguous from Dye 3 and unequivocal from Summit and NGRIP ice cores (Masson-Delmotte et al., 2010a; North Greenland Ice Core Project members, 2004), has been strengthened. Data from the new NEEM ice core (Dahl Jensen et al., submitted) point to above present-day elevation at the beginning of the last interglacial period, followed by a decrease of 7 cm yr^{-1} and reaching 130 m below present day level at 122 ka. This new constraint can be combined with results from ice sheet models (Figure 5.16), showing different responses in southern and northeast Greenland. Ice sheet model simulations with contributions > ~2 m cannot be reconciled with the NEEM and other ice core data. It is unlikely that the GIS has contributed more than ~2 m to the LIG high stand (Dahl-Jensen et al., submitted) (medium confidence), implying a significant contribution from the WAIS and/or EAIS.

Geological and biological evidence for the WAIS margins during the LIG is equivocal due to inadequate age control, but it does imply that open water conditions existed in the Ross Sea and the Siple Coast at some time in the last 800,000 years (McKay et al., 2011; Scherer et al., 1998; Vaughan et al., 2011). A potential upper-limit estimate based on the volume of ice that sits below present day sea level, and is thus susceptible to marine ice sheet instabilities as melt-rates at marine grounding-lines increase, is ~7−8m sea level equivalent (Pollard & DeConto, 2009), with 3.3 m from the WAIS (Bamber et al., 2009), and potentially several metres from the EAIS (2.3 m from the Amery ice shelf sector, and up to 4.7 m from the Trans-Antarctic Mountains bottleneck, Pingree et al, 2011). Ackert et al., (2011) dated glacial erratics and ice-cored moraines across the Ohio Mountain Range and concluded that the elevation of the EAIS within this region was similar during the LIG and today. Sensitivity tests where the WAIS was removed were conducted with one atmospheric model, showing warming in East Antarctica consistent with ice core estimates (Holden et al., 2010b), and with GIA models (Bradley et al., 2012), showing no detectable elevation signal in East Antarctic ice cores. Due to the

lack of observations or simulations, no assessment of the contribution of the EAIS to LIG sea level can be performed.

[INSERT FIGURE 5.16 HERE]

Figure 5.16: Simulated Greenland ice-sheet elevation at the LIG in transient (a–e) and constant-forcing experiments (f). (a) GRISLI ice-sheet model with transient climate forcing derived from IPSL simulations and paleoclimate reconstructions (Quiquet et al., 2012). (b) ANICE ice-sheet model asynchronously two-way coupled with the regional climate model RACMO2 forced with ECHO-G simulated climate from 130–115ka (Helsen et al., submitted). (c) IcIES ice-sheet model with transient climate forcing from 135–115 ka from MIROC GCM (Abe-Ouchi et al., 2007; Greve et al., 2011). (d) "Best-guess" simulation from ensemble runs with the SICOPOLIS ice-sheet model driven by transient LIG climate simulations downscaled from CLIMBER2 with the regional model REMBO (Robinson et al., 2011). (e) "Best guess" simulation from ensemble simulations with the Glimmer ice-sheet model forced with transient climate forcing from 135–120 ka with HadCM3 (Stone et al., submitted). (f) SICOPOLIS ice model forced with a constant Eemian climate simulation of IPSL (at 126 ka), running for 6000 years starting from fully glaciated present-day GIS, as in Otto-Bliesner et al, (2006) in AR4 (Born and Nisancioglu, submitted). White squares in each panel show the locations of ice core sites at which ice from the LIG has been found (Dahl-Jensen et al., submitted; Dansgaard et al., 1985; North Greenland Ice Core Project members, 2004) : GRIP/GISP (G), NGRIP (NG), NEEM (NE), Camp Century (C), and possibly Dye3 (D). For ice sheet simulations using transient climate forcing, the minimum in ice volume is illustrated. The discrepancy of model outputs regarding timing and topography for minimum ice volume results from differences in climate forcings (cf. Figure 5.15g), ice-sheet models including their melt schemes (van de Berg et al., 2011), as well as differences in present-day climate (Quiquet et al., 2012). Compared to present-day, the average Greenland ice sheet volume of the 4 transient ice sheet models in panels a–e, which depict ice at the NEEM location, corresponds to 1.8 m sea level change. All panels use original model resolution and grids.

5.6.2.5 MIS 11

Published studies of the magnitude of emergent shorelines attributed to MIS 11 (~400 ka) have generated highly divergent estimates, from ~22 m above present (Hearty et al., 1999, for Bermuda and the Bahamas, but see; McMurtry et al., 2007, and; Mylroie, 2008 for different interpretations of the geological data) to levels near present (Bowen, 2010). However, none of these estimates have been corrected for GIA effects. Modelling by Raymo and Mitrovica (2012) indicates that the GIA correction can be at least +10 m for Bermuda and the Bahamas which both lie within the peripheral bulge of the Laurentian ice complex. After correcting for GIA Raymo and Mitrovica (2012) estimate that peak eustatic during MIS 11 was +6 m to +13 m. More recently, Muhs et al., (2012) derived estimates for Curaçao of +8.4 m to +10 m, a location for which the GIA effects are small (Dutton and Lambeck, 2012; Raymo and Mitrovica, 2012).

Proxy indicators point to global levels near present. The Waelbroeck et al., (2002) analysis of benthic $\delta^{18}O$ records from the North Atlantic and Equatorial Pacific points to a GMSL of ~5 ± 15 m. The Red Sea $\delta^{18}O$ (Rohling et al., 2009; Rohling et al., 2010) indicates MIS 11 paleo-sea level to be similar to that of the Holocene, within their uncertainties (~ 3−5 m).

From the limited evidence available, our assessment is that with medium confidence MIS 11 GMSL reached 5−15 m higher than present. The high-end range would require a loss of most of the GIS and WAIS plus a reduction in the EAIS of up to 5 m equivalent sea level.

5.6.3 Last Glacial Termination and Holocene.

The onset of melting of the LGM ice sheets occurred at approximately 20 ka and was followed by a GMSL rise of ~13 0 m in ~13 kyr (Lambeck et al., 2002a). Within this interval, at about 14.6 ka and coeval with the Bølling warming in the NH, a particularly rapid rise of ~ 20 m occurred (Meltwater Pulse 1A, MWP-1A) as most recently documented by Deschamps et al., (2012) from a new Tahiti coral record. At this location sea level rose between 14 and 18 m at a rate exceeding 40 mm yr^{-1}. The source of MWP-1A has been widely debated with most attention being on scenarios in which the Antarctic ice sheet contributed either significantly (Bassett et al., 2005; Clark et al., 2002; Clark et al., 2009) or very little (Bentley et al., 2010; Mackintosh et al., 2011). Because of the Earth-ocean (including gravitational, deformational and rotational) response to rapid changes in ice volume, the amplitude of the associated sea level change is spatially variable (Clark et al., 2002) and it can thus provide insight into the source region. Based on the comparison of the new Tahiti record with records from Barbados (Fairbanks, 1989) and the Sunda Shelf (Hanebuth et al., 2011), Deschamps et al., (2012) conclude that a significant melt-water contribution, of at least 7 m,

originated from Antarctica. One ice sheet modelling study shows that the separation of the North American Laurentide and Cordilleran ice sheets may be in part the cause of MWP-1A with a GMSL rise of 9 m in 500 years (Gregoire et al., 2012). Another modelling study (Carlson et al., 2012) finds 6−8 m in 500 years from the Laurentide at the onset of the Bølling warming over North America of which about half is in response to the warming itself. In contrast, there are no modelling results that show a retreat or partial collapse of the Antarctic ice sheet at this time.

Since AR4, higher resolution sea level records suggest further periods of rapid ice-mass loss. For example, a rapid rise of ~14 m from ~9.5−8.0 ka has been recorded in Singapore (Bird et al., 2007) or from ~9.0−7.5 ka possibly punctuated with one or two short periods of higher rates (Cronin et al., 2007 for Chesapeake Bay; Hijma and Cohen, 2010 for the Netherlands coast), followed by a short interval of a much reduced rise centred on about 8.2 ka (Bird et al., 2010, for Singapore) and by a final above-average rise of ~4 m at ~7.6 ka (Yu et al., 2007, for southern Sweden). (These have to be interpreted against a background of rapid sea level rise (average rate of ~15 mm per year) from ~11 ka (Bard et al., 1990; Edwards et al., 1993) until ~7 ka (Lambeck et al., 2002b). The short-duration increases in sea level have been attributed to either a multi-stage draining of glacial Lake Agassiz (Hijma and Cohen, 2010) , to a rapid melting of the Labrador and Baffin ice domes (Carlson et al., 2007; Gregoire et al., 2012), or Antarctic ice-sheet decay (Bird et al., 2007; Cronin et al., 2007).

From ~ 7 ka to 2 ka, the rate of change of GMSLwas reduced, increasing ocean volume by an equivalent 2–3 m (Lambeck et al., 2004; Lambeck et al., 2010b). About 10% of this late Holocene ocean-volume increase can be attributed to a Late Holocene ice reduction over Marie Byrd Land, Antarctica (Stone et al., 2003). Elevation histories derived from central Greenland ice core data (Lecavalier et al., submitted; Vinther et al., 2009) have presented evidence for thinning from 8 ka to 6 ka but no integrated observation-based estimates for the total ice sheet are yet available.

Spatial variability in sea level change during the late Holocene was significant because of the residual isostatic response to the last deglaciation for which comprehensive and predictive models exist (Milne and Mitrovica, 2008). After correction for GIA, local sea level records based on consistent sea level indicators (Figure 5.17), reveal with high confidence that amplitudes of any fluctuations in GMSL during this interval did not exceed approximately ±25 cm on time scales of a few hundred years.

Resolving decimetre-scale sea level fluctuations is critical for understanding the causes of sea level during the last millennium. Three types of proxies have this capability: salt-marsh plants and microfauna that form distinctive elevation zones reflecting variations in tolerances to the frequency and duration of tidal inundation (Donnelly et al., 2004; Gehrels et al., 2008; Horton and Edwards, 2006; Kemp et al., 2009; Long et al., 2012); coral microatolls found in intertidal environments close to lowest spring tides (Goodwin and Harvey, 2008; Smithers and Woodroffe, 2001; Woodroffe and McLean, 1990); and coastal archaeological features constructed with direct (e.g., fish ponds and certain harbour structures) or indirect (e.g., water table level changes in ancient wells) relationships to sea level (Anzidei et al., 2011; Auriemma and Solinas, 2009; Lambeck et al., 2004; Sivan et al., 2004).

Of these, the salt marsh records are particularly important because they have been validated against regional tide-gauge records. This justifies their application to time periods prior to tide-gauge observations. Regionally, as along the US Atlantic coast and Gulf of Mexico coast, these records reveal some consistencies in sea level oscillations over multi-decadal and centennial timescales (González and Törnqvist, 2009; Kemp et al., 2011; van de Plassche et al., 1998) (Figure 5.17), but they have not yet been identified as truly global phenomena. The most robust signal captured in the salt-marsh proxy sea level records from both northern and southern hemispheres is an acceleration, either late in the nineteenth century or in early twentieth century (Figure 5.17), that marks the transition from relatively low rates of change during the late Holocene (order tenths of mm yr^{-1}) to modern rates (order mm yr^{-1}) (see also FAQ 5.2). Variability in both the magnitude and the timing (1840−1920 CE) of this acceleration has been reported (Gehrels et al., 2008; Gehrels et al., 2011; Gehrels et al., 2006; Kemp et al., 2011; Kemp et al., 2009). Gehrels and Woodworth (submitted) have re-evaluated the evidence and conclude that the previously reported mismatches can be reconciled and that the proxy and instrumental datasets all record sea level rise above the late Holocene background rate starting at ~1925 CE ± 20 years (1 standard deviation) (Figure 5.17).

[INSERT FIGURE 5.17 HERE]

Figure 5.17: Observational evidence for sea level change in recent and late Holocene time. Left panels (a-d): High resolution relative sea level results from saltmarsh data at representative sites, without corrections for glacial isostatic movement of land and sea surfaces. Locations are given on the map. The North Carolina (a) result is representative of other North American Atlantic coast locations (Kemp et al., 2011). The rate of change occurring late in the 19th century are seen in all high resolution saltmarsh records – e.g., (c) Gehrels et al., (2008) (see also Gehrels and Woodworth, submitted); (d) Garcia-Artola et al., (2009); Leorri et al., (2008) –that extend into modern time and is consistent with Roman archaeological evidence (Lambeck et al., 2004). The oscillation in sea level at about 1000 CE seen in the North Carolina record occurs in some (González and Törnqvist, 2009; van de Plassche et al., 1998) but not all records (c.f., Gehrels et al., 2011; Kemp et al., 2011). Right hand side panels (e-h) Observational evidence for sea level change from lower resolution but longer period records. All records, except for Blekinge (h) where the isostatic signal dominates the observed sea level change (Yu et al., 2007), are uncorrected for isostatic effects. The Kiritimati record (Christmas Island) consists of coral microatoll elevations whose fossil elevations are with respect to the growth position of living microatolls (Woodroffe et al., 2012). The Orpheus Island record (f) is also based on microatoll evidence (Chappell, 1983; Lambeck et al., 2002b). The data from Mediterranean France (g) is based on biological indicators (Laborel et al., 1994) restricted to three nearby locations between which differential isostatic effects are less than the observational errors (Lambeck and Bard, 2000). The Blekinge result (h), corrected for isostatic rebound, is based on the analysis of transgression and regression sequences in marginal basins (Yu et al., 2007). The two global records are estimates of change in global mean sea level from (i) the instrumental record (Jevrejeva et al., 2008), and (j) from a range of geological and archaeological indicators (Lambeck et al., 2010b), with the contributing records corrected for the isostatic effects at each location.

5.7 Evidence and Processes of Abrupt Climate Change

Paleoclimate archives document climate changes that happened at a rate faster than background climate change. A variety of mechanisms have been suggested to explain the emergence of such abrupt climate changes. Most of them invoke the existence of nonlinearities or, more specifically, thresholds in the underlying dynamics of one or more Earth-system components. Both internal dynamics as well as external forcings can generate abrupt changes in the climate state. Documentation of abrupt climate changes in the past using multiple sources of proxy evidence can provide important benchmarks to test climate models; their instability mechanisms and sensitivities even to future forcings, as well as their capacity to simulate teleconnection patterns and interhemispheric linkages which are relevant for projections of future climate changes. This assessment of abrupt climate change on timescales of 10–100 years focuses on Dansgaard-Oeschger (DO) events and iceberg and meltwater discharges during Heinrich stadials, especially the advances since AR4 in reconstructing and understanding their global impacts and in extending the record of millennial-scale variability back in time to ~800 ka.

Twenty-five abrupt DO events (North Greenland Ice Core Project members, 2004) and several centennial scale events (Capron et al., 2010b) occurred during the last glacial period. DO events were marked by an abrupt transition (on a timescale of a few decades) from a cold phase (stadial) into a warm phase (interstadial). Subsequently, a more gradual cooling preceded a rapid jump to cold stadial conditions that lasted for centuries up to millennia (Figure 5.18). Thermal gas-fractionation methods (Huber et al., 2006; Landais et al., 2004) suggest that for instance for DO24 abrupt warming in Greenland reached levels of up to 16°C ± 2.5°C (Capron et al., 2010b) within several decades and was accompanied by abrupt shifts in dust and deuterium excess, representing major reorganizations in atmospheric circulation (Steffensen et al., 2008; Thomas et al., 2009). Corresponding variations in high-resolution SST reconstructions from the eastern subtropical North Atlantic attain values up to 5°C (e.g., Martrat et al., 2007). More accurate synchronization between Greenland and high-resolution Antarctic records (Capron et al., 2012; Capron et al., 2010a; Capron et al., 2010b; EPICA Community Members, 2006; Stenni et al., 2011) has further revealed that all but DO25 Northern Hemispheric DO transitions terminated gradual warming trends in Antarctica that accompanied stadial phases in the Northern Hemisphere. Processes such as sea ice cover (Li et al., 2010b), atmospheric circulation changes and ice-sheet topography (Wunsch, 2006) may have contributed to the magnitude and abruptness of DO related regional climate impacts. It still remains controversial whether DO variability represents a series of stochastically generated events (Ditlevsen and Ditlevsen, 2009), whether it was related to solar forcing (Braun and Kurths, 2010; Woillez et al., 2012) or internal dynamics.

As witnessed by the presence of massive layers of ice-rafted detritus in North Atlantic marine sediments and other sedimentary indicators, some DO stadials, known as Heinrich stadials were associated with iceberg discharges originating from the Northern Hemispheric ice-sheets. During these periods global sea level rose

by up to several tens of meters (Chappell, 2002; Gonzalez and Dupont, 2009; Rohling et al., 2008b; Siddall et al., 2008; Yokoyama and Esat, 2011), with remaining uncertainties on the timing of the sea level rise, stadial cooling and ocean circulation changes relative to the iceberg discharge (Arz et al., 2007; Gonzalez and Dupont, 2009; Hall et al., 2006; Hodell et al., 2010). Based on ice-sheet climate modelling experiments internal instabilities of the Laurentide ice-sheet can cause massive calving and meltwater events similar to those reconstructed from proxy records (Calov et al., 2002; Calov et al., 2010; Marshall and Koutnik, 2006). An alternative hypothesis for the emergence of these instabilities (Alvarez-Solas et al., 2010; Marcott et al., 2011) calls for an external forcing of the ice-sheet. Here, an initial weakening of the AMOC leads to subsurface warming in parts of the North Atlantic (Shaffer et al., 2004) and subsequent basal melting of the Labrador ice-shelves and a resulting acceleration of ice streams and iceberg discharge. At present, unresolved dynamics in ice-sheet models and limited proxy information do not allow to distinguish the two mechanisms with confidence.

Since AR4 a better understanding of the global imprints of DO events and Heinrich stadials has been presented for various regions. Abrupt events, such as the Bølling and Allerød sub-hemispheric warmings and the Younger Dryas sub-hemispheric cooling left a detectable and widespread imprint on North Pacific SSTs (Harada et al., 2008; Harada et al., 2012; Pak et al., 2012). Atmospheric changes in response to North Atlantic cooling (Okumura et al., 2009; Xie et al., 2008), as well as large-scale Pacific ocean circulation changes in response to a weakening of the AMOC (Harada et al., 2009; Okazaki et al., 2010; Saenko et al., 2004; Schmittner et al., 2007), have been suggested to explain the presence of millennial-scale variability in the Pacific. Southward displacement of Southern Ocean fronts during cold DO stadials and concommittant southward influence of tropical waters towards the Southern Ocean have been reported (De Deckker et al., 2012; Denton et al., 2010), further documenting the interhemispheric character of these events. North Atlantic stadial cooling (Krebs and Timmermann, 2007; Otto-Bliesner and Brady, 2010) (Figure 5.4b) and sea ice variations (Chiang and Bitz, 2005), associated with DO events and Heinrich stadials, such as Heinrich stadial 1 (18.5–14.8 ka), caused changes in the large-scale atmospheric circulation which in turn affected interhemispheric tropical rainfall patterns. Related hydroclimate changes included a southward shift of the North Atlantic ITCZ (Peterson and Haug, 2006) leading to massive drying of equatorial western African and Southern Arabia (Higginson et al., 2004; Itambi et al., 2009; Ivanochko et al., 2005; Mulitza et al., 2008; Tjallingii et al., 2008; Weldeab, 2012; Weldeab et al., 2007) and the eastern Mediterranean (Fleitmann et al., 2009) and increased hydrological signals in South America (Kanner et al., 2012) (Figure 5.4h). The hydrological response in southern Africa during HS1 is debated. Furthermore, reconstructions document an increased moisture supply to Southwestern North America (Asmerom et al., 2010; Wagner et al., 2010), a reduction of hydroclimate indicators in the Asian Summer and Winter monsoon regions (Cai et al., 2010; Wang et al., 2008) (see Figure 5.4e) as well as for the Australian-Indonesian monsoon (Mohtadi et al., 2011).

Since AR4, climate model simulations (Kageyama et al., 2010; Liu et al., 2009b; Menviel et al., 2011; Otto-Bliesner and Brady, 2010) have further confirmed the notion (high confidence) that changes of the AMOC induce abrupt climate changes with magnitude and pattern resembling reconstructed paleo-proxy data of DO and Heinrich events. However, GCMs still have difficulties simulating the rate of reconstructed warming during the AMOC recovery phase in some regions such as Greenland (Liu et al., 2009b).

Newly available marine records (Grützner and Higgins, 2010; Kleiven et al., 2011; Margari et al., 2010; Martrat et al., 2007), Antarctic trace gas records (Loulergue et al., 2008; Schilt et al., 2010) and statistical analyses of Antarctic data combined with bipolar seesaw modelling (Barker et al., 2011) have increased the confidence to a high level that abrupt climate change events, similar to the DO events and Heinrich stadials of the last glacial cycle, occurred during previous glacial cycles extending back ~800 ka (Figure 5.18) and, with less confidence, to 1100 ka.

[INSERT FIGURE 5.18 HERE]

Figure 5.18: Dependence of millennial-scale bipolar seesaw activity (a measure of DO variability) on climate background state: Benthic $\delta^{18}O$ stack (blue) (Lisiecki and Raymo, 2005) representing a combination of global ice-volume, deep ocean temperature and hydrography, terciles of millennial-scale bipolar seesaw activity index (gray shading, showing periods with low frequency of events in black and high frequency in white) (Barker et al., 2011), and $\delta^{18}O$ analogue for Greenland (red) empirically derived from Antarctic ice core data using bipolar seesaw methods and assumptions on orbital lags (Barker et al., 2011).

5.8 Paleoclimate Perspective on Irreversibility in the Climate System

The notion of irreversibility implies that after a perturbation the climate system will not return to its initial state even when the perturbation is removed. This requires the existence of multiple equilibrium states in the system. In practice, considering the timescales of perturbations and climate components, irreversibility of climate change can be defined such that the recovery timescale to reach the initial state (through natural processes) is significantly longer than the duration of causal perturbation.

5.8.1 Cryosphere

Modeling studies suggest the existence of multiple equilibrium states for different ice sheets with respect to temperature, CO_2 concentration and orbital forcing phase spaces (Calov and Ganopolski, 2005; DeConto and Pollard, 2003; Ridley et al., 2010). This implies a possibility of irreversible changes in the climate-cryosphere system in the past and future. An abrupt increase in global ice volume (mostly in the Antarctic ice sheet) at the Eocene/Oligocene boundary, 33 Ma, likely caused by gradual atmospheric CO_2 concentration decline on geological time scale (Pagani et al., 2005; Pearson et al., 2009), is consistent with the existence of threshold behaviour in the East Antarctic Ice sheet simulated by the ice sheet models under CO_2 concentrations of 500–1000 ppm (DeConto and Pollard, 2003; Langebroek et al., 2009). Proxy records suggest that WAIS collapse might have happened during some previous interglaciations (Naish et al., 2009b; Vaughan et al., 2011) when climate conditions were not very different from present ones and it is likely that WAIS was absent during warm periods of the Pliocene when CO_2 concentration was not higher than 420 ppm (see Section 5.2.2.2). At the same time results of model simulation (Pollard and DeConto, 2009) suggests that WAIS is very sensitive to the subsurface ocean temperature. This imply with a medium degree of confidence that a large part of the WAIS will be eventually lost if the atmospheric CO_2 concentration will stay above 420 ppm for several millennia.

Observational evidence suggest that the Greenland ice sheet was much smaller than today during the middle Pliocene when atmospheric CO_2 concentration and global temperature were only moderately higher than present (see Sections 5.6.1 and 5.2.2.2) (Alley et al., 2010) which is supported by the results of simulations with ice sheet models (Dolan et al., 2011; Koenig et al., 2011). The Greenland ice sheet was also likely considerably reduced during interglaciations exceptionally long (Marine Isotope Stage 11) and exceptionally warm in the Arctic (Marine Isotope Stage 5.5) (Section 5.6.2). This supports modelling results which indicate that temperature or CO_2 thresholds for melting and re-growth of the Greenland ice sheet may lie in close proximity to the present climate state (Gregory and Huybrechts, 2006; Lunt et al., 2008) (Section 5.6.1) and that the Greenland ice sheet may have multiple equilibrium states under present day climate state (Born and Nisancioglu, submitted; Ridley et al., 2010). Therefore, paleodata and results of model simulations indicate with a medium degree of confidence that the Greenland and the West Antarctic Ice sheets could be destabilized by temperature rise which is expected already in this century although the time scales of the ice sheets response to climate change are very long (multi-centuries to millennia).

5.8.2 Ocean Circulation

Numerous modelling studies demonstrate that increased freshwater flux into the North Atlantic leads to weakening of the AMOC (Stouffer et al., 2006). Results of intermediate complexity models (Rahmstorf et al., 2005) and several coupled GCMs also suggest that under present or glacial climate conditions AMOC may have multiple equilibrium states (Hawkins et al., 2011; Hu et al., 2012). Experiments with coupled climate models provide evidence that the sensitivity of the AMOC to freshwater perturbation is larger for glacial boundary conditions than for interglacial conditions (Swingedouw et al., 2009) and that the recovery timescale of the AMOC is longer for LGM conditions than for the Holocene (Bitz et al., 2007).

The abrupt climate-change event at 8.2 ka is an example with which to study the recovery time of the AMOC to freshwater perturbation under near-modern boundary conditions (Rohling and Pälike, 2005). Since AR4, substantial new observational and model evidence are published. The pattern of reconstructed and modelled surface ocean and atmospheric climate anomalies is consistent with a reduction in the strength of the AMOC (Figure 5.19a,b,d). Although only indirect evidence for changes in AMOC strength can be inferred from proxy records, available proxy records from the North Atlantic support the hypothesis that freshwater input into the North Atlantic reduced the amount of deep and central water-mass formation as reduced Nordic Seas

overflows, reduced intermediate water temperatures and reduced ventilation state of North Atlantic Deep Water (Figure 5.19c,d) (Bamberg et al., 2010; Ellison et al., 2006; Kleiven et al., 2008; McManus et al., 2004). A concomitant cooling of SST and atmospheric temperatures in the North Atlantic and in Greenland has been observed (Figure 5.19a,b) with the climate anomaly associated with the event lasting 100–160 years (Daley et al., 2011). The additional freshwater that entered the North Atlantic during the 8.2-ka event is estimated to range between $1.6 \cdot 10^{14}$ m^3 and $8 \cdot 10^{14}$ m^3 (Barber et al., 1999; Clarke et al., 2004; von Grafenstein et al., 1998). The duration of the meltwater pulse may have been as short as 0.5 years (Clarke et al., 2004), but new estimates based on meltwater drainage following a collapse of saddle between remaining Laurentide ice domes indicate an up to 200 year-duration in two separate stages (Gregoire et al., 2012). A four model ensemble with a one-year 2.5 Sv freshwater perturbation only give temperature anomalies half of the reconstructed and shorter duration than observed, resulting either from imprecise representation of Holocene climate state or a too short duration of the freshwater forcing (Morrill et al., submitted-a). Based on the paleoceanographic reconstructions, the freshwater perturbation of this size was insufficient to trigger a complete collapse of the AMOC (Figure 5.19d). The reconstructions consistently show that the shallow and deep overturning circulation of the North Atlantic recovered completely after the cessation of the meltwater perturbation. The recovery timescale was on the order of 200 years (Bamberg et al., 2010; Ellison et al., 2006) (Figure 5.19c, d). One record points to a partial recovery on a decadal timescale (Kleiven et al., 2008). It is possible that this record is affected by a threshold effect due to the vertical displacement of deep water masses. Both recovery timescale and sensitivity of the AMOC to the freshwater perturbation are consistent with model experiments for the 8.2-ka event using coarse-resolution models, GCMs and eddy permitting models (LeGrande and Schmidt, 2008; Li et al., 2009; Spence et al., 2008). The recovery of temperatures out of the cold anomaly appears overprinted with natural variability in the proxy data, and is more gradual in data than in the GCM experiments (Figure 5.19e, f).

Associated with the North Atlantic climate and AMOC induced anomalies is a characteristic teleconnection pattern with widespread Northern Hemisphere cooling and drying and a southward displacement of the ITCZ (See Figure 5.19e, f), and a wetting of SH tropics (Morrill et al., submitted-b). These patterns are highly consistent between paleoclimate observations and the ensemble response to a freshwater perturbation in the North Atlantic of 0.1 Sv. Model experiments indicate that a hemispheric see-saw pattern existed during the event, and there is some support from observations that this likely was the case.

[INSERT FIGURE 5.19 HERE]

Figure 5.19: Compilation of selected paleoenvironmental and climate model data for the abrupt Holocene cold event at ca. 8.2 ka, documenting temperature and ocean circulation changes around the event and the spatial extent of climate anomalies following the event. Published age constraints for the period of release of freshwater from glacier Lakes Agassiz and Ojibway are bracketed inside the vertical blue bar. Vertical grey bar denotes the time of the main cold event as found in Greenland Ice core records (Thomas et al., 2007). **a)** Black curve: NGrip $\delta^{18}O$ (temperature proxy) from Greenland Summit (North Greenland Ice Core project members (2004). Red curve: Simulated Greenland temperature in an 8.2-ka event simulation with the ECBilt-CLIO-VECODE model (Wiersma et al., 2011). Blue curve: Simulated Greenland temperature in an 8.2-ka event simulation with the CCSM3 model (Morrill et al., 2011). **b)** North Atlantic/Nordic Seas SST-reconstructions, age models are aligned on the peak of the cold-event (less than 100-year adjustment). Blue curve: Nordic Seas (Risebrobakken et al., 2011). Black curve: Gardar Drift south of Iceland (Ellison et al., 2006). **c)** Deep- and intermediate water records. Black curve: Sortable silt record (overflow strength proxy) from Gardar Drift south of Iceland (Ellison et al., 2006), Atlantic intermediate water temperature reconstruction (Bamberg et al., 2010). **d)** Black curve: $\delta^{13}C$ (deep water ventilation proxy) at 3.4 km water depth south of Greenland (Kleiven et al., 2008). Age model is aligned on the minimum overflow strength in c) (less than 100-year adjustment). Modelled change in the strength of the AMOC: Green curve: An 8.2-ka event simulation with the GISS model (LeGrande et al., 2006). Red curve: An 8.2-ka event simulation with the ECBilt-CLIO-VECODE (v. 3) model (Wiersma et al., 2011). Blue curve: An 8.2-ka event simulation with the CCSM3 model (Morrill et al., 2011). **e)** Spatial distribution of the ensemble mean annual mean surface temperature anomaly (°C) from a multi-model water hosing experiment with 0.1 Sv freshwater forcing in the NW Atlantic (Stouffer et al., 2006). Paleoclimate data from records resolving the 8.2-ka event are plotted with symbols: C=cold anomaly, W=warm anomaly, X=No significant anomaly. Main data sources: (Wiersma et al., 2011); (Morrill et al., 2011) **f)** Spatial distribution of the ensemble mean annual mean precipitation anomaly (mm day^{-1}) from a multi-model water hosing experiment with 0.1 Sv freshwater forcing in the NW Atlantic (Stouffer et al., 2006). Paleoclimate data from records resolving the 8.2-ka event are plotted with symbols: D=dry anomaly, W=wet anomaly, X=No significant anomaly. Main data sources: (Wiersma et al., 2011); (Morrill et al., 2011).

[START FAQ 5.1 HERE]

FAQ 5.1: Is the Sun a Major Driver of Climate Changes?

The Sun is the ultimate source of the energy that powers the climate system. The strength of that energy output varies over a wide range of timescales, from billions of years to just a few days. Over the past 120 years, solar variability is one of three recognised natural sources of climate variability that, together with anthropogenic factors, combine to explain much of the observed changes in global surface temperatures (Chapter 10). However, that variability has made only a minor contribution to the observed increase in global surface temperatures over the past 120 years.

The Sun's core is a massive nuclear fusion reactor that converts hydrogen into helium. This produces energy which radiates throughout the solar system as electromagnetic radiation. The amount of energy striking the top of Earth's atmosphere varies over time scales ranging from days to billions of years, depending on the generation and emission of electromagnetic energy by the Sun, and on the Earth's orbital path around the Sun.

Satellite-based radiometers have directly measured total solar irradiance (TSI) since 1978, and indicate that ~1360 W m^{-2} reaches the top of the Earth's atmosphere when the Earth is located at 149,598,000 kilometres (one Astronomical Unit) from the Sun. The total power received by the Earth amounts to 1.7×10^{17} W. Earth's surface and atmosphere reflect about 30% of this energy back into space.

Satellite-based radiometers record higher levels of TSI overall when the Sun is more active. Higher solar activity produces more dark sunspots, which decrease solar irradiance, but also more bright regions, called faculae, which increase solar irradiance. TSI variations have a prominent 11-year activity cycle, during which TSI values (in recent years) increased on average by about 0.1% (1.4 W m^{-2}), when the number of sunspots increased from a minimum to a maximum.

Many studies have shown that the global surface temperature record over the past 30 years can best be explained by a combination of natural and anthropogenic factors (FAQ 5.1, Figure 1). Natural factors include solar variability, volcanic eruptions and internal variability, each of which produces characteristic patterns of regional climate responses.

When solar activity surges during the 11-year cycle, the resultant increase in TSI produces global warming in the order of 0.1°C. When large volcanic eruptions, such as that of Mt Pinatubo in 1991, inject aerosols into the atmosphere, they can cool the Earth's surface by around 0.3°C to 0.4°C for a few years. Natural climate variability associated with the El Niño Southern Oscillation warm global surface temperatures during El Niño events, and cool global surface temperatures during La Niñas. Global temperatures rose by around 0.2ºC during the large El Niño of 1997–1998.

During the last 30 years, anthropogenic factors, including rising concentrations of greenhouse gases, and other changes in atmospheric composition and land use, have produced warmed global surface temperatures by about 0.4°C. Hence, the Sun's role in climate change is modest: it is not a major driver of systematic climate warming over the past 30 years, especially in terms of global mean surface temperatures.

TSI variations have nevertheless featured in the past 120 years of observed climate change (FAQ 5.1, Figure 1). Here again, a combination of natural and anthropogenic factors are involved, but these forcing factors vary over time. TSI variations prior to 1978 have been reconstructed using observed sunspot numbers (back to 1610 CE), or indirectly from estimates of solar activity based on radioisotopes archived in polar ice and tree rings. Distinct 50- to 100-year long periods of very low activity are commonly referred to as grand solar minima (e.g., Maunder minimum; 1645–1715 CE), during which times TSI levels are thought to be reduced. Most estimates of the average TSI change between the Maunder minimum and the Modern maxima (1950 CE to the present) range from 0.1 to 0.2%—roughly between one and two times the amplitude of the TSI change during the 11-year solar activity cycle.

Internal variability is a noisy signal, which can produce warmings and coolings without long-term trend. Volcanic forcing, which produces cooling, is initially abrupt, and its effects dissipate within a few years. The model-based solar irradiance record suggests an increasing warming trend during the first half of the 20th century, underlying alternating warming and cooling with a strong 11-year cyclicity.

But only a significant anthropogenic forcing can account for the magnitude of the observed global surface temperature warming—by around 0.8°C—over the past 120 years, especially the prominent increase over the last 30 years. However, solar forcing provides a diminishing contribution, relative to anthropogenic forcing, to the observed increase in global surface temperatures over the past 120 years.

[INSERT FAQ 5.1, FIGURE 1 HERE]

FAQ 5.1, Figure 1: Global surface temperature variations from 1899 to 2006 and natural (internal, volcanic, and solar) and anthropogenic factors that influence surface temperatures (modified from Lean, 2010). a) Observed (black line) and model (red line) composed from the monthly mean global surface temperature time series in panels b to e. b) The El Niño Southern Ocean index, used as an indicator of short-term internal variability that cannot be directly attributed to an external forcing. c) Short-lived, but strong, cooling effects of volcanic eruptions, d) Solar forcing which consists of the 11-year sunspot cycle, superimposed on a steadily increasing trend during the first half of the 20th century. e) Anthropogenic forcing, consisting of a warming component due to greenhouse gases, and a cooling component due to aerosols.

In other words, climate change is caused by a combination of different factors (internal, solar, volcanic, greenhouse gases) and the contribution of the different factors is changing with time. This important conclusion is demonstrated in the FAQ 5.1, Figure 1. It shows the mean global monthly temperature from 1899 to 2006 (black curve panel a) together with the four factors (internal variability, solar, volcanic, and anthropogenic forcing) depicted in panel b to e which are needed to explain it (Lean et al., 2011). For each factor the estimated contribution to the mean global temperature is given in degrees centigrade. Adding up all the contributions leads to the red curve shown in panel a. Panel b shows the El Niño Southern Ocean index which is used as an indicator of the short-term internal variability which cannot be directly attributed to an external forcing. The short-lived but strong cooling effects of volcanic eruptions are depicted in panel c. Panel d shows the solar forcing which consists of the 11-year sunspot cycle superimposed on steadily increasing trend during the first half of the 20th century. Finally, panel e comprises the anthropogenic effect consisting of a warming component due to the greenhouse gases and a cooling component due to aerosols.

The figure is divided into two time intervals. During the first period from 1890 CE to 1965 CE the temperature increased by about 0.25°C. This increase which was reduced by volcanic activity between 1880 CE and 1910 CE is attributed mainly to solar (0.1°C) and anthropogenic (0.15°C) forcing. After 1965 solar forcing does not show an increasing trend, but anthropogenic forcing increases rapidly and contributes 0.55°C to the global warming which is interrupted by cooling episodes due to the eruptions of El Chichon (1982) and Pinatubo (1991). The figure indicates that natural forcing factors played an important role for climate change up to about 1965, but that anthropogenic forcing became the dominant factor since that time.

This raises the question of the future role of solar forcing in climate change. Reconstruction of the solar activity throughout the past 10,000 years tells us that solar forcing fluctuates between grand maxima and minima. Compared to the past 10,000 years, the Sun has been very active during the past 60 years. According to most predictions, solar forcing will decrease for the next few decades and then increase again to present-day levels. With a high degree of confidence, the data from the past 10,000 years tells us that the forcing range between Grand solar maxima and Grand solar minima is much smaller than the anthropogenic effect.

In summary, solar forcing together with volcanic forcing and internal variability played a dominant role in the past 10,000 years when the greenhouse gases were almost constant. During the past decades the anthropogenic effect became the dominant forcing factor. During the future decades solar forcing will only play a minor role.

[END FAQ 5.1 HERE]

[START FAQ 5.2 HERE]

FAQ 5.2: How Unusual is the Current Sea Level Rate of Change?

The current rate of mean global sea level change, estimated at 1.7 ± 0.3 mm yr^{-1} for the entire 20th century and 3.2 ± 0.5 mm yr^{-1} since 1993 CE (the satellite altimetry era), (Chapter 13), is unusual in the context of

the last two millennia. However, this rate is not unusually rapid relative to past periods of rapid ice sheet deglaciation, such as transitions between glacial and interglacial periods. Exceptional tectonic effects can also drive very rapid local sea level changes, with rates exceeding the current rates of change.

Sea level is commonly thought of as where the ocean meets the land. Earth scientists define sea level as a measure of the position of the sea surface relative to the land, both of which may be moving relative to the center of the Earth, reflecting a combination of climate and geophysical factors. Climate factors affecting sea level include changes in ocean temperature and thermal expansion/contraction, and changes in terrestrial glacier ice mass and current velocities. Geophysical factors affecting sea level include land subsidence or uplift, glacial isostatic adjustments, and changes in Earth's rotation. Glacial isostatic adjustments (GIA) refer to the response of relative sea level to changes in the distribution of mass on the Earth, specifically water and ice. Local and regional changes in these climate and geophysical factors result in significant deviations from the global estimate of the mean rate of sea level change. For example, sea level is falling at rates approaching 10 mm yr^{-1} along the Swedish coast of the Gulf of Bothnia, due to ongoing uplift caused by the loss of continental ice since the last glacial period. In contrast, sea level rose at rate of about 12 mm yr^{-1} from 1940 to 2005 in Bangkok, mainly in response to ground subsidence.

The average rate of global sea level rise over the 20th century (about 1.7 ± 0.3 mm yr^{-1}) may seem small relative to observations of wave and tidal oscillations around the globe, which can be orders of magnitude larger. However, when this rate is integrated over time, the magnitude of this rise becomes quite significant, especially in the heavily populated, low-lying coastal regions of the Earth.

Prior to about 1700 CE (the instrumental period), estimates of the global rate of sea level change are derived from indirect measures of sea level change recorded in sedimentary, biological and archaeological archives. These proxy records are spatially limited, and reflect both local and global conditions. Reconstruction of a global signal is strengthened when individual records from widely different environmental settings converge on a common signal.

Sea level reconstructions for the last two millennia offer an opportunity to use proxy records to overlap with, but extend beyond the instrumental period. A recent example of such a reconstruction used sedimentary evidence from salt-marsh deposits on the Atlantic Coast of the United States, combined with sea level reconstructions based on tide gauge data and model predictions, to document an average rate of sea level change since the late 19th century of 2.1 mm yr^{-1} (1.9 to 2.2 mm yr^{-1}). This century-long rate of sea level rise exceeded any other century-scale sea level change rate in the entire 2000 year record.

On longer timescales, much larger rates and amplitudes of sea level changes were sometimes encountered. Glacial-interglacial climate cycles over the past 500,000 years resulted in global sea level changes of up to about 120 to 140 m. Much of this sea level change occurred over 10,000–15,000 year intervals corresponding to the transition from a full glacial period to an interglacial period, at average rates of 10–15 mm yr^{-1}. These high rates are only sustainable when the planet is emerging from periods of extreme glaciation when there are large high-latitude ice sheets in contact with the oceans. During one interval of the transition from the last glacial maximum (about 21,000 years ago) to the present interglaciation (Holocene, last 11,700 years), fossil coral reef deposits indicate that global sea level rose abruptly by 14–18 m in less than 500 years, which translates to rates exceeding 40 mm per year of sea level rise over this interval of time.

On even longer geologic timescales, major geological processes such as formation of a submerged ocean basaltic plateau can displace sufficient water to raise sea level by 5–10 m but the duration of plateau formation is millions to tens-of-millions of years and the maximum rate of the associated change in sea level is less than 0.01 mm yr^{-1}.

It is important to note that these examples from longer timescales, which indicate rates of sea level change greater than observed today, all occur in special circumstances in either time or location: at times of transition from full glacial to interglacial condition; at locations where the long-term after-effects of these transitions are still occurring; at locations of major tectonic upheavals or at locations in major deltas where subsidence due to a sediment compaction, sometimes amplified by human factors such as ground-fluid extraction.

In summary, the instrumental and geologic record support the conclusion that the current rate of mean global sea level change is unusual relative to that observed and/or estimated over the last two millennia.

[INSERT FAQ 5.2, FIGURE 1 HERE]

FAQ 5.2, Figure 1: Estimates of the average rate of sea level change (mm yr^{-1}) for 4 select time intervals: last 5 glacial/interglacial transitions; last 2 millennia; 20th century; satellite altimetry era (1993–2010).

[END FAQ 5.2 HERE]

References

Abbot, D. S., and E. Tziperman, 2008: A high-latitude convective cloud feedback and equable climates. *Quarterly Journal of the Royal Meteorological Society*, **134**, 165-185.

——, 2009: Controls on the Activation and Strength of a High-Latitude Convective Cloud Feedback. *Journal of the Atmospheric Sciences*, **66**, 519-529.

Abe-Ouchi, A., T. Segawa, and F. Saito, 2007: Climatic Conditions for modelling the Northern Hemisphere ice sheets throughout the ice age cycle. *Climate of the Past*, **3**, 423-438.

Ackert Jr, R. P., S. Mukhopadhyay, D. Pollard, R. M. DeConto, A. E. Putnam, and H. W. Borns Jr, 2011: West Antarctic Ice Sheet elevations in the Ohio Range: Geologic constraints and ice sheet modeling prior to the last highstand. *Earth and Planetary Science Letters*, **307**, 83-93.

Adams, J. B., M. E. Mann, and C. M. Ammann, 2003: Proxy evidence for an El Niño-like response to volcanic forcing. *Nature*, **426**, 274-278.

Adler, R. E., et al., 2009: Sediment record from the western Arctic Ocean with an improved Late Quaternary age resolution: HOTRAX core HLY0503-8JPC, Mendeleev Ridge. *Global and Planetary Change*, **68**, 18-29.

Agatova, A. R., A. N. Nazarov, R. K. Nepop, and H. Rodnight, 2012: Holocene glacier fluctuations and climate changes in the southeastern part of the Russian Altai (South Siberia) based on a radiocarbon chronology. *Quaternary Science Reviews*, **43**, 74-93.

Ahn, J., and E. J. Brook, 2008: Atmospheric CO_2 and climate on millennial time scales during the last glacial period. *Science*, **322**, 83-85.

Akkemik, Ü., R. D'Arrigo, P. Cherubini, N. Köse, and G. C. Jacoby, 2008: Tree-ring reconstructions of precipitation and streamflow for north-western Turkey. *International Journal of Climatology*, **28**, 173-183.

Alley, R. B., et al., 2010: History of the Greenland Ice Sheet: paleoclimatic insights. *Quaternary Science Reviews*, **29**, 1728-1756.

Alvarez-Solas, J., S. Charbit, C. Ritz, D. Paillard, G. Ramstein, and C. Dumas, 2010: Links between ocean temperature and iceberg discharge during Heinrich events. *Nature Geoscience*, **3**, 122-126.

Ammann, C., and E. Wahl, 2007: The importance of the geophysical context in statistical evaluations of climate reconstruction procedures. *Climatic Change*, **85**, 71-88.

Ammann, C., M. Genton, and B. Li, 2010: Technical Note: Correcting for signal attenuation from noisy proxy data in climate reconstructions. *Climate of the Past*, **6**, 273-279.

Ammann, C., F. Joos, D. Schimel, B. Otto-Bliesner, and R. Tomas, 2007: Solar influence on climate during the past millennium: Results from transient simulations with the NCAR Climate System Model. *Proc. Natl. Acad. Sci. U. S. A.*, **104**, 3713-3718.

Ammann, C. M., G. A. Meehl, W. M. Washington, and C. S. Zender, 2003: A monthly and latitudinally varying volcanic forcing dataset in simulations of 20th century climate. *Geophysical Research Letters*, **30**, 1657.

Anchukaitis, K. J., and J. E. Tierney, submitted: Identifying coherent spatiotemporal modes in time-uncertain proxy paleoclimate records. *Climate Dynamics*.

Anchukaitis, K. J., B. M. Buckley, E. R. Cook, B. I. Cook, R. D. D'Arrigo, and C. M. Ammann, 2010: Influence of volcanic eruptions on the climate of the Asian monsoon region. *Geophysical Research Letters*, **37**, L22703.

Anchukaitis, K. J., et al., 2012: Tree-ring reconstructed summer temperatures from northwestern North America during the last nine centuries. *Journal of Climate*, advance online publication.

Anchukaitis, K. J., et al., submitted: No evidence for misdating of tree-ring chronologies associated with volcanic cooling. *Nature Geoscience*.

Anderson, R., S. Ali, L. Bradtmiller, S. Nielsen, M. Fleisher, B. Anderson, and L. Burckle, 2009: Wind-driven upwelling in the Southern Ocean and the deglacial rise in atmospheric CO_2. *Science*, **323**, 1443-1448.

Anderson, R. K., G. H. Miller, J. P. Briner, N. A. Lifton, and S. B. DeVogel, 2008: A millennial perspective on Arctic warming from ^{14}C in quartz and plants emerging from beneath ice caps. *Geophysical Research Letters*, **35**, L01502.

Andersson, C., F. S. R. Pausata, E. Jansen, B. Risebrobakken, and R. J. Telford, 2010: Holocene trends in the foraminifer record from the Norwegian Sea and the North Atlantic Ocean. *Climate of the Past*, **6**, 179-193.

Andrews, T., J. M. Gregory, M. J. Webb, and K. E. Taylor, 2012: Forcing, feedbacks and climate sensitivity in CMIP5 coupled atmosphere-ocean climate models. *Geophysical Research Letters*, **39**, L09712.

Annan, J. D., and J. C. Hargreaves, 2006: Using multiple observationally-based constraints to estimate climate sensitivity. *Geophysical Research Letters*, **33**, L06704.

——, submitted: A global reconstruction of temperature changes at the Last Glacial Maximum. *Nature Geoscience*.

Annan, J. D., J. C. Hargreaves, R. Ohgaito, A. Abe-Ouchi, and S. Emori, 2005: Efficiently Constraining Climate Sensitivity with Ensembles of Paleoclimate Simulations. *Scientific Online Letters of the Atmosphere*, **1**, 181-184.

Antoine, P., et al., 2009: Rapid and cyclic aeolian deposition during the Last Glacial in European loess: a high-resolution record from Nussloch, Germany. *Quaternary Science Reviews*, **28**, 2955-2973.

Antoniades, D., P. Francus, R. Pienitz, G. St-Onge, and W. F. Vincent, 2011: Holocene dynamics of the Arctic's largest ice shelf. *Proceedings of the National Academy of Sciences*, **108**, 18899-18904.

Anzidei, M., F. Antonioli, A. Benini, K. Lambeck, D. Sivan, E. Serpelloni, and P. Stocchi, 2011: Sea level change and vertical land movements since the last two millennia along the coasts of southwestern Turkey and Israel. *Quaternary International*, **232**, 13-20.
Archer, D., and A. Ganopolski, 2005: A movable trigger: Fossil fuel CO2 and the onset of the next glaciation. *Geochemistry, Geophysics, Geosystems*, **6**, Q05003.
Arz, H., F. Lamy, A. Ganopolski, N. Nowaczyk, and J. Patzold, 2007: Dominant Northern Hemisphere climate control over millennial-scale glacial sea level variability. *Quaternary Science Reviews*, **26**, 312-321.
Asmerom, Y., V. J. Polyak, and S. J. Burns, 2010: Variable winter moisture in the southwestern United States linked to rapid glacial climate shifts. *Nature Geoscience*, **3**, 114-117.
Asmerom, Y., V. Polyak, S. Burns, and J. Rassmussen, 2007: Solar forcing of Holocene climate: New insights from a speleothem record, southwestern United States. *Geology*, **35**, 1-4.
Ault, T. R., et al., submitted: The continuum of drought variability in western North America: insights from instrumental, paleoclimate and global climate model data. *Journal of Climate*.
Auriemma, R., and E. Solinas, 2009: Archaeological remains as sea level change markers: A review. *Quaternary International*, **206**, 134-146.
Baker, V. R., 2008: Paleoflood hydrology: Origin, progress, prospects. *Geomorphology*, **101**, 1-13.
Bakker, P., submitted: The last interglacial period; an intercomparison of transient climate model simulations. *Climate of the Past Discussions*.
Ballantyne, A. P., M. Lavine, T. J. Crowley, J. Liu, and P. B. Baker, 2005: Meta-analysis of tropical surface temperatures during the Last Glacial Maximum. *Geophysical Research Letters*, **32**, L05712.
Balmaceda, L., N. Krivova, and S. Solanki, 2007: Reconstruction of solar irradiance using the group sunspot number. *Advances in Space Research*, **40**, 986-989.
Bamber, J. L., R. E. M. Riva, B. L. A. Vermeersen, and A. M. LeBrocq, 2009: Reassessment of the Potential Sea level Rise from a Collapse of the West Antarctic Ice Sheet. *Science*, **324**, 901-903.
Bamberg, A., Y. Rosenthal, A. Paul, D. Heslop, S. Mulitza, C. Rühlemann, and M. Schulz, 2010: Reduced North Atlantic Central Water formation in response to early Holocene ice-sheet melting. *Geophysical Research Letters*, **37**, L17705.
Bar-Matthews, M., A. Ayalon, M. Gilmour, A. Matthews, and C. J. Hawkesworth, 2003: Sea–land oxygen isotopic relationships from planktonic foraminifera and speleothems in the Eastern Mediterranean region and their implication for paleorainfall during interglacial intervals. *Geochimica et Cosmochimica Acta*, **67**, 3181-3199.
Barber, D., et al., 1999: Forcing of the cold event of 8,200 years ago by catastrophic drainage of Laurentide lakes. *Nature*, **400**, 344-348.
Bard, E., and R. E. M. Rickaby, 2009: Migration of the subtropical front as a modulator of glacial climate. *Nature*, **460**, 380-383.
Bard, E., B. Hamelin, and R. G. Fairbanks, 1990: U-Th ages obtained by mass spectrometry in corals from Barbados: sea level during the past 130,000 years. *Nature*, **346**, 456-458.
Bard, E., G. Raisbeck, F. Yiou, and J. Jouzel, 2000: Solar irradiance during the last 1200 years based on cosmogenic nuclides. *Tellus B*, **52**, 985-992.
Barker, S., et al., 2011: 800,000 Years of Abrupt Climate Variability. *Science*, **334**, 347-351.
Baroni, M., M. H. Thiemens, R. J. Delmas, and J. Savarino, 2007: Mass-Independent Sulfur Isotopic Compositions in Stratospheric Volcanic Eruptions. *Science*, **315**, 84-87.
Baroni, M., J. Savarino, J. Cole-Dai, V. Rai, and M. Thiemens, 2008: Anomalous sulfur isotope compositions of volcanic sulfate over the last millennium in Antarctic ice cores. *Journal of Geophysical Research-Atmospheres*, **113**, D20112.
Barrett, P. J., in press: Resolving views on Antarctic Neogene glacial history – the Sirius debate. *Transactions of the Royal Society of Edinburgh*.
Barriendos, M., and F. S. Rodrigo, 2006: Study of historical flood events on Spanish rivers using documentary data. *Hydrological Sciences Journal*, **51**, 765-783.
Barriopedro, D., E. M. Fischer, J. Luterbacher, R. M. Trigo, and R. García-Herrera, 2011: The Hot Summer of 2010: Redrawing the Temperature Record Map of Europe. *Science*, **332**, 220-224.
Bartlein, P., et al., 2011: Pollen-based continental climate reconstructions at 6 and 21 ka: a global synthesis. *Climate Dynamics*, **37**, 775-802.
Bartoli, G., B. Hönisch, and R. E. Zeebe, 2011: Atmospheric CO_2 decline during the Pliocene intensification of Northern Hemisphere glaciations. *Paleoceanography*, **26**, PA4213.
Bassett, S., G. Milne, J. Mitrovica, and P. Clark, 2005: Ice sheet and solid earth influences on far-field sea level histories. *Science*, **309**, 925-928.
Battle, M., et al., 1996: Atmospheric gas concentrations over the past century measured in air from firn at the South Pole. *Nature*, **383**, 231-235.
Bauch, H. A., E. S. Kandiano, J. Helmke, N. Andersen, A. Rosell-Mele, and H. Erlenkeuser, 2011: Climatic bisection of the last interglacial warm period in the Polar North Atlantic. *Quaternary Science Reviews*, **30**, 1813-1818.
Beal, L. M., W. P. M. De Ruijter, A. Biastoch, and R. Zahn, 2011: On the role of the Agulhas system in ocean circulation and climate. *Nature*, **472**, 429-436.
Beerling, D., and D. Royer, 2011: Convergent Cenozoic CO_2 history. *Nature Geoscience*, **4**, 418-420.

Beerling, D. J., A. Fox, and C. W. Anderson, 2009: Quantitative uncertainty analyses of ancient atmospheric CO_2 estimates from fossil leaves. *American Journal of Science*, **309**, 775-787.

Bekryaev, R. V., I. V. Polyakov, and V. A. Alexeev, 2010: Role of Polar Amplification in Long-Term Surface Air Temperature Variations and Modern Arctic Warming. *Journal of Climate*, **23**, 3888-3906.

Belt, S. T., G. Massé, S. J. Rowland, M. Poulin, C. Michel, and B. LeBlanc, 2007: A novel chemical fossil of palaeo sea ice: IP25. *Organic Geochemistry*, **38**, 16-27.

Benito, G., A. Díez-Herrero, and M. Fernández De Villalta, 2003: Magnitude and frequency of flooding in the Tagus basin (Central Spain) over the last millennium. *Climatic Change*, **58**, 171-192.

Benito, G., A. Sopeña, Y. Sánchez-Moya, M. J. Machado, and A. Pérez-González, 2003b: Palaeoflood record of the Tagus River (Central Spain) during the Late Pleistocene and Holocene. *Quaternary Science Reviews*, **22**, 1737-1756.

Benito, G., V. R. Thorndycraft, M. Rico, Y. Sanchez-Moya, and A. Sopena, 2008: Palaeoflood and floodplain records from Spain: Evidence for long-term climate variability and environmental changes. *Geomorphology*, **101**, 68-77.

Benito, G., et al., 2011: Hydrological response of a dryland ephemeral river to southern African climatic variability during the last millennium. *Quaternary Research*, **75**, 471-482.

Bentley, M. J., C. J. Fogwill, A. M. Le Brocq, A. L. Hubbard, D. E. Sugden, T. J. Dunai, and S. P. H. T. Freeman, 2010: Deglacial history of the West Antarctic Ice Sheet in the Weddell Sea embayment: Constraints on past ice volume change. *Geology*, **38**, 411-414.

Bereiter, B., D. Lüthi, M. Siegrist, S. Schüpbach, T. F. Stocker, and H. Fischer, 2012: Mode change of millennial CO_2 variability during the last glacial cycle associated with a bipolar marine carbon seesaw. *Proceedings of the National Academy of Sciences*, **109**, 9755-9760.

Berger, A., and M. F. Loutre, 1991: Insolation values for the climate of the last 10 million years. *Quaternary Sciences Reviews*, **10**, 297-317.

Berkelhammer, M., A. Sinha, M. Mudelsee, H. Cheng, R. L. Edwards, and K. Cannariato, 2010: Persistent multidecadal power of the Indian Summer Monsoon. *Earth and Planetary Science Letters*, **290**, 166-172.

Bertrand, S., K. A. Hughen, F. Lamy, J. B. W. Stuut, F. Torrejón, and C. B. Lange, 2012: Precipitation as the main driver of Neoglacial fluctuations of Gualas glacier, Northern Patagonian Icefield. *Climate of the Past*, **8**, 519-534.

Bhatt, U. S., et al., 2010: Circumpolar Arctic Tundra Vegetation Change Is Linked to Sea Ice Decline. *Earth Interactions*, **14**, 1-20.

Bird, B., M. Abbott, B. Finney, and B. Kutchko, 2009: A 2000 year varve-based climate record from the central Brooks Range, Alaska. *Journal of Paleolimnology*, **41**, 25-41.

Bird, B. W., M. B. Abbott, D. T. Rodbell, and M. Vuille, 2011: Holocene tropical South American hydroclimate revealed from a decadally resolved lake sediment $\delta^{18}O$ record. *Earth and Planetary Science Letters*, **310**, 192-202.

Bird, M. I., L. K. Fifield, T. S. Teh, C. H. Chang, N. Shirlaw, and K. Lambeck, 2007: An inflection in the rate of early mid-Holocene eustatic sea level rise: A new sea level curve from Singapore. *Estuarine, Coastal and Shelf Science*, **71**, 523-536.

Bird, M. I., W. E. N. Austin, C. M. Wurster, L. K. Fifield, M. Mojtahid, and C. Sargeant, 2010: Punctuated eustatic sea level rise in the early mid-Holocene. *Geology*, **38**, 803-806.

Bitz, C. M., J. C. H. Chiang, W. Cheng, and J. J. Barsugli, 2007: Rates of thermohaline recovery from freshwater pluses in modern, Last Glacial Maximum, and greenhouse warming climates. *Geophysical Research Letters*, **34**, L07708.

Black, D. E., M. A. Abahazi, R. C. Thunell, A. Kaplan, E. J. Tappa, and L. C. Peterson, 2007: An 8-century tropical Atlantic SST record from the Cariaco Basin: Baseline variability, twentieth-century warming, and Atlantic hurricane frequency. *Paleoceanography*, **22**, PA4204.

Blanchon, P., A. Eisenhauer, J. Fietzke, and V. Liebetrau, 2009: Rapid sea level rise and reef back-stepping at the close of the last interglacial highstand. *Nature*, **458**, 881-884.

Blunier, T., and E. Brook, 2001: Timing of millennial-scale climate change in Antarctica and Greenland during the last glacial period. *Science*, **291**, 109-112.

Blunier, T., J. Chappellaz, J. Schwander, B. Stauffer, and D. Raynaud, 1995: Variations in atmospheric methane concentration during the Holocene epoch. *Nature*, **374**, 46-49.

Blunier, T., R. Spahni, J. M. Barnola, J. Chappellaz, L. Loulergue, and J. Schwander, 2007: Synchronization of ice core records via atmospheric gases. *Climate of the Past*, **3**, 325-330.

Blunier, T., et al., 1997: Timing of the Antarctic cold reversal and the atmospheric CO2 increase with respect to the Younger Dryas event. *Geophysical Research Letters*, **24**, 2683-2686.

Bock, M., J. Schmitt, L. Moller, R. Spahni, T. Blunier, and H. Fischer, 2010: Hydrogen Isotopes Preclude Marine Hydrate CH_4 Emissions at the Onset of Dansgaard-Oeschger Events. *Science*, **328**, 1686-1689.

Bonelli, S., S. Charbit, M. Kageyama, M. N. Woillez, G. Ramstein, C. Dumas, and A. Quiquet, 2009: Investigating the evolution of major Northern Hemisphere ice sheets during the last glacial-interglacial cycle. *Climate of the Past*, **5**, 329-345.

Boninsegna, J. A., et al., 2009: Dendroclimatological reconstructions in South America: A review. *Palaeogeography, Palaeoclimatology, Palaeoecology*, **281**, 210-228.

Bonnet, S., A. de Vernal, C. Hillaire-Marcel, T. Radi, and K. Husum, 2010: Variability of sea-surface temperature and sea ice cover in the Fram Strait over the last two millennia. *Marine Micropaleontology*, **74**, 59-74.
Born, A., and K. H. Nisancioglu, submitted: Melting of Northern Greenland during the last interglaciation. *The Cryosphere*, **5**, 3517-3539.
Born, A., K. Nisancioglu, and P. Braconnot, 2010: Sea ice induced changes in ocean circulation during the Eemian. *Climate Dynamics*, **35**, 1361-1371.
Bothe, O., J. H. Jungclaus, D. Zanchettin, and E. Zorita, submitted: Climate of the last millennium: ensemble consistency of simulations and reconstructions. *Climate of the Past Discussion*, **8**, 2409-2444.
Boucher, É., J. Guiot, and E. Chapron, 2011: A millennial multi-proxy reconstruction of summer PDSI for Southern South America. *Climate of the Past*, **7**, 957-974.
Bowen, D., 2010: Sea level similar to 400 000 years ago (MIS 11): analogue for present and future sea level? *Climate of the Past*, **6**, 19-29.
Bowerman, N. D., and D. H. Clark, 2011: Holocene glaciation of the central Sierra Nevada, California. *Quaternary Science Reviews*, **30**, 1067-1085.
Bozbiyik, A., M. Steinacher, F. Joos, T. F. Stocker, and L. Menviel, 2011: Fingerprints of changes in the terrestrial carbon cycle in response to large reorganizations in ocean circulation. *Climate of the Past*, **7**, 319-338.
Braconnot, P., Y. Luan, S. Brewer, and W. Zheng, 2012a: Impact of Earth's orbit and freshwater fluxes on Holocene climate mean seasonal cycle and ENSO characteristics. *Climate Dynamics*, **38**, 1081-1092.
Braconnot, P., C. Marzin, L. Grégoire, E. Mosquet, and O. Marti, 2008: Monsoon response to changes in Earth's orbital parameters: comparisons between simulations of the Eemian and of the Holocene. *Climate of the Past*, **4**, 281-294.
Braconnot, P., et al., 2012b: Evaluation of climate models using palaeoclimatic data. *Nature Climate Change*, **2**, 417-424.
Braconnot, P., et al., 2007: Results of PMIP2 coupled simulations of the Mid-Holocene and Last Glacial Maximum-Part 1: experiments and large-scale features. *Climate of the Past*, **3**, 261-277.
Bradley, S. L., M. Siddall, G. A. Milne, V. Masson-Delmotte, and E. Wolff, 2012: Where might we find evidence of a Last Interglacial West Antarctic Ice Sheet collapse in Antarctic ice core records? *Global and Planetary Change*, **88-89**, 64-75.
Brady, E. C., B. L. Otto-Bliesner, and N. Rosenbloom, submitted: Sensitivity to Glacial Forcing in the CCSM4. *Journal of Climate*.
Braun, H., and J. Kurths, 2010: Were Dansgaard-Oeschger events forced by the Sun? *European Physical Journal-Special Topics*, **191**, 117-129.
Brázdil, R., Z. W. Kundzewicz, and G. Benito, 2006: Historical hydrology for studying flood risk in Europe. *Hydrological Sciences Journal*, **51**, 739-764.
Brázdil, R., C. Pfister, H. Wanner, H. von Storch, and J. Luterbacher, 2005: Historical climatology in Europe - The state of the art. *Climatic Change*, **70**, 363-430.
Brázdil, R., Z. W. Kundzewicz, G. Benito, G. Demaree, N. MacDonald, and L. A. Roald, 2012: Historical floods in Europe in the past millennium. *Changes of Flood Risk in Europe*, Z. W. Kundzewicz, Ed., 121-166.
Breecker, D. O., Z. D. Sharp, and L. D. McFadden, 2010: Atmospheric CO_2 concentrations during ancient greenhouse climates were similar to those predicted for AD 2100. *Proc. Natl. Acad. Sci. U. S. A.*, **107**, 576-580.
Briffa, K., T. Osborn, F. Schweingruber, I. Harris, P. Jones, S. Shiyatov, and E. Vaganov, 2001: Low-frequency temperature variations from a northern tree ring density network. *Journal of Geophysical Research-Atmospheres*, **106**, 2929-2941.
Briffa, K. R., and T. M. Melvin, 2011: A Closer Look at Regional Curve Standardization of Tree-Ring Records: Justification of the Need, a Warning of Some Pitfalls, and Suggested Improvements in Its Application Dendroclimatology. *Developments in Paleoenvironmental Research*, M. K. Hughes, T. W. Swetnam, and H. F. Diaz, Eds., Springer, 113-145.
Briffa, K. R., F. H. Schweingruber, P. D. Jones, T. J. Osborn, S. G. Shiyatov, and E. A. Vaganov, 1998: Reduced sensitivity of recent tree-growth to temperature at high northern latitudes. *Nature*, **391**, 678-682.
Briner, J. P., H. A. M. Stewart, N. E. Young, W. Philipps, and S. Losee, 2010: Using proglacial-threshold lakes to constrain fluctuations of the Jakobshavn Isbræ ice margin, western Greenland, during the Holocene. *Quaternary Science Reviews*, **29**, 3861-3874.
Brohan, P., R. Allan, E. Freeman, D. Wheeler, C. Wilkinson, and F. Williamson, submitted: Constraining the temperature history of the past millennium using early instrumental observations. *Climate of the Past Discussion*, **8**, 1653-1685.
Brovkin, V., J. H. Kim, M. Hofmann, and R. Schneider, 2008: A lowering effect of reconstructed Holocene changes in sea surface temperatures on the atmospheric CO2 concentration. *Global Biogeochemical Cycles*, **22**.
Buckley, B. M., et al., 2010: Climate as a contributing factor in the demise of Angkor, Cambodia. *Proc. Natl. Acad. Sci. U. S. A.*, **107**, 6748-6752.
Büntgen, U., D. C. Frank, D. Nievergelt, and J. Esper, 2006: Summer temperature variations in the European Alps, AD 755-2004. *Journal of Climate*, **19**, 5606-5623.
Büntgen, U., J. Esper, D. Frank, K. Nicolussi, and M. Schmidhalter, 2005: A 1052-year tree-ring proxy for Alpine summer temperatures. *Climate Dynamics*, **25**, 141-153.

Büntgen, U., et al., 2011a: Causes and Consequences of Past and Projected Scandinavian Summer Temperatures, 500–2100 AD. *PLoS ONE*, **6**, e25133.
Büntgen, U., et al., 2011b: 2500 Years of European Climate Variability and Human Susceptibility. *Science*, **331**, 578-582.
Büntgen, U. L. F., D. Frank, R. O. B. Wilson, M. Carrer, C. Urbinati, and J. A. N. Esper, 2008: Testing for tree-ring divergence in the European Alps. *Global Change Biology*, **14**, 2443-2453.
Bürger, G., 2007: Comment on "The Spatial Extent of 20th-Century Warmth in the Context of the Past 1200 Years". *Science*, **316**, 1844.
Butzin, M., M. Prange, and G. Lohmann, 2005: Radiocarbon simulations for the glacial ocean: The effects of wind stress, Southern Ocean sea ice and Heinrich events. *Earth and Planetary Science Letters*, **235**, 45-61.
Cahalan, R. F., G. Wen, J. W. Harder, and P. Pilewskie, 2010: Temperature responses to spectral solar variability on decadal time scales. *Geophysical Research Letters*, **37**, L07705.
Cai, Y. J., et al., 2010: The variation of summer monsoon precipitation in central China since the last deglaciation. *Earth and Planetary Science Letters*, **291**, 21-31.
Caillon, N., J. P. Severinghaus, J. Jouzel, J.-M. Barnola, J. Kang, and V. Y. Lipenkov, 2003: Timing of atmospheric CO_2 and Antarctic temperature changes across termination III. *Science*, **299**, 1728-1731.
Calenda, G., C. P. Mancini, and E. Volpi, 2005: Distribution of the extreme peak floods of the Tiber River from the XV century. *Advances in Water Resources*, **28**, 615-625.
Calov, R., and A. Ganopolski, 2005: Multistability and hysteresis in the climate-cryosphere system under orbital forcing. *Geophysical Research Letters*, **32**, L21717.
Calov, R., A. Ganopolski, V. Petoukhov, M. Claussen, and R. Greve, 2002: Large-scale instabilities of the Laurentide ice sheet simulated in a fully coupled climate-system model. *Geophysical Research Letters*, **29**, 2216.
Calov, R., et al., 2010: Results from the Ice-Sheet Model Intercomparison Project-Heinrich Event INtercOmparison (ISMIP HEINO). *Journal of Glaciology*, **56**, 371-383.
Camuffo, D., and S. Enzi, Eds., 1996: *The analysis of two bi-millenary series: Tiber and Po river floods*. Springer, 433-450 pp.
Candy, I., G. R. Coope, J. R. Lee, S. A. Parfitt, R. C. Preece, J. Rose, and D. C. Schreve, 2010: Pronounced warmth during early Middle Pleistocene interglacials: Investigating the Mid-Brunhes Event in the British terrestrial sequence. *Earth-Science Reviews*, **103**, 183-196.
Capron, E., et al., 2012: A global picture of the first abrupt climatic event occurring during the last glacial inception. *Geophysical Research Letters*, **39**, L15703.
Capron, E., et al., 2010a: Synchronising EDML and NorthGRIP ice cores using $\delta^{18}O$ of atmospheric oxygen ($\delta^{18}O$ atm) and CH_4 measurements over MIS5 (80-123 kyr). *Quaternary Science Reviews*, **29**, 222-234.
Capron, E., et al., 2010b: Millennial and sub-millennial scale climatic variations recorded in polar ice cores over the last glacial period. *Climate of the Past*, **6**, 345-365.
Carlson, A. E., P. U. Clark, G. M. Raisbeck, and E. J. Brook, 2007: Rapid Holocene deglaciation of the Labrador sector of the Laurentide Ice Sheet. *Journal of Climate*, **20**, 5126-5133.
Carlson, A. E., D. J. Ullman, F. S. Anslow, F. He, P. U. Clark, Z. Liu, and B. L. Otto-Bliesner, 2012: Modeling the surface mass-balance response of the Laurentide Ice Sheet to Bølling warming and its contribution to Meltwater Pulse 1A. *Earth and Planetary Science Letters*, **315–316**, 24-29.
Carre, M., I. Bentaleb, M. Fontugne, and D. Lavallee, 2005: Strong El Niño events during the early Holocene: stable isotope evidence from Peruvian sea shells. *The Holocene*, **15**, 42-47.
Chappell, J., 1983: Evidence for smoothly falling sea level relative to north Queensland, Australia, during the past 6,000 yr. *Nature*, **302**, 406-408.
Chappell, J., 2002: Sea level changes forced ice breakouts in the Last Glacial cycle: new results from coral terraces. *Quaternary Science Reviews*, **21**, 1229-1240.
Chase, B. M., M. E. Meadows, A. S. Carr, and P. J. Reimer, 2010: Evidence for progressive Holocene aridification in southern Africa recorded in Namibian hyrax middens: Implications for African Monsoon dynamics and the "African Humid Period". *Quaternary Research*, **74**, 36-45.
Chavaillaz, Y., F. Codron, and M. Kageyama, submitted: Southern Westerlies in LGM and future (RCP4.5) climates. *Climate of the Past Discussion*.
Chen, J. H., H. A. Curran, B. White, and G. J. Wasserburg, 1991: Precise chronology of the last interglacial period: 234U-230Th data from fossil coral reefs in the Bahamas. *Geological Society of America Bulletin*, **103**, 82-97.
Chen, W., B. W. Dong, and R. Y. Lu, 2010: Impact of the Atlantic Ocean on the multidecadal fluctuation of El Niño-Southern Oscillation-South Asian monsoon relationship in a coupled general circulation model. *Journal of Geophysical Research-Atmospheres*, **115**, D17109.
Cheng, H., et al., 2009: Ice Age Terminations. *Science*, **326**, 248-252.
Chiang, J. C. H., and C. M. Bitz, 2005: Influence of high latitude ice cover on the marine Intertropical Convergence Zone. *Climate Dynamics*, **25**, 477-496.
Christiansen, B., 2011: Reconstructing the NH mean temperature: Can underestimation of trends and variability be avoided? *Journal of Climate*, **24**, 674-692.
Christiansen, B., and F. C. Ljungqvist, 2012: The extra-tropical Northern Hemisphere temperature in the last two millennia: reconstructions of low-frequency variability. *Climate of the Past*, **8**, 765-786.

Christiansen, B., T. Schmith, and P. Thejll, 2009: A Surrogate Ensemble Study of Climate Reconstruction Methods: Stochasticity and Robustness. *Journal of Climate*, **22**, 951-976.
Chu, G., et al., 2011: Seasonal temperature variability during the past 1600 years recorded in historical documents and varved lake sediment profiles from northeastern China. *The Holocene*, **22**, 785-792.
Chylek, P., C. K. Folland, G. Lesins, M. K. Dubey, and M. Y. Wang, 2009: Arctic air temperature change amplification and the Atlantic Multidecadal Oscillation. *Geophysical Research Letters*, **36**, L14801.
Claquin, T., et al., 2003: Radiative forcing of climate by ice-age atmospheric dust. *Climate Dynamics*, **20**, 193-202.
Clark, P. U., J. X. Mitrovica, G. A. Milne, and M. E. Tamisiea, 2002: Sea level Fingerprinting as a Direct Test for the Source of Global Meltwater Pulse IA. *Science*, **295**, 2438-2441.
Clark, P. U., et al., 2009: The Last Glacial Maximum. *Science*, **325**, 710-714.
Clark, P. U., et al., 2012: Global climate evolution during the last deglaciation. *Proceedings of the National Academy of Sciences*. advanced online publication.
Clarke, G., D. Leverington, J. Teller, and A. Dyke, 2004: Paleohydraulics of the last outburst flood from glacial Lake Agassiz and the 8200 BP cold event. *Quaternary Science Reviews*, **23**, 389-407.
Clemens, S. C., W. L. Prell, and Y. Sun, 2010: Orbital-scale timing and mechanisms driving Late Pleistocene Indo-Asian summer monsoons: Reinterpreting cave speleothem $\delta^{18}O$. *Paleoceanography*, **25**, PA4207.
CLIMAP Project Members, 1976: The Surface of the Ice-Age Earth. *Science*, **191**, 1131-1137.
——, 1981: *Seasonal reconstructions of the Earth's surface at the last glacial maximum*. Geological Society of America.
Cobb, K. M., C. D. Charles, H. Cheng, R. L. Edwards, H. R. Sayani, and N. Westphal, submitted: Highly variable El Niño-Southern Oscillation throughout the Holocene. *Science*.
Cochelin, A.-S., L. Mysak, and Z. Wang, 2006: Simulation of long-term future climate changes with the green McGill paleoclimate model: the next glacial inception. *Climatic Change*, **79**, 381-401.
Cole-Dai, J., D. Ferris, A. Lanciki, J. Savarino, M. Baroni, and M. Thiemens, 2009: Cold decade (AD 1810-1819) caused by Tambora (1815) and another (1809) stratospheric volcanic eruption. *Geophysical Research Letters*, **36**, L22703.
Colville, E. J., A. E. Carlson, B. L. Beard, R. G. Hatfield, J. S. Stoner, A. V. Reyes, and D. J. Ullman, 2011: Sr-Nd-Pb Isotope Evidence for Ice-Sheet Presence on Southern Greenland During the Last Interglacial. *Science*, **333**, 620-623.
Conroy, J. L., J. T. Overpeck, J. E. Cole, T. M. Shanahan, and M. Steinitz-Kannan, 2008: Holocene changes in eastern tropical Pacific climate inferred from a Galapagos lake sediment record. *Quaternary Science Reviews*, **27**, 1166-1180.
Cook, E., B. Buckley, J. G. Palmer, P. Fenwick, M. Peterson, G. Boswijk, and A. Fowler, 2006: Millennia-long tree-ring records from Tasmania and New Zealand: a basis for modelling climate variability and forcing, past, present and future. *Journal of Quaternary Science*, **21**, 689-699.
Cook, E. R., R. D. D'Arrigo, and M. E. Mann, 2002: A well-verified, multiproxy reconstruction of the winter North Atlantic Oscillation index since AD 1400. *Journal of Climate*, **15**, 1754-1764.
Cook, E. R., C. A. Woodhouse, C. M. Eakin, D. M. Meko, and D. W. Stahle, 2004: Long-Term Aridity Changes in the Western United States. *Science*, **306**, 1015-1018.
Cook, E. R., R. Seager, R. R. Heim, R. S. Vose, C. Herweijer, and C. Woodhouse, 2010a: Megadroughts in North America: placing IPCC projections of hydroclimatic change in a long-term palaeoclimate context. *Journal of Quaternary Science*, **25**, 48-61.
Cook, E. R., K. J. Anchukaitis, B. M. Buckley, R. D. D'Arrigo, G. C. Jacoby, and W. E. Wright, 2010b: Asian Monsoon Failure and Megadrought During the Last Millennium. *Science*, **328**, 486-489.
Cooper, R., T. Melvin, I. Tyers, R. Wilson, and K. Briffa, 2012: A tree-ring reconstruction of East Anglian (UK) hydroclimate variability over the last millennium. *Climate Dynamics*. doi:10.1007/s00382-012-1328-x, advanced online publication.
Cornes, R. C., P. D. Jones, K. R. Briffa, and T. J. Osborn, 2012: Estimates of the North Atlantic Oscillation back to 1692 using a Paris-London westerly index, **32**, 1135-1150.
Corona, C., J. Guiot, J. Edouard, F. Chalie, U. Büntgen, P. Nola, and C. Urbinati, 2010: Millennium-long summer temperature variations in the European Alps as reconstructed from tree rings. *Climate of the Past*, **6**, 379-400.
Corona, C., J.-L. Edouard, F. Guibal, J. Guiot, S. Bernard, A. Thomas, and N. Denelle, 2011: Long-term summer (AD751–2008) temperature fluctuation in the French Alps based on tree-ring data. *Boreas*, **40**, 351-366.
Cramer, B. S., K. G. Miller, P. J. Barrett, and J. D. Wright, 2011: Late Cretaceous & Neogene trends in deep ocean temperature and continental ice volume: Reconciling records of benthic foraminiferal geochemistry ($\delta 1^8O$ and Mg/Ca) with sea level history. *Journal of Geophysical Research*, **116**, C12023.
Crespin, E., H. Goosse, T. Fichefet, and M. E. Mann, 2009: The 15th century Arctic warming in coupled model simulations with data assimilation. *Climate of the Past*, **5**, 389-401.
Cronin, T. M., P. R. Vogt, D. A. Willard, R. Thunell, J. Halka, M. Berke, and J. Pohlman, 2007: Rapid sea level rise and ice sheet response to 8,200-year climate event. *Geophysical Research Letters*, **34**, L20603.
Crouch, A., P. Charbonneau, G. Beaubien, and D. Paquin-Ricard, 2008: A model for the total solar irradiance based on active region decay. *Astrophysical Journal*, **677**, 723-741.

Crowley, T., and M. Unterman, submitted: Technical Details Concerning Development of a 1200-Year Proxy Index for Global Volcanism. *Climate of the Past Discussion*. doi:10.5194/essdd-5-1-2012.
Crowley, T. J., 2000: Causes of Climate Change Over the Past 1000 Years. *Science*, **289**, 270-277.
Crowley, T. J., and W. T. Hyde, 2008: Transient nature of late Pleistocene climate variability. *Nature*, **456**, 226-230.
Crowley, T. J., S. K. Baum, K.-Y. Kim, G. C. Hegerl, and W. T. Hyde, 2003: Modeling ocean heat content changes during the last millennium. *Geophysical Research Letters*, **30**, 1932.
Crucifix, M., 2006: Does the Last Glacial Maximum constrain climate sensitivity? *Geophysical Research Letters*, **33**, L18701.
Cruz, F. W., et al., 2009: Orbitally driven east-west antiphasing of South American precipitation. *Nature Geoscience*, **2**, 210-214.
Cunningham, L. K., et al., submitted: Reconstructions of surface ocean conditions from the North East Atlantic and Nordic Seas during the last millennium. *The Holocene*.
Curry, J. A., J. L. Schramm, and E. E. Ebert, 1995: Sea Ice-Albedo Climate Feedback Mechanism. *Journal of Climate*, **8**, 240-247.
D'Arrigo, R., R. Wilson, and G. Jacoby, 2006: On the long-term context for late twentieth century warming. *Journal of Geophysical Research*, **111**, D03103.
D'Arrigo, R., R. Wilson, B. Liepert, and P. Cherubini, 2008: On the 'Divergence Problem' in Northern Forests: A review of the tree-ring evidence and possible causes. *Global and Planetary Change*, **60**, 289-305.
D'Arrigo, R., E. R. Cook, R. J. Wilson, R. Allan, and M. E. Mann, 2005: On the variability of ENSO over the past six centuries. *Geophysical Research Letters*, **32**, L03711.
D'Arrigo, R., et al., 2009: Tree growth and inferred temperature variability at the North American Arctic treeline. *Global and Planetary Change*, **65**, 71-82.
Dahl-Jensen, D., et al., submitted: Eemian interglacial reconstructed from Greenland folded NEEM ice core strata. *Nature*.
Daley, T. J., et al., 2011: The 8200-yr BP cold event in stable isotope records from the North Atlantic region. *Global and Planetary Change*, **79**, 288-302.
Dansgaard, W., H. B. Clausen, N. Gundestrup, S. J. Johnsen, and C. Rygner, 1985: Dating and climatic interpretation of two deep Greenland ice cores, in Greenland Ice Core: Geophysics, Geochemistry, and the Environment, Geophys. *Geophysical Monograph Series*, C. C. Langway Jr., H. Oeschger, and W. Dansgaard, Eds., 71–76.
Davis, P. T., B. Menounos, and G. Osborn, Eds., 2009: *Holocene and Latest Pleistocene Alpine Glacier Fluctuations: A Global Perspective*. Vol. 28, 2021-2238 pp.
De Deckker, P., M. Moros, K. Perner, and E. Jansen, 2012: Influence of the tropics and southern westerlies on glacial interhemispheric asymmetry. *Nature Geoscience*, **5**, 266-269.
De Deckker, P., M. Norman, I. D. Goodwin, A. Wain, and F. X. Gingele, 2010: Lead isotopic evidence for an Australian source of aeolian dust to Antarctica at times over the last 170,000 years. *Palaeogeography Palaeoclimatology Palaeoecology*, **285**, 205-223.
de Garidel-Thoron, T., Y. Rosenthal, L. Beaufort, E. Bard, C. Sonzogni, and A. C. Mix, 2007: A multiproxy assessment of the western equatorial Pacific hydrography during the last 30 kyr. *Paleoceanography*, **22**, PA3204.
DeConto, R. M., and D. Pollard, 2003: Rapid Cenozoic glaciation of Antarctica induced by declining atmospheric CO_2. *Nature*, **421**, 245-249.
DeConto, R. M., et al., 2012: Past extreme warming events linked to massive carbon release from thawing permafrost. *Nature*, **484**, 87-91.
Delaygue, G., and E. Bard, 2011: An Antarctic view of Beryllium-10 and solar activity for the past millennium. *Climate Dynamics*, **36**, 2201-2218.
Delworth, T., and M. Mann, 2000: Observed and simulated multidecadal variability in the Northern Hemisphere. *Climate Dynamics*, **16**, 661-676.
Denis, D., X. Crosta, L. Barbara, G. Massé, H. Renssen, O. Ther, and J. Giraudeau, 2010: Sea ice and wind variability during the Holocene in East Antarctica: insight on middle–high latitude coupling. *Quaternary Science Reviews*, **29**, 3709-3719.
Denton, G. H., R. F. Anderson, J. R. Toggweiler, R. L. Edwards, J. M. Schaefer, and A. E. Putnam, 2010: The Last Glacial Termination. *Science*, **328**, 1652-1656.
Derbyshire, E., 2003: Loess, and the Dust Indicators and Records of Terrestrial and Marine Palaeoenvironments (DIRTMAP) database. *Quaternary Science Reviews*, **22**, 1813-1819.
Deschamps, P., et al., 2012: Ice-sheet collapse and sea level rise at the Bolling warming 14,600-years ago. *Nature*, **483**, 559-564.
Diaz, H. F., R. M. Trigo, M. K. Hughes, M. E. Mann, E. Xoplaki, and D. Barriopedro, 2011: Spatial and temporal characteristics of Climate in medieval times revisited. *Bulletin of the American Meteorological Society*, **92**, 1487–1500.
Diffenbaugh, N. S., M. Ashfaq, B. Shuman, J. W. Williams, and P. J. Bartlein, 2006: Summer aridity in the United States: Response to mid-Holocene changes in insolation and sea surface temperature. *Geophysical Research Letters*, **33**, L22712.
Ditlevsen, P. D., and O. D. Ditlevsen, 2009: On the Stochastic Nature of the Rapid Climate Shifts during the Last Ice Age. *Journal of Climate*, **22**, 446-457.

Divine, D. V., and C. Dick, 2006: Historical variability of sea ice edge position in the Nordic Seas. *Journal of Geophysical Research*, **111**, C01001.
Dobrovolný, P., et al., 2010: Monthly, seasonal and annual temperature reconstructions for Central Europe derived from documentary evidence and instrumental records since AD 1500. *Climatic Change*, **101**, 69-107.
Dolan, A. M., A. M. Haywood, D. J. Hill, H. J. Dowsett, S. J. Hunter, D. J. Lunt, and S. J. Pickering, 2011: Sensitivity of Pliocene ice sheets to orbital forcing. *Palaeogeography, Palaeoclimatology, Palaeoecology*, **309**, 98-110.
Donders, T. H., F. Wagner-Cremer, and H. Visscher, 2008: Integration of proxy data and model scenarios for the mid-Holocene onset of modern ENSO variability. *Quaternary Science Reviews*, **27**, 571-579.
Donnelly, J. P., P. Cleary, P. Newby, and R. Ettinger, 2004: Coupling instrumental and geological records of sea level change: Evidence from southern New England of an increase in the rate of sea level rise in the late 19th century. *Geophysical Research Letters*, **31**, L05203.
Dowsett, H. J., M. M. Robinson, and K. M. Foley, 2009: Pliocene three-dimensional global ocean temperature reconstruction. *Climate of the Past*, **5**, 769-783.
Dowsett, H. J., et al., 2012: Assessing confidence in Pliocene sea surface temperatures to evaluate predictive models. *Nature Climate Change*, **2**, 365-371.
Dutton, A., and K. Lambeck, 2012: Ice Volume and Sea Level During the Last Interglacial. *Science*, **337**, 216-219.
Dwyer, G. S., and M. A. Chandler, 2009: Mid-Pliocene sea level and continental ice volume based on coupled benthic Mg/Ca palaeotemperatures and oxygen isotopes. *Philosophical Transactions of the Royal Society A: Mathematical, Physical and Engineering Sciences*, **367**, 157-168.
Edwards, R. L., et al., 1993: A Large Drop in Atmospheric $^{14}C/^{12}C$ and Reduced Melting in the Younger Dryas, Documented with ^{230}Th Ages of Corals. *Science*, **260**, 962-968.
Edwards, T., M. Crucifix, and S. Harrison, 2007: Using the past to constrain the future: how the palaeorecord can improve estimates of global warming. *Progress in Physical Geography*, **31**, 481-500.
Eisenman, I., C. M. Bitz, and E. Tziperman, 2009: Rain driven by receding ice sheets as a cause of past climate change. *Paleoceanography*, **24**, PA4209.
Elderfield, H., et al., 2010: A record of bottom water temperature and seawater $\delta^{18}O$ for the Southern Ocean over the past 440-kyr based on Mg/Ca of benthic foraminiferal *Uvigerina* spp. *Quaternary Science Reviews*, **29**, 160-169.
Ellison, C. R. W., M. R. Chapman, and I. R. Hall, 2006: Surface and deep ocean interactions during the cold climate event 8200 years ago. *Science*, **312**, 1929-1932.
Elsig, J., et al., 2009: Stable isotope constraints on Holocene carbon cycle changes from an Antarctic ice core. *Nature*, **461**, 507-510.
Ely, L. L., 1997: Response of extreme floods in the southwestern United States to climatic variations in the late Holocene. *Geomorphology*, **19**, 175-201.
Ely, L. L., Y. Enzel, V. R. Baker, and D. R. Cayan, 1993: A 5000-Year Record of Extreme Floods and Climate Change in the Southwestern United States. *Science*, **262**, 410-412.
Emile-Geay, J., R. Seager, M. A. Cane, E. R. Cook, and G. H. Haug, 2008: Volcanoes and ENSO over the past millennium. *Journal of Climate*, **21**, 3134-3148.
England, J. H., T. R. Lakeman, D. S. Lemmen, J. M. Bednarski, T. G. Stewart, and D. J. A. Evans, 2008: A millennial-scale record of Arctic Ocean sea ice variability and the demise of the Ellesmere Island ice shelves. *Geophysical Research Letters*, **35**, L19502.
Enzel, Y., L. L. Ely, P. K. House, V. R. Baker, and R. H. Webb, 1993: Paleoflood evidence for a natural upper bound to flood magnitudes in the Colorado River Basin. *Water Resources Research*, **29**, 2287-2297.
EPICA Community Members, 2006: One-to-one coupling of glacial climate variability in Greenland and Antarctica. *Nature*, **444**, 195-198.
Esper, J., and D. Frank, 2009: Divergence pitfalls in tree-ring research. *Climatic Change*, **94**, 261-266.
Esper, J., U. Büntgen, M. Timonen, and D. C. Frank, 2012a: Variability and extremes of northern Scandinavian summer temperatures over the past two millennia. *Global and Planetary Change*, **88–89**, 1-9.
Esper, J., U. Büntgen, J. Luterbacher, and P. J. Krusic, submitted: No evidence for globally missing rings in temperature sensitive dendrochronological data. *Dendrochonologia*.
Esper, J., D. Frank, R. Wilson, U. Büntgen, and K. Treydte, 2007a: Uniform growth trends among central Asian low- and high-elevation juniper tree sites. *Trees-Structure and Function*, **21**, 141-150.
Esper, J., R. Wilson, D. Frank, A. Moberg, H. Wanner, and J. Luterbacher, 2005: Climate: past ranges and future changes. *Quaternary Science Reviews*, **24**, 2164-2166.
Esper, J., D. Frank, U. Büntgen, A. Verstege, J. Luterbacher, and E. Xoplaki, 2007b: Long-term drought severity variations in Morocco. *Geophysical Research Letters*, **34**, L17702.
Esper, J., et al., 2012b: Orbital forcing of tree-ring data. *Nature Climate Change*, **advance online publication**.
Esper, J. A. N., D. Frank, U. L. F. BÜNtgen, A. Verstege, R. M. Hantemirov, and A. V. Kirdyanov, 2010: Trends and uncertainties in Siberian indicators of 20th century warming. *Global Change Biology*, **16**, 386-398.
Etheridge, D. M., L. P. Steele, R. J. Francey, and R. L. Langenfelds, 1998: Atmospheric methane between 1000 A.D. and present: Evidence of anthropogenic emissions and climatic variability. *Journal of Geophysical Research*, **103**, 15979-15993.

Etheridge, D. M., L. P. Steele, R. L. Langenfelds, R. J. Francey, J. M. Barnola, and V. I. Morgan, 1996: Natural and anthropogenic changes in atmospheric CO_2 over the last 1000 years from air in Antarctic ice and firn. *Journal of Geophysical Research*, **101**, 4115-4128.

Euler, C., and U. Ninnemann, 2010: Climate and Antarctic Intermediate Water coupling during the late Holocene. *Geology*, **38**, 647-650.

Fairbanks, R. G., 1989: A 17,000 year glacio-eustatic sea level record : influence of glacial melting rates on the Younger Dryas event and deep ocean circulation. *Nature*, **342**, 637-642.

Fan, F. X., M. E. Mann, and C. M. Ammann, 2009: Understanding Changes in the Asian Summer Monsoon over the Past Millennium: Insights from a Long-Term Coupled Model Simulation. *Journal of Climate*, **22**, 1736-1748.

Fedorov, A. V., et al., 2006: The Pliocene paradox (mechanisms for a permanent El Niño). *Science*, **312**, 1485-1489.

Felis, T., et al., 2012: Pronounced interannual variability in tropical South Pacific temperatures during Heinrich Stadial 1. *Nature communications*, **3**, 965.

Feng, S., and Q. Hu, 2008: How the North Atlantic Multidecadal Oscillation may have influenced the Indian summer monsoon during the past two millennia. *Geophysical Research Letters*, **35**, L01707.

Fernández-Donado, L., et al., submitted: Temperature response to external forcing in simulations and reconstructions of the last millennium. *Climate of the Past Discussion*.

Ferretti, D., et al., 2005: Unexpected changes to the global methane budget over the past 2000 years. *Science*, **309**, 1714-1717.

Feulner, G., 2011: Are the most recent estimates for Maunder Minimum solar irradiance in agreement with temperature reconstructions? *Geophysical Research Letters*, **38**, L16706.

Fischer, H., M. Wahlen, J. Smith, D. Mastroiani, and B. Deck, 1999: Ice core records of atmospheric CO_2 around the last three glacial terminations. *Science*, **283**, 1712-1714.

Fischer, H., M. L. Siggaard-Andersen, U. Ruth, R. Röthlisberger, and E. Wolff, 2007: Glacial/interglacial changes in mineral dust and sea-salt records in polar ice cores: Sources, transport, and deposition. *Reviews of Geophysics*, **45**, RG1002.

Fischer, H., et al., 2008: Changing boreal methane sources and constant biomass burning during the last termination. *Nature*, **452**, 864-867.

Fischer, N., and J. H. Jungclaus, 2010: Effects of orbital forcing on atmosphere and ocean heat transports in Holocene and Eemian climate simulations with a comprehensive Earth system model. *Climate of the Past*, **6**, 155-168.

Fleitmann, D., et al., 2009: Timing and climatic impact of Greenland interstadials recorded in stalagmites from northern Turkey. *Geophysical Research Letters*, **36**.

Fletcher, M. S., and P. I. Moreno, 2011: Zonally symmetric changes in the strength and position of the Southern Westerlies drove atmospheric CO_2 variations over the past 14 k.y. *Geology*, **39**, 419-422.

Flückiger, J., et al., 2002: High-resolution Holocene N2O ice core record and its relationship with CH4 and CO2. *Global Biogeochemical Cycles*, **16**, 1010.

Foster, G., 2008: Seawater pH, pCO_2 and $[CO^{2-}_3]$ variations in the Caribbean Sea over the last 130 kyr: A boron isotope and B/Ca study of planktic forminifera. *Earth and Planetary Science Letters*, **271**, 254-266.

Fowler, A. M., et al., 2012: Multi-centennial tree-ring record of ENSO-related activity in New Zealand. *Nature Climate Change*, **2**, 172-176.

Francey, R. J., et al., 1999: A 1000-year high precision record of δ13C in atmospheric CO2. *Tellus B*, **51**, 170-193.

Frank, D., J. Esper, and E. R. Cook, 2007: Adjustment for proxy number and coherence in a large-scale temperature reconstruction. *Geophysical Research Letters*, **34**, L16709.

Frank, D., J. Esper, E. Zorita, and R. Wilson, 2010a: A noodle, hockey stick, and spaghetti plate: a perspective on high-resolution paleoclimatology. *Wiley Interdisciplinary Reviews: Climate Change*, **1**, 507-516.

Frank, D. C., J. Esper, C. C. Raible, U. Buntgen, V. Trouet, B. Stocker, and F. Joos, 2010b: Ensemble reconstruction constraints on the global carbon cycle sensitivity to climate. *Nature*, **463**, 527-530.

Funder, S., et al., 2011: A 10,000-Year Record of Arctic Ocean Sea ice Variability—View from the Beach. *Science*, **333**, 747-750.

Gabrielli, P., et al., 2010: A major glacial-interglacial change in aeolian dust composition inferred from Rare Earth Elements in Antarctic ice. *Quaternary Science Reviews*, **29**, 265-273.

Gagen, M., et al., 2011: Cloud response to summer temperatures in Fennoscandia over the last thousand years. *Geophysical Research Letters*, **38**, L05701.

Gallup, C. D., H. Cheng, F. W. Taylor, and R. L. Edwards, 2002: Direct Determination of the Timing of Sea Level Change During Termination II. *Science*, **295**, 310-313.

Ganopolski, A., and D. M. Roche, 2009: On the nature of lead-lag relationships during glacial-interglacial climate transitions. *Quaternary Science Reviews*, **28**, 3361-3378.

Ganopolski, A., and R. Calov, 2011: The role of orbital forcing, carbon dioxide and regolith in 100 kyr glacial cycles. *Climate of the Past*, **7**, 2391-2411.

Ganopolski, A., R. Calov, and M. Claussen, 2010: Simulation of the last glacial cycle with a coupled climate ice-sheet model of intermediate complexity. *Climate of the Past*, **6**, 229-244.

Gao, C., A. Robock, and C. Ammann, 2008: Volcanic forcing of climate over the past 1500 years: An improved ice core-based index for climate models. *Journal of Geophysical Research-Atmospheres*, **113**, D23111.

Gao, C., et al., 2006: The 1452 or 1453 A.D. Kuwae eruption signal derived from multiple ice core records: Greatest volcanic sulfate event of the past 700 years. *Journal of Geophysical Research-Atmospheres*, **111**, D12107.
García-Artola, A., A. Cearreta, E. Leorri, M. Irabien, and W. Blake, 2009: Las marismas costeras como archivos geológicos de las variaciones recientes en el nivel marino/Coastal salt-marshes as geological archives of recent sea level changes. *Geogaceta*, **47**, 109-112.
Garcin, Y., et al., 2007: Solar and anthropogenic imprints on Lake Masoko (southern Tanzania) during the last 500 years. *Journal of Paleolimnology*, **37**, 475-490.
Gayer, E., J. Lavé, R. Pik, and C. France-Lanord, 2006: Monsoonal forcing of Holocene glacier fluctuations in Ganesh Himal (Central Nepal) constrained by cosmogenic ^{3}He exposure ages of garnets. *Earth and Planetary Science Letters*, **252**, 275-288.
Ge, Q., S. Wang, and J. Zheng, 2006: Reconstruction of temperature series in China for the last 5000 years. *Progress in Natural Science*, **16**, 838-845.
Ge, Q., J. Zheng, Z. Hao, X. Shao, W. Wang, and J. Luterbacher, 2010: Temperature variation through 2000 years in China: An uncertainty analysis of reconstruction and regional difference. *Geophysical Research Letters*, **37**, L03703.
Gehrels, W. R., and P. L. Woodworth, submitted: When did modern rates of sea level rise start? *Global and Planetary Change*.
Gehrels, W. R., B. W. Hayward, R. M. Newnham, and K. E. Southall, 2008: A 20th century acceleration of sea level rise in New Zealand. *Geophysical Research Letters*, **35**, L02717.
Gehrels, W. R., B. P. Horton, A. C. Kemp, and D. Sivan, 2011: Two millennia of sea level data: The key to predicting change. *Eos Transactions AGU*, **92**.
Gehrels, W. R., et al., 2006: Rapid sea level rise in the North Atlantic Ocean since the first half of the nineteenth century. *The Holocene*, **16**, 949-965.
Ghatak, D., A. Frei, G. Gong, J. Stroeve, and D. Robinson, 2010: On the emergence of an Arctic amplification signal in terrestrial Arctic snow extent. *Journal of Geophysical Research-Atmospheres*, **115**, D24105.
Giguet-Covex, C., et al., 2012: Frequency and intensity of high-altitude floods over the last 3.5 ka in northwestern French Alps (Lake Anterne). *Quaternary Research*, **77**, 12-22.
Gillett, N., T. Kell, and P. Jones, 2006: Regional climate impacts of the Southern Annular Mode. *Geophysical Research Letters*, **33**, L23704.
Gillett, N., et al., 2008: Attribution of polar warming to human influence. *Nature Geoscience*, **1**, 750-754.
Gladstone, R. M., et al., 2005: Mid-Holocene NAO: A PMIP2 model intercomparison. *Geophysical Research Letters*, **32**, L16707.
Glaser, R., et al., 2010: The variability of European floods since AD 1500. *Climatic Change*, **101**, 235-256.
González-Rouco, F., H. von Storch, and E. Zorita, 2003: Deep soil temperature as proxy for surface air-temperature in a coupled model simulation of the last thousand years. *Geophys. Res. Lett.*, **30**, 2116.
Gonzalez-Rouco, J., H. Beltrami, E. Zorita, and H. von Storch, 2006: Simulation and inversion of borehole temperature profiles in surrogate climates: Spatial distribution and surface coupling. *Geophysical Research Letters*, **33**, L01703.
Gonzalez, C., and L. Dupont, 2009: Tropical salt marsh succession as sea level indicator during Heinrich events. *Quaternary Science Reviews*, **28**, 939-946.
González, J. L., and T. E. Törnqvist, 2009: A new Late Holocene sea level record from the Mississippi Delta: evidence for a climate/sea level connection? *Quaternary Science Reviews*, **28**, 1737-1749.
Goodwin, I. D., and N. Harvey, 2008: Subtropical sea level history from coral microatolls in the Southern Cook Islands, since 300 AD. *Marine Geology*, **253**, 14-25.
Goosse, H., J. Guiot, M. E. Mann, S. Dubinkina, and Y. Sallaz-Damaz, 2012a: The medieval climate anomaly in Europe: Comparison of the summer and annual mean signals in two reconstructions and in simulations with data assimilation. *Global and Planetary Change*, **84–85**, 35-47.
Goosse, H., et al., 2012b: The role of forcing and internal dynamics in explaining the "Medieval Climate Anomaly". *Climate Dynamics*. doi:10.1007/s00382-012-1297-0, advance online publication.
Goosse, H., et al., accepted: Antarctic temperature changes during the last millennium: evaluation of simulations and reconstructions. *Quaternary Science Review*.
Govin, A., et al., 2012: Persistent influence of ice sheet melting on high northern latitude climate during the early Last Interglacial. *Climate of the Past*, **8**, 483-507.
Grachev, A., E. Brook, J. Severinghaus, and N. Pisias, 2009: Relative timing and variability of atmospheric methane and GISP2 oxygen isotopes between 68 and 86 ka. *Global Biogeochemical Cycles*, **23**, GB2009.
Graham, N., C. Ammann, D. Fleitmann, K. Cobb, and J. Luterbacher, 2011: Support for global climate reorganization during the "Medieval Climate Anomaly". *Climate Dynamics*, **37**, 1217-1245.
Graham, N. E., et al., 2007: Tropical Pacific - mid-latitude teleconnections in medieval times. *Climatic Change*, **83**, 241-285.
Graversen, R. G., and M. H. Wang, 2009: Polar amplification in a coupled climate model with locked albedo. *Climate Dynamics*, **33**, 629-643.
Gray, L. J., et al., 2010: Solar influences on climate. *Review of Geophysics*, **48**, RG4001.

Gray, S. T., L. J. Graumlich, J. L. Betancourt, and G. T. Pederson, 2004: A tree-ring based reconstruction of the Atlantic Multidecadal Oscillation since 1567 A.D. *Geophysical Research Letters*, **31**, L12205.
Greenbaum, N., A. P. Schick, and V. R. Baker, 2000: The palaeoflood record of a hyperarid catchment, Nahal Zin, Negev Desert, Israel. *Earth Surface Processes and Landforms*, **25**, 951-971.
Greenbaum, N., N. Porat, E. Rhodes, and Y. Enzel, 2006: Large floods during late Oxygen Isotope Stage 3, southern Negev desert, Israel. *Quaternary Science Reviews*, **25**, 704-719.
Gregoire, L. J., A. J. Payne, and P. J. Valdes, 2012: Deglacial rapid sea level rises caused by ice-sheet saddle collapses. *Nature*, **487**, 219-222.
Gregory, J. M., 2000: Vertical heat transports in the ocean and their effect an time-dependent climate change. *Climate Dynamics*, **16**, 501-515.
Gregory, J. M., and P. Huybrechts, 2006: Ice-sheet contributions to future sea level change. *Philosophical Transactions of the Royal Society A: Mathematical, Physical and Engineering Sciences*, **364**, 1709-1732.
Greve, R., F. Saito, and A. Abe-Ouchi, 2011: Initial results of the SeaRISE numerical experiments with the models SICOPOLIS and IcIES for the Greenland ice sheet. *Annals of Glaciology*, **52**, 23-30.
Grützner, J., and S. M. Higgins, 2010: Threshold behavior of millennial scale variability in deep water hydrography inferred from a 1.1 Ma long record of sediment provenance at the southern Gardar Drift. *Paleoceanography*, **25**, PA4204.
Guiot, J., C. Corona, and ESCARSEL members, 2010: Growing Season Temperatures in Europe and Climate Forcings Over the Past 1400 Years. *PLoS ONE*, **5**, E9972.
Haigh, J. D., A. R. Winning, R. Toumi, and J. W. Harder, 2010: An influence of solar spectral variations on radiative forcing of climate. *Nature*, **467**, 696-699.
Hald, M., et al., 2007: Variations in temperature and extent of Atlantic Water in the northern North Atlantic during the Holocene. *Quaternary Science Reviews*, **26**, 3423-3440.
Hall, B. L., T. Koffman, and G. H. Denton, 2010: Reduced ice extent on the western Antarctic Peninsula at 700-970 cal. yr B.P. *Geology*, **38**, 635-638.
Hall, I. R., S. B. Moran, R. Zahn, P. C. Knutz, C. C. Shen, and R. L. Edwards, 2006: Accelerated drawdown of meridional overturning in the late-glacial Atlantic triggered by transient pre-H event freshwater perturbation. *Geophysical Research Letters*, **33**, L16616.
Handorf, D., K. Dethloff, A. G. Marshall, and A. Lynch, 2009: Climate Regime Variability for Past and Present Time Slices Simulated by the Fast Ocean Atmosphere Model. *Journal of Climate*, **22**, 58-70.
Hanebuth, T. J. J., H. K. Voris, Y. Yokoyama, Y. Saito, and J. i. Okuno, 2011: Formation and fate of sedimentary depocentres on Southeast Asia's Sunda Shelf over the past sea level cycle and biogeographic implications. *Earth-Science Reviews*, **104**, 92-110.
Hansen, J., G. Russell, A. Lacis, I. Fung, D. Rind, and P. Stone, 1985: Climate response-times- Dependence on climate sensitivity and ocean mixing. *Science*, **229**, 857-859.
Hansen, J., et al., 2008: Target Atmospheric CO_2: Where Should Humanity Aim? *Open Atmospheric Science Journal*, **2**, 217-231.
Harada, N., M. Sato, and T. Sakamoto, 2008: Freshwater impacts recorded in tetraunsaturated alkenones and alkenone sea surface temperatures from the Okhotsk Sea across millennial-scale cycles. *Paleoceanography*, **23**, PA3201.
Harada, N., K. Kimoto, Y. Okazaki, K. Nagashima, A. Timmermann, and A. Abe-Ouchi, 2009: Millennial time scale changes in surface to intermediate-deep layer circulation recorded in sediment cores from the northwestern North Pacific. *Quaternary Research (Tokyo)*, **48**, 179-194.
Harada, N., et al., 2012: Sea surface temperature changes in the Okhotsk Sea and adjacent North Pacific during the last glacial maximum and deglaciation. *Deep-Sea Research Part II-Topical Studies in Oceanography*, **61-64**, 93-105.
Harden, T. M., J. E. O'Connor, D. G. Driscoll, and J. F. Stamm, 2011: Flood-frequency analyses from paleoflood investigations for Spring, Rapid, Boxelder, and Elk Creeks, Black Hills, western South Dakota, 136 pp.
Harder, J. W., J. M. Fontenla, P. Pilewskie, E. C. Richard, and T. N. Woods, 2009: Trends in solar spectral irradiance variability in the visible and infrared. *Geophysical Research Letters*, **36**, L07801.
Hargreaves, J., A. Abe-Ouchi, and J. Annan, 2007: Linking glacial and future climates through an ensemble of GCM simulations. *Climate of the Past*, **3**, 77-87.
Harmon, R. S., et al., 1983: U-series and amino-acid racemization geochronology of Bermuda: Implications for eustatic sea level fluctuation over the past 250,000 years. *Palaeogeography, Palaeoclimatology, Palaeoecology*, **44**, 41-70.
Harrison, S. P., et al., submitted: Model benchmarking with glacial and mid-Holocene climates. *Science*.
Hawkins, E., R. Smith, L. Allison, J. Gregory, T. Woollings, H. Pohlmann, and B. de Cuevas, 2011: Bistability of the Atlantic overturning circulation in a global climate model and links to ocean freshwater transport. *Geophysical Research Letters*, **38**, L10605.
Haywood, A., et al., submitted: Large-scale features of Pliocene Climate: results from Pliocene Model Intercomparison Project. *Climate of the Past Discussions*, **8**, 2969-3013.
Haywood, A. M., P. J. Valdes, and V. L. Peck, 2007: A permanent El Niño-like state during the Pliocene? *Paleoceanography*, **22**, PA1213.
Hearty, P. J., P. Kindler, H. Cheng, and R. L. Edwards, 1999: A +20 m middle Pleistocene sea level highstand (Bermuda and the Bahamas) due to partial collapse of Antarctic ice. *Geology*, **27**, 375-378.

Hearty, P. J., J. T. Hollin, A. C. Neumann, M. J. O'Leary, and M. McCulloch, 2007: Global sea level fluctuations during the Last Interglaciation (MIS 5e). *Quaternary Science Reviews*, **26**, 2090-2112.
Hegerl, G., T. Crowley, W. Hyde, and D. Frame, 2006: Climate sensitivity constrained by temperature reconstructions over the past seven centuries. *Nature*, **440**, 1029-1032.
Hegerl, G. C., T. J. Crowley, M. Allen, W. T. Hyde, H. N. Pollack, J. Smerdon, and E. Zorita, 2007: Detection of human influence on a new, validated 1500-year temperature reconstruction. *Journal of Climate*, **20**, 650-666.
Helama, S., M. M. Fauria, K. Mielikäinen, M. Timonen, and M. Eronen, 2010: Sub-Milankovitch solar forcing of past climates: Mid and late Holocene perspectives. *Geological Society of America Bulletin*, **122**, 1981-1988.
Helsen, M. M., W. J. van de Berg, R. S. W. van de Wal, M. R. van den Broeke, and J. Oerlemans, submitted: Limited Greenland ice loss during the Eemian. *Nature*.
Hély, C., P. Braconnot, J. Watrin, and W. Zheng, 2009: Climate and vegetation: Simulating the African humid period. *Comptes Rendus Geoscience*, **341**, 671-688.
Henderiks, J., and M. Pagani, 2007: Refining ancient carbon dioxide estimates: Significance of coccolithophore cell size for alkenone-based pCO_2 records. *Paleoceanography*, **22**, PA3202.
Herbert, T. D., L. C. Peterson, K. T. Lawrence, and Z. Liu, 2010: Tropical Ocean Temperatures Over the Past 3.5 Million Years. *Science*, **328**, 1530-1534.
Hereid, K. A., T. M. Quinn, F. W. Taylor, C.-C. Shen, R. L. Edwards, and H. Cheng, in press: Coral record of reduced El Niño activity in the early 15th to middle 17th centur^{y}. *Geology*.
Herget, J., and H. Meurs, 2010: Reconstructing peak discharges for historic flood levels in the city of Cologne, Germany. *Global and Planetary Change*, **70**, 108-116.
Herold, N., Q. Z. Yin, M. P. Karami, and A. Berger, submitted: Modeling the diversity of the warm interglacials. *Climate Dynamics*.
Herrington, A., and C. Poulsen, 2012: Terminating the Last Interglacial: The Role of Ice Sheet-Climate Feedbacks in a GCM Asynchronously Coupled to an Ice Sheet Model. *Journal of Climate*, **25**, 1871-1882.
Herweijer, C., R. Seager, E. R. Cook, and J. Emile-Geay, 2007: North American droughts of the last millennium from a gridded network of tree-ring data. *Journal of Climate*, **20**, 1353-1376.
Heyman, J., A. P. Stroeven, J. M. Harbor, and M. W. Caffee, 2011: Too young or too old: Evaluating cosmogenic exposure dating based on an analysis of compiled boulder exposure ages. *Earth and Planetary Science Letters*, **302**, 71-80.
Higginson, M. J., M. A. Altabet, D. W. Murray, R. W. Murray, and T. D. Herbert, 2004: Geochemical evidence for abrupt changes in relative strength of the Arabian monsoons during a stadial/interstadial climate transition. *Geochimica et Cosmochimica Acta*, **68**, 3807-3826.
Hijma, M. P., and K. M. Cohen, 2010: Timing and magnitude of the sea level jump preluding the 8200 yr event. *Geology*, **38**, 275-278.
Hill, D. J., A. M. Dolan, A. M. Haywood, S. J. Hunter, and D. K. Stoll, 2010: Sensitivity of the Greenland Ice Sheet to Pliocene sea surface temperatures. *Stratigraphy*, **7**, 111 – 122.
Hind, A., and A. Moberg, submitted: Past millennial solar forcing magnitude: a statistical hemispheric-scale climate model vs. proxy data comparison. *Climate Dynamics*.
Hodell, D. A., H. F. Evans, J. E. T. Channell, and J. H. Curtis, 2010: Phase relationships of North Atlantic ice-rafted debris and surface-deep climate proxies during the last glacial period. *Quaternary Science Reviews*, **29**, 3875-3886.
Hodgson, D. A., 2011: First synchronous retreat of ice shelves marks a new phase of polar deglaciation. *Proceedings of the National Academy of Sciences*, **108**, 18859-18860.
Hofer, D., C. Raible, and T. Stocker, 2011: Variations of the Atlantic Meridional circulation in control and transient simulations of the last millennium. *Climate of the Past*, **7**, 133-150.
Holden, P., N. Edwards, K. Oliver, T. Lenton, and R. Wilkinson, 2010a: A probabilistic calibration of climate sensitivity and terrestrial carbon change in GENIE-1. *Climate Dynamics*, **35**, 785-806.
Holden, P. B., N. R. Edwards, E. W. Wolff, N. J. Lang, J. S. Singarayer, P. J. Valdes, and T. F. Stocker, 2010b: Interhemispheric coupling, the West Antarctic Ice Sheet and warm Antarctic interglacials. *Climate of the Past*, **6**, 431-443.
Hollis, C. J., et al., submitted: Southwest Pacific marine temperature variation from late Paleocene to middle Eocene: Revisited. *Earth and Planetary Science Letters*.
Holmes, J. A., E. R. Cook, and B. Yang, 2009: Climate change over the past 2000 years in Western China. *Quaternary International*, **194**, 91-107.
Holz, A., and T. T. Veblen, 2011: Variability in the Southern Annular Mode determines wildfire activity in Patagonia. *Geophysical Research Letters*, **38**, L14710.
Holzhauser, H., M. Magny, and H. J. Zumbuühl, 2005: Glacier and lake-level variations in west-central Europe over the last 3500 years. *The Holocene*, **15**, 789-801.
Hönisch, B., N. G. Hemming, D. Archer, M. Siddall, and J. F. McManus, 2009: Atmospheric Carbon Dioxide Concentration Across the Mid-Pleistocene Transition. *Science*, **324**, 1551-1554.
Horton, B., and R. Edwards, 2006: *Quantifying Holocene sea level change using intertidal foraminifera: lessons from the British Isles*. Vol. 40, 1-97 pp.

Hu, A., et al., 2012: Role of the Bering Strait on the hysteresis of the ocean conveyor belt circulation and glacial climate stability. *Proc. Natl. Acad. Sci. U. S. A.*, **109**, 6417-6422.
Hu, C., G. M. Henderson, J. Huang, S. Xie, Y. Sun, and K. R. Johnson, 2008: Quantification of Holocene Asian monsoon rainfall from spatially separated cave records. *Earth and Planetary Science Letters*, **266**, 221-232.
Huang, C. C., J. Pang, X. Zha, Y. Zhou, H. Su, H. Wan, and B. Ge, 2012: Sedimentary records of extraordinary floods at the ending of the mid-Holocene climatic optimum along the Upper Weihe River, China. *The Holocene*, **22**, 675-686.
Huber, C., et al., 2006: Isotope calibrated Greenland temperature record over Marine Isotope Stage 3 and its relation to CH_4. *Earth and Planetary Science Letters*, **243**, 504-519.
Huber, M., and R. Caballero, 2011: The early Eocene equable climate problem revisited. *Climate of the Past*, **7**, 603-633.
Hughes, A. L. C., E. Rainsley, T. Murray, C. J. Fogwill, C. Schnabel, and S. Xu, 2012: Rapid response of Helheim Glacier, southeast Greenland, to early Holocene climate warming. *Geology*, **40**, 427-430.
Hughes, M., and C. Ammann, 2009: The future of the past—an earth system framework for high resolution paleoclimatology: editorial essay. *Climatic Change*, **94**, 247-259.
Huybers, P., 2006: Early Pleistocene glacial cycles and the integrated summer insolation forcing. *Science*, **313**, 508-511.
IPCC, 2012: Managing the Risks of Extreme Events and Disasters to Advance Climate Change Adaptation. A Special Report of Working Groups I and II of the Intergovernmental Panel on Climate Change. Cambridge University Press, 582 pp.
Israelson, C., and B. Wohlfarth, 1999: Timing of the Last-Interglacial High Sea Level on the Seychelles Islands, Indian Ocean. *Quaternary Research*, **51**, 306-316.
Itambi, A. C., T. von Dobeneck, S. Mulitza, T. Bickert, and D. Heslop, 2009: Millennial-scale northwest African droughts related to Heinrich events and Dansgaard-Oeschger cycles: Evidence in marine sediments from offshore Senegal. *Paleoceanography*, **24**, PA1205.
Ivanochko, T. S., R. S. Ganeshram, G. J. A. Brummer, G. Ganssen, S. J. A. Jung, S. G. Moreton, and D. Kroon, 2005: Variations in tropical convection as an amplifier of global climate change at the millennial scale. *Earth and Planetary Science Letters*, **235**, 302-314.
Jaccard, S., E. Galbraith, D. Sigman, and G. Haug, 2010: A pervasive link between Antarctic ice core and subarctic Pacific sediment records over the past 800 kyrs. *Quaternary Science Reviews*, **29**, 206-212.
Jansen, E., et al., 2007: Palaeoclimate. *Climate Change 2007: The Physical Science Basis. Contribution of Working Group I to the Fourth Assessment Report of the Intergovernmental Panel on Climate Change*, D. Qin, M. Manning, Z. Chen, M. Marquis, K. B. Averyt, M. Tignor, and H. L. Miller, Eds., Cambridge University Press.
Jevrejeva, S., J. C. Moore, A. Grinsted, and P. L. Woodworth, 2008: Recent global sea level acceleration started over 200 years ago? *Geophysical Research Letters*, **35**, L08715.
Joerin, U., K. Nicolussi, A. Fischer, T. Stocker, and C. Schlüchter, 2008: Holocene optimum events inferred from subglacial sediments at Tschierva Glacier, Eastern Swiss Alps. *Quaternary Science Reviews*, **27**, 337-350.
Johns, T. C., et al., 2003: Anthropogenic climate change for 1860 to 2100 simulated with the HadCM3 model under updated emissions scenarios. *Climate Dynamics*, **20**, 583-612.
Jomelli, V., V. Favier, A. Rabatel, D. Brunstein, G. Hoffmann, and B. Francou, 2009: Fluctuations of glaciers in the tropical Andes over the last millennium and palaeoclimatic implications: A review. *Palaeogeography, Palaeoclimatology, Palaeoecology*, **281**, 269-282.
Jones, P. D., et al., 2009: High-resolution palaeoclimatology of the last millennium: a review of current status and future prospects. *The Holocene*, **19**, 3-49.
Joos, F., and R. Spahni, 2008: Rates of change in natural and anthropogenic radiative forcing over the past 20,000 years. *Proceedings of the National Academy of Sciences*, **105**, 1425-1430.
Joshi, M. M., and G. S. Jones, 2009: The climatic effects of the direct injection of water vapour into the stratosphere by large volcanic eruptions. *Atmospheric Chemistry and Physics*, **9**, 6109-6118.
Jouzel, J., et al., 2007: Orbital and millennial Antarctic climate variability over the past 800,000 years. *Science*, **317**, 793-796.
Juckes, M. N., et al., 2007: Millennial temperature reconstruction intercomparison and evaluation. *Climate of the Past*, **3**, 591-609.
Jungclaus, J. H., et al., 2010: Climate and carbon-cycle variability over the last millennium. *Climate of the Past*, **6**, 723-737.
Justino, F., and W. R. Peltier, 2005: The glacial North Atlantic Oscillation. *Geophysical Research Letters*, **32**, L21803.
Justino, F., A. Timmermann, U. Merkel, and E. P. Souza, 2005: Synoptic reorganization of atmospheric flow during the last glacial maximum. *Journal of Climate*, **18**, 2826-2846.
Justwan, A., and N. Koç, 2008: A diatom based transfer function for reconstructing sea ice concentrations in the North Atlantic. *Marine Micropaleontology*, **66**, 264-278.
Kageyama, M., A. Paul, D. M. Roche, and C. J. Van Meerbeeck, 2010: Modelling glacial climatic millennial-scale variability related to changes in the Atlantic meridional overturning circulation: a review. *Quaternary Science Reviews*, **29**, 2931-2956.

Kaiser, J., E. Schefuß, F. Lamy, M. Mohtadi, and D. Hebbeln, 2008: Glacial to Holocene changes in sea surface temperature and coastal vegetation in north central Chile: high versus low latitude forcing. *Quaternary Science Reviews*, **27**, 2064-2075.
Kale, V., 2008: Palaeoflood hydrology in the Indian context. *Journal of the Geological Society of India*, **71**, 56-66.
Kanner, L. C., S. J. Burns, H. Cheng, and R. L. Edwards, 2012: High-Latitude Forcing of the South American Summer Monsoon During the Last Glacial. *Science*, **335**, 570-573.
Kaufman, D. S., et al., 2009: Recent Warming Reverses Long-Term Arctic Cooling. *Science*, **325**, 1236-1239.
Kawamura, K., et al., 2007: Northern Hemisphere forcing of climatic cycles in Antarctica over the past 360,000 years. *Nature*, **448**, 912-916.
Kemp, A. C., B. P. Horton, J. P. Donnelly, M. E. Mann, M. Vermeer, and S. Rahmstorf, 2011: Climate related sea level variations over the past two millennia. *Proceedings of the National Academy of Sciences*, **108**, 11017-11022.
Kemp, A. C., et al., 2009: Timing and magnitude of recent accelerated sea level rise (North Carolina, United States). *Geology*, **37**, 1035-1038.
Kilbourne, K. H., T. M. Quinn, R. Webb, T. Guilderson, J. Nyberg, and A. Winter, 2008: Paleoclimate proxy perspective on Caribbean climate since the year 1751: Evidence of cooler temperatures and multidecadal variability. *Paleoceanography*, **23**, PA3220.
Kim, S. J., et al., 2010: Climate response over Asia/Arctic to change in orbital parameters for the last interglacial maximum. *Geosciences Journal*, **14**, 173-190.
Kinnard, C., C. M. Zdanowicz, R. M. Koerner, and D. A. Fisher, 2008: A changing Arctic seasonal ice zone: Observations from 1870-2003 and possible oceanographic consequences. *Geophysical Research Letters*, **35**, L02507.
Kinnard, C., C. M. Zdanowicz, D. A. Fisher, E. Isaksson, A. de Vernal, and L. G. Thompson, 2011: Reconstructed changes in Arctic sea ice over the past 1,450 years. *Nature*, **479**, 509-512.
Kirkbride, M. P., and S. Winkler, 2012: Correlation of Late Quaternary moraines: impact of climate variability, glacier response, and chronological resolution. *Quaternary Science Reviews*, **46**, 1-29.
Kirshner, A. E., J. B. Anderson, M. Jakobsson, M. O'Regan, W. Majewski, and F. O. Nitsche, 2012: Post-LGM deglaciation in Pine Island Bay, West Antarctica. *Quaternary Science Reviews*, **38**, 11-26.
Kleiven, H. F., E. Jansen, T. Fronval, and T. M. Smith, 2002: Intensification of Northern Hemisphere glaciations in the circum Atlantic region (3.5-2.4 Ma) - ice-rafted detritus evidence. *Palaeogeography Palaeoclimatology Palaeoecology*, **184**, 213-223.
Kleiven, H. F., I. R. Hall, I. N. McCave, G. Knorr, and E. Jansen, 2011: Coupled deep-water flow and climate variability in the middle Pleistocene North Atlantic. *Geology*, **39**, 343-346.
Kleiven, H. F., C. Kissel, C. Laj, U. S. Ninnemann, T. O. Richter, and E. Cortijo, 2008: Reduced North Atlantic Deep Water coeval with the glacial Lake Agassiz freshwater outburst. *Science*, **319**, 60-64.
Klochko, K., A. J. Kaufman, W. Yao, R. H. Byrne, and J. A. Tossell, 2006: Experimental measurement of boron isotope fractionation in seawater. *Earth and Planetary Science Letters*, **248**, 276-285.
Knight, J. R., R. J. Allan, C. K. Folland, M. Vellinga, and M. E. Mann, 2005: A signature of persistent natural thermohaline circulation cycles in observed climate. *Geophysical Research Letters*, **32**, L20708.
Knox, J. C., 2000: Sensitivity of modern and Holocene floods to climate change. *Quaternary Science Reviews*, **19**, 439-457.
Knudsen, M. F., M.-S. Seidenkrantz, B. H. Jacobsen, and A. Kuijpers, 2011: Tracking the Atlantic Multidecadal Oscillation through the last 8,000 years. *Nature Communications*, **2**, 178.
Kobashi, T., J. P. Severinghaus, J. M. Barnola, K. Kawamura, T. Carter, and T. Nakaegawa, 2010: Persistent multi-decadal Greenland temperature fluctuation through the last millennium. *Climatic Change*, **100**, 733-756.
Kobashi, T., et al., 2011: High variability of Greenland surface temperature over the past 4000 years estimated from trapped air in an ice core. *Geophysical Research Letters*, **38**, L21501.
Koch, J., and J. Clague, 2011: Extensive glaciers in northwest North America during Medieval time. *Climatic Change*, **107**, 593-613.
Koenig, S., R. DeConto, and D. Pollard, 2011: Late Pliocene to Pleistocene sensitivity of the Greenland Ice Sheet in response to external forcing and internal feedbacks. *Climate Dynamics*, **37**, 1247-1268.
Köhler, P., G. Knorr, D. Buiron, A. Lourantou, and J. Chappellaz, 2011: Abrupt rise in atmospheric CO_2 at the onset of the Bølling/Allerød: in-situ ice core data versus true atmospheric signals. *Climate of the Past*, **7**, 473-486.
Köhler, P., R. Bintanja, H. Fischer, F. Joos, R. Knutti, G. Lohmann, and V. Masson-Delmotte, 2010: What caused Earth's temperature variations during the last 800,000 years? Data-based evidence on radiative forcing and constraints on climate sensitivity. *Quaternary Science Reviews*, **29**, 129-145.
Kopp, G., and J. L. Lean, 2011: A new, lower value of total solar irradiance: Evidence and climate significance. *Geophysical Research Letters*, **38**, L01706.
Kopp, R. E., F. J. Simons, J. X. Mitrovica, A. C. Maloof, and M. Oppenheimer, 2009: Probabilistic assessment of sea level during the last interglacial stage. *Nature*, **462**, 863-867.
Koutavas, A., and J. P. Sachs, 2008: Northern timing of deglaciation in the eastern equatorial Pacific from alkenone paleothermometry. *Paleoceanography*, **23**, PA4205.

Koutavas, A., P. B. Demenocal, G. C. Olive, and J. Lynch-Stieglitz, 2006: Mid-Holocene El Niño-Southern Oscillation (ENSO) attenuation revealed by individual foraminifera in eastern tropical Pacific sediments. *Geology*, **34**, 993-996.

Kravitz, B., and A. Robock, 2011: Climate effects of high-latitude volcanic eruptions: Role of the time of year. *Journal of Geophysical Research*, **116**, D01105.

Krebs, U., and A. Timmermann, 2007: Tropical air-sea interactions accelerate the recovery of the Atlantic Meridional Overturning Circulation after a major shutdown. *Journal of Climate*, **20**, 4940-4956.

Kriegler, E., J. W. Hall, H. Held, R. Dawson, and H. J. Schellnhuber, 2009: Imprecise probability assessment of tipping points in the climate system. *Proc. Natl. Acad. Sci. U. S. A.*, **106**, 5041-5046.

Krivova, N., and S. Solanki, 2008: Models of solar irradiance variations: Current status. *Journal of Astrophysics and Astronomy*, **29**, 151-158.

Krivova, N., L. Balmaceda, and S. Solanki, 2007: Reconstruction of solar total irradiance since 1700 from the surface magnetic flux. *Astronomy & Astrophysics*, **467**, 335-346.

Krivova, N., S. Solanki, and Y. Unruh, 2011: Towards a long-term record of solar total and spectral irradiance. *Journal of Atmospheric and Solar-Terrestrial Physics*, **73**, 223-234.

Küttel, M., et al., 2010: The importance of ship log data: reconstructing North Atlantic, European and Mediterranean sea level pressure fields back to 1750. *Climate Dynamics*, **34**, 1115-1128.

Kutzbach, J. E., X. D. Liu, Z. Y. Liu, and G. S. Chen, 2008: Simulation of the evolutionary response of global summer monsoons to orbital forcing over the past 280,000 years. *Climate Dynamics*, **30**, 567-579.

Kutzbach, J. E., S. J. Vavrus, W. F. Ruddiman, and G. Philippon-Berthier, 2011: Comparisons of atmosphere–ocean simulations of greenhouse gas-induced climate change for pre-industrial and hypothetical 'no-anthropogenic' radiative forcing, relative to present day. *The Holocene*, **21**, 793-801.

Laborel, J., C. Morhange, R. Lafont, J. Le Campion, F. Laborel-Deguen, and S. Sartoretto, 1994: Biological evidence of sea level rise during the last 4500 years on the rocky coasts of continental southwestern France and Corsica. *Marine Geology*, **120**, 203-223.

Lambeck, K., and M. Nakada, 1992: Constraints on the age and duration of the last interglacial period and on sea level variations. *Nature*, **357**, 125-128.

Lambeck, K., and E. Bard, 2000: Sea level change along the French Mediterranean coast for the past 30 000 years. *Earth and Planetary Science Letters*, **175**, 203-222.

Lambeck, K., T. Esat, and E. Potter, 2002a: Links between climate and sea levels for the past three million years. *Nature*, **419**, 199-206.

Lambeck, K., Y. Yokoyama, and T. Purcell, 2002b: Into and out of the Last Glacial Maximum: sea level change during Oxygen Isotope Stages 3 and 2. *Quaternary Science Reviews*, **21**, 343-360.

Lambeck, K., A. Purcell, and A. Dutton, 2012: The anatomy of interglacial sea levels: The relationship between sea levels and ice volumes during the Last Interglacial. *Earth and Planetary Science Letters*, **315–316**, 4-11.

Lambeck, K., A. Purcell, J. Zhao, and N.-O. Svensson, 2010a: The Scandinavian Ice Sheet: from MIS 4 to the end of the Last Glacial Maximum. *Boreas*, **39**, 410-435.

Lambeck, K., M. Anzidei, F. Antonioli, A. Benini, and A. Esposito, 2004: Sea level in Roman time in the Central Mediterranean and implications for recent change. *Earth and Planetary Science Letters*, **224**, 563-575.

Lambeck, K., A. Purcell, S. Funder, K. H. KjæR, E. Larsen, and P. E. R. Moller, 2006: Constraints on the Late Saalian to early Middle Weichselian ice sheet of Eurasia from field data and rebound modelling. *Boreas*, **35**, 539-575.

Lambeck, K., C. D. Woodroffe, F. Antonioli, M. Anzidei, W. R. Gehrels, J. Laborel, and A. J. Wright, 2010b: Paleoenvironmental records, geophysical modelling, and reconstruction of sea level trends and variability on centennial and Longer Timescales. *Understanding sea level rise and variability*, J. A. Church, P. L. Woodworth, T. Aarup, and W. S. Wilson, Eds., Wiley-Blackwell, 61-121.

Lambert, F., et al., submitted: The role of mineral dust aerosols in polar amplification. *Nature Climate Change*.

Lambert, F., et al., 2008: Dust-climate couplings over the past 800,000 years from the EPICA Dome C ice core. *Nature*, **452**, 616-619.

Lamy, F., R. Kilian, H. W. Arz, J. P. François, J. Kaiser, M. Prange, and T. Steinke, 2010: Holocene changes in the position and intensity of the southern westerly wind belt. *Nature Geoscience*, **3**, 695-699.

Lanciki, A., J. Cole-Dai, M. H. Thiemens, and J. Savarino, 2012: Sulfur isotope evidence of little or no stratospheric impact by the 1783 Laki volcanic eruption. *Geophysical Research Letters*, **39**, L01806.

Landais, A., et al., 2004: A continuous record of temperature evolution over a sequence of Dansgaard-Oeschger events during Marine Isotopic Stage 4 (76 to 62 kyr BP). *Geophysical Research Letters*, **31**, L22211.

Landrum, L., B. Otto-Bliesner, E. Wahl, A. Conley, P. Lawrence, and H. Teng, submitted: Last Millennium Climate and Its Variability in CCSM4. *Journal of Climate*.

Lang, N., and E. W. Wolff, 2011: Interglacial and glacial variability from the last 800 ka in marine, ice and terrestrial archives. *Climate of the Past*, **7**, 361-380.

Langebroek, P., A. Paul, and M. Schulz, 2009: Antarctic ice-sheet response to atmospheric CO_2 and insolation in the Middle Miocene. *Climate of the Past*, **5**, 633-646.

Lara, A., R. Villalba, and R. Urrutia, 2008: A 400-year tree-ring record of the Puelo River summer–fall streamflow in the Valdivian Rainforest eco-region, Chile. *Climatic Change*, **86**, 331-356.

Larocque-Tobler, I., M. Grosjean, O. Heiri, M. Trachsel, and C. Kamenik, 2010: Thousand years of climate change reconstructed from chironomid subfossils preserved in varved lake Silvaplana, Engadine, Switzerland. *Quaternary Science Reviews*, **29**, 1940-1949.

Larocque-Tobler, I., M. M. Stewart, R. Quinlan, M. Trachsel, C. Kamenik, and M. Grosjean, 2012: A last millennium temperature reconstruction using chironomids preserved in sediments of anoxic Seebergsee (Switzerland): consensus at local, regional and Central European scales. *Quaternary Science Reviews*, **41**, 49-56.

Larsen, N. K., K. H. Kjær, J. Olsen, S. Funder, K. K. Kjeldsen, and N. Nørgaard-Pedersen, 2011: Restricted impact of Holocene climate variations on the southern Greenland Ice Sheet. *Quaternary Science Reviews*, **30**, 3171-3180.

Laskar, J., P. Robutel, F. Joutel, M. Gastineau, A. Correia, and B. Levrard, 2004: A long-term numerical solution for the insolation quantities of the Earth. *Astronomy & Astrophysics*, **428**, 261-285.

Lea, D. W., D. K. Pak, and H. J. Spero, 2000: Climate Impact of Late Quaternary Equatorial Pacific Sea Surface Temperature Variations. *Science*, **289**, 1719-1724.

Lea, D. W., D. K. Pak, C. L. Belanger, H. J. Spero, M. A. Hall, and N. J. Shackleton, 2006: Paleoclimate history of Galápagos surface waters over the last 135,000 yr. *Quaternary Science Reviews*, **25**, 1152-1167.

Lean, J., J. Beer, and R. Bradley, 1995a: Reconstruction of solar irradiance since 1610: Implications for climate change. *Geophysical Research Letters*, **22**, 3195-3198.

Lean, J., T. Woods, F. Eparvier, R. Meier, D. Strickland, J. Correira, and J. Evans, 2011: Solar extreme ultraviolet irradiance: Present, past, and future. *Journal of Geophysical Research-Space Physics*, **116**, A01102.

Lean, J. L., 2010: Cycles and trends in solar irradiance and climate. *Wiley Interdisciplinary Reviews-Climate Change*, **1**, 111-122.

Lean, J. L., O. R. White, and A. Skumanich, 1995b: On the Solar Ultraviolet Spectral Irradiance During the Maunder Minimum. *Global Biogeochemical Cycles*, **9**, 171-182.

Lecavalier, B. t. S., G. A. Milne , B. M. Vinther, D. A. Fisher, A. S. Dyke, and M. J. R. Simpson, submitted: Revised estimates of Greenland ice sheet thinning histories based on ice-core records. *Quaternary Science Review*.

Leclercq, P., and J. Oerlemans, 2012: Global and hemispheric temperature reconstruction from glacier length fluctuations. *Climate Dynamics*. doi:10.1007/s00382-011-1145-7, advance online publication.

Leclercq, P. W., and J. Oerlemans, 2011: Global and Hemispheric temperature reconstruction from glacier length fluctuations. *Climate Dynamics*, **38**, 1065-1079.

Leduc, G., R. Schneider, J. H. Kim, and G. Lohmann, 2010: Holocene and Eemian sea surface temperature trends as revealed by alkenone and Mg/Ca paleothermometry. *Quaternary Science Reviews*, **29**, 989-1004.

Leduc, G., L. Vidal, K. Tachikawa, F. Rostek, C. Sonzogni, L. Beaufort, and E. Bard, 2007: Moisture transport across Central America as a positive feedback on abrupt climatic changes. *Nature*, **445**, 908-911.

Lee, T., F. Zwiers, and M. Tsao, 2008: Evaluation of proxy-based millennial reconstruction methods. *Climate Dynamics*, **31**, 263-281.

LeGrande, A. N., and G. A. Schmidt, 2008: Ensemble, water isotope-enabled, coupled general circulation modeling insights into the 8.2 ka event. *Paleoceanography*, **23**, PA3207.

LeGrande, A. N., et al., 2006: Consistent simulation of multiple proxy responses to an abrupt climate change event (vol 103, pg 837, 2006). *Proc. Natl. Acad. Sci. U. S. A.*, **103**, 10527-10527.

Lehner, F., C. C. Raible, and T. F. Stocker, 2012: Testing the robustness of a precipitation proxy-based North Atlantic Oscillation reconstruction. *Quaternary Science Reviews*, **45**, 85-94.

Lemieux-Dudon, B., et al., 2010: Consistent dating for Antarctic and Greenland ice cores. *Quaternary Science Reviews*, **29**, 8-20.

Leorri, E., B. P. Horton, and A. Cearreta, 2008: Development of a foraminifera-based transfer function in the Basque marshes, N. Spain: Implications for sea level studies in the Bay of Biscay. *Marine Geology*, **251**, 60-74.

Lewis, S. C., A. N. LeGrande, M. Kelley, and G. A. Schmidt, 2010: Water vapour source impacts on oxygen isotope variability in tropical precipitation during Heinrich events. *Climate of the Past*, **6**, 325-343.

Li, B., D. W. Nychka, and C. M. Ammann, 2010a: The Value of Multiproxy Reconstruction of Past Climate. *Journal of the American Statistical Association*, **105**, 883-895.

Li, C., and D. S. Battisti, 2008: Reduced Atlantic storminess during last glacial maximum: Evidence from a coupled climate model. *Journal of Climate*, **21**, 3561-3579.

Li, C., D. S. Battisti, and C. M. Bitz, 2010b: Can North Atlantic Sea Ice Anomalies Account for Dansgaard-Oeschger Climate Signals? *Journal of Climate*, **23**, 5457-5475.

Li, J., et al., 2011: Interdecadal modulation of El Niño amplitude during the past millennium. *Nature Climate Change*, **1**, 114-118.

Li, Y., H. Renssen, A. Wiersma, and T. Törnqvist, 2009: Investigating the impact of Lake Agassiz drainage routes on the 8.2 ka cold event with a climate model. *Climate of the Past*, **5**, 471-480.

Licciardi, J. M., J. M. Schaefer, J. R. Taggart, and D. C. Lund, 2009: Holocene Glacier Fluctuations in the Peruvian Andes Indicate Northern Climate Linkages. *Science*, **325**, 1677-1679.

Linderholm, H., et al., 2010: Dendroclimatology in Fennoscandia - from past accomplishments to future potential. *Climate of the Past*, **5**, 1415-1462.

Linderholm, H. W., and P. Jansson, 2007: Proxy data reconstructions of the Storglaciaren (Sweden) mass-balance record back to AD 1500 on annual to decadal timescales. *Annals of Glaciology*, **46**, 261-267.

Linsley, B. K., Y. Rosenthal, and D. W. Oppo, 2010: Holocene evolution of the Indonesian throughflow and the western Pacific warm pool. *Nature Geoscience*, **3**, 578-583.
Linsley, B. K., P. P. Zhang, A. Kaplan, S. S. Howe, and G. M. Wellington, 2008: Interdecadal-decadal climate variability from multicoral oxygen isotope records in the South Pacific Convergence Zone region since 1650 A.D. *Paleoceanography*, **23**, PA2219.
Lisiecki, L., and M. Raymo, 2005: A Pliocene-Pleistocene stack of 57 globally distributed benthic $\delta^{18}O$ records. *Paleoceanography*, **20**, PA1003.
Lisiecki, L. E., M. E. Raymo, and W. B. Curry, 2008: Atlantic overturning responses to Late Pleistocene climate forcings. *Nature*, **456**, 85-88.
Liu, J., B. Wang, Q. Ding, X. Kuang, W. Soon, and E. Zorita, 2009a: Centennial Variations of the Global Monsoon Precipitation in the Last Millennium: Results from ECHO-G Model. *Journal of Climate*, **22**, 2356-2371.
Liu, X. D., Z. Y. Liu, S. Clemens, W. Prell, and J. Kutzbach, 2007a: A coupled model study of glacial Asian monsoon variability and Indian ocean dipole. *Journal of the Meteorological Society of Japan*, **85**, 1-10.
Liu, Z., et al., 2007b: Simulating the transient evolution and abrupt change of Northern Africa atmosphere-ocean-terrestrial ecosystem in the Holocene. *Quaternary Science Reviews*, **26**, 1818-1837.
Liu, Z., et al., 2009b: Transient Simulation of Last Deglaciation with a New Mechanism for Bølling-Allerød Warming. *Science*, **325**, 310-314.
Ljungqvist, F. C., 2010: A new reconstruction of temperature variability in the extra-tropical Northern Hemisphere during the last two millennia. *Geografiska Annaler: Series A, Physical Geography*, **92**, 339–351.
Ljungqvist, F. C., P. J. Krusic, G. Brattström, and H. S. Sundqvist, 2012: Northern Hemisphere temperature patterns in the last 12 centuries. *Climate of the Past*, **8**, 227-249.
Lloyd, A. H., and A. G. Bunn, 2007: Responses of the circumpolar boreal forest to 20th century climate variability. *Environmental Research Letters*, **2**, 045013.
Loeb, N. G., et al., 2009: Toward Optimal Closure of the Earth's Top-of-Atmosphere Radiation Budget. *Journal of Climate*, **22**, 748-766.
Loehle, C., and J. H. McCulloch, 2008: Correction to: A 2000-Year Global Temperature Reconstruction Based on Non-Tree Ring Proxies. *Energy & Environment*, **19**, 93-100.
Lohmann, G., M. Pfeiffer, T. Laepple, G. Leduc, and J. H. Kim, submitted: A model-data comparison of the Holocene global sea surface temperature evolution. *Climate of the Past Discussion*, **8**, 1005-1056.
Long, A. J., S. A. Woodroffe, G. A. Milne, C. L. Bryant, M. J. R. Simpson, and L. M. Wake, 2012: Relative sea level change in Greenland during the last 700-yrs and ice sheet response to the Little Ice Age. *Earth and Planetary Science Letters*, **315-316**, 76-85.
Loso, M., 2009: Summer temperatures during the Medieval Warm Period and Little Ice Age inferred from varved proglacial lake sediments in southern Alaska. *Journal of Paleolimnology*, **41**, 117-128.
Lough, J. M., 2011: Great Barrier Reef coral luminescence reveals rainfall variability over northeastern Australia since the 17th century. *Paleoceanography*, **26**, PA2201.
Loulergue, L., et al., 2008: Orbital and millennial-scale features of atmospheric CH_4 over the past 800,000 years. *Nature*, **453**, 383-386.
Lourantou, A., J. Chappellaz, J. Barnola, V. Masson-Delmotte, and D. Raynaud, 2010a: Changes in atmospheric CO_2 and its carbon isotopic ratio during the penultimate deglaciation. *Quaternary Science Reviews*, **29**, 1983-1992.
Lourantou, A., et al., 2010b: Constraint of the CO_2 rise by new atmospheric carbon isotopic measurements during the last deglaciation. *Global Biogeochemical Cycles*, **24**, GB2015.
Loutre, M., and A. Berger, 2000: Future climatic changes: Are we entering an exceptionally long interglacial? *Climatic Change*, **46**, 61-90.
Lowenstein, T. K., and R. V. Demicco, 2006: Elevated Eocene Atmospheric CO_2 and Its Subsequent Decline. *Science*, **313**, 1928-1928.
Lu, J., and M. Cai, 2009: Seasonality of polar surface warming amplification in climate simulations. *Geophysical Research Letters*, **36**, L16704.
Lu, R., B. Dong, and H. Ding, 2006: Impact of the Atlantic multidecadal oscillation on the Asian summer monsoon. *Geophysical Research Letters*, **33**, L24701.
Luckman, B., and R. Villalba, 2001: Assessing the synchroneity of glacier fluctuations in the western Cordillera of the Americas during the last millenium. *Interhemispheric climate linkages*, V. Markgraf, Ed., Academic Press, 119-140.
Luckman, B. H., and R. J. S. Wilson, 2005: Summer temperatures in the Canadian Rockies during the last millennium: a revised record. *Climate Dynamics*, **24**, 131-144.
Lü, J. M., S. J. Kim, A. Abe-Ouchi, Y. Q. Yu, and R. Ohgaito, 2010: Arctic Oscillation during the Mid-Holocene and Last Glacial Maximum from PMIP2 Coupled Model Simulations. *Journal of Climate*, **23**, 3792-3813.
Lüthi, D., et al., 2008: High-resolution carbon dioxide concentration record 650,000-800,000 years before present. *Nature*, **453**, 379-382.
Lunt, submitted: A multi-model assessment of last Interglaciation temperatures. *Climate of the Past Discussions*.
Lunt, D. J., G. L. Foster, A. M. Haywood, and E. J. Stone, 2008: Late Pliocene Greenland glaciation controlled by a decline in atmospheric CO_2 levels. *Nature*, **454**, 1102-1105.

Lunt, D. J., A. M. Haywood, G. A. Schmidt, U. Salzmann, P. J. Valdes, and H. J. Dowsett, 2010: Earth system sensitivity inferred from Pliocene modelling and data. *Nature Geoscience*, **3**, 60-64.

Lunt, D. J., A. M. Haywood, G. A. Schmidt, U. Salzmann, P. J. Valdes, H. J. Dowsett, and C. A. Loptson, 2012: On the causes of mid-Pliocene warmth and polar amplification. *Earth and Planetary Science Letters*, **321–322**, 128-138.

Luo, F. F., S. L. Li, and T. Furevik, 2011: The connection between the Atlantic Multidecadal Oscillation and the Indian Summer Monsoon in Bergen Climate Model Version 2.0. *Journal of Geophysical Research-Atmospheres*, **116**, D19117.

Luterbacher, J., et al., 2002: Reconstruction of sea level pressure fields over the Eastern North Atlantic and Europe back to 1500. *Climate Dynamics*, **18**, 545-561.

Luterbacher, J., et al., 2012: A review of 2000 years of paleoclimatic evidence in the Mediterranean. *The Climate of the Mediterranean region: from the past to the future*, P. Lionello, Ed., Elsevier, 87-185.

MacDonald, G., D. Porinchu, N. Rolland, K. Kremenetsky, and D. Kaufman, 2009: Paleolimnological evidence of the response of the central Canadian treeline zone to radiative forcing and hemispheric patterns of temperature change over the past 2000 years. *Journal of Paleolimnology*, **41**, 129-141.

Macdonald, N., 2007: On Epigraphic Records: A Valuable Resource in Reassessing Flood Risk and Long-Term Climate Variability. *Environmental History*, **12**, 136-140.

Macdonald, N., and A. R. Black, 2010: Reassessment of flood frequency using historical information for the River Ouse at York, UK (1200-2000). *Hydrological Science Journal*, **55**, 1152-1162.

MacFarling Meure, C., et al., 2006: Law Dome CO_2, CH_4 and N_2O ice core records extended to 2000 years BP. *Geophysical Research Letters*, **10**, L14810.

Machado, M. J., G. Benito, M. Barriendos, and F. S. Rodrigo, 2011: 500 Years of rainfall variability and extreme hydrological events in southeastern Spain drylands. *Journal of Arid Environments*, **75**, 1244-1253.

Macias Fauria, M., et al., 2010: Unprecedented low twentieth century winter sea ice extent in the Western Nordic Seas since AD 1200. *Climate Dynamics*, **34**, 781-795.

Mackintosh, A., et al., 2011: Retreat of the East Antarctic ice sheet during the last glacial termination. *Nature Geoscience*, **4**, 195-202.

Macklin, M. G., et al., 2006: Past hydrological events reflected in the Holocene fluvial record of Europe. *Catena*, **66**, 145-154.

Maher, B. A., J. M. Prospero, D. Mackie, D. Gaiero, P. P. Hesse, and Y. Balkanski, 2010: Global connections between aeolian dust, climate and ocean biogeochemistry at the present day and at the last glacial maximum. *Earth-Science Reviews*, **99**, 61-97.

Mahowald, N., S. Albani, S. Engelstaedter, G. Winckler, and M. Goman, 2011: Model insight into glacial–interglacial paleodust records. *Quaternary Science Reviews*, **30**, 832-854.

Mahowald, N. M., M. Yoshioka, W. D. Collins, A. J. Conley, D. W. Fillmore, and D. B. Coleman, 2006: Climate response and radiative forcing from mineral aerosols during the last glacial maximum, pre-industrial, current and doubled-carbon dioxide climates. *Geophysical Research Letters*, **33**, L20705.

Mann, M., R. Bradley, and M. Hughes, 1998: Global-scale temperature patterns and climate forcing over the past six centuries. *Nature*, **392**, 779-787.

——, 1999: Northern hemisphere temperatures during the past millennium: Inferences, uncertainties, and limitations. *Geophysical Research Letters*, **26**, 759-762.

Mann, M., S. Rutherford, E. Wahl, and C. Ammann, 2007: Robustness of proxy-based climate field reconstruction methods. *Journal of Geophysical Research-Atmospheres*, **112**, D12109.

Mann, M. E., J. D. Fuentes, and S. Rutherford, 2012: Underestimation of volcanic cooling in tree-ring-based reconstructions of hemispheric temperatures. *Nature Geoscience*, **advance online publication**.

Mann, M. E., M. A. Cane, S. E. Zebiak, and A. Clement, 2005: Volcanic and solar forcing of the tropical Pacific over the past 1000 years. *Journal of Climate*, **18**, 447-456.

Mann, M. E., Z. H. Zhang, M. K. Hughes, R. S. Bradley, S. K. Miller, S. Rutherford, and F. B. Ni, 2008: Proxy-based reconstructions of hemispheric and global surface temperature variations over the past two millennia. *Proc. Natl. Acad. Sci. U. S. A.*, **105**, 13252-13257.

Mann, M. E., et al., 2009: Global Signatures and Dynamical Origins of the Little Ice Age and Medieval Climate Anomaly. *Science*, **326**, 1256-1260.

Marchitto, T., R. Muscheler, J. Ortiz, J. Carriquiry, and A. van Geen, 2010: Dynamical Response of the Tropical Pacific Ocean to Solar Forcing During the Early Holocene. *Science*, **330**, 1378-1381.

Marcott, S., et al., 2011: Ice-shelf collapse from subsurface warming as a trigger for Heinrich events. *Proc. Natl. Acad. Sci. U. S. A.*, **108**, 13415-13419.

Margari, V., L. C. Skinner, P. C. Tzedakis, A. Ganopolski, M. Vautravers, and N. J. Shackleton, 2010: The nature of millennial-scale climate variability during the past two glacial periods. *Nature Geoscience*, **3**, 127-131.

MARGO Project Members, 2009: Constraints on the magnitude and patterns of ocean cooling at the Last Glacial Maximum. *Nature Geoscience*, **2**, 127-132.

Marland, G., T. A. Boden, and R. J. Andres, 2003: Global, Regional, and National Fossil-Fuel CO_2 Emissions. O. R. N. L. Carbon Dioxide Information Analysis Center, U.S. Department of Energy, Ed.

Marshall, S. J., and M. R. Koutnik, 2006: Ice sheet action versus reaction: Distinguishing between Heinrich events and Dansgaard-Oeschger cycles in the North Atlantic. *Paleoceanography*, **21**, PA2021.

Martinez-Garcia, A., A. Rosell-Mele, S. L. Jaccard, W. Geibert, D. M. Sigman, and G. H. Haug, 2011: Southern Ocean dust-climate coupling over the past four million years. *Nature*, **476**, 312-315.

Martrat, B., J. O. Grimalt, N. J. Shackleton, L. de Abreu, M. A. Hutterli, and T. F. Stocker, 2007: Four climate cycles of recurring deep and surface water destabilizations on the Iberian margin. *Science*, **317**, 502-507.

Marzeion, B., and A. Nesje, 2012: Spatial patterns of North Atlantic Oscillation influence on mass balance variability of European glaciers. *The Cryosphere*, **6**, 661-673.

Masson-Delmotte, V., et al., 2011: Sensitivity of interglacial Greenland temperature and $\delta^{18}O$: ice core data, orbital and increased CO_2 climate simulations. *Climate of the Past*, **7**, 1041-1059.

Masson-Delmotte, V., et al., 2010a: EPICA Dome C record of glacial and interglacial intensities. *Quaternary Science Reviews*, **29**, 113-128.

Masson-Delmotte, V., et al., 2010b: Abrupt change of Antarctic moisture origin at the end of Termination II. *Proc. Natl. Acad. Sci. U. S. A.*, **107**, 12091-12094.

Masson-Delmotte, V., et al., 2008: A review of Antarctic surface snow isotopic composition: Observations, atmospheric circulation, and isotopic modeling. *Journal of Climate*, **21**, 3359-3387.

Matthews, J. A., and P. Q. Dresser, 2008: Holocene glacier variation chronology of the Smørstabbtindan massif, Jotunheimen, southern Norway, and the recognition of century- to millennial-scale European Neoglacial Events. *The Holocene*, **18**, 181-201.

McCarroll, D., et al., submitted: A 1200-year multi-proxy record of tree growth and summer temperature at the northern pine forest limit of Europe. *The Holocene*.

McGee, D., W. S. Broecker, and G. Winckler, 2010: Gustiness: The driver of glacial dustiness? *Quaternary Science Reviews*, **29**, 2340-2350.

McGregor, S., and A. Timmermann, 2010: The Effect of Explosive Tropical Volcanism on ENSO. *Journal of Climate*, **24**, 2178-2191.

McGregor, S., A. Timmermann, and O. Timm, 2010: A unified proxy for ENSO and PDO variability since 1650. *Climate of the Past*, **6**, 1-17.

McKay, N. P., D. S. Kaufman, and N. Michelutti, 2008: Biogenic silica concentration as a high-resolution, quantitative temperature proxy at Hallet Lake, south-central Alaska. *Geophysical Research Letters*, **35**, L05709.

McKay, N. P., J. T. Overpeck, and B. L. Otto-Bliesner, 2011: The role of ocean thermal expansion in Last Interglacial sea level rise. *Geophysical Research Letters*, **38**, L14605.

McKay, R., et al., 2012: Antarctic and Southern Ocean influences on Late Pliocene global cooling. *Proceedings of the National Academy of Sciences*.

McManus, J., R. Francois, J. Gherardi, L. Keigwin, and S. Brown-Leger, 2004: Collapse and rapid resumption of Atlantic meridional circulation linked to deglacial climate changes. *Nature*, **428**, 834-837.

McMurtry, G. M., D. R. Tappin, P. N. Sedwick, I. Wilkinson, J. Fietzke, and B. Sellwood, 2007: Elevated marine deposits in Bermuda record a late Quaternary megatsunami. *Sedimentary Geology*, **200**, 155-165.

McShane, B. B., and A. J. Wyner, 2011: A statistical analysis of multiple temperature proxies: are reconstructions of surface temperatures over the last 1000 years reliable? *Annals of Applied Statistics*, **5**, 5-44.

Meckler, A. N., M. O. Clarkson, K. M. Cobb, H. Sodemann, and J. F. Adkins, 2012: Interglacial Hydroclimate in the Tropical West Pacific Through the Late Pleistocene. *Science*. advance online publication.

Meehl, G. A., J. M. Arblaster, K. Matthes, F. Sassi, and H. van Loon, 2009: Amplifying the Pacific Climate System Response to a Small 11-Year Solar Cycle Forcing. *Science*, **325**, 1114-1118.

Meko, D. M., C. A. Woodhouse, C. A. Baisan, T. Knight, J. J. Lukas, M. K. Hughes, and M. W. Salzer, 2007: Medieval drought in the upper Colorado River Basin. *Geophysical Research Letters*, **34**, L10705.

Melles, M., et al., 2012: 2.8 Million Years of Arctic Climate Change from Lake El'gygytgyn, NE Russia. *Science*, **337**, 315-320.

Melvin, T., H. Grudd, and K. Briffa, accepted: Potential bias in "updating" tree-ring chronologies using Regional Curve Standardisation: re-processing the Torneträsk tree-ring data. *The Holocene*.

Menounos, B., G. Osborn, J. Clague, and B. Luckman, 2009: Latest Pleistocene and Holocene glacier fluctuations in western Canada. *Quaternary Science Reviews*, **28**, 2049-2074.

Menviel, L., A. Timmermann, O. E. Timm, and A. Mouchet, 2011: Deconstructing the Last Glacial termination: the role of millennial and orbital-scale forcings. *Quaternary Science Reviews*, **30**, 1155-1172.

Merkel, U., M. Prange, and M. Schulz, 2010: ENSO variability and teleconnections during glacial climates. *Quaternary Science Reviews*, **29**, 86-100.

Miller, K. G., et al., 2012: High tide of the warm Pliocene: Implications of global sea level for Antarctic deglaciation. *Geology*. advance online publication.

Millet, L., F. Arnaud, O. Heiri, M. Magny, V. Verneaux, and M. Desmet, 2009: Late-Holocene summer temperature reconstruction from chironomid assemblages of Lake Anterne, northern French Alps. *The Holocene*, **19**, 317-328.

Milne, G., and J. Mitrovica, 2008: Searching for eustasy in deglacial sea level histories. *Quaternary Science Reviews*, **27**, 2292-2302.

Mischler, J. A., et al., 2009: Carbon and hydrogen isotopic composition of methane over the last 1000 years. *Global Biogeochemical Cycles*, **23**, GB4024.

Moberg, A., 2012: Comments on "Reconstruction of the extra-tropical NH mean temperature over the last millennium with a method that preserves low-frequency variability". *Journal of Climate*. doi:10.1175/JCLI-D-11-00404.1, advance online publication.
Moberg, A., D. M. Sonechkin, K. Holmgren, N. M. Datsenko, and W. Karlén, 2005: Highly variable Northern Hemisphere temperatures reconstructed from low- and high-resolution proxy data. *Nature*, **433**, 613-617.
Mohtadi, M., D. W. Oppo, S. Steinke, J.-B. W. Stuut, R. De Pol-Holz, D. Hebbeln, and A. Lückge, 2011: Glacial to Holocene swings of the Australian-Indonesian monsoon. *Nature Geoscience*, **4**, 540-544.
Monnin, E., et al., 2001: Atmospheric CO_2 concentrations over the last glacial termination. *Science*, **291**, 112-114.
Moore, J. C., E. Beaudon, S. Kang, D. Divine, E. Isaksson, V. A. Pohjola, and R. S. W. van de Wal, 2012: Statistical extraction of volcanic sulphate from nonpolar ice cores. *Journal of Geophysical Research*, **117**, D03306.
Morales, M. S., et al., 2012: Precipitation changes in the South American Altiplano since 1300 AD reconstructed by tree-rings. *Climate of the Past*, **8**, 653-666.
Moros, M., J. T. Andrews, D. D. Eberl, and E. Jansen, 2006: Holocene history of drift ice in the northern North Atlantic: Evidence for different spatial and temporal modes. *Paleoceanography*, **21**, PA2017.
Moros, M., P. De Deckker, E. Jansen, K. Perner, and R. J. Telford, 2009: Holocene climate variability in the Southern Ocean recorded in a deep-sea sediment core off South Australia. *Quaternary Science Reviews*, **28**, 1932-1940.
Morrill, C., A. J. Wagner, B. L. Otto-Bliesner, and N. Rosenbloom, 2011: Evidence for significant climate impacts in monsoonal Asia at 8.2 ka from multiple proxies and model simulations. *Journal of Earth Environmental*, **2**, 426-441.
Morrill, C., A. N. LeGrande, H. Renssen, P. Bakker, and B. L. Otto-Bliesner, submitted-a: Model sensitivity to North Atlantic freshwater forcing at 8.2 ka. *Climate of the Past Discussion*.
Morrill, C., et al., submitted-b: Proxy benchmarks for intercomparison of 8.2 ka simulations. *Climate of the Past Discussion*.
Moucha, R., A. M. Forte, J. X. Mitrovica, D. B. Rowley, S. Quéré, N. A. Simmons, and S. P. Grand, 2008: Dynamic topography and long-term sea level variations: There is no such thing as a stable continental platform. *Earth and Planetary Science Letters*, **271**, 101-108.
Mudelsee, M., 2001: The phase relations among atmospheric CO_2 content, temperature and global ice volume over the past 420 ka. *Quaternary Science Reviews*, **20**, 583-589.
Mudelsee, M., J. Fohlmeister, and D. Scholz, submitted: Effects of dating errors on nonparametric trend analyses of speleothem time series. *Climate of the Past Discussion*, **8**, 1973-2005.
Mudelsee, M., M. Borngen, G. Tetzlaff, and U. Grunewald, 2003: No upward trends in the occurrence of extreme floods in central Europe. *Nature*, **425**, 166-169.
Müller, J., A. Wagner, K. Fahl, R. Stein, M. Prange, and G. Lohmann, 2011: Towards quantitative sea ice reconstructions in the northern North Atlantic: A combined biomarker and numerical modelling approach. *Earth and Planetary Science Letters*, **306**, 137-148.
Müller, R. D., M. Sdrolias, C. Gaina, B. Steinberger, and C. Heine, 2008: Long-Term Sea level Fluctuations Driven by Ocean Basin Dynamics. *Science*, **319**, 1357-1362.
Muhs, D. R., K. R. Simmons, and B. Steinke, 2002a: Timing and warmth of the Last Interglacial period: new U-series evidence from Hawaii and Bermuda and a new fossil compilation for North America. *Quaternary Science Reviews*, **21**, 1355-1383.
Muhs, D. R., K. R. Simmons, G. L. Kennedy, and T. K. Rockwell, 2002b: The last interglacial period on the Pacific Coast of North America: Timing and paleoclimate. *Geological Society of America Bulletin*, **114**, 569-592.
Muhs, D. R., K. R. Simmons, R. R. Schumann, and R. B. Halley, 2011: Sea level history of the past two interglacial periods: new evidence from U-series dating of reef corals from south Florida. *Quaternary Science Reviews*, **30**, 570-590.
Muhs, D. R., J. M. Pandolfi, K. R. Simmons, and R. R. Schumann, 2012: Sea level history of past interglacial periods from uranium-series dating of corals, Curaçao, Leeward Antilles islands. *Quaternary Research*, **37**, 1-25.
Mulitza, S., et al., 2008: Sahel megadroughts triggered by glacial slowdowns of Atlantic meridional overturning. *Paleoceanography*, **23**, PA4206.
Muscheler, R., F. Joos, J. Beer, S. A. Müller, M. Vonmoos, and I. Snowball, 2007: Solar activity during the last 1000 yr inferred from radionuclide records. *Quaternary Science Reviews*, **26**, 82-97.
Mylroie, J. E., 2008: Late Quaternary sea level position: Evidence from Bahamian carbonate deposition and dissolution cycles. *Quaternary International*, **183**, 61-75.
Naish, T., et al., 2009a: Obliquity-paced Pliocene West Antarctic ice sheet oscillations. *Nature*, **458**, 322-328.
Naish, T. R., and G. S. Wilson, 2009: Constraints on the amplitude of Mid-Pliocene (3.6–2.4 Ma) eustatic sea level fluctuations from the New Zealand shallow-marine sediment record. *Philosophical Transactions of the Royal Society A: Mathematical, Physical and Engineering Sciences*, **367**, 169-187.
Naish, T. R., L. Carter, E. Wolff, D. Pollard, and R. D. Powell, 2009b: Late Pliocene–Pleistocene Antarctic Climate Variability at Orbital and Suborbital Scale: Ice Sheet, Ocean and Atmospheric Interactions. *Developments in Earth & Environmental Sciences*, F. Florindo, and S. M., Eds., Elsevier, 465-529.
Neppel, L., et al., 2010: Flood frequency analysis using historical data: accounting for random and systematic errors. *Hydrological Sciences Journal-Journal Des Sciences Hydrologiques*, **55**, 192-208.

Nesje, A., 2009: Latest Pleistocene and Holocene alpine glacier fluctuations in Scandinavia. *Quaternary Science Reviews*, **28**, 2119-2136.
Nesje, A., et al., 2011: The climatic significance of artefacts related to prehistoric reindeer hunting exposed at melting ice patches in southern Norway. *The Holocene*, **22**, 485-496.
Neukom, R., and J. Gergis, 2011: Southern Hemisphere high-resolution palaeoclimate records of the last 2000 years. *The Holocene*, **22**, 501-524.
Neukom, R., et al., 2011: Multiproxy summer and winter surface air temperature field reconstructions for southern South America covering the past centuries. *Climate Dynamics*, **37**, 35-51.
Newby, P. E., B. N. Shuman, J. P. Donnelly, and D. MacDonald, 2011: Repeated century-scale droughts over the past 13,000 yr near the Hudson River watershed, USA. *Quaternary Research*, **75**, 523-530.
Nicault, A., S. Alleaume, S. Brewer, M. Carrer, P. Nola, and J. Guiot, 2008: Mediterranean drought fluctuation during the last 500 years based on tree-ring data. *Climate Dynamics*, **31**, 227-245.
Nicolussi, K., M. Kaufmann, T. M. Melvin, J. van der Plicht, P. Schießling, and A. Thurner, 2009: A 9111 year long conifer tree-ring chronology for the European Alps: a base for environmental and climatic investigations. *The Holocene*, **19**, 909-920.
Nørgaard-Pedersen, N., N. Mikkelsen, S. J. Lassen, Y. Kristoffersen, and E. Sheldon, 2007: Reduced sea ice concentrations in the Arctic Ocean during the last interglacial period revealed by sediment cores off northern Greenland. *Paleoceanography*, **22**, PA1218.
North Greenland Ice Core Project members, 2004: High-resolution record of Northern Hemisphere climate extending into the last interglacial period. *Nature*, **431**, 147-151.
O'Donnell, R., N. Lewis, S. McIntyre, and J. Condon, 2010: Improved Methods for PCA-Based Reconstructions: Case Study Using the Steig et al., (2009) Antarctic Temperature Reconstruction. *Journal of Climate*, **24**, 2099-2115.
Öberg, L., and L. Kullman, 2011: Recent Glacier Recession – a New Source of Postglacial Treeline and Climate History in the Swedish Scandes. *Landscape Online*, **26**, 1-38.
Oerlemans, J., 1980: Model experiments on the 100,000-yr glacial cycle. *Nature*, **287**, 430-432.
Oglesby, R., S. Feng, Q. Hu, and C. Rowe, 2012: The role of the Atlantic Multidecadal Oscillation on medieval drought in North America: Synthesizing results from proxy data and climate models. *Global and Planetary Change*, **84–85**, 56-65.
Okazaki, Y., et al., 2010: Deepwater Formation in the North Pacific During the Last Glacial Termination. *Science*, **329**, 200-204.
Okumura, Y. M., C. Deser, A. Hu, A. Timmermann, and S. P. Xie, 2009: North Pacific Climate Response to Freshwater Forcing in the Subarctic North Atlantic: Oceanic and Atmospheric Pathways. *Journal of Climate*, **22**, 1424-1445.
Oman, L., A. Robock, G. Stenchikov, G. A. Schmidt, and R. Ruedy, 2005: Climatic response to high-latitude volcanic eruptions. *Journal of Geophysical Research-Atmospheres*, **110**, D13103.
Oppo, D. W., Y. Rosenthal, and B. K. Linsley, 2009: 2,000-year-long temperature and hydrology reconstructions from the Indo-Pacific warm pool. *Nature*, **460**, 1113-1116.
Orsi, A. J., B. D. Cornuelle, and J. P. Severinghaus, 2012: Little Ice Age cold interval in West Antarctica: Evidence from borehole temperature at the West Antarctic Ice Sheet (WAIS) Divide. *Geophysical Research Letters*, **39**, L09710.
Osborn, T., and K. Briffa, 2007: Response to comment on "The spatial extent of 20th-century warmth in the context of the past 1200 years". *Science*, **316**, 1844.
Osborn, T., S. Raper, and K. Briffa, 2006: Simulated climate change during the last 1,000 years: comparing the ECHO-G general circulation model with the MAGICC simple climate model. *Climate Dynamics*, **27**, 185-197.
Oswald, W. W., and D. R. Foster, 2011: A record of late-Holocene environmental change from southern New England, USA. *Quaternary Research*, **76**, 314-318.
Ottera, O. H., M. Bentsen, H. Drange, and L. L. Suo, 2010: External forcing as a metronome for Atlantic multidecadal variability. *Nature Geoscience*, **3**, 688-694.
Otto-Bliesner, B., S. Marsha, J. Overpeck, G. Miller, A. Hu, and C. L. I. P. Mem, 2006: Simulating arctic climate warmth and icefield retreat in the last interglaciation. *Science*, **311**, 1751-1753.
Otto-Bliesner, B., et al., 2009: A comparison of PMIP2 model simulations and the MARGO proxy reconstruction for tropical sea surface temperatures at last glacial maximum. *Climate Dynamics*, **32**, 799-815.
Otto-Bliesner, B. L., and E. C. Brady, 2010: The sensitivity of the climate response to the magnitude and location of freshwater forcing: last glacial maximum experiments. *Quaternary Science Reviews*, **29**, 56-73.
Otto-Bliesner, B. L., N. Rosenbloom, E. J. Stone, N. McKay, D. Lunt, E. C. Brady, and J. T. Overpeck, submitted: How well do models reproduce Last Interglacial warmth? New model-data comparisons. *Philosophical Transactions of the Royal Soceity A*.
Otto, J., T. Raddatz, M. Claussen, V. Brovkin, and V. Gayler, 2009: Separation of atmosphere-ocean-vegetation feedbacks and synergies for mid-Holocene climate. *Geophysical Research Letters*, **36**, L09701.
Overpeck, J., B. Otto-Bliesner, G. Miller, D. Muhs, R. Alley, and J. Kiehl, 2006: Paleoclimatic evidence for future ice-sheet instability and rapid sea level rise. *Science*, **311**, 1747-1750.
Pagani, M., Z. Liu, J. LaRiviere, and A. Ravelo, 2010: High Earth-system climate sensitivity determined from Pliocene carbon dioxide concentrations. *Nature Geoscience*, **3**, 27-30.

Pagani, M., J. Zachos, K. Freeman, B. Tipple, and S. Bohaty, 2005: Marked decline in atmospheric carbon dioxide concentrations during the Paleogene. *Science*, **309**, 600-603.
PAGES 2k Consortium, submitted: Temperature variability at the continental scale over two millennia. *Science*.
Pahnke, K., R. Zahn, H. Elderfield, and M. Schulz, 2003: 340,000-year centennial-scale marine record of Southern Hemisphere climatic oscillation. *Science*, **301**, 948-952.
Pahnke, K., J. P. Sachs, L. Keigwin, A. Timmermann, and S. P. Xie, 2007: Eastern tropical Pacific hydrologic changes during the past 27,000 years from D/H ratios in alkenones. *Paleoceanography*, **22**, PA4214.
Pak, D. K., D. W. Lea, and J. P. Kennett, 2012: Millennial scale changes in sea surface temperature and ocean circulation in the northeast Pacific, 10-60 kyr BP. *Paleoceanography*, **27**, PA1212.
PALAEOSENS Project Members, accepted: Making sense of palaeoclimate sensitivity. *Nature*.
Palastanga, V., G. van der Schrier, S. Weber, T. Kleinen, K. Briffa, and T. Osborn, 2011: Atmosphere and ocean dynamics: contributors to the European Little Ice Age? *Climate Dynamics*, **36**, 973-987.
Parrenin, F., et al., submitted: Zero phasing between CO_2 and Antarctic temperature during the last deglacial warming.
Patadia, F., E.-S. Yang, and S. A. Christopher, 2009: Does dust change the clear sky top of atmosphere shortwave flux over high surface reflectance regions? *Geophysical Research Letters*, **36**, L15825.
Pausata, F. S. R., D. S. Battisti, K. H. Nisancioglu, and C. M. Bitz, 2011a: Chinese stalagmite delta^{18}O controlled by changes in the Indian monsoon during a simulated Heinrich event. *Nature Geoscience*, **4**, 474-480.
Pausata, F. S. R., C. Li, J. J. Wettstein, K. H. Nisancioglu, and D. S. Battisti, 2009: Changes in atmospheric variability in a glacial climate and the impacts on proxy data: a model intercomparison. *Climate of the Past*, **5**, 489-502.
Pausata, F. S. R., C. Li, J. J. Wettstein, M. Kageyama, and K. H. Nisancioglu, 2011b: The key role of topography in altering North Atlantic atmospheric circulation during the last glacial period. *Climate of the Past*, **7**, 1089-1101.
Pearson, P., and M. Palmer, 2000: Atmospheric carbon dioxide concentrations over the past 60 million years. *Nature*, **406**, 695-699.
Pearson, P. N., G. L. Foster, and B. S. Wade, 2009: Atmospheric carbon dioxide through the Eocene-Oligocene climate transition. *Nature*, **461**, 1110-1113.
Pedro, J., et al., 2011: The last deglaciation: timing the bipolar seesaw. *Climate of the Past*, **7**, 671-683.
Pedro, J. B., S. O. Rasmussen, and T. D. van Ommen, 2012: Tightened constraints on the time-lag between Antarctic temperature and CO_2 during the last deglaciation. *Climate of the Past*, **8**, 1213-1221.
Pépin, L., D. Raynaud, J.-M. Barnola, and M. F. Loutre, 2001: Hemispheric roles of climate forcings during glacial-interglacial transitions as deduced from the Vostok record and LLN-2D model experiments. *Journal of Geophysical Research*, **106**, 31885-31892.
Peterson, L. C., and G. H. Haug, 2006: Variability in the mean latitude of the Atlantic Intertropical Convergence Zone as recorded by riverine input of sediments to the Cariaco Basin (Venezuela). *Palaeogeography Palaeoclimatology Palaeoecology*, **234**, 97-113.
Petit, J. R., and B. Delmonte, 2009: A model for large glacial–interglacial climate-induced changes in dust and sea salt concentrations in deep ice cores (central Antarctica): palaeoclimatic implications and prospects for refining ice core chronologies. *Tellus*, **61B**, 768-790.
Petit, J. R., et al., 1999: Climate and atmospheric history of the past 420,000 years from the Vostok ice core, Antarctica. *Nature*, **399**, 429-436.
Petrenko, V. V., et al., 2009: $^{14}CH_4$ Measurements in Greenland Ice: Investigating Last Glacial Termination CH_4 Sources. *Science*, **324**, 506-508.
Phipps, S., et al., submitted: Palaeoclimate data-model comparison: Concepts and application to the climate of Ausstralasia over the past 1500 years. *Journal of Climate*.
Phipps, S. J., L. D. Rotstayn, H. B. Gordon, J. L. Roberts, A. C. Hirst, and W. F. Budd, 2011: The CSIRO Mk3L climate system model version 1.0 – Part 1: Description and evaluation. *Geoscientific Model Development*, **4**, 483-509.
Piccarreta, M., M. Caldara, D. Capolongo, and F. Boenzi, 2011: Holocene geomorphic activity related to climatic change and human impact in Basilicata, Southern Italy. *Geomorphology*, **128**, 137-147.
Pingree, K., M. Lurie, and T. Hughes, 2011: Is the East Antarctic ice sheet stable? *Quaternary Research*, **75**, 417-429.
Pollack, H. N., and J. E. Smerdon, 2004: Borehole climate reconstructions: Spatial structure and hemispheric averages. *Journal of Geophysical Research*, **109**, D11106.
Pollard, D., and R. M. DeConto, 2009: Modelling West Antarctic ice sheet growth and collapse through the past five million years. *Nature*, **458**, 329-332.
Polyak, L., et al., 2010: History of sea ice in the Arctic. *Quaternary Science Reviews*, **29**, 1757-1778.
Polyakov, I. V., et al., 2010: Arctic Ocean Warming Contributes to Reduced Polar Ice Cap. *Journal of Physical Oceanography*, **40**, 2743-2756.
Ponton, C., L. Giosan, T. I. Eglinton, D. Q. Fuller, J. E. Johnson, P. Kumar, and T. S. Collett, 2012: Holocene aridification of India. *Geophysical Research Letters*, **39**, L03704.
Porter, T. J., and M. F. J. Pisaric, 2011: Temperature-growth divergence in white spruce forests of Old Crow Flats, Yukon Territory, and adjacent regions of northwestern North America. *Global Change Biology*, **17**, 3418-3430.
Prieto, M. d. R., and R. García Herrera, 2009: Documentary sources from South America: Potential for climate reconstruction. *Palaeogeography, Palaeoclimatology, Palaeoecology*, **281**, 196-209.

Prokopenko, A., L. Hinnov, D. Williams, and M. Kuzmin, 2006: Orbital forcing of continental climate during the Pleistocene: a complete astronomically tuned climatic record from Lake Baikal, SE Siberia. *Quaternary Science Reviews*, **25**, 3431-3457.

Prokopenko, A. A., D. F. Williams, M. I. Kuzmin, E. B. Karabanov, G. K. Khursevich, and J. A. Peck, 2002: Muted climate variations in continental Siberia during the mid-Pleistocene epoch. *Nature*, **418**, 65-68.

Putnam, A. E., et al., in press: Regional climate control of glaciers in New Zealand and Europe during the preindustrial Holocene. *Nature Geoscience*. doi:0.1038/NGEO1548.

Qiuzhen, Y., A. Berger, E. Driesschaert, H. Goosse, M. F. Loutre, and M. Crucifix, 2008: The Eurasian ice sheet reinforces the East Asian summer monsoon during the interglacial 500 000 years ago. *Clim. Past*, **4**, 79-90.

Quiquet, A., C. Ritz, H. J. Punge, and D. Salas y M´elia, 2012: Contribution of Greenland ice sheet melting to sea level rise during the last interglacial period: an approach combining ice sheet modelling and proxy data. *Climate of the Past Discussion*, **8**, 3345-3377.

Raddatz, T., et al., 2007: Will the tropical land biosphere dominate the climate–carbon cycle feedback during the twenty-first century? *Climate Dynamics*, **29**, 565-574.

Radic, V., and R. Hock, 2011: Regionally differentiated contribution of mountain glaciers and ice caps to future sea level rise. *Nature Geoscience*, **4**, 91-94.

Rahmstorf, S., et al., 2005: Thermohaline circulation hysteresis: A model intercomparison. *Geophysical Research Letters*, **32**, L23605.

Rasmussen, S. O., et al., 2006: A new Greenland ice core chronology for the last glacial termination. *Journal of Geophysical Research*, **111**, D06102.

Raymo, M. E., and J. X. Mitrovica, 2012: Collapse of polar ice sheets during the stage 11 interglacial. *Nature*, **483**, 453-456.

Raymo, M. E., J. X. Mitrovica, M. J. O'Leary, R. M. DeConto, and P. J. Hearty, 2011: Departures from eustasy in Pliocene sea level records. *Nature Geoscience*, **4**, 328-332.

Renssen, H., H. Seppä, X. Crosta, H. Goosse, and D. M. Roche, 2012: Global characterization of the Holocene Thermal Maximum. *Quaternary Science Reviews*, **48**, 7-19.

Reuter, J., L. Stott, D. Khider, A. Sinha, H. Cheng, and R. L. Edwards, 2009: A new perspective on the hydroclimate variability in northern South America during the Little Ice Age. *Geophysical Research Letters*, **36**, L21706.

Ridley, J., J. Gregory, P. Huybrechts, and J. Lowe, 2010: Thresholds for irreversible decline of the Greenland ice sheet. *Climate Dynamics*, **35**, 1049-1057.

Rimbu, N., G. Lohmann, J. H. Kim, H. W. Arz, and R. Schneider, 2003: Arctic/North Atlantic Oscillation signature in Holocene sea surface temperature trends as obtained from alkenone data. *Geophysical Research Letters*, **30**, 4.

Risebrobakken, B., T. Dokken, L. H. Smedsrud, C. Andersson, E. Jansen, M. Moros, and E. V. Ivanova, 2011: Early Holocene temperature variability in the Nordic Seas: The role of oceanic heat advection versus changes in orbital forcing. *Paleoceanography*, **26**, PA4206.

Ritz, S., T. Stocker, and F. Joos, 2011: A Coupled Dynamical Ocean-Energy Balance Atmosphere Model for Paleoclimate Studies. *Journal of Climate*, **24**, 349-375.

Robertson, A., et al., 2001: Hypothesized climate forcing time series for the last 500 years. *Journal of Geophysical Research*, **106**, 14783-14803.

Robinson, A., R. Calov, and A. Ganopolski, 2011: Greenland ice sheet model parameters constrained using simulations of the Eemian Interglacial. *Climate of the Past*, **7**, 381-396.

Robinson, A., R. Calov, and A. Ganopolski, 2012: Multistability and critical thresholds of the Greenland ice sheet. *Nature Climate Change*, **2**, 429-432.

Roe, G. H., and R. S. Lindzen, 2001: The mutual interaction between continental-scale ice sheets and atmospheric stationary waves. *Journal of Climate*, **14**, 1450-1465.

Rohling, E. J., and H. Pälike, 2005: Centennial-scale climate cooling with a sudden cold event around 8,200 years ago. *Nature*, **434**, 975-979.

Rohling, E. J., M. Medina-Elizalde, J. G. Shepherd, M. Siddall, and J. D. Stanford, 2012: Sea surface and high-latitude temperature sensitivity to radiative forcing of climate over several glacial cycles. *Journal of Climate*, **25**, 1635-1656.

Rohling, E. J., K. Grant, C. Hemleben, M. Siddall, B. A. A. Hoogakker, M. Bolshaw, and M. Kucera, 2008a: High rates of sea level rise during the last interglacial period. *Nature Geoscience*, **1**, 38-42.

Rohling, E. J., K. Grant, M. Bolshaw, A. P. Roberts, M. Siddall, C. Hemleben, and M. Kucera, 2009: Antarctic temperature and global sea level closely coupled over the past five glacial cycles. *Nature Geoscience*, **2**, 500-504.

Rohling, E. J., K. Braun, K. Grant, M. Kucera, A. P. Roberts, M. Siddall, and G. Trommer, 2010: Comparison between Holocene and Marine Isotope Stage-11 sea level histories. *Earth and Planetary Science Letters*, **291**, 97-105.

Rohling, E. J., et al., 2008b: New constraints on the timing of sea level fluctuations during early to middle marine isotope stage 3. *Paleoceanography*, **23**, PA3219.

Rojas, M., et al., 2009: The Southern Westerlies during the last glacial maximum in PMIP2 simulations. *Climate Dynamics*, **32**, 525-548.

Routson, C. C., C. A. Woodhouse, and J. T. Overpeck, 2011: Second century megadrought in the Rio Grande headwaters, Colorado: How unusual was medieval drought? *Geophys. Res. Lett.*, **38**, L22703.

Ruddiman, W. F., J. E. Kutzbach, and S. J. Vavrus, 2011: Can natural or anthropogenic explanations of late-Holocene CO_2 and CH_4 increases be falsified? *The Holocene*, **21**, 865-8879.
Rupper, S., G. Roe, and A. Gillespie, 2009: Spatial patterns of Holocene glacier advance and retreat in Central Asia. *Quaternary Research*, **72**, 337-346.
Russell, J., H. Eggermont, R. Taylor, and D. Verschuren, 2009: Paleolimnological records of recent glacier recession in the Rwenzori Mountains, Uganda-D. R. Congo. *Journal of Paleolimnology*, **41**, 253-271.
Russell, J. M., and T. C. Johnson, 2005: A high-resolution geochemical record from Lake Edward, Uganda Congo and the timing and causes of tropical African drought during the late Holocene. *Quaternary Science Reviews*, **24**, 1375-1389.
Russell, J. M., and T. C. Johnson, 2007: Little Ice Age drought in equatorial Africa: Intertropical Convergence Zone migrations and El Niño-Southern Oscillation variability. *Geology*, **35**, 21-24.
Russon, T., A. W. Tudhope, G. C. Hegerl, M. Collins, and A. Schurer, submitted: The unforced contribution to changes in ENSO variability over the last millennium. *Geophysical Research Letters*.
Saenger, C., A. Cohen, D. Oppo, R. Halley, and J. Carilli, 2009: Surface-temperature trends and variability in the low-latitude North Atlantic since 1552. *Nature Geoscience*, **2**, 492-495.
Saenko, O. A., A. Schmittner, and A. J. Weaver, 2004: The Atlantic-Pacific Seesaw. *Journal of Climate*, **17**, 2033-2038.
Salisbury, E. J., 1928: On the causes and ecological significance of stomatal frequency, with special reference to the woodland flora. *Philosophical Transactions of the Royal Society of London Series B-Containing Papers of a Biological Character*, **216**, 1-65.
Salzer, M., and K. Kipfmueller, 2005: Reconstructed temperature and precipitation on a millennial timescale from tree-rings in the Southern Colorado Plateau, USA. *Climatic Change*, **70**, 465-487.
Salzmann, U., A. M. Haywood, D. J. Lunt, P. J. Valdes, and D. J. Hill, 2008: A new global biome reconstruction and data-model comparison for the Middle Pliocene. *Global Ecology and Biogeography*, **17**, 432-447.
Salzmann, U., et al., submitted: How well do models reproduce warm terrestrial climates of the Pliocene? *Nature Climate Change*.
Sánchez Goñi, M. F., et al., 2012: European climate optimum and enhanced Greenland melt during the Last Interglacial. *Geology*, **40**, 627-630.
Sarnthein, M., U. Pflaumann, and M. Weinelt, 2003a: Past extent of sea ice in the northern North Atlantic inferred from foraminiferal paleotemperature estimates. *Paleoceanography*, **18**, 1047.
Sarnthein, M., S. Van Kreveld, H. Erlenkeuser, P. Grootes, M. Kucera, U. Pflaumann, and M. Schulz, 2003b: Centennial-to-millennial-scale periodicities of Holocene climate and sediment injections off the western Barents shelf, 75 degrees N. *Boreas*, **32**, 447-461.
Scapozza, C., C. Lambiel, E. Reynard, J.-M. Fallot, M. Antognini, and P. Schoeneich, 2010: Radiocarbon dating of fossil wood remains buried by the Piancabella rock glacier, Blenio Valley (Ticino, southern Swiss Alps): Implications for rock glacier, treeline and climate history. *Permafrost and Periglacial Processes*, **21**, 90-96.
Schaefer, J. M., et al., 2009: High-Frequency Holocene Glacier Fluctuations in New Zealand Differ from the Northern Signature. *Science*, **324**, 622-625.
Schellmann, G., and U. Radtke, 2004: A revised morpho- and chronostratigraphy of the Late and Middle Pleistocene coral reef terraces on Southern Barbados (West Indies). *Earth-Science Reviews*, **64**, 157-187.
Scherer, D., M. Gude, M. Gempeler, and E. Parlow, 1998: Atmospheric and hydrological boundary conditions for slushflow initiation due to snowmelt. *Annals of Glaciology*, **26**, 377-380.
Schilt, A., M. Baumgartner, T. Blunier, J. Schwander, R. Spahni, H. Fischer, and T. F. Stocker, 2010: Glacial–interglacial and millennial-scale variations in the atmospheric nitrous oxide concentration during the last 800,000 years. *Quaternary Science Reviews*, **29**, 182-192.
Schmidt, A., T. Thordarson, L. D. Oman, A. Robock, and S. Sell, submitted: The 1783-1784 CE Laki eruption produced stratospheric injection and long-lived climate impacts.
Schmidt, G. A., et al., 2011: Climate forcing reconstructions for use in PMIP simulations of the last millennium (v1.0). *Geoscientific Model Development*, **4**, 33-45.
Schmidt, G. A., et al., 2012: Climate forcing reconstructions for use in PMIP simulations of the Last Millennium (v1.1). *Geoscientific Model Development*, **5**, 185-191.
Schmidt, G. A., et al., 2006: Present-day atmospheric simulations using GISS ModelE: Comparison to in situ, satellite, and reanalysis data. *Journal of Climate*, **19**, 153-192.
Schmitt, J., et al., 2012: Carbon Isotope Constraints on the Deglacial CO2 Rise from Ice Cores. *Science*, **336**, 711-714.
Schmittner, A., E. D. Galbraith, S. W. Hostetler, T. F. Pedersen, and R. Zhang, 2007: Large fluctuations of dissolved oxygen in the Indian and Pacific oceans during Dansgaard-Oeschger oscillations caused by variations of North Atlantic Deep Water subduction. *Paleoceanography*, **22**, PA3207.
Schmittner, A., et al., 2011: Climate Sensitivity Estimated from Temperature Reconstructions of the Last Glacial Maximum. *Science*, **334**, 1385-1388.
Schneider, B., G. Leduc, and W. Park, 2010: Disentangling seasonal signals in Holocene climate trends by satellite-model-proxy integration. *Paleoceanography*, **25**, PA4217.

Schneider, D. P., C. M. Ammann, B. L. Otto-Bliesner, and D. S. Kaufman, 2009: Climate response to large, high-latitude and low-latitude volcanic eruptions in the Community Climate System Model. *Journal of Geophysical Research-Atmospheres*, **114**, D15101.

Schneider von Deimling, T., H. Held, A. Ganopolski, and S. Rahmstorf, 2006a: Climate sensitivity estimated from ensemble simulations of glacial climate. *Climate Dynamics*, **27**, 149-163.

Schneider von Deimling, T., A. Ganopolski, H. Held, and S. Rahmstorf, 2006b: How cold was the Last Glacial Maximum? *Geophysical Research Letters*, **33**, L14709.

Schrag, D. P., J. F. Adkins, K. McIntyre, J. L. Alexander, D. A. Hodell, C. D. Charles, and J. F. McManus, 2002: The oxygen isotopic composition of seawater during the Last Glacial Maximum. *Quaternary Science Reviews*, **21**, 331-342.

Schrijver, C. J., W. C. Livingston, T. N. Woods, and R. A. Mewaldt, 2011: The minimal solar activity in 2008-2009 and its implications for long-term climate modeling. *Geophysical Research Letters*, **38**, L06701.

Schulz, H., U. von Rad, and H. Erlenkeuser, 1998: Correlation between Arabian Sea and Greenland climate oscillations of the past 110,000 years. *Nature*, **393**, 54-57.

Schurer, A., G. Hegerl, M. E. Mann, S. F. B. Tett, and S. J. Phipps, submitted: Separating forced from chaotic climate variability over the last millennium.

Schurgers, G., U. Mikolajewicz, M. Gröger, E. Maier-Reimer, M. Vizcaino, and A. Winguth, 2007: The effect of land surface changes on Eemian climate. *Climate Dynamics*, **29**, 357-373.

Screen, J. A., and I. Simmonds, 2010: The central role of diminishing sea ice in recent Arctic temperature amplification. *Nature*, **464**, 1334-1337.

Scroxton, N., S. G. Bonham, R. E. M. Rickaby, S. H. F. Lawrence, M. Hermoso, and A. M. Haywood, 2011: Persistent El Niño-Southern Oscillation variation during the Pliocene Epoch. *Paleoceanography*, **26**, PA2215.

Seager, R., N. Graham, C. Herweijer, A. Gordon, Y. Kushnir, and E. Cook, 2007: Blueprints for Medieval hydroclimate. *Quaternary Science Reviews*, **26**, 2322-2336.

Seager, R., R. Burgman, Y. Kushnir, A. Clement, E. Cook, N. Naik, and J. Miller, 2008: Tropical Pacific Forcing of North American Medieval Megadroughts: Testing the Concept with an Atmosphere Model Forced by Coral-Reconstructed SSTs. *Journal of Climate*, **21**, 6175-6190.

Seki, O., G. Foster, D. Schmidt, A. Mackensen, K. Kawamura, and R. Pancost, 2010: Alkenone and boron-based Pliocene pCO_2 records. *Earth and Planetary Science Letters*, **292**, 201-211.

Semenov, V. A., M. Latif, D. Dommenget, N. S. Keenlyside, A. Strehz, T. Martin, and W. Park, 2010: The Impact of North Atlantic-Arctic Multidecadal Variability on Northern Hemisphere Surface Air Temperature. *Journal of Climate*, **23**, 5668-5677.

Seong, Y., L. Owen, C. Yi, and R. Finkel, 2009: Quaternary glaciation of Muztag Ata and Kongur Shan: Evidence for glacier response to rapid climate changes throughout the Late Glacial and Holocene in westernmost Tibet. *Geological Society of America Bulletin*, **129**, 348-365.

Serreze, M. C., and R. G. Barry, 2011: Processes and impacts of Arctic amplification: A research synthesis. *Global and Planetary Change*, **77**, 85-96.

Serreze, M. C., A. P. Barrett, J. C. Stroeve, D. N. Kindig, and M. M. Holland, 2009: The emergence of surface-based Arctic amplification. *The Cryosphere*, **3**, 11-19.

Servonnat, J., P. Yiou, M. Khodri, D. Swingedouw, and S. Denvil, 2010: Influence of solar variability, CO_2 and orbital forcing between 1000 and 1850 AD in the IPSLCM4 model. *Climate of the Past*, **6**, 445-460.

Shackleton, N. J., 2000: The 100,000-year ice-age cycle identified and found to lag temperature, carbon dioxide, and orbital eccentricity. *Science*, **289**, 1897-1902.

Shaffer, G., S. M. Olsen, and C. J. Bjerrum, 2004: Ocean subsurface warming as a mechanism for coupling Dansgaard-Oeschger climate cycles and ice-rafting events. *Geophysical Research Letters*, **31**, L24202.

Shakun, J. D., et al., 2012: Global warming preceded by increasing carbon dioxide concentrations during the last deglaciation. *Nature*, **484**, 49-54.

Shanahan, T. M., et al., 2009: Atlantic Forcing of Persistent Drought in West Africa. *Science*, **324**, 377-380.

Shapiro, A., W. Schmutz, E. Rozanov, M. Schoell, M. Haberreiter, and S. Nyeki, in press: New reconstruction technique reveals large historical variability in solar radiative forcing. *Astronomy & Astrophysics*, **in press**.

Sheffer, N. A., M. Rico, Y. Enzel, G. Benito, and T. Grodek, 2008: The Palaeoflood record of the Gardon River, France: A comparison with the extreme 2002 flood event. *Geomorphology*, **98**, 71-83.

Shevenell, A. E., A. E. Ingalls, E. W. Domack, and C. Kelly, 2011: Holocene Southern Ocean surface temperature variability west of the Antarctic Peninsula. *Nature*, **470**, 250-254.

Shulmeister, J., et al., 2004: The Southern Hemisphere westerlies in the Australasian sector over the last glacial cycle: a synthesis. *Quaternary International*, **118–119**, 23-53.

Shuman, B., P. Pribyl, T. A. Minckley, and J. J. Shinker, 2010: Rapid hydrologic shifts and prolonged droughts in Rocky Mountain headwaters during the Holocene. *Geophysical Research Letters*, **37**, L06701.

Shuman, B., A. K. Henderson, C. Plank, I. Stefanova, and S. S. Ziegler, 2009: Woodland-to-forest transition during prolonged drought in Minnesota after ca. AD 1300. *Ecology*, **90**, 2792-2807.

Sicre, M. A., et al., 2008: A 4500-year reconstruction of sea surface temperature variability at decadal time-scales off North Iceland. *Quaternary Science Reviews*, **27**, 2041-2047.

Siddall, M., E. J. Rohling, W. G. Thompson, and C. Waelbroeck, 2008: Marine isotope stage 3 sea level fluctuations: Data synthesis and new outlook. *Reviews of Geophysics*, **46**, RG4003.
Siegenthaler, U., et al., 2005: Stable carbon cycle-climate relationship during the late Pleistocene. *Science*, **310**, 1313-1317.
Sikes, E. L., W. R. Howard, C. R. Samson, T. S. Mahan, L. G. Robertson, and J. K. Volkman, 2009: Southern Ocean seasonal temperature and Subtropical Front movement on the South Tasman Rise in the late Quaternary. *Paleoceanography*, **24**, PA2201.
Sime, L. C., E. W. Wolff, K. I. C. Oliver, and J. C. Tindall, 2009: Evidence for warmer interglacials in East Antarctic ice cores. *Nature*, **462**, 342-345.
Sime, L. C., C. Risib, J. C. Tindall, J. Sjolted, E. W. Wolff, V. Masson-Delmotte, and E. Caprona, submitted: Warm climate isotopic simulations: What do we learn about interglacial signals in Greenland ice cores? *Quaternary Science Reviews*.
Simms, A. R., K. T. Milliken, J. B. Anderson, and J. S. Wellner, 2011: The marine record of deglaciation of the South Shetland Islands, Antarctica since the Last Glacial Maximum. *Quaternary Science Reviews*, **30**, 1583-1601.
Singarayer, J. S., and P. J. Valdes, 2010: High-latitude climate sensitivity to ice-sheet forcing over the last 120 kyr. *Quaternary Science Reviews*, **29**, 43-55.
Singarayer, J. S., P. J. Valdes, P. Friedlingstein, S. Nelson, and D. J. Beerling, 2011: Late Holocene methane rise caused by orbitally controlled increase in tropical sources. *Nature*, **470**, 82-85.
Sinha, A., et al., 2007: A 900-year (600 to 1500 A.D.) record of the Indian summer monsoon precipitation from the core monsoon zone of India. *Geophysical Research Letters*, **34**, L16707.
Sivan, D., K. Lambeck, R. Toueg, A. Raban, Y. Porath, and B. Shirman, 2004: Ancient coastal wells of Caesarea Maritima, Israel, an indicator for relative sea level changes during the last 2000 years. *Earth and Planetary Science Letters*, **222**, 315-330.
Smerdon, J. E., 2012: Climate models as a test bed for climate reconstruction methods: pseudoproxy experiments. *Wiley Interdisciplinary Reviews: Climate Change*, **3**, 63-77.
Smerdon, J. E., A. Kaplan, D. Chang, and M. N. Evans, 2010: A Pseudoproxy Evaluation of the CCA and RegEM Methods for Reconstructing Climate Fields of the Last Millennium. *Journal of Climate*, **23**, 4856–4880.
Smerdon, J. E., A. Kaplan, E. Zorita, J. F. Gonzalez-Rouco, and M. N. Evans, 2011: Spatial performance of four climate field reconstruction methods targeting the Common Era. *Geophysical Research Letters*, **38**, L11705.
Smith, J. A., et al., 2011: Deglacial history of the West Antarctic Ice Sheet in the western Amundsen Sea Embayment. *Quaternary Science Reviews*, **30**, 488-505.
Smith, R., and J. Gregory, 2012: The last glacial cycle: transient simulations with an AOGCM. *Climate Dynamics*, **38**, 1545-1559.
Smithers, S. G., and C. D. Woodroffe, 2001: Coral microatolls and 20th century sea level in the eastern Indian Ocean. *Earth and Planetary Science Letters*, **191**, 173-184.
Soden, B. J., I. M. Held, R. Colman, K. M. Shell, J. T. Kiehl, and C. A. Shields, 2008: Quantifying Climate Feedbacks Using Radiative Kernels. *Journal of Climate*, **21**, 3504-3520.
Sorrel, P., S.-M. Popescu, S. Klotz, J.-P. Suc, and H. Oberhänsli, 2007: Climate variability in the Aral Sea basin (Central Asia) during the late Holocene based on vegetation changes. *Quaternary Research*, **67**, 357-370.
Sosdian, S., and Y. Rosenthal, 2009: Deep-Sea Temperature and Ice Volume Changes Across the Pliocene-Pleistocene Climate Transitions. *Science*, **325**, 306-310.
Sowers, T., 2006: Late Quaternary atmospheric CH_4 isotope record suggests marine clathrates are stable. *Science*, **311**, 838-840.
Sowers, T., 2010: Atmospheric methane isotope records covering the Holocene period. *Quaternary Science Reviews*, **29**, 213-221.
Sowers, T., and M. Bender, 1995: CLIMATE RECORDS COVERING THE LAST DEGLACIATION. *Science*, **269**, 210-214.
Speed, R. C., and H. Cheng, 2004: Evolution of marine terraces and sea level in the last interglacial, Cave Hill, Barbados. *Geological Society of America Bulletin*, **116**, 219-232.
Spence, J. P., M. Eby, and A. J. Weaver, 2008: The Sensitivity of the Atlantic Meridional Overturning Circulation to Freshwater Forcing at Eddy-Permitting Resolutions. *Journal of Climate*, **21**, 2697-2710.
Spielhagen, R. F., et al., 2011: Enhanced Modern Heat Transfer to the Arctic by Warm Atlantic Water. *Science*, **331**, 450-453.
Stager, J. C., D. Ryves, B. F. Cumming, L. D. Meeker, and J. Beer, 2005: Solar variability and the levels of Lake Victoria, East Africa, during the last millenium. *Journal of Paleolimnology*, **33**, 243-251.
Stager, J. C., C. Cocquyt, R. Bonnefille, C. Weyhenmeyer, and N. Bowerman, 2009: A late Holocene paleoclimatic history of Lake Tanganyika, East Africa. *Quaternary Research*, **72**, 47-56.
Stambaugh, M. C., R. P. Guyette, E. R. McMurry, E. R. Cook, D. M. Meko, and A. R. Lupo, 2011: Drought duration and frequency in the U.S. Corn Belt during the last millennium (AD 992–2004). *Agricultural and Forest Meteorology*, **151**, 154-162.
Starkel, L., R. Soja, and D. J. Michczyńska, 2006: Past hydrological events reflected in Holocene history of Polish rivers. *CATENA*, **66**, 24-33.

Steffensen, J. P., et al., 2008: High-resolution Greenland Ice Core data show abrupt climate change happens in few years. *Science*, **321**, 680-684.
Steig, E. J., D. P. Schneider, S. D. Rutherford, M. E. Mann, J. C. Comiso, and D. T. Shindell, 2009: Warming of the Antarctic ice-sheet surface since the 1957 International Geophysical Year. *Nature*, **457**, 459-462.
Stein, M., G. J. Wasserburg, P. Aharon, J. H. Chen, Z. R. Zhu, A. Bloom, and J. Chappell, 1993: TIMS U-series dating and stable isotopes of the last interglacial event in Papua New Guinea. *Geochimica et Cosmochimica Acta*, **57**, 2541-2554.
Steinhilber, F., J. Beer, and C. Fröhlich, 2009: Total solar irradiance during the Holocene. *Geophysical Research Letters*, **36**, L19704.
Steinhilber, F., et al., 2012: 9,400 years of cosmic radiation and solar activity from ice cores and tree rings. *Proceedings of the National Academy of Sciences*.
Steinke, S., M. Kienast, J. Groeneveld, L.-C. Lin, M.-T. Chen, and R. Rendle-Bühring, 2008: Proxy dependence of the temporal pattern of deglacial warming in the tropical South China Sea: toward resolving seasonality. *Quaternary Science Reviews*, **27**, 688-700.
Steinman, B. A., M. B. Abbott, M. E. Mann, N. D. Stansell, and B. P. Finney, 2012: 1,500 year quantitative reconstruction of winter precipitation in the Pacific Northwest. *Proceedings of the National Academy of Sciences*. advance online publication.
Stendel, M., I. Mogensen, and J. Christensen, 2006: Influence of various forcings on global climate in historical times using a coupled atmosphere–ocean general circulation model. *Climate Dynamics*, **26**, 1-15.
Stenni, B., et al., 2010: The deuterium excess records of EPICA Dome C and Dronning Maud Land ice cores (East Antarctica). *Quaternary Science Reviews*, **29**, 146-159.
Stenni, B., et al., 2011: Expression of the bipolar see-saw in Antarctic climate records during the last deglaciation. *Nature Geoscience*, **4**, 46-49.
Steph, S., et al., 2010: Early Pliocene increase in thermohaline overturning: A precondition for the development of the modern equatorial Pacific cold tongue. *Paleoceanography*, **25**, PA2202.
Stewart, M. M., I. Larocque-Tobler, and M. Grosjean, 2011a: Quantitative inter-annual and decadal June–July–August temperature variability ca. 570 BC to AD 120 (Iron Age–Roman Period) reconstructed from the varved sediments of Lake Silvaplana, Switzerland. *Journal of Quaternary Science*, **26**, 491-501.
Stewart, M. M., M. Grosjean, F. G. Kuglitsch, S. U. Nussbaumer, and L. von Gunten, 2011b: Reconstructions of late Holocene paleofloods and glacier length changes in the Upper Engadine, Switzerland (ca. 1450 BC–AD 420). *Palaeogeography, Palaeoclimatology, Palaeoecology*, **311**, 215-223.
Stine, S., 1994: Extreme and persistent drought in California and Patagonia during mediaeval time. *Nature*, **369**, 546-549.
Stirling, C., T. Esat, K. Lambeck, and M. McCulloch, 1998: Timing and duration of the Last Interglacial: evidence for a restricted interval of widespread coral reef growth. *Earth and Planetary Science Letters*, **160**, 745-762.
Stirling, C. H., and M. B. Andersen, 2009: Uranium-series dating of fossil coral reefs: Extending the sea level record beyond the last glacial cycle. *Earth and Planetary Science Letters*, **284**, 269-283.
Stirling, C. H., T. M. Esat, M. T. McCulloch, and K. Lambeck, 1995: High-precision U-series dating of corals from Western Australia and implications for the timing and duration of the Last Interglacial. *Earth and Planetary Science Letters*, **135**, 115-130.
Stocker, T., and S. Johnsen, 2003: A minimum thermodynamic model for the bipolar seesaw. *Paleoceanography*, **18**, 1087.
Stone, E. J., D. J. Lunt, J. D. Annan, and J. C. Hargreaves, submitted: Quantification of Greenland ice-sheet contribution to Last Interglacial sea level rise. *Nature Geoscience*.
Stone, J. O., G. A. Balco, D. E. Sugden, M. W. Caffee, L. C. Sass, S. G. Cowdery, and C. Siddoway, 2003: Holocene Deglaciation of Marie Byrd Land, West Antarctica. *Science*, **299**, 99-102.
Støren, E. N., E. W. Kolstad, and Ø. Paasche, 2012: Linking past flood frequencies in Norway to regional atmospheric circulation anomalies. *Journal of Quaternary Science*, **27**, 71-80.
Stott, L., A. Timmermann, and R. Thunell, 2007: Southern Hemisphere and Deep-Sea Warming Led Deglacial Atmospheric CO_2 Rise and Tropical Warming. *Science*, **318**, 435-438.
Stott, L., K. Cannariato, R. Thunell, G. H. Haug, A. Koutavas, and S. Lund, 2004: Decline of surface temperature and salinity in the western tropical Pacific Ocean in the Holocene epoch. *Nature*, **431**, 56-59.
Stouffer, R., et al., 2006: Investigating the causes of the response of the thermohaline circulation to past and future climate changes. *Journal of Climate*, **19**, 1365-1387.
Stríkis, N. M., et al., 2011: Abrupt variations in South American monsoon rainfall during the Holocene based on a speleothem record from central-eastern Brazil. *Geology*, **39**, 1075-1078.
Stuiver, M., and T. F. Braziunas, 1993: Sun, ocean, climate and atmospheric $^{14}CO_2$: an evaluation of causal and spectral relationships. *The Holocene*, **3**, 289-305.
Svensson, A., et al., 2008: A 60 000 year Greenland stratigraphic ice core chronology. *Climate of the Past*, **4**, 47-57.
Swingedouw, D., J. Mignot, P. Braconnot, E. Mosquet, M. Kageyama, and R. Alkama, 2009: Impact of Freshwater Release in the North Atlantic under Different Climate Conditions in an OAGCM. *Journal of Climate*, **22**, 6377-6403.

Swingedouw, D., L. Terray, C. Cassou, A. Voldoire, D. Salas-Mélia, and J. Servonnat, 2011: Natural forcing of climate during the last millennium: fingerprint of solar variability. *Climate Dynamics*, **36**, 1349-1364.
Tagliabue, A., et al., 2009: Quantifying the roles of ocean circulation and biogeochemistry in governing ocean carbon-13 and atmospheric carbon dioxide at the last glacial maximum. *Climate of the Past*, **5**, 695-706.
Takemura, T., M. Egashira, K. Matsuzawa, H. Ichijo, R. O'ishi, and A. Abe-Ouchi, 2009: A simulation of the global distribution and radiative forcing of soil dust aerosols at the Last Glacial Maximum. *Atmospheric Chemistry and Physics*, **9**, 3061-3073.
Tan, L., Y. Cai, R. Edwards, H. Cheng, C. Shen, and H. Zhang, 2011: Centennial- to decadal-scale monsoon precipitation variability in the semi-humid region, northern China during the last 1860 years: Records from stalagmites in Huangye Cave. *The Holocene*, **21**, 287-296.
Tarasov, L., and W. R. Peltier, 2007: Coevolution of continental ice cover and permafrost extent over the last glacial-interglacial cycle in North America. *Journal of Geophysical Research*, **112**, F02S08.
Tarasov, P. E., et al., 2011: Progress in the reconstruction of Quaternary climate dynamics in the Northwest Pacific: A new modern analogue reference dataset and its application to the 430-kyr pollen record from Lake Biwa. *Earth-Science Reviews*, **108**, 64-79.
Telford, R. J., C. Li, and M. Kucera, submitted: Mismatch between the depth habitat 1 of planktonic foraminifera and the calibration depth of SST transfer functions may bias reconstructions. *Climate of the Past Discussion*.
Tett, S., et al., 2007: The impact of natural and anthropogenic forcings on climate and hydrology since 1550. *Climate Dynamics*, **28**, 3-34.
Thomas, E., and J. Briner, 2009: Climate of the past millennium inferred from varved proglacial lake sediments on northeast Baffin Island, Arctic Canada. *Journal of Paleolimnology*, **41**, 209-224.
Thomas, E. R., E. W. Wolff, R. Mulvaney, S. J. Johnsen, J. P. Steffensen, and C. Arrowsmith, 2009: Anatomy of a Dansgaard-Oeschger warming transition: High-resolution analysis of the North Greenland Ice Core Project ice core. *Journal of Geophysical Research-Atmospheres*, **114**, D08102.
Thomas, E. R., et al., 2007: The 8.2ka event from Greenland ice cores. *Quaternary Science Reviews*, **26**, 70-81.
Thompson, W. G., and S. L. Goldstein, 2005: Open-System Coral Ages Reveal Persistent Suborbital Sea level Cycles. *Science*, **308**, 401-404.
Thompson, W. G., M. W. Spiegelman, S. L. Goldstein, and R. C. Speed, 2003: An open-system model for U-series age determinations of fossil corals. *Earth and Planetary Science Letters*, **210**, 365-381.
Thompson, W. G., H. Allen Curran, M. A. Wilson, and B. White, 2011: Sea level oscillations during the last interglacial highstand recorded by Bahamas corals. *Nature Geoscience*, **4**, 684-687.
Thorndycraft, V. R., and G. Benito, 2006: Late Holocene fluvial chronology of Spain: The role of climatic variability and human impact. *CATENA*, **66**, 34-41.
Tierney, J., M. Mayes, N. Meyer, C. Johnson, P. Swarzenski, A. Cohen, and J. Russell, 2010: Late-twentieth-century warming in Lake Tanganyika unprecedented since AD 500. *Nature Geoscience*, **3**, 422-425.
Tierney, J. E., J. E. Smerdon, K. J. Anchukaitis, and R. Seager, submitted: Decadal-to-centennial variability in East African hydroclimate controlled by the Indian Ocean.
Tierney, J. E., S. C. Lewis, B. I. Cook, A. N. LeGrande, and G. A. Schmidt, 2011: Model, proxy and isotopic perspectives on the East African Humid Period. *Earth and Planetary Science Letters*, **307**, 103-112.
Timm, O., E. Ruprecht, and S. Kleppek, 2004: Scale-dependent reconstruction of the NAO index. *Journal of Climate*, **17**, 2157-2169.
Timm, O., P. Köhler, A. Timmermann, and L. Menviel, 2010: Mechanisms for the Onset of the African Humid Period and Sahara Greening 14.5-11 ka BP. *Journal of Climate*, **23**, 2612-2633.
Timm, O., A. Timmermann, A. Abe-Ouchi, F. Saito, and T. Segawa, 2008: On the definition of seasons in paleoclimate simulations with orbital forcing. *Paleoceanography*, **23**, PA2221.
Timmermann, A., O. Timm, L. Stott, and L. Menviel, 2009: The Roles of CO_2 and Orbital Forcing in Driving Southern Hemispheric Temperature Variations during the Last 21 000 Yr. *Journal of Climate*, **22**, 1626-1640.
Timmermann, A., et al., 2007: The influence of a weakening of the Atlantic meridional overturning circulation on ENSO. *Journal of Climate*, **20**, 4899-4919.
Timmreck, C., S. J. Lorenz, T. J. Crowley, S. Kinne, T. J. Raddatz, M. A. Thomas, and J. H. Jungclaus, 2009: Limited temperature response to the very large AD 1258 volcanic eruption. *Geophysical Research Letters*, **36**, L21708.
Tingley, M. P., and P. Huybers, 2010: A Bayesian Algorithm for Reconstructing Climate Anomalies in Space and Time. Part I: Development and Applications to Paleoclimate Reconstruction Problems. *Journal of Climate*, **23**, 2759-2781.
Tingley, M. P., P. F. Craigmile, M. Haran, B. Li, E. Mannshardt, and B. Rajaratnam, 2012: Piecing together the past: statistical insights into paleoclimatic reconstructions. *Quaternary Science Reviews*, **35**, 1-22.
Tjallingii, R., et al., 2008: Coherent high- and low-latitude control of the northwest African hydrological balance. *Nature Geoscience*, **1**, 670-675.
Toggweiler, J. R., J. L. Russell, and S. R. Carson, 2006: Midlatitude westerlies, atmospheric CO_2, and climate change during the ice ages. *Paleoceanography*, **21**, PA2005.
Torrence, C., and G. P. Compo, 1998: A practical guide to wavelet analysis. *Bulletin of the American Meteorological Society*, **79**, 61-78.

Touchan, R., K. J. Anchukaitis, D. M. Meko, S. Attalah, C. Baisan, and A. Aloui, 2008: Long term context for recent drought in northwestern Africa. *Geophysical Research Letters*, **35**, L13705.
Touchan, R., K. Anchukaitis, D. Meko, M. Sabir, S. Attalah, and A. Aloui, 2011: Spatiotemporal drought variability in northwestern Africa over the last nine centuries. *Climate Dynamics*, **37**, 237-252.
Trachsel, M., et al., 2012: Multi-archive summer temperature reconstruction for the European Alps, AD 1053–1996. *Quaternary Science Reviews*, **46**, 66-79.
Trouet, V., J. D. Scourse, and C. C. Raible, 2012: North Atlantic storminess and Atlantic Meridional Overturning Circulation during the last Millennium: Reconciling contradictory proxy records of NAO variability. *Global and Planetary Change*, **84-85**, 48-55.
Trouet, V., J. Esper, N. E. Graham, A. Baker, J. D. Scourse, and D. C. Frank, 2009: Persistent Positive North Atlantic Oscillation Mode Dominated the Medieval Climate Anomaly. *Science*, **324**, 78-80.
Tudhope, A. W., et al., 2001: Variability in the El Niño-Southern Oscillation Through a Glacial-Interglacial Cycle. *Science*, **291**, 1511-1517.
Turney, C. S. M., and R. T. Jones, 2010: Does the Agulhas Current amplify global temperatures during super-interglacials? *Journal of Quaternary Science*, **25**, 839-843.
Tzedakis, P. C., J. E. T. Channell, D. A. Hodell, H. F. Kleiven, and L. C. Skinner, 2012: Determining the natural length of the current interglacial. *Nature Geoscience*, **5**, 138-141.
Uemura, R., V. Masson-Delmotte, J. Jouzel, A. Landais, H. Motoyama, and B. Stenni, 2012: Ranges of moisture-source temperature estimated from Antarctic ice cores stable isotope records over glacial–interglacial cycles. *Climate of the Past*, **8**, 1109-1125.
Urrutia, R., A. Lara, R. Villalba, D. Christie, C. Le Quesne, and A. Cuq, 2011: Multicentury tree ring reconstruction of annual streamflow for the Maule River watershed in south central Chile. *Water Resources Research*, **47**, W06527.
van de Berg, W. J., M. van den Broeke, J. Ettema, E. van Meijgaard, and F. Kaspar, 2011: Significant contribution of insolation to Eemian melting of the Greenland ice sheet. *Nature Geoscience*, **4**, 679-683.
van de Plassche, O., K. van der Borg, and A. F. M. de Jong, 1998: Sea level–climate correlation during the past 1400 yr. *Geology*, **26**, 319-322.
van den Berg, J., R. S. W. van de Wal, G. A. Milne, and J. Oerlemans, 2008: Effect of isostasy on dynamical ice sheet modeling: A case study for Eurasia. *Journal of Geophysical Research-Solid Earth*, **113**, B05412.
Varma, V., et al., 2012: Holocene evolution of the Southern Hemisphere westerly winds in transient simulations with global climate models. *Climate of the Past*, **8**, 391-402.
Vasskog, K., Ø. Paasche, A. Nesje, J. F. Boyle, and H. J. B. Birks, 2012: A new approach for reconstructing glacier variability based on lake sediments recording input from more than one glacier. *Quaternary Research*, **77**, 192-204.
Vaughan, D. G., D. K. A. Barnes, P. T. Fretwell, and R. G. Bingham, 2011: Potential seaways across West Antarctica. *Geochemistry Geophysics Geosystems*, **12**, Q10004.
Vavrus, S., 2004: The impact of cloud feedbacks on Arctic climate under greenhouse forcing. *Journal of Climate*, **17**, 603-615.
Velichko, A. A., O. K. Borisova, and E. M. Zelikson, 2008: Paradoxes of the Last Interglacial climate: reconstruction of the northern Eurasia climate based on palaeofloristic data. *Boreas*, **37**, 1-19.
Verleyen, E., et al., 2011: Post-glacial regional climate variability along the East Antarctic coastal margin-Evidence from shallow marine and coastal terrestrial records. *Earth-Science Reviews*, **104**, 199-212.
Verschuren, D., K. Laird, and B. Cumming, 2000: Rainfall and drought in equatorial East Africa during the past 1000 years. *Nature*, **403**, 410-414.
Verschuren, D., J. S. Sinninghe Damste, J. Moernaut, I. Kristen, M. Blaauw, M. Fagot, and G. H. Haug, 2009: Half-precessional dynamics of monsoon rainfall near the East African Equator. *Nature*, **462**, 637-641.
Vettoretti, G., and W. R. Peltier, 2011: The impact of insolation, greenhouse gas forcing and ocean circulation changes on glacial inception. *The Holocene*, **21**, 803-817.
Viau, A. E., M. Ladd, and K. Gajewski, 2012: The climate of North America during the past 2000-years reconstructed from pollen data. *Global and Planetary Change*, **84–85**, 75-83.
Vieira, L. E., S. K. Solanki , A. V. Krivov, and I. G. Usoskin 2011: Evolution of the solar irradiance during the Holocene. *Astronomy & Astrophysics*, **531**, A6.
Vieira, L. E. A., and S. K. Solanki, 2010: Evolution of the solar magnetic flux on time scales of years to millenia. *Astronomy & Astrophysics*, **509**, A100.
Villalba, R., M. Grosjean, and T. Kiefer, 2009: Long-term multi-proxy climate reconstructions and dynamics in South America (LOTRED-SA): State of the art and perspectives. *Palaeogeography, Palaeoclimatology, Palaeoecology*, **281**, 175-179.
Villalba, R. L., et al., submitted: Unprecedented tree-growth patterns in the Southern Hemisphere induced by atmospheric circulation changes. *Nature Geoscience*.
Vimeux, F., P. Ginot, M. Schwikowski, M. Vuille, G. Hoffmann, L. G. Thompson, and U. Schotterer, 2009: Climate variability during the last 1000 years inferred from Andean ice cores: A review of methodology and recent results. *Palaeogeography, Palaeoclimatology, Palaeoecology*, **281**, 229-241.

Vinther, B., P. Jones, K. Briffa, H. Clausen, K. Andersen, D. Dahl-Jensen, and S. Johnsen, 2010: Climatic signals in multiple highly resolved stable isotope records from Greenland. *Quaternary Science Reviews*, **29**, 522-538.
Vinther, B. M., et al., 2009: Holocene thinning of the Greenland ice sheet. *Nature*, **461**, 385-388.
von Grafenstein, U., E. Erlenkeuser, J. Müller, J. Jouzel, and S. Johnsen, 1998: The cold event 8,200 years ago documented in oxygen isotope records of precipitation in Europe and Greenland. *Climate Dynamics*, **14**, 73-81.
von Gunten, L., M. Grosjean, B. Rein, R. Urrutia, and P. Appleby, 2009: A quantitative high-resolution summer temperature reconstruction based on sedimentary pigments from Laguna Aculeo, central Chile, back to AD 850. *The Holocene*, **19**, 873-881.
von Storch, H., E. Zorita, J. Jones, F. Gonzalez-Rouco, and S. Tett, 2006: Response to Comment on "Reconstructing Past Climate from Noisy Data". *Science*, **312**, 1872-1873.
Vuille, M., et al., 2012: A review of the South American Monsoon history as recorded in stable isotopic proxies over the past two millennia. Climate of the Past Discussion, 637-668.
Waelbroeck, C., et al., 2002: Sea level and deep water temperature changes derived from benthic foraminifera isotopic records. *Quaternary Science Reviews*, **21**, 295-305.
Wagner, J. D. M., J. E. Cole, J. W. Beck, P. J. Patchett, G. M. Henderson, and H. R. Barnett, 2010: Moisture variability in the southwestern United States linked to abrupt glacial climate change. *Nature Geoscience*, **3**, 110-113.
Wagner, S., et al., 2007: Transient simulations, empirical reconstructions and forcing mechanisms for the Mid-holocene hydrological climate in southern Patagonia. *Climate Dynamics*, **29**, 333-355.
Wahl, E., et al., 2010: An archive of high-resolution temperature reconstructions over the past 2+millennia. *Geochemistry Geophysics Geosystems*, **11**, Q01001.
Wahl, E. R., D. M. Ritson, and C. M. Ammann, 2006: Comment on "Reconstructing past climate from noisy data". *Science*, **312**, 529.
Wahl, E. R., H. F. Diaz, and C. Ohlwein, 2012: A pollen-based reconstruction of summer temperature in central North America and implications for circulation patterns during medieval times. *Global and Planetary Change*, **84–85**, 66-74.
Walter, K. M., S. A. Zimov, J. P. Chanton, D. Verbyla, and F. S. Chapin, 2006: Methane bubbling from Siberian thaw lakes as a positive feedback to climate warming. *Nature*, **443**, 71-75.
Wan, S., J. Tian, S. Steinke, A. Li, and T. Li, 2010: Evolution and variability of the East Asian summer monsoon during the Pliocene: Evidence from clay mineral records of the South China Sea. *Palaeogeography, Palaeoclimatology, Palaeoecology*, **293**, 237-247.
Wanamaker, A. D., P. G. Butler, J. D. Scourse, J. Heinemeier, J. Eiríksson, K. L. Knudsen, and C. A. Richardson, 2012: Surface changes in the North Atlantic meridional overturning circulation during the last millennium. *Nature Communications*, **3**, 899.
Wang, B., and Q. Ding, 2008: Global monsoon: Dominant mode of annual variation in the tropics. *Dynamics of Atmospheres and Oceans*, **44**, 165-183.
Wang, S., X. Wen, Y. Luo, W. Dong, Z. Zhao, and B. Yang, 2007: Reconstruction of temperature series of China for the alst 1000 years. *Chinese Science Bulletin*, **52**, 3272-3280.
Wang, Y. J., H. Cheng, R. L. Edwards, Z. S. An, J. Y. Wu, C. C. Shen, and J. A. Dorale, 2001: A high-resolution absolute-dated Late Pleistocene monsoon record from Hulu Cave, China. *Science*, **294**, 2345-2348.
Wang, Y. J., et al., 2008: Millennial- and orbital-scale changes in the East Asian monsoon over the past 224,000 years. *Nature*, **451**, 1090-1093.
Wang, Y. M., J. Lean, and N. Sheeley, 2005: Modeling the Sun's Magnetic Field and Irradiance since 1713. *The Astrophysical Journal*, **625**, 522-538.
Wang, Y. M., S. L. Li, and D. H. Luo, 2009: Seasonal response of Asian monsoonal climate to the Atlantic Multidecadal Oscillation. *Journal of Geophysical Research-Atmospheres*, **114**, D02112.
Wanner, H., O. Solomina, M. Grosjean, S. P. Ritz, and M. Jetel, 2011: Structure and origin of Holocene cold events. *Quaternary Science Reviews*, **30**, 3109-3123.
Wanner, H., et al., 2008: Mid- to Late Holocene climate change: an overview. *Quaternary Science Reviews*, **27**, 1791-1828.
Waple, A. M., M. E. Mann, and R. S. Bradley, 2002: Long-term patterns of solar irradiance forcing in model experiments and proxy based surface temperature reconstructions. *Climate Dynamics*, **18**, 563-578.
Wara, M. W., A. C. Ravelo, and M. L. Delaney, 2005: Permanent El Niño-Like Conditions During the Pliocene Warm Period. *Science*, **309**, 758-761.
Watanabe, O., J. Jouzel, S. Johnsen, F. Parrenin, H. Shoji, and N. Yoshida, 2003: Homogeneous climate variability across East Antarctica over the past three glacial cycles. *Nature*, **422**, 509-512.
Watanabe, T., et al., 2011: Permanent El Niño during the Pliocene warm period not supported by coral evidence. *Nature*, **471**, 209-211.
Wegner, A., et al., 2012: Change in dust variability in the Atlantic sector of Antarctica at the end of the last deglaciation. *Climate of the Past*, **8**, 135-147.
Weldeab, S., 2012: Bipolar modulation of millennial-scale West African monsoon variability during the last glacial (75,000-25,000 years ago). *Quaternary Science Reviews*, **40**, 21-29.

Weldeab, S., R. R. Schneider, and M. Kölling, 2006: Deglacial sea surface temperature and salinity increase in the western tropical Atlantic in synchrony with high latitude climate instabilities. *Earth and Planetary Science Letters*, **241**, 699-706.

Weldeab, S., D. W. Lea, R. R. Schneider, and N. Andersen, 2007: 155,000 years of West African monsoon and ocean thermal evolution. *Science*, **316**, 1303-1307.

Wenzler, T., S. Solanki, and N. Krivova, 2005: Can surface magnetic fields reproduce solar irradiance variations in cycles 22 and 23? *Astronomy & Astrophysics*, **432**, 1057-1061.

Wenzler, T., S. K. Solanki, N. A. Krivova, and C. Fröhlich, 2006: Reconstruction of solar irradiance variations in cycles 21–23 based on surface magnetic fields. *Astronomy & Astrophysics*, **460**, 583-595.

Werner, J. P., J. Luterbacher, and J. E. Smerdon, in press: A Pseudoproxy Evaluation of Bayesian Hierarchical Modelling and Canonical Correlation Analysis for Climate Field Reconstructions over Europe. *Journal of Climate*.

Wetter, O., C. Pfister, R. Weingartner, J. Luterbacher, T. Reist, and J. Trösch, 2011: The largest floods in the High Rhine basin since 1268 assessed from documentary and instrumental evidence. *Hydrological Sciences Journal*, **56**, 733-758.

Widmann, M., H. Goosse, G. van der Schrier, R. Schnur, and J. Barkmeijer, 2010: Using data assimilation to study extratropical Northern Hemisphere climate over the last millennium. *Climate of the Past*, **6**, 627-644.

Wiersma, A., D. Roche, and H. Renssen, 2011: Fingerprinting the 8.2 ka event climate response in a coupled climate model. *Journal of Quaternary Science*, **26**, 118-127.

Wiles, G. C., D. J. Barclay, P. E. Calkin, and T. V. Lowell, 2008: Century to millennial-scale temperature variations for the last two thousand years indicated from glacial geologic records of Southern Alaska. *Global and Planetary Change*, **60**, 115-125.

Wiles, G. C., D. E. Lawson, E. Lyon, N. Wiesenberg, and R. D. D'Arrigo, 2011: Tree-ring dates on two pre-Little Ice Age advances in Glacier Bay National Park and Preserve, Alaska, USA. *Quaternary Research*, **76**, 190-195.

Wilhelm, B., et al., 2012: 1400 years of extreme precipitation patterns over the Mediterranean French Alps and possible forcing mechanisms. *Quaternary Research*, **78**, 1-12.

Wilmes, S. B., C. C. Raible, and T. F. Stocker, 2012: Climate variability of the mid- and high-latitudes of the Southern Hemisphere in ensemble simulations from 1500 to 2000 AD. *Climate of the Past*, **8**, 373-390.

Wilson, R., E. Cook, R. D'Arrigo, N. Riedwyl, M. N. Evans, A. Tudhope, and R. Allan, 2010: Reconstructing ENSO: the influence of method, proxy data, climate forcing and teleconnections. *Journal of Quaternary Science*, **25**, 62-78.

Wilson, R., D. Miles, N. Loader, T. Melvin, L. Cunningham, R. Cooper, and K. Briffa, 2012: A millennial long March–July precipitation reconstruction for southern-central England. *Climate Dynamics*. doi:10.1007/s00382-012-1318-z, advance online publication.

Wilson, R., et al., 2007: A matter of divergence: Tracking recent warming at hemispheric scales using tree ring data. *Journal of Geophysical Research*, **112**, D17103.

Winckler, G., R. F. Anderson, M. Q. Fleisher, D. McGee, and N. Mahowald, 2008: Covariant Glacial-Interglacial Dust Fluxes in the Equatorial Pacific and Antarctica. *Science*, **320**, 93-96.

Winkler, S., and J. Matthews, 2010: Holocene glacier chronologies: Are 'high-resolution' global and inter-hemispheric comparisons possible? *The Holocene*, **20**, 1137-1147.

Winter, A., et al., 2011: Evidence for 800 years of North Atlantic multi-decadal variability from a Puerto Rican speleothem. *Earth and Planetary Science Letters*, **308**, 23-28.

Woillez, M. N., G. Krinner, K. M., and D. G., 2012: Impact of solar forcing on the surface mass balance of northern ice sheets for glacial conditions. *Earth and Planetary Science Letters*, **335-336**, 18-24.

Wolff, C., et al., 2011: Reduced Interannual Rainfall Variability in East Africa During the Last Ice Age. *Science*, **333**, 743-747.

Woodhouse, C., and J. Overpeck, 1998: 2000 years of drought variability in the central United States. *Bulletin of the American Meteorological Society*, **79**, 2693-2714.

Woodhouse, C. A., D. M. Meko, G. M. MacDonald, D. W. Stahle, and E. R. Cook, 2010: A 1,200-year perspective of 21st century drought in southwestern North America. *Proceedings of the National Academy of Sciences*, **107**, 21283-21288.

Woodroffe, C., and R. McLean, 1990: Microatolls and recent sea level change on coral atolls. *Nature*, **344**, 531-534.

Woodroffe, C. D., M. R. Beech, and M. K. Gagan, 2003: Mid-late Holocene El Niño variability in the equatorial Pacific from coral microatolls. *Geophysical Research Letters*, **30**, 1358.

Woodroffe, C. D., H. V. McGregor, K. Lambeck, S. G. Smithers, and D. Fink, 2012: Mid-Pacific microatolls record sea level stability over the past 5000 yr. *Geology*. advance online publication.

Wu, T., 2012: A mass-flux cumulus parameterization scheme for large-scale models: description and test with observations. *Climate Dynamics*, **38**, 725-744.

Wu, T., et al., submitted: Global carbon budgets simulated by the Beijing Climate Center Climate System Model for the last century. *Journal of Climate*.

Wunsch, C., 2006: Abrupt climate change: An alternative view. *Quaternary Research*, **65**, 191-203.

Xie, S. P., Y. Okumura, T. Miyama, and A. Timmermann, 2008: Influences of Atlantic climate change on the tropical Pacific via the Central American Isthmus. *Journal of Climate*, **21**, 3914-3928.

Yadav, R., A. Braeuning, and J. Singh, 2011: Tree ring inferred summer temperature variations over the last millennium in western Himalaya, India. *Climate Dynamics*, **36**, 1545-1554.
Yang, B., A. Bräuning, Z. Dong, Z. Zhang, and J. Keqing, 2008: Late Holocene monsoonal temperate glacier fluctuations on the Tibetan Plateau. *Global and Planetary Change*, **60**, 126-140.
Yang, B., J. Wang, A. Bräuning, Z. Dong, and J. Esper, 2009: Late Holocene climatic and environmental changes in and central Asia. *Quaternary International*, **194**, 68-78.
Yin, Q., and A. Berger, 2012: Individual contribution of insolation and CO_2 to the interglacial climates of the past 800,000 years. *Climate Dynamics*, **38**, 709-724.
Yin, Q. Z., and A. Berger, 2010: Insolation and CO_2 contribution to the interglacial climate before and after the Mid-Brunhes Event. *Nature Geoscience*, **3**, 243-246.
Yiou, P., J. Servonnat, M. Yoshimori, D. Swingedouw, M. Khodri, and A. Abe-Ouchi, 2012: Stability of weather regimes during the last millennium from climate simulations. *Geophysical Research Letters*, **39**, L08703.
Yokoyama, Y., and T. M. Esat, 2011: Global climate and sea level: Enduring variability and rapid fluctuations over the past 150,000 years. *Oceanography*, **24**, 54–69.
Yoshimori, M., T. Yokohata, and A. Abe-Ouchi, 2009: A Comparison of Climate Feedback Strength between CO_2 Doubling and LGM Experiments. *Journal of Climate*, **22**, 3374-3395.
Yoshimori, M., J. C. Hargreaves, J. D. Annan, T. Yokohata, and A. Abe-Ouchi, 2011: Dependency of Feedbacks on Forcing and Climate State in Physics Parameter Ensembles. *Journal of Climate*, **24**, 6440-6455.
Yu, S.-Y., B. E. Berglund, P. Sandgren, and K. Lambeck, 2007: Evidence for a rapid sea level rise 7600 yr ago. *Geology*, **35**, 891-894.
Yu, Z., J. Loisel, D. P. Brosseau, D. W. Beilman, and S. J. Hunt, 2010: Global peatland dynamics since the Last Glacial Maximum. *Geophysical Research Letters*, **37**, L13402.
Yue, X., H. Wang, H. Liao, and D. Jiang, 2010: Simulation of the Direct Radiative Effect of Mineral Dust Aerosol on the Climate at the Last Glacial Maximum. *Journal of Climate*, **24**, 843-858.
Zachos, J. C., G. R. Dickens, and R. E. Zeebe, 2008: An early Cenozoic perspective on greenhouse warming and carbon-cycle dynamics. *Nature*, **451**, 279-283.
Zha, X., C. Huang, and J. Pang, 2009: Palaeofloods recorded by slackwater deposits on the Qishuihe River in the Middle Yellow River. *Journal of Geographical Sciences*, **19**, 681-690.
Zhang, P. Z., et al., 2008: A Test of Climate, Sun, and Culture Relationships from an 1810-Year Chinese Cave Record. *Science*, **322**, 940-942.
Zhang, Q., H. S. Sundqvist, A. Moberg, H. Kornich, J. Nilsson, and K. Holmgren, 2010: Climate change between the mid and late Holocene in northern high latitudes - Part 2: Model-data comparisons. *Climate of the Past*, **6**, 609-626.
Zhang, R., and T. L. Delworth, 2006: Impact of Atlantic multidecadal oscillations on India/Sahel rainfall and Atlantic hurricanes. *Geophysical Research Letters*, **33**, L17712.
Zhang, Y., Z. Kong, S. Yan, Z. Yang, and J. Ni, 2009: "Medieval Warm Period" on the northern slope of central Tianshan Mountains, Xinjiang, NW China. *Geophysical Research Letters*, **36**, L11702.
Zheng, J. Y., W. C. Wang, Q. S. Ge, Z. M. Man, and P. Y. Zhang, 2006: Precipitation variability and extreme events in eastern China during the past 1500 years. *Terrestrial Atmospheric and Oceanic Sciences*, **17**, 579-592.
Zheng, W., P. Braconnot, E. Guilyardi, U. Merkel, and Y. Yu, 2008: ENSO at 6ka and 21ka from ocean-atmosphere coupled model simulations. *Climate Dynamics*, **30**, 745-762.
Zhou, T., B. Li, W. Man, L. Zhang, and J. Zhang, 2011: A comparison of the Medieval Warm Period, Little Ice Age and 20th century warming simulated by the FGOALS climate system model. *Chinese Science Bulletin*, **56**, 3028-3041.
Zhu, H., F. Zheng, X. Shao, X. Liu, X. Yan, and E. Liang, 2008: Millennial temperature reconstruction based on tree-ring widths of Qilian juniper from Wulan, Qinghai province, China. *Chinese Science Bulletin*, **53**, 3914-3920.
Zinke, J., M. Pfeiffer, O. Timm, W. C. Dullo, and G. Brummer, 2009: Western Indian Ocean marine and terrestrial records of climate variability: a review and new concepts on land–ocean interactions since AD 1660. *International Journal of Earth Sciences*, **98**, 115-133.

Appendix 5.A: Supplementary Material

Table 5.A.1: Summary of Atmospheric CO_2 Proxy Methods and Confidence Assessment of their Main Assumptions.

Method	Scientific Rationale	Estimated Applicability	Limitations	Main Assumptions (*relative confidence*)
Alkenone (phytoplankton biomarker) carbon isotopes	Measurements of carbon isotope ratios of marine sedimentary alkenones (or other organic compounds) allows determination of the isotopic fractionation factor during carbon fixation (ε_p) from which pCO_2 can be calculated.	100– ~4000 ppm; 0–100 Ma	Alkenones are often rare in oligotrophic areas and sometimes absent. Method relies on empirical calibration and $\delta^{13}C$ is sensitive to other environmental factors, especially nutrient-related variables. Method has been used successfully to reconstruct glacial-interglacial changes.	Measured alkenone carbon isotope ratio is accurate and precise (*high*). Ambient aqueous pCO_2 has a quantifiable relationship with ε_p that can be distinguished from the nutrient-related physiological factors such as algal growth rate, cell size, cell geometry and light-limited growth (*medium*). Aqueous pCO_2 is in equilibrium with atmospheric pCO_2 (*medium*). Carbon isotope fractionation in modern alkenone-producing species is the same in ancient species and constant through time (*medium*). Levels of biological productivity (e.g., dissolved phosphate concentrations) can be calculated (*high*). Carbon isotope ratio of aqueous CO_2 in the mixed layer can be determined (*medium*). Sea surface temperature can be determined (*high*). Atmospheric pO_2 is known or assumed (*medium*). Diagenetic effects are minimal, or can be quantified *(medium*).
Boron isotopes in foraminifera	Boron isotope ratios ($\delta^{11}B$) in foraminifera (or other calcifying organisms) give paleo-pH from which pCO_2 can be calculated if a value for a second carbonate system parameter (e.g., alkalinity) is assumed	100– ~4000 ppm; 0–100 Ma	Calculated pCO_2 is very sensitive to the boron isotope ratio of seawater which is relatively poorly known, especially for the earlier Cenozoic. Effects of foraminiferal preservation are not well understood. Method has been used successfully to reconstruct glacial-interglacial changes.	Measured boron isotope ratio is accurate and precise (*high*): The equilibrium constant for dissociation of boric acid and boron isotopic fractionation between $B(OH)_3$ and $B(OH)_4^-$ are well known (*high*): Boron incorporation into carbonate is exclusively from borate ion (*high*). Boron isotope ratio of foraminifer calcification reflects ambient surface seawater pH (*high*). Aqueous pCO_2 is in equilibrium with atmospheric pCO_2 (*high*) Habitats of extinct species can be determined (*high*) There is no vital effect fractionation in extinct species, or it can be determined (*high*). The boron isotope ratio of seawater ($\delta^{11}B_{sw}$) can be determined (*medium*). Ocean alkalinity or concentration of Total Dissolved Inorganic Carbon can be determined (*high*). Sea surface temperature (SST) and salinity (SSS) can be determined (*high*). Diagenetic effects are minimal or can be quantified (*medium*).
Carbon isotopes in soil carbonate and organic matter	Atmospheric pCO_2 affects the relationship between the $\delta^{13}C$ of soil CO_2 and the $\delta^{13}C$ of soil organic matter at depth in certain soil types, hence measurement of	100– ~2000 ppm; 0–400 Ma	Method works better for some soil types than others. CO_2 loss is difficult to quantify and method and effects of late diagenesis may be difficult to determine.	Isotopic composition of soil CO_2 is reflected in soil carbonates below a depth of 50 cm. (*medium*) The concentration of respired CO_2 in the soil is known or assumed (*medium*). Isotopic composition of atmospheric CO_2 is known or can be inferred

	these parameters in paleosols can be used to calculate past pCO_2			(*low*) Soil carbonates were precipitated in the vadose zone in exchange with atmospheric CO_2 (*high*).The original depth profile of a paleosol can be determined (*low*). Burial (late) diagenetic effects are minimal or can be quantified (*high*).
Stomata in plant leaves	The relative frequency of stomata on fossil leaves (Stomatal Index; (Salisbury, 1928)) can be used to calculate past atmospheric CO_2 levels	100– ~700 ppm; 0–400 Ma	Closely related species have very different responses to pCO_2. The assumption that short-term response is the same as the evolutionary response is difficult to test. This and the shape of the calibration curves mean that much greater confidence applies to low pCO_2 and short timescales.	Measured stomatal index is accurate and precise (*high*). Measured stomatal index is representative of the plant (*high*) The target plants adjust their stomatal index of leaves to optimize CO_2 uptake (*medium*). Atmospheric pCO_2 close to the plant is representative of the atmosphere as a whole (*medium*). The quantitative relationship between stomatal index and CO_2 observed on short timescales (ecophenotypic or 'plastic response') applies over evolutionary time (*low*). Environmental factors such as irradiance, atmospheric moisture, water availability, temperature, and nutrient availability do not affect the relationship between stomatal index and CO_2 (*medium*). Stomatal index response to CO_2 of extinct species can be determined or assumed (*low*). Taphonomic processes do not affect stomatal index counts (*high*). Diagenetic processes do not affect stomatal index counts (*high*).

Table 5.A.2: Summary of SST proxy methods and confidence assessment of their main assumptions.

Method	Scientific Rationale	Estimated Applicability	Limitations	Main Assumptions (*relative confidence*)
$\delta^{18}O$ of mixed-layer planktonic foraminifera	Partitioning of $^{18}O/^{16}O$ from seawater into calcite shells of all foraminifera is temperature dependent. Verified by theoretical, field and laboratory studies. Utilizes extant and extinct species that resided in the photic zone.	0–50°C, 0–150 Ma	The $^{18}O/^{16}O$ ratios of recrystallized planktonic foraminifer shells in carbonate-rich sediments are biased toward colder seafloor temperatures, and at most, can only constrain the lower limit of SST. The transition in preservation is progressive with age. Well-preserved forams from clay rich sequences on continental margins are preferred. Diagenetic calcite is detectable by visual and microscopic techniques	Analytical errors are negligible (*high*) Sensitivity to T is high and similar to modern descendants (*high*) Seawater $\delta^{18}O$ is known. The uncertainty varies with time depending on presence of continental ice-sheets, though error is negligible in the Pleistocene and during minimal ice periods such as the Eocene (<±0.25°C). Error doubles during periods of Oligocene and early Neogene glaciation because of weak constraints on ice-volume. (*medium to high*) Species lives in the mixed-layer and thus records SST (*high*) Local salinity/seawater $\delta^{18}O$ is known (*low* to *medium*) Carbonate ion/pH is similar to modern (*medium*, *high*) Foraminifera from clay-rich sequences are well preserved and ratios unaffected by diagenesis (*high)* Foraminifera from carbonate-rich pelagic sequences are well preserved and ratios unaffected by diagenesis *(high to low; decreasing confidence*

				with age) Biased towards summer SST in polar oceans (*medium*)
Mg/Ca in mixed-layer planktonic foraminifera	Partitioning of Mg/Ca from seawater into calcite shells is temperature dependent. Calibration to T is based on empirical field and laboratory culturing studies, as Mg concentrations of inorganically precipitated calcite are an order of magnitude higher than in biogenic calcite. There is no ice-volume influence on seawater Mg/Ca, though sensitivity does change with seawater Mg concentration	5–35°C, 0–65 Ma	Diagenetic recrystallization of foram shells can bias ratios, though the direction of bias is unknown and comparisons with other proxies suggest it is minor. The Mg/Ca is also slightly sensitive to seawater pH. Long-term changes in seawater Mg/Ca, on the order of a 2–5 %/10 myr, must be constrained via models.	Analytical errors are negligible (*high*) Mg containing oxide and organic contaminants have been removed by oxidative/reductive cleaning (*high*) Sensitivity to T in extinct species is similar to modern species (*medium*) Species lives in the mixed-layer and thus records SST (*high*) Seawater Mg/Ca is known (*high to medium*: *decreasing confidence with time*). Surface water carbonate ion/pH is similar to modern (*medium*) Forams from clay-rich sequences are well preserved and ratios unaffected by diagenesis (*high)* Forams from carbonate-rich pelagic sequences are well preserved and ratios unaffected by diagenesis *(high to low; decreasing confidence with age*) Biased towards summer SST in polar oceans (*medium*)
TEX_{86} index in Archea	The ratio of cyclopentane rings in archaeal tetraether lipids (TEX), i.e., isoprenoid glycerol dibiphytanyl glycerol tetraethers (GDGTs), is sensitive to the temperature of growth environment. The relationship and calibration with temperature is empirical (based on core tops), as the underlying mechanism(s) for this relationship has yet to be identified. Verification of field calibrations with laboratory cultures is still in progress. The compounds are extracted from bulk sediments.	1–40°C, 0–150 Ma	The depth from which the bulk of sedimentary GDGT's are produced is assumed to be the mixed-layer though this cannot be verified, for the modern or past. At least two species with differing ecologies appear to be producing the tetraethers. The GDGT signal is ultimately an integrated community signal allowing the potential for evolutionary changes to influence regional signals over time. Tetraethers are found in measurable abundances on continental shelves and/or organic rich sediments.	Analytical errors are small (*high*) Sensitivity to T similar to modern (*medium*) Species that produced tropical sedimentary GDGT's resided mainly in the mixed-layer and thus records SST (*medium to high*) Species that produced the sedimentary GDGT's in the sub-polar to polar regions mainly resided in the mixed-layer and thus records SST (*low*) No alteration of GDGT ratios during degradation of compounds (*medium to low: decreasing confidence with age*) No contamination by GDGT's derived from terrestrial sources (*medium to high depending on location of samples)* Biased towards summer SST in polar oceans (*medium*)
UK_{37} Index in Algae	Based on the relative concentration of C_{37} methyl ketones derived from the cells of haptophyte phytoplankton. Calibrations are empirically derived through field and culture studies	5–28°C, 0–50 Ma	The distribution of haptophyte algae ranges from sub-polar to tropical	Analytical errors are negligible (*high*) Sensitivity to SST similar to modern (*medium to high; decreasing confidence with time*) Species that produced the sedimentary alkenones lived in the mixed-layer and thus record SST (*high*) No alteration of alkenone saturation index during degradation of compounds (*medium; decreasing confidence with age*) Biased towards summer SST in polar oceans (*medium*)

Microfossil census modern analogue techniques	Utilises a statistical correlation between extant planktonic microfossil assemblage data (most commonly foraminifera, but also diatoms and radiolarian) and modern analogue databases. Most commonly used statistical methods are modern analogue technique (MAT) and artificial neural network (ANN).	0–40 °C 0–5 Ma	Dependent on quality, coverage, size and representativeness of the core top modern analogue data base. Extant species reduce with increasing age. This and paleogeographic and ocean circulation differences with age-limit applicability beyond 5 Ma.	The ecology of modern assemblages is largely controlled by SST (*high*) Sensitivity of paleo-assemblages to SST is similar to modern (*high, but decreases with increasing age*) Eurythermal assemblages responding to non-temperature (e.g., nutrient availability) influences can be identified (*medium*) That the extant species used to reconstruct SST mainly reside in the mixed layer (*medium to high*). Depositional and post-depositional processes have not biased the assemblage (*medium to high*)

Table 5.A.3: Assessment of leads and lags between Antarctic, hemispheric temperatures and atmospheric CO_2 concentration during terminations. Chronological synthesis of publications, main findings, incorporation in IPCC assessments and key uncertainties.

Reference	Investigated Period	Source CO_2 Data	Source Temperature Data	Lag Quantification Method	Lag Between Temperature and CO_2 (positive, temperature lead)	Key Limitations
TAR : From a detailed study of the last three glacial terminations in the Vostok ice core, Fischer et al., (1999) conclude that CO_2 increases started 600 ± 400 years after the Antarctic warming. However, considering the large uncertainty in the ages of the CO_2 and ice (1000 years or more if we consider the ice accumulation rate uncertainty), Petit et al., (1999) felt it premature to ascertain the sign of the phase relationship between CO_2 and Antarctic temperature at the initiation of the terminations. In any event, CO_2 changes parallel Antarctic temperature changes during deglaciations (Blunier et al., 1997; Petit et al., 1999; Sowers and Bender, 1995).						
(Fischer et al., 1999)	Termination I Terminations I, II, III	Taylor Dome, Byrd* (CH_4 synchonized age scales) Vostok* (gas age scales based on firn modeling)	Byrd d^{18}O, Vostok dD (CH_4 synchonized age) Vostok* dD (GT4 ice age scale)	Maximum at onset of interglacial periods	Antarctica: 600 ± 400 years	Ice core synchronization for Termination I (~300 years) Gas age-ice age difference simulated by firn models for interglacial conditions could be overestimated by ~400 years Signal to noise ratio Resolution of CO_2 measurements and firnification smoothing (~300 years)
(Petit et al., 1999) (Pépin et al., 2001)	Terminations I, II, III, IV	Vostok* (GT4 gas age scale based on firn modeling)	Vostok dD (GT4 ice age age)	Onset of transitions	Antarctica: in phase within uncertainties Positive	Gas age-ice age difference simulated by firn models for glacial conditions could be overestimated by up to 1500 yr Resolution of CO_2 measurements and firnification smoothing (~300 yr)

(Mudelsee, 2001)	0–430 ky		Entire record	Antarctica : 1300 ± 1000 years	Signal to noise ratio (1 ice core)	

AR4: High-resolution ice core records of temperature proxies and CO_2 during deglaciation indicates that Antarctic temperature starts to rise several hundred years before CO_2 (Caillon et al., 2003; Monnin et al., 2001). During the last deglaciation, and likely also the three previous ones, the onset of warming at both high southern and northern latitudes preceded by several thousand years the first signals of significant sea level increase resulting from the melting of the northern ice sheets linked with the rapid warming at high northern latitudes (Pépin et al., 2001; Petit et al., 1999; Shackleton, 2000). Current data are not accurate enough to identify whether warming started earlier in the Southern Hemisphere (SH) or Northern Hemisphere (NH), but a major deglacial feature is the difference between North and South in terms of the magnitude and timing of strong reversals in the warming trend, which are not in phase between the hemispheres and are more pronounced in the NH (Blunier and Brook, 2001).

(Monnin et al., 2001)	Termination I	High resolution data from EDC on EDC1 gas age scale (based on firn modeling)	EDC on EDC1 ice age scale	Crossing points of linear fit	Antarctica: 800 ± 600 years	Gas age-ice age difference (±1000 years) Signal to noise ratio (1 ice core)
(Caillon et al., 2003)	Termination III	Vostok on GT4 gas age scale	Vostok $d^{40}Ar$ on GT4 gas age scale	Maximum lagged correlation	Antarctica: 800 ± 200 years	Relationship between $d^{40}Ar$ and temperature assumed to be instantaneous. The 800 yr is a minimum CO_2-temperature lag which does not account for a possible delayed response of firn gravitational fractionation to surface temperature change

AR5 : Continental temperatures in Antarctica are governed by a number of processes, including the dominant CO2 radiative effect, orbital forcing and changes in ice-sheet height. Previous reconstructions indicated a lead of Antarctic temperature over CO2 concentration during previous glacial terminations by 800 ± 600 years (Caillon et al., 2003; Monnin et al., 2001; Appendix 5.3). Recently an improved estimate of gas ice-ice age differences in different ensembles of Antarctic ice cores suggested that earlier studies likely overestimated this lead. For the last glacial termination the most recent estimate is indistinguishable from zero (Parrenin et al., submitted; Pedro et al., 2012).

Large-scale reconstuctions of Southern Hemisphere climate change (Shakun et al., 2012) for the last glacial termination document a lead of Southern Hemisphere averaged temperature over Northern Hemisphere temperature. This lead can be explained by the bipolar thermal seesaw concept (Stocker and Johnsen, 2003) (see also Section 5.7) related to changes in the interhemispheric ocean heat transport caused by weakening of the AMOC during glacial termination (Ganopolski and Roche, 2009). Southern Hemisphere warming prior to Northern Hemisphere warming can also be explained by the fast sea ice response to changes in austral spring insolation (Stott et al., 2007; Timmermann et al., 2009). According to these mechanisms, southern temperature lead over Northern Hemisphere neither contradicts the northern hemisphere forcing of deglacial ice volume changes (high confidence), nor the important role of CO2 in generating glacial-interglacial temperature variations due to the greenhouse effect.

(Shakun et al., 2012)	Termination I	EDC age scale synchronized to GICC05^{+}(Lemieux-Dudon et al., 2010)	NH : stack of 50 records including 2 Greenland ice cores SH : stack of 30 records incl. 4 ice cores (Vostok, EDML, EDC, Dome	Lag correlation (20 to 10 ka) using Monte-Carlo statistics	SH : 620 ± 660 years NH : –720 ± 660 years Global : –460 ± 340 years	Uncertainties in the original age scales of each record: e.g., reservoir ages of marine sediments, radiocarbon calibration (intCal04), Antarctic gas / ice chronology Similar limitations as in earlier studies for Antarctic temperature lead on CO_2 Non stability of the phase lags : global temperature leads

		F)* on their original age scale			CO_2 at the onset of deglacial warming
(Pedro et al., 2012)	Siple Dome and Byrd, synchronized to GICC05$^+$ age scale	$d^{18}O$ composite (Law Dome, Siple Dome, Byrd, EDML and TALDICE* ice cores) synchronized to GICC05$^+$ using firn modelling (Pedro et al., 2011)	Lag correlation (9–21 ka) and derivative lag correlation	Antarctica: 200 ± 200 years	Uncertainty on gas – ice age difference in high accumulation sites (<300 years) and on synchronization methods to GICC05; data resolution Temperature versus other (e.g., elevation, moisture origin) signals in coastal ice core $d^{18}O$ Correlation method sensitive to minima, maxima and inflexion points
(Parrenin et al., submitted)	EDC, new gas age scale produced from the modified EDC3 ice age scale using lock-in depth derived from $d^{15}N$ of N_2 and adjusted to be consistent with GICC05$^+$ gas age scale. Processes affecting the gas lock-in depth such as impurities are implicitly taken into account when using $d^{15}N$ (no use of firn models).	Stack temperature profile derived from water isotopes from EDC*, Vostok*, Dome Fuji*, TALDICE* and EDML* synchronized to a modified EDC3 ice age scale	Monte-Carlo algorithm at linear break points	Antarctica: Warming onset: –70 ± 260 years Bølling onset: 300 ± 180 years Younger Dryas onset: –20 ± 150 years Holocene onset: 540 ± 120 years	Accuracy, resolution and interpolation of $d^{15}N$ of N_2; assumption of no firn convective zone at EDC under glacial conditions. Data resolution and noise (e.g., precipitation intermittency biases in stable isotope records)

Notes:

* Names of different Antarctic ice cores (Byrd, Taylor Dome, Vostok, Siple Dome, Law Dome, TALDICE, Dome Fuji, EDML, EDC), with different locations, surface climate and firnification conditions. For the most inland sites (Vostok, EDC, Dome Fuji), at a given ice core depth, gas ages are lower than ice ages by 1500–2000 years (interglacial conditions) and 5000–5500 years (glacial conditions) while this gas age-ice age difference is lower (400–800. years) for coastal, higher accumulation sites (Byrd, Law Dome, Siple Dome).

$^+$GICC05: Greenland Ice Core Chronology 2005, based on annual layer counting in Greenland (NGRIP, GRIP and DYE3 ice cores) (Rasmussen et al., 2006), back to 60 ka(Svensson et al., 2008). The synchronism between rapid shifts in Greenland climate and in atmospheric CH_4 variations allows to transfer GICC05 to Greenland and then to Antarctic CH_4 variations (Blunier et al., 2007).

Additional point: CO_2-Antarctic temperature phase during AIM events

Studies on CO_2 phasing relative to CH_4 during Dansgaard Oeschger event onsets (Ahn and Brook, 2008; Bereiter et al., 2012) suggest a lag of maximum CO_2 concentration relative to the Antarctic Isotope Maxima (AIM) 19, 20, 21, 23 and 24 by 260±220 yr during MIS5 and 670–870 yr±360 yr relative to AIM 12, 14, 17 during MIS3 (Bereiter et al., 2012). Accordingly, the lag is dependent on the climate state. A lag is not discernable for shorter AIM. This study avoids the ice age/gas age difference problem, but relies on the bipolar seesaw concept, i.e., it assumes that maximum Antarctic temperatures are coincident to the onset of DO events and the concurrent CH_4 increase.

5.A.1 Supplemental Information for Figure 5.8

Comparisons of simulated and reconstructed NH temperature changes. The reconstructions and simulations that contribute to each panel are indicated in the appendix of the main text (Tables 5.A1 and 5.A2, respectively). Note that some reconstructions represent a smaller spatial domain than the full NH or a specific season, while annual temperatures for the full NH mean are shown for the simulations.

(a) Multi-model mean and estimated 90% multi-model range are shown by the thick and thin lines, respectively, for two groups of simulations: those forced by stronger (weaker) solar variability in red (blue). Note that the strength of the solar variability is not the only difference between these groups: the GCMs and the other forcings are also different between the groups. Overlap of reconstructed temperatures shown by green shading. All timeseries are expressed as anomalies from their 1500–1850 CE mean; and smoothed with a 30-year Gaussian-weighted filter, truncated 7 years from the end of each series to reduce end-effects of the filter. The grey shading represents a measure of the overlapping reconstruction confidence intervals, with scores of 1 and 2 assigned to temperatures within ±1.645 (90% confidence range) or ±1 standard deviation, respectively, then summed over all reconstructions and scaled so that the maximum score is dark grey, and minimum score is pale grey.

(b-d) Superposed composites (time segments from selected periods positioned so that the years with peak negative forcing are aligned) of the forcing and temperature response to (b) individual volcanic forcing events; (c) multi-decadal changes in volcanic activity; (d) multi-decadal changes in solar irradiance. Upper panels show the volcanic forcing (b), 40-year smoothed volcanic forcing (c), or 40-year difference in band-pass filtered solar forcing (d) for the individual selected periods (think lines) and the composite mean (thick). In (d), the thick green line shows the composite mean of the volcanic forcing, also band-pass filtered, but constructed using the solar composite periods to demonstrate the changes in volcanic forcing that are coincident with solar variability. Lower panels show the NH temperature composite means and estimated 90% range of simulations (red line, pink shading) and reconstructions (grey line and shading), with overlap between the simulated and reconstructed ranges (darker shading). Each composite is shifted to have zero mean during the (b) 5 or (c–d) 40 years preceding the peak negative forcing. Only reconstructions capable of resolving (b) interannual or (c–d) interdecadal variations are used. Reconstructed and simulated temperature timeseries were first (c) smoothed with a 40-year Gaussian-weighted filter or (d) 20-to-160-year band-pass filtered.

(b) The individual volcanic forcing events are identified using the Ammann et al., (2007) volcanic forcing history, selecting only events from 1400–1999 that exceed –1.0 W m^{-2} below the mean volcanic forcing for the period 1500–1899. An event is not selected if a larger negative volcanic forcing event was present within 6 years (before or after) the event. The composite is formed by aligned time segments centred on 13 years: 1452, 1460, 1587, 1600, 1621, 1641, 1695, 1815, 1823, 1835, 1884, 1903 and 1992.

(c) The periods of strongest multi-decadal changes in volcanic forcing are identified using the Ammann et al., (2007) volcanic forcing history from 850–1999, smoothing with a 40-year Gaussian-weighted filter. All 80-year periods centred on years when the smoothed forcing exceeds –0.25 W m^{-2} below the 1500–1899 mean volcanic forcing are selected, except that a period is not selected if its central year is within 39 years of the central year of another period that has a larger negative 40-year smoothed volcanic forcing. The composite is formed by aligned time segments centred on 5 years: 1176, 1259, 1454, 1598 and 1814.

(d) The periods of strongest multi-decadal changes in solar forcing are identified using the Ammann et al., (2007) solar forcing history from 850–1999 CE, band-pass filtered to remove variations on timescales shorter than 20 years or longer than 160 years. The central year of each 80-year period is selected if the difference in band-passed solar forcing between that year and the value 40 years earlier exceeds –0.1 W m^{-2}. A period is not selected if its central year is within 39 years of the central year of another period that has a larger 40-year reduction in band-pass filtered solar forcing. The composite is formed by aligned time segments centred on 7 years: 1044, 1177, 1451, 1539, 1673, 1801 and 1905.

(e–f) Mean NH temperature difference between (e) MCA (950–1250 CE) and LIA (1400–1700 CE) and (f) 20th century (1900–2000 CE) and LIA, from reconstructions (grey), multi-reconstruction mean and range (dark grey), multi-model mean and range (brown), and model simulations (red/blue for models forced by

stronger/weaker solar variability). Time averages over shorter periods are used where data are incomplete (e.g., 1000–1250 CE is used for the MCA for reconstructions or simulations that begin in 1000 CE) providing that there are at least 200 years of data for the MCA and LIA periods, and at least 70 years for the 20th century. Where an ensemble of simulations is available from one model experiment, the ensemble mean is show in solid and the individual ensemble members by open circles. Results are sorted into ascending order and labelled.

5.A.2 Supplemental Information to Section 5.3.5

Section 5.3.5 assesses knowledge of changes in hemispheric and global temperature over the last 2 ka from a range of studies, reconstructions and simulations. Tables 5.A.4 and 5.A.5 provide further information about the datasets used in Figures 5.7–5.9, and the construction of Figure 5.8 is described in more detail.

Figure 5.8 compares simulated and reconstructed NH temperature changes (see caption). In (a), all timeseries are expressed as anomalies from their 1500–1850 CE mean; and smoothed with a 30-year Gaussian-weighted filter, truncated 7 years from the end of each series to reduce end-effects of the filter. The grey shading represents a measure of the overlapping reconstruction confidence intervals, with scores of 1 and 2 assigned to temperatures within ±1.645 standard deviation (90% confidence range) or ±1 standard deviation, respectively, then summed over all reconstructions and scaled so that the maximum score is dark grey, and minimum score is pale grey. The composite of individual volcanic forcing events shown in (b) is formed by aligned time segments centred on the thirteen years: 1452, 1460, 1587, 1600, 1621, 1641, 1695, 1815, 1823, 1835, 1884, 1903 and 1992 CE. These are the years from 1400–1999 CE in the Ammann et al., (2007) volcanic forcing history that exceed –1.0 W m^{-2} below the mean volcanic forcing for the period 1500–1899 CE, excluding events with within 6 years (before or after) of a stronger event. The composite in (c) is formed by aligned time segments centred on the five years: 1176, 1259, 1454, 1598 and 1814 CE, selected where the Ammann et al., (2007) volcanic forcing history from 850–1999 CE, smoothing with a 40-year Gaussian-weighted filter exceeds –0.25 W m^{-2} below the 1500–1899 CE mean. The composite in (d) is formed by aligned time segments centred on the seven years: 1044, 1177, 1451, 1539, 1673, 1801 and 1905 CE. These are the years with the strongest multi-decadal changes in the Ammann et al., (2007) solar forcing history during 850–1999 CE, identified where the band-pass filtered forcing (retaining variations on timescales between 20 and 160 years) shows reductions of at least –0.1 W m^{-2} over a 40-year period. The thick green line in Figure 5.8d shows the composite mean of the volcanic forcing, also band-pass filtered, but constructed using the solar composite periods to demonstrate the changes in volcanic forcing that are coincident with solar variability. Each composite is shifted to have zero mean during the (b) 5 or (c–d) 40 years preceding the peak negative forcing. Only reconstructions capable of resolving (b) interannual or (c–d) interdecadal variations are used. Reconstructed and simulated temperature timeseries were first smoothed with a 40-year Gaussian-weighted filter in (c) or 20-to-160-year band-pass filtered in (d).

Table 5.A.4: NH climate reconstructions assessed in Table 5.1 and used in Figures 5.7–5.8.

Reference [Identifier]	Period (CE)	Resolution	Region[a]	Proxy Coverage[b] H	M	L	O	Method and Data
Ammann and Wahl (2007) [AW2007]	1000–1980	Annual	L+S 0–90°N	☒	☒	⊡	⊡	Modification of the Mann et al., (1998, 1999) method; principal component inverse regression Multi-proxy network
Briffa et al., (2001) [only used in Figure 5.8b–d due to divergence issue]	1402–1960	Annual (summer)	L 20°N–90°N	☒	⊡	□	□	Principal component forward regression of regional composite averages Tree-ring density network, age effect removed via age-band decomposition
Christiansen and Ljungqvist et al., (2012) [CL2012]	1–1973	Annual	L+S 30°N–90°N	☒	☒	□	□	Composite average of local records calibrated by local inverse regression Multi-proxy network

D'Arrigo et al., (2006) [DWJ2006]	713–1995	Annual	L 0–90°N	☒ ⊡ ☐ ☐	Forward linear regression of composite average Network of long tree-ring width chronologies, age effect removed by Regional Curve Standardisation
Frank et al., (2007) [FEC2007]	831–1992	Annual	L 20°N –90°N	⊡ ⊡ ☐ ☐	Variance matching of composite average, adjusted for artificial changes in variance Network of long tree-ring width chronologies, age effect removed by Regional Curve Standardisation
Hegerl et al., (2007) [He..2007]	558–1960	Annual	L 20–90°N	⊡ ⊡ ☐ ☐	Total Least Squares regression Multi-proxy network
Juckes et al., (2007) [Ju..2007]	1000–1980	Annual	L 0–90°N	⊡ ⊡ ☐ ☐	Variance matching of composite average Multi-proxy network
Leclercq and Oerlemans (Leclercq and Oerlemans, 2011) [LO2011]	1600–2000	Multi-decadal	L 0-90°N L 90°S–0° L 90°S–90°N	⊡ ☒ ⊡ ☐	Inversion of glacier length response model 308 glacier records
Ljungqvist (2010) [L2010]	1–1999	Decadal	L 30°N–90°N	⊡ ⊡ ☐ ☐	Variance matching of composite average Multi-proxy network
Loehle and McCulloch (2008) [LM2008]	16–1935	Multi-decadal	L	⊡ ⊡ ☐ ⊡	Average of calibrated local records Multi-proxy network
Mann et al., (2008) [Ma..2008]	200–1980	Decadal	L and L+S versions, 0–90°N, 0–90°S, and 90°S–90°N	☒ ☒ ⊡ ⊡	(i) Variance matching of composite average (ii) Total Least Sqaures regression Multi-proxy network
Mann et al., (2009) [Ma..2009]	500–1849	Decadal	L+S 0–90°N	☒ ☒ ⊡ ⊡	Regularized Expectation Maximization with Truncated Total Least Squares Multi-proxy network
Moberg et al., (2005) [Mo..2005]	1–1979	Annual	L+S 0–90°N	☒ ☒ ⊡ ⊡	Variance matching of composites of wavelet decomposed records Tree-ring width network for short timescales; non-tree-ring network for long timescales
Pollack and Smerdon (2004) [PS2004]	1500–2000	Centennial	L 0–90°N L 0–90°S L 90°S–90°N	⊡ ☒ ⊡ ☐	Borehole inversion

Notes:
(a) Region: L = land only, L+S = land and sea, latitude range indicated;
(b) Proxy location and coverage: H = high latitude, M = mid latitude, L = low latitude, O = oceans;
☐=none or very few
⊡=limited
☒=moderate

Table 5.A.5: Summary of the AOGCM simulations used in Figure 5.8, 5.9 and 5.12. Acronyms describing forcings: SS (solar forcing, stronger variability), SW (solar forcing, weaker variability), V (volcanic activity), G (GHG concentration), A (aerosols), L (Land-use changes), O (orbital changes), Z (other forcings such as tropospheric and/or stratospheric ozone changes). The table is divided into experiments previous to and those belonging to the CMIP5/PMIP3 project (Braconnot et al., 2012b). Super indices in forcing acronyms refer to original references to solar, volcanic and GHG forcing reconstructions used as boundary conditions for simulations. PMIP3 experiments follow forcing guidelines provided in Schmidt et al (2011; 2012). See Fernández-Donado et al., (submitted) for more information on pre-CMIP5/PMIP3 forcing configurations.

Model (Label)	**(no. simulations) Time Interval**	**Forcings**	**Reference**
Pre CMIP5/PMIP3 Experiments			
CCSM3	(1x) 1000–2098 CE	$SS^{11}\cdot V^{21}\cdot G^{31,35,38}$	Hofer et al., (2011)

	(3x) 1500–2098 CE		
CSM1.4	(1x) 850–1990 CE	$SS^{12}\cdot V^{21}\cdot G^{31,35,38}\cdot A$	Ammann et al., (2007)
CSIRO-MK3L-1-2	(3x) 102–2001 CE	$SW^{14}\cdot G^{34}\cdot O$	Phipps et al., (submitted)
	(3x) 501–2001 CE	$SW^{14}\cdot V^{24}\cdot G^{34}\cdot O$	
ECHAM4/OPYC	(1x) 1500–2000 CE	$SS^{11}\cdot V^{21,26}\cdot G^{39}\cdot A\cdot L$	Stendel et al., (2006)
ECHAM5/MPIOM	(5x) 800–2005 CE	$SW^{13}\cdot V^{25}\cdot G^{33,34}\cdot A\cdot L\cdot O$	Jungclaus et al., (2010)
	(3x) 800–2100 CE	$SS^{12}\cdot V^{25}\cdot G^{33,34}\cdot A\cdot L\cdot O$	
ECHO-G	(1x) 1000–1990 CE	$SS^{11}\cdot V^{22}\cdot G^{31,36,37}$	González-Rouco et al (2003); NH average adjusted by Osborn et al., (2006); González-Rouco et al., (2006); Wagner et al., (2007)
	(1x) 1000–1990 CE	$SS^{11}\cdot V^{22}\cdot G^{31,36,37}$	
	(3x) 6000–1998 CE	$SS^{11}\cdot G^{31,36,37}\cdot O$	
HadCM3	(1x) 1492–1999 CE	$SS^{11}\cdot V^{23}\cdot G^{32}\cdot A\cdot L\cdot O\cdot Z$	Tett et al., (2007)
IPSLCM4	(1x) 1001–2000 CE	$SS^{11}\cdot G^{34,35,38}\cdot A\cdot O$	Servonnat et al., (2010)
CMIP5/PMIP3 Experiments			
BCC-csm1-1	(1x) 851–2000 CE	$SW^{15}\cdot V^{24}\cdot G^{xx}\cdot O$	Wu (2012)
CCSM4	(1x) 850–2004 CE	$SW^{15}\cdot V^{24}\cdot G^{34}\cdot A\cdot O$	Landrum et al., (submitted)
CSIRO-MK3L-1-2	(1x) 851–2000 CE	$SW^{14}\cdot V^{25}\cdot G^{34}\cdot O$	Phipps et al., (submitted)
GISS-E2-R	(1x) 850–2004 CE	$SW^{14}\cdot V^{25}\cdot G^{34}\cdot A\cdot L\cdot O$	
	(1x) 850–2004 CE	$SW^{14}\cdot V^{24}\cdot G^{34}\cdot A\cdot L\cdot O$	
	(1x) 850–2004 CE	$SW^{15}\cdot V^{25}\cdot G^{34}\cdot A\cdot L\cdot O$	
	(1x) 850–2004 CE	$SW^{15}\cdot V^{24}\cdot G^{34}\cdot A\cdot L\cdot O$	
FGOALS-gl	(1x) 1000–1999 CE	$SW^{xx}\cdot V^{xx}\cdot G^{xx}\cdot A$	Zhou et al (2011)
HadCM3	(1x) 800–2000 CE	$SW^{xx}\cdot V^{xx}\cdot G^{xx}\cdot A\cdot L\cdot O$	Schurer et al., (submitted)
MPI-ESM	(1x) 850–2005 CE	$SW^{xx}\cdot V^{xx}\cdot G^{xx}\cdot A\cdot L\cdot O$	

Notes:
(*) Key for super indices in column 3. Original references for:
[1] Solar:
[11] Bard et al (2000) spliced to Lean et al (1995a)
[12] Bard et al (2000)
[13] Krivova et al (2007)
[14] Steinhilber et al (2009)
[15] Vieira et al (2010)

[2] Volcanic:
[21] Ammann et al (2003)
[22] Crowley (2000)
[23] Crowley et al (2003)
[24] Gao et al (2008)
[25] Crowley and Uterman (submitted)
[26] Robertson et al (2001)

[3] GHGs:
[31] Etheridge et al (1996)
[32] Johns et al (2003)
[33] Diagnosed + Marland et al (2003)
[34] MacFarling Meure et al (2006)
[35] Blunier et al (1995)
[36] Etheridge et al (1998)
[37] Battle et al (1996)
[38] Fluckiger et al (2002)
[39] Robertson et al (2001)

[xx] [PLACEHOLDER FOR FINAL DRAFT: Information to be provided]

5.A.3 Sea Level Estimates from Pliocene Benthic $\delta^{18}O$ Records

If the signal only records ice volume, then based on the relationship of the $\delta^{18}O$ of seawater to ice volume derived from pore water chemistry (~0.08‰ per 10 m of sea level equivalent (Schrag et al., 2002), and assuming this relationship still held during the Pliocene, the lowest $\delta^{18}O$ values in the LR04 stack (Lisiecki and Raymo, 2005) suggest peak sea levels ~12–31 m higher than present. In contrast, Dowsett et al., (2009) reconstructed Pliocene deep-water (>2000 m water depth) temperature anomalies at 20 sites that ranged from –0.9°C to +4.2°C, with an average of 1 ± 1.2°C (1 standard deviation) warmer than present. A temperature sensitivity of 0.28‰ per °C suggests that the lowest Pliocene benthic $\delta^{18}O$ values may be entirely explained

by warmer deepwater temperature. Other attempts to constrain the temperature component in benthic $\delta^{18}O$ records indicate higher-than-present sea level during mid-Pliocene warm periods (Dwyer and Chandler, 2009; Sosdian and Rosenthal, 2009), but these have large uncertainties (±15–25 m) (Miller et al., 2012). Assuming $\delta^{18}O$ isotopic compositions for the GIS (Greenland Ice Sheet), WAIS (Wais Antarctic Ice Sheet) and EAIS (East Antarctic Ice Sheet), and a deep-ocean temperature contribution of between 20–50% of the glacial-interglacial signal in the Pliocene $\delta^{18}O$ benthic record, Naish and Wilson (2009) and Miller et al., (2012) also concluded that peak sea levels were higher than present during the warmest mid-Pliocene intervals, but these also have large uncertainties (±15–25 m).

5.A.3.1 Estimates of the Start and Duration of the LIG

Following Stirling et al., (1995), the start of the LIG is defined by the time at which penultimate glaciation sea levels, at sites far from former ice sheets, first reached their present value. The end is likewise defined by the time at which these far-field levels fell below present. These definitions are maintained here although the first is inconsistent with the definition of the onset of the Holocene and is also ambiguous since the isostatic response results in sea level not reaching this level simultaneously everywhere (Lambeck and Nakada, 1992).

There have been a number of attempts to model open-system behaviour of fossil corals in order to "correct" apparent ages that do not show closed-system behaviour (e.g., Thompson et al., 2003). Geochronologists are currently debating the reliability of these open-system models (see Stirling and Andersen, 2009), but there are still too few studies for an overall assessment. Thus, we take a conservative approach and use only those published U-series ages that show reasonable evidence of closed-system history, based on a lack of original aragonite alteration (<5%), U contents similar to modern corals, low Th contents, and $\delta^{234}U$ initial values that fall within ±8‰ of the modern seawater value. Analytical errors (2 standard deviations) on individual ages range from 0.2–2.2 kyr; most are 1.0 kyr or less.

Some of the differences between the duration of the LIG in the coral records can be explained by biological, geological and geophysical factors. The apparent early start of the LIG on Barbados may be due in part to the reefs here being dominated by the rapidly growing reef crest species *Acropora palmata*, resulting in construction of a "keep-up" reef that keeps pace with a rising sea level. In contrast, Florida Keys LIG reefs generally lack *A. palmata* and may have been "catch-up" reefs that responded more slowly to sea level rise. In Bermuda, California and parts of Hawaii, the shorelines are erosional marine terraces overlain by coral-bearing marine sediments. Here, the early part of the LIG may have been occupied by bench cutting and the ages are from detrital corals that were deposited during the later part of the LIG. Also, the start time of reef development depends on other factors, such as water temperature and changes in ocean currents. Geochemical alteration from undetected diagenesis may also be responsible for some of the outlying values. Finally GIA contributes a complex spatial-temporal sea level signal throughout an ice age cycle, including during interglacial phases (Kopp et al., 2009; Lambeck and Nakada, 1992; Lambeck et al., 2012). For example, during interglacial periods, sea level will rise due to GIA on the subsiding bulges at the periphery of the former continental ice sheets whereas at further distance, in the so-called far-field, they will fall.

Chapter 5: Information from Paleoclimate Archives

Coordinating Lead Authors: Valérie Masson-Delmotte (France), Michael Schulz (Germany)

Lead Authors: Ayako Abe-Ouchi (Japan), Juerg Beer (Switzerland), Andrey Ganopolski (Germany), Jesus Fidel González Rouco (Spain), Eystein Jansen (Norway), Kurt Lambeck (Australia), Juerg Luterbacher (Germany), Tim Naish (New Zealand), Timothy Osborn (UK), Bette Otto-Bliesner (USA), Terrence Quinn (USA), Rengaswamy Ramesh (India), Maisa Rojas (Chile), XueMei Shao (China), Axel Timmermann (USA)

Contributing Authors: Kevin Anchukaitis (USA), Patrick J. Bartlein (USA), Gerardo Benito (Spain), Peter Clark (USA), Thomas Crowley (USA), Patrick De Deckker (Australia), Barbara Delmonte (Italy), Pedro DiNezio (USA), Trond Dokken (Norway), Harry J. Dowsett, R. Lawrence Edwards (USA), Hubertus Fischer (Switzerland), Dominik Fleitmann (UK), Claus Fröhlich (Switzerland), Aline Govin (Germany), Alan Haywood (UK), Chris Hollis (New Zealand), Ben Horton (USA), Robert Kopp(USA), Amaelle Landais (France), Camille Li (Norway), Dan Lunt (UK), Natalie Mahowald (USA), Shayne McGregor (USA), Jerry X. Mitrovica (USA), Anders Moberg (Sweden), Daniel R. Muhs (USA), Stefan Mulitza (Germany), Frédéric Parrenin (France), Paul Pearson (UK), Alan Robock (USA), Eelco Rohling (UK), Ulrich Salzmann (UK), Joel Savarino (France), Jason Smerdon (USA), Olga Solomina (Russia), Pavel Tarasov (Germany), Claire Waelbroeck (France), Dieter Wolf-Gladrow (Germany), Yusuke Yokoyama (Japan), Masakazu Yoshimori (Japan), James Zachos (USA), Dan Zwartz (New Zealand)

Review Editors: Anil K. Gupta (India), Fatemeh Rahimzadeh (Iran), Dominique Raynaud (France), Heinz Wanner (Switzerland)

Date of Draft: 5 October 2012

Notes: TSU Compiled Version

Figures

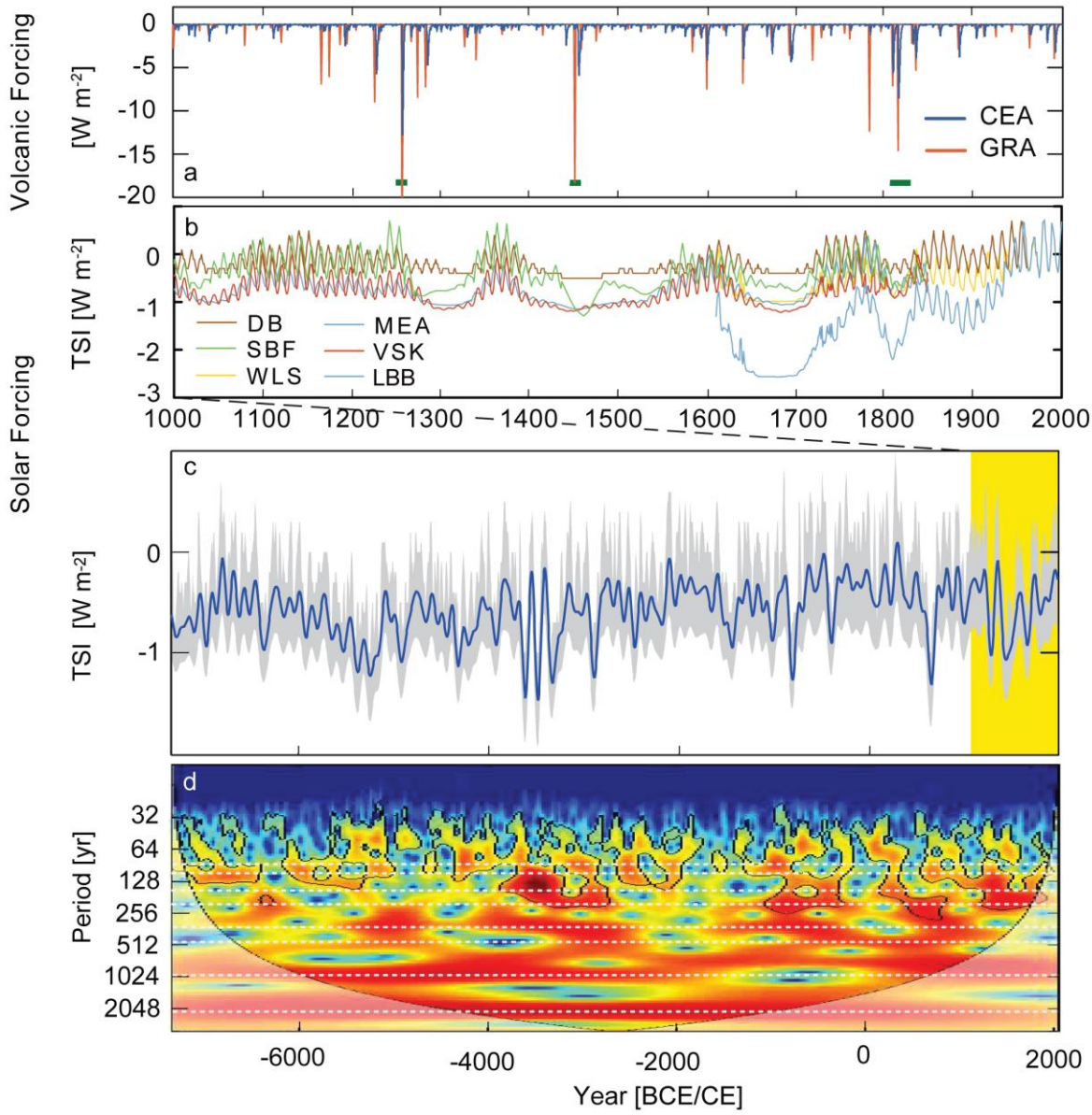

Figure 5.1: a) Two reconstructions of volcanic forcing for the past 1000 years derived from ice core sulfate and used for PMIP3-CMIP5 (Coupled Model Intercomparison Project) simulations (Schmidt et al., 2011). GRA: (Gao et al., 2008); CEA: (Crowley and Unterman, submitted; Crowley and Hyde, 2008; Timmreck et al., 2009). Volcanic sulfate peaks identified from their isotopic composition as originating from the stratosphere (Cole-Dai et al., 2009) are indicated by squares (green: Greenland; brown: Antarctica) (Baroni et al., 2008). b) TSI reconstructions back to 1000 CE. Proxies of solar activity (e.g., sunspots, ^{10}Be) are used to estimate the parameters of the models or directly TSI. All records except LBB (Lean et al., 1995) have been used for PMIP3-CMIP5 simulations (Schmidt et al., 2011). DB: (Delaygue and Bard, 2011); MEA: (Muscheler et al., 2007); SBF: (Steinhilber et al., 2009); WLS: (Wang et al., 2005); VSK: (Vieira et al., 2011). Before 1600 CE, the 11-year cycle has been added artificially to the original data. c) TSI reconstruction (100-year low-pass filtered; grey shading: 1 standard deviation uncertainty range) for the past 9300 years (Steinhilber et al., 2009). The reconstruction is based on ^{10}Be and calibrated using the relationship between instrumental data of the open magnetic field, which modulates the production of ^{10}Be and TSI for the past 4 solar minima. d) Wavelet analysis (Torrence and Compo, 1998) of TSI showing the existence of several preferred periodicities (87, 104, 150, 208, 350, 510, ~980, ~2200 years) with varying amplitudes.

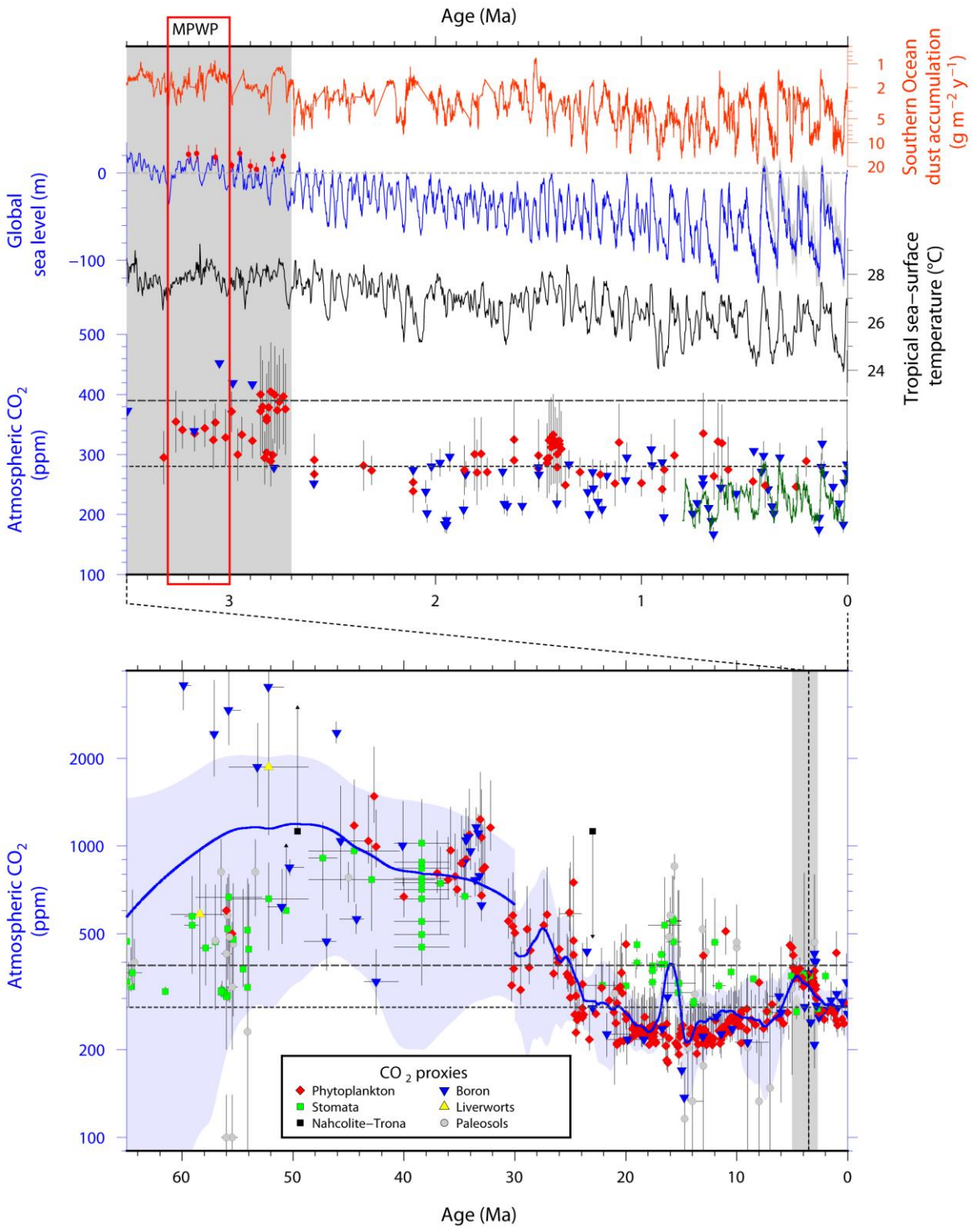

Figure 5.2: (Top) Radiative forcings and perturbations and orbital-scale Earth system responses 3.6 Ma to present. Reconstructed dust mass accumulation rate from the Atlantic sector of the Southern Ocean (red) (Martinez-Garcia et al., 2011). Sea level curve (purple) is the stacked benthic oxygen isotope proxy for ice volume and ocean temperature (Lisiecki and Raymo, 2005) calibrated to global average eustatic sea level (Miller et al., 2012; Naish and Wilson, 2009). Also shown are global eustatic sea level reconstructions for the last 500 kyr based on sea level calibration of the $\delta^{18}O$ curve using dated coral shorelines (grey line; Waelbroeck et al., 2002) and weighted mean estimates (2 standard deviation uncertainty) for far-field reconstructions of eustatic peaks during mid-Pliocene interglaciations (red dots; Miller et al., 2012). The dashed horizontal line represents modern sea level. Tropical sea surface temperature (black line) based on a stack of 4 alkenone-based SST reconstructions (Herbert et al., 2010). Atmospheric CO_2 measured from EPICA Dome C ice core (blue line; Lüthi et al., 2008), and estimates of CO_2 from boron $\delta^{11}B$ isotopes in foraminifera

in marine sediments (blue triangles; Honisch et al., 2009; Seki et al., 2010), and phytoplankton alkenone-derived carbon isotope proxies (red diamonds; Pagani et al., 2010; Seki et al., 2010), plotted with 2 standard deviation uncertainty. Present (2012 CE) and pre-industrial CO_2 concentrations are indicated with long-dashed and short-dashed grey lines, respectively. (Bottom) Concentration of atmospheric CO_2 for the last 65 Myr is reconstructed from marine and terrestrial proxies and complied by Beerling and Royer (2011; additional boron CO_2 proxy data from Pearson and Palmer (2000) are also included). Individual proxy methods are colour-coded. Errors represent reported uncertainties (plotted with 2 standard deviation uncertainty; see also Table 5.1 for assessment of confidence of proxies). Most of the data points for CO_2 proxies are based on duplicate and multiple analyses. The blue line is a kernel regression through all the data points with a bandwidth of 8 Myr prior to 30 Ma, and 1 Myr to present. The blue shading is a 1 standard deviation. Uncertainty band constructed using block bootstrap resampling (Mudelsee et al., submitted). Shaded grey vertical band highlights global warmth during the Pliocene (~5–2.7 Ma; about +2–3°C global mean; see also Box 5.2 Figure 1). The red box labelled MPWP represents the Mid Pliocene Warm Period from 3.3–3 Ma)

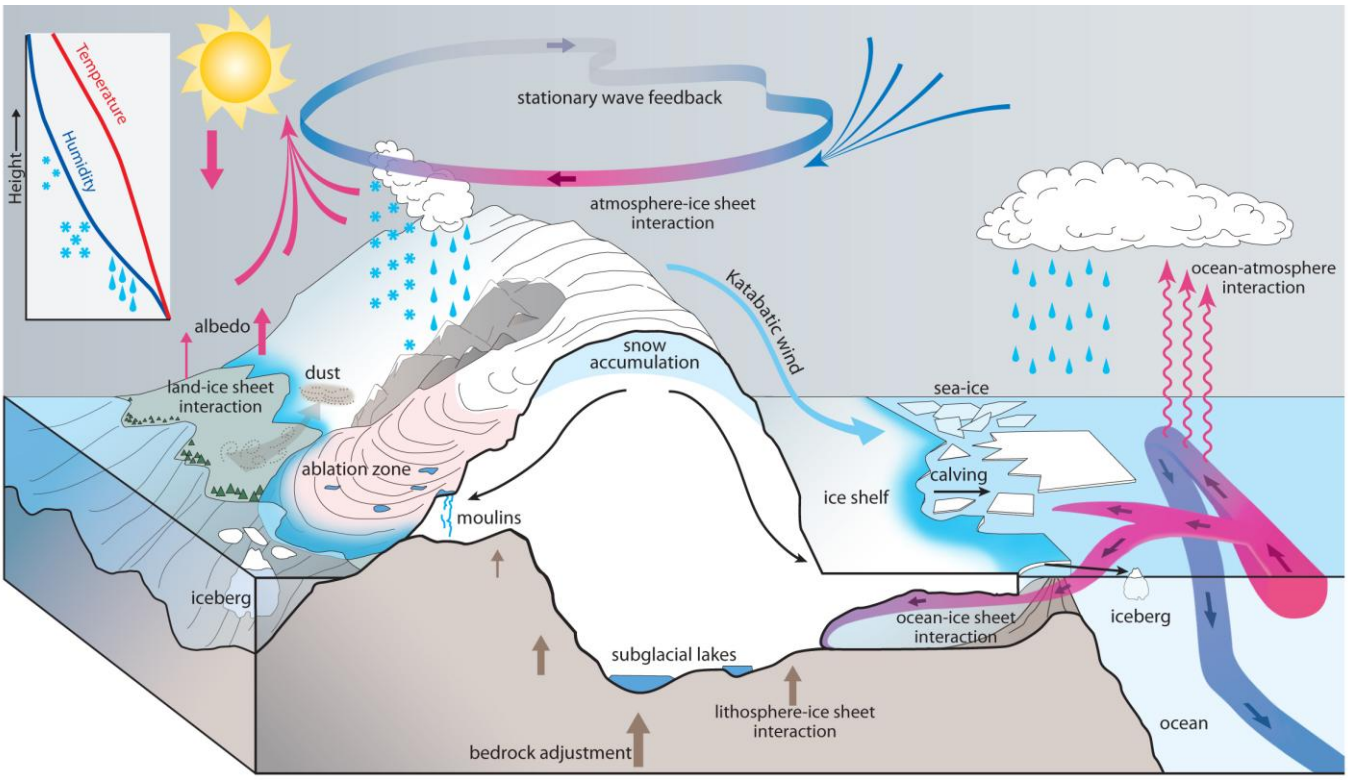

Box 5.1, Figure 1: Schematic illustration of multiple interactions between ice sheets, solid Earth, and climate system which can drive internal variability and affect the coupled ice sheet–climate response to external forcings on timescales of hours to millions of years.

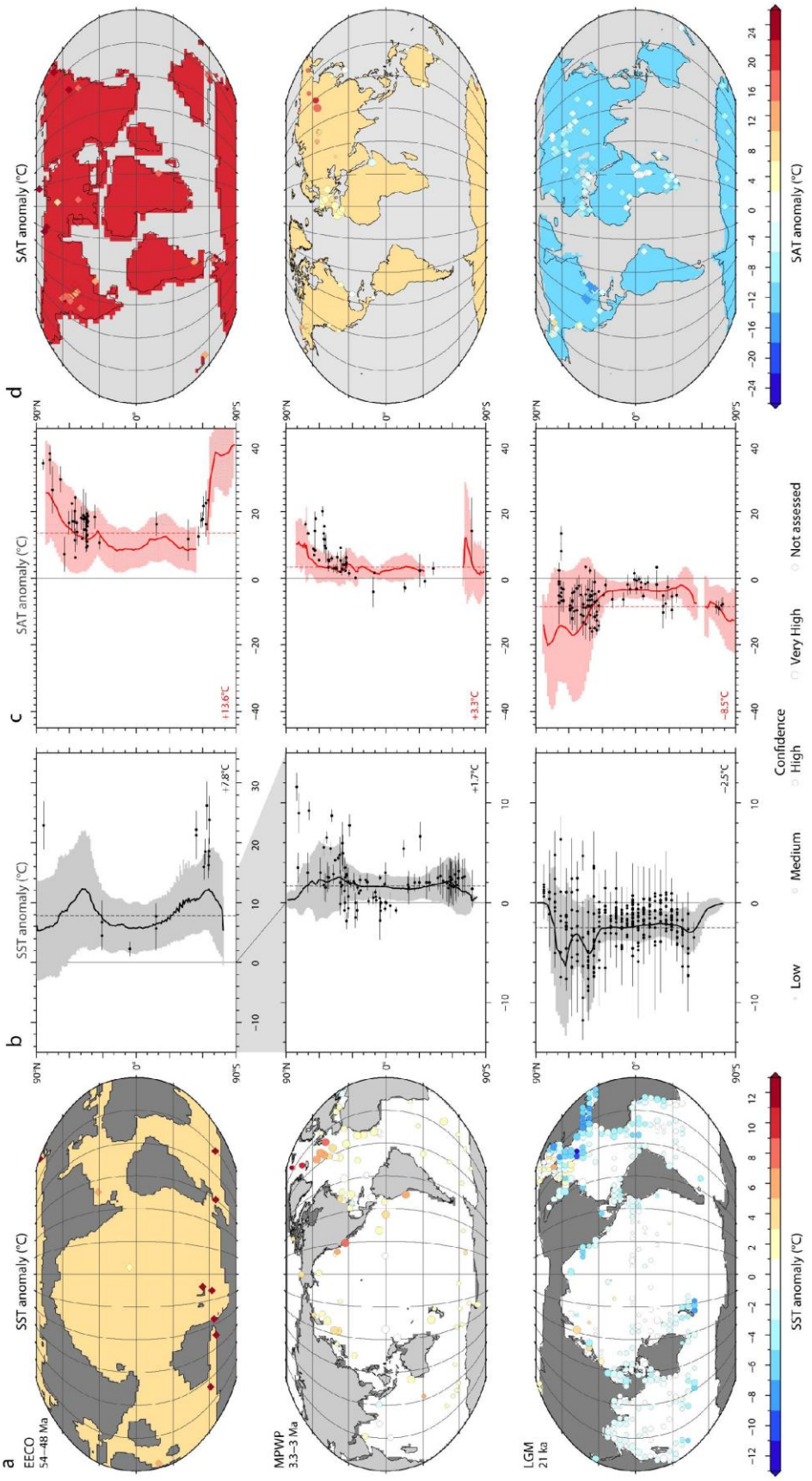

Box 5.2, Figure 1: Data and multi model mean (MMM) comparisons of a) SST, b) zonally-averaged MMM SST gradient and proxy SST, c) zonally averaged MMM surface air temperature (SAT) gradient and proxy SAT, and d) SAT anomalies for the Early Eocene Climatic Optimum (EECO, top row), the mid-Pliocene warm period (MPWP, middle row) and the LGM (bottom row). Model temperature anomalies are calculated relative to the pre-industrial value of

each model in the ensemble prior to calculating the MMM anomaly (a, d; colour shading). Zonal MMM gradients (b, c) are plotted with a shaded band indicating 2 standard deviation uncertainty. Site specific temperature anomalies estimated from proxy data are calculated relative to present site temperatures and are plotted (a, d) using the same colour scale as the model data, and a circle size scaled to estimates of confidence. In the zonal plots (b, c) the proxy data anomalies are shown with error bars indicating 2 standard deviation uncertainty. Proxy data compilations for the LGM are from MARGO Project Members (2009) and Bartlein et al., (2011), for the MPWP are from Dowsett et al., (2012) and Salzmann et al., (2008), and for the EECO are from Hollis et al., (submitted) and Lunt et al., (2012). Model ensemble simulations for the LGM are after (Harrison et al., submitted), for the Pliocene are from Haywood et al., (submitted), and for the EECO are after Lunt et al., (2012).

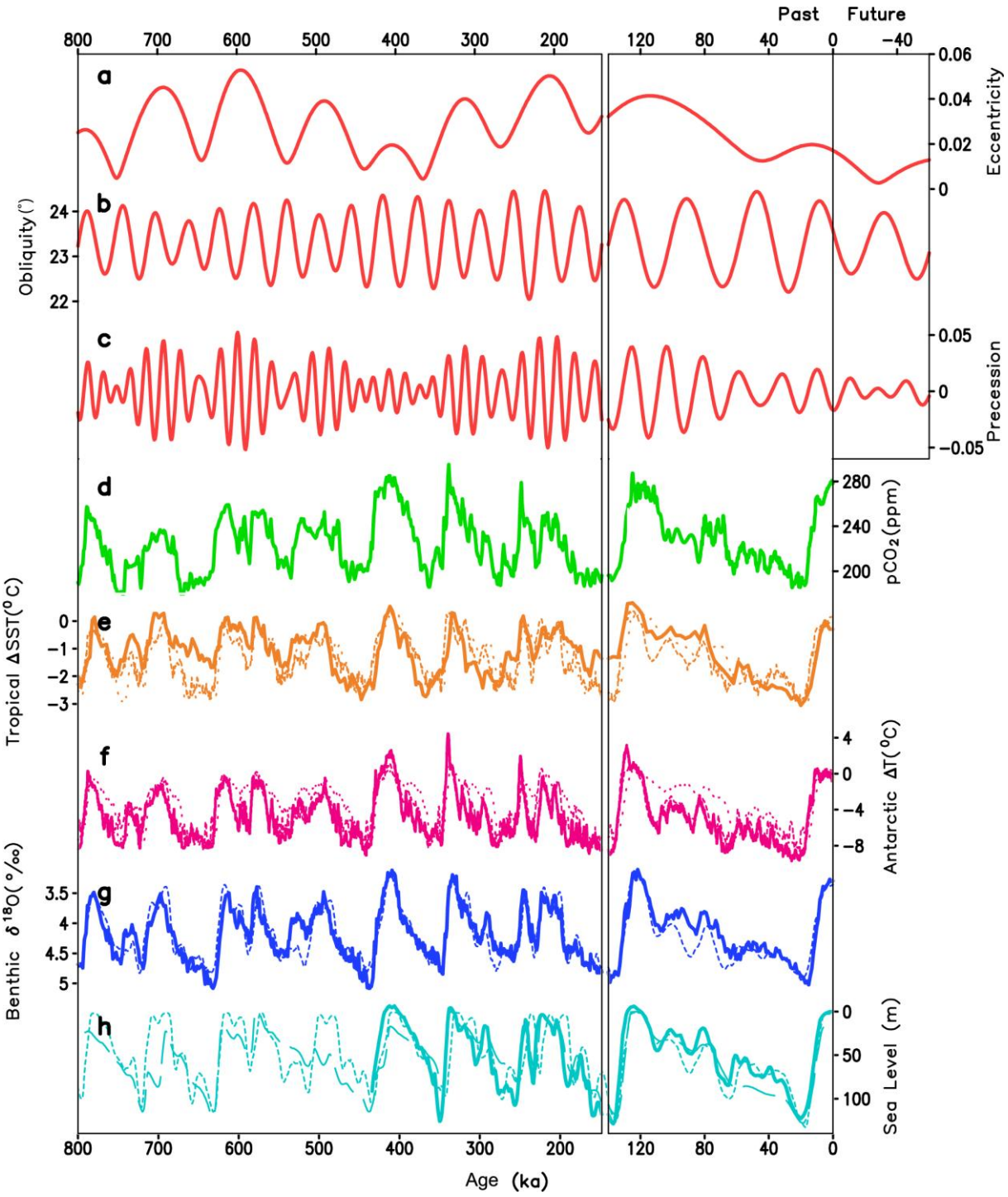

Figure 5.3: Orbital parameters and proxy records over the past 800 kyr. (a) Eccentricity, (b) obliquity, (c) precessional parameter (Berger and Loutre, 1991), (d) atmospheric concentration of CO_2 from Antarctic ice cores (Ahn and Brook, 2008; Lüthi et al., 2008; Petit et al., 1999; Siegenthaler et al., 2005), (e) tropical SST stack (Herbert et al., 2010), (f) Antarctic temperature stack based on up to seven different ice cores (Blunier and Brook, 2001; EPICA Community Members, 2006; Jouzel et al., 2007; Petit et al., 1999; Stenni et al., 2011; Watanabe et al., 2003), (g) stack of benthic $\delta^{18}O$, a proxy for global ice volume and deep ocean temperature (Lisiecki and Raymo, 2005), (h) reconstructed sea level (Waelbroeck et al., 2002). Solid lines represent orbital forcing and proxy records, dashed lines depict results of simulations with climate and climate-ice sheet models forced by variations of the orbital parameters and the atmospheric concentrations of the major greenhouse gases. Short dashed line: CLIMBER-2 (Ganopolski and Calov, 2011), long dashed line: IcIES (Abe-Ouchi et al., 2007), dotted line: Bern3D (Ritz et al., 2011). Note the change of the age-axis scale at 140 ka.

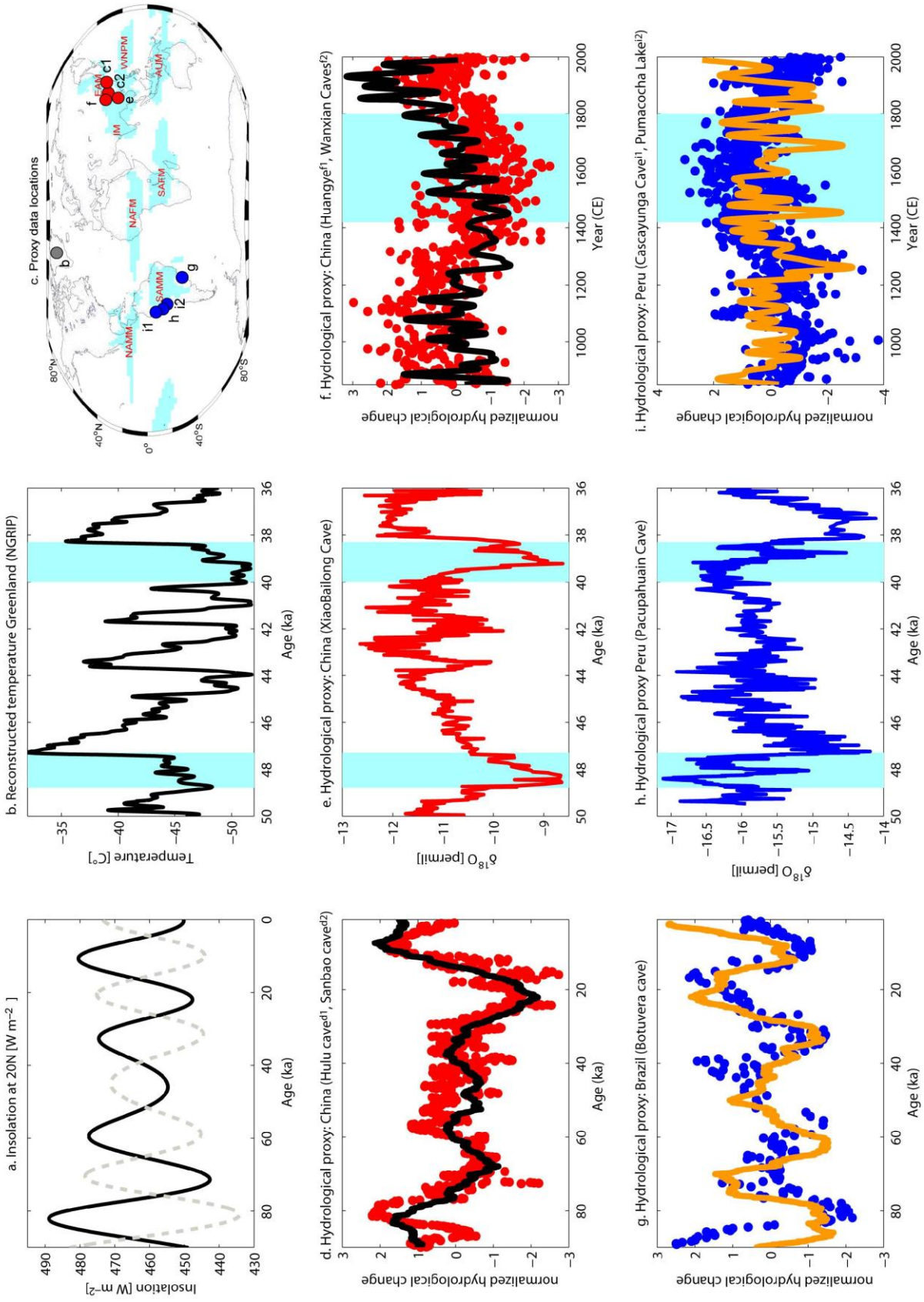

Figure 5.4: Interhemispheric response of monsoon systems to orbital forcing, AMOC changes, and radiative forcing since 850 CE: a. boreal summer insolation changes at 20°N (black) (W m^{-2}), austral summer insolation changes at 20°S (blue); b. Temperature changes in Greenland (°C) reconstructed from NGRIP ice core on SS09 timescale (Huber et al., 2006), location indicated by black circle in c; c. Location of proxy records displayed in relation to the global monsoon regions (Wang and Ding, 2008) North American Monsoon (NAMM), South American Monsoon (SAMM), NAFM

(North African Monsoon), SAFM (South African Monsoon), IM (Indian Monsoon), EAM (East Asian Monsoon), WNPM (Western North Pacific Monsoon), AUM (Australian Monsoon). d. Reconstructed (purple) standardized negative $\delta^{18}O$ anomaly in East Asian Summer Monsoon region derived from Hulu cave (Wang et al., 2001) and Sanbao cave speleothem records, China (Wang et al., 2008) and simulated standardized multi-model average (black) of annual mean rainfall anomalies averaged over region 108°E–123°E and 25°N–40°N using the transient runs conducted with LOVECLIM (Timm et al., 2008), FAMOUS (Smith and Gregory, 2012), and the HadCM3 snapshot simulations (Singarayer and Valdes, 2010); e. $\delta^{18}O$ from Xiaobailong cave, China (Cai et al., 2010); f. standardized negative $\delta^{18}O$ anomalies (purple) in Huangye (Tan et al., 2011) and Wanxian Caves (Zhang et al., 2008), China, and simulated standardized annual mean and 30-year low pass filtered rainfall anomalies (black) in region 100°E –110°E, 20°N–35°N, ensemble averaged over the Last Millennium experiments conducted with CCSM4, ECHO-G, MPI-ESM, CSIRO-MARK3, MIROC, HADCM3; g. standardized negative $\delta^{18}O$ anomaly (blue) from Botuvera speleothem, Brazil (e.g., Cruz et al., 2009) and simulated standardized multi-model average (black) of annual mean rainfall anomalies averaged over region 45°W–60°W and 35°S–15°S using same experiments as in panel d; h. standardized negative $\delta^{18}O$ anomaly (brown) from Pacupahuain cave, Peru (Kanner et al., 2012); i. standardized $\delta^{18}O$ anomalies (blue) from Cascayunga Cave, Peru (Reuter et al., 2009) and Pumacocha Lake, Peru (Bird et al., 2011) and simulated standardized annual mean and 30-year low-pass filtered rainfall anomalies (black) in region 76°W–70°W, 15.7°S–8°S, ensemble averaged over the Last Millennium experiments from f.

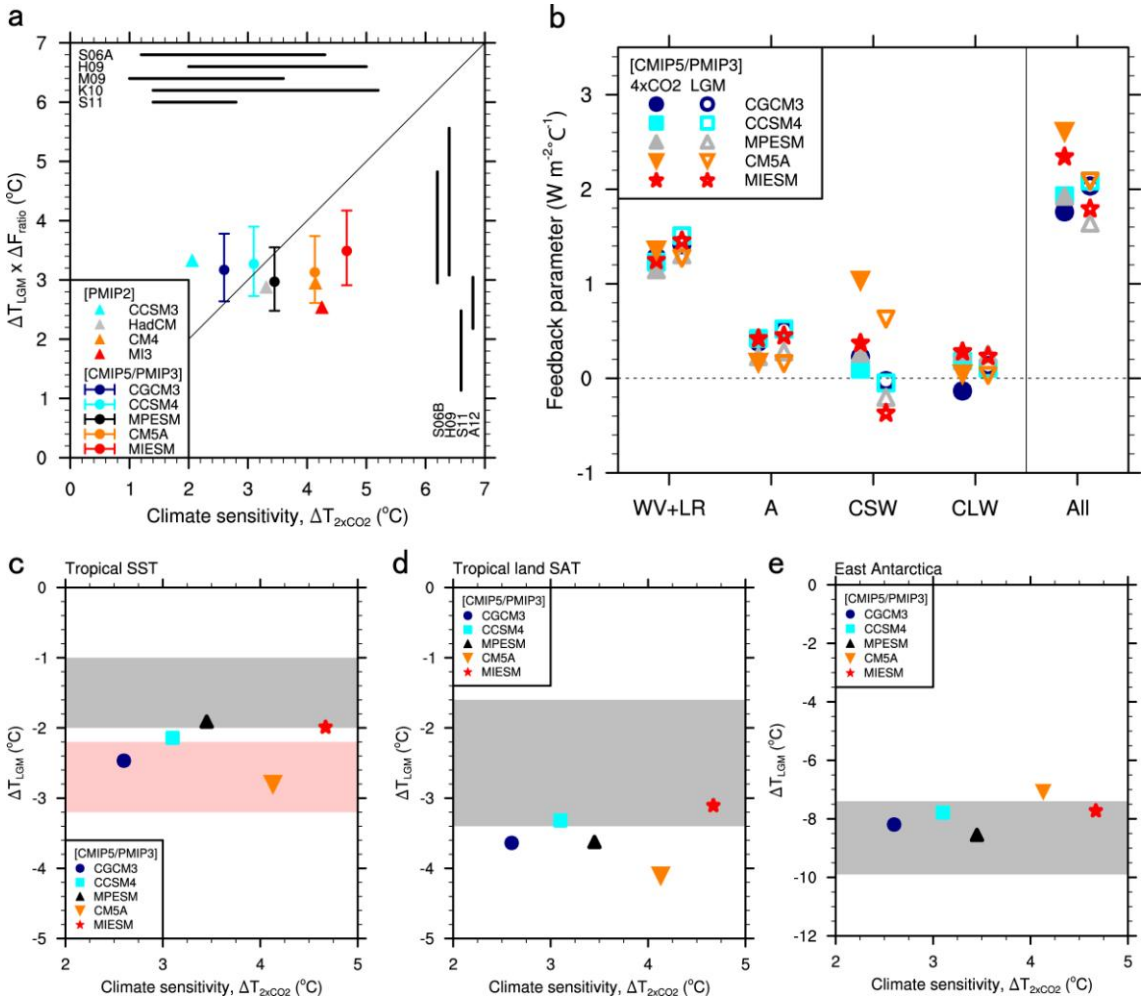

Figure 5.5: a) Relation between equilibrium climate sensitivity estimated from 2 × CO_2 or abrupt 4 × CO_2 experiments and that estimated from LGM simulations. Climate sensitivity of PMIP2 AOGCMs was taken from Crucifix (2006) and that of CMIP5/PMIP3 models was taken from Andrews et al., (2012) and Brady et al., (submitted). Climate sensitivity based on LGM simulations were derived by multiplying the ratio of radiative forcing between 2 × CO_2 and LGM (ΔF_{ratio}). ΔF_{ratio} for three PMIP2 models (CCSM3, HadCM, CM4) were taken from Crucifix (2006), and it was taken from Yoshimori et al., (2009) for MI3. Its range, –0.80 to –0.56, with a mean of –0.67 was used for CMIP5/PMIP3 models. Horizontal bars represent 90% confidence interval for the estimated climate sensitivity based on glacial climates in literatures: "S06a", "M09", "H10", "K10" and "S11" denote Schneider von Deimling et al., (2006a), MARGO Project Members (2009), Holden et al., (2010a), Köhler et al., (2010), and Schmittner et al., (2011), respectively. Vertical bars represent 90% confidence interval for LGM global mean temperature change in literatures multiplied by the mean of ΔF_{ratio}. "S06b" and "A12" denote Schneider von Deimling et al., (2006b) and Annan and Hargreaves (submitted), respectively. Also plotted is a one-to-one line; b) Strength of individual feedbacks for the CMIP5/PMIP3 abrupt4 × CO_2 (131–150 years) and LGM (stable states) experiments following the method in Yoshimori et al., (2011). "WV+LR", "A", "CSW", "CLW" denote water vapour plus lapse-rate, surface albedo, shortwave cloud, and longwave cloud feedbacks, respectively. "All" denotes the sum of all feedbacks except for the Planck response. Feedback parameter here is defined as the change in net radiation at the top of the atmosphere due to the change in individual fields such as water vapour, and it is normalized by the global mean surface air temperature change. Climate sensitivity depends on forcings, feedbacks and ocean heat uptake. Positive (negative) value indicates that the feedback amplifies (suppresses) the initial temperature response; c) Relation between models' climate sensitivity and LGM tropical SST change from today; d) Same as in c but for tropical surface air temperature over land; and e) Same as in c but for surface air temperature in East Antarctica. Gray shadings in c-e are 90% confidence intervals for temperature reconstructions from Annan and Hargreaves (submitted) and a range for East Antarctica based on reconstructions from stable isotopes from several ice cores (Dome F, Vostok, EDC and EDML) from Stenni et al., (2010) and Uemura et al., (2012). Pink shading in c represents estimates by Ballantyne et al., (2005) with ±1 standard deviation. "HadCM", "CM4", "MI3", "CGCM3", "MPESM", "CM5A", and "MIESM" denote "HadCM3", "IPSL-CM4", "MIROC3.2", "MRI-CGCM3", "MPI-ESM-P", "IPSL-CM5A-LR", and "MIROC-ESM", respectively.

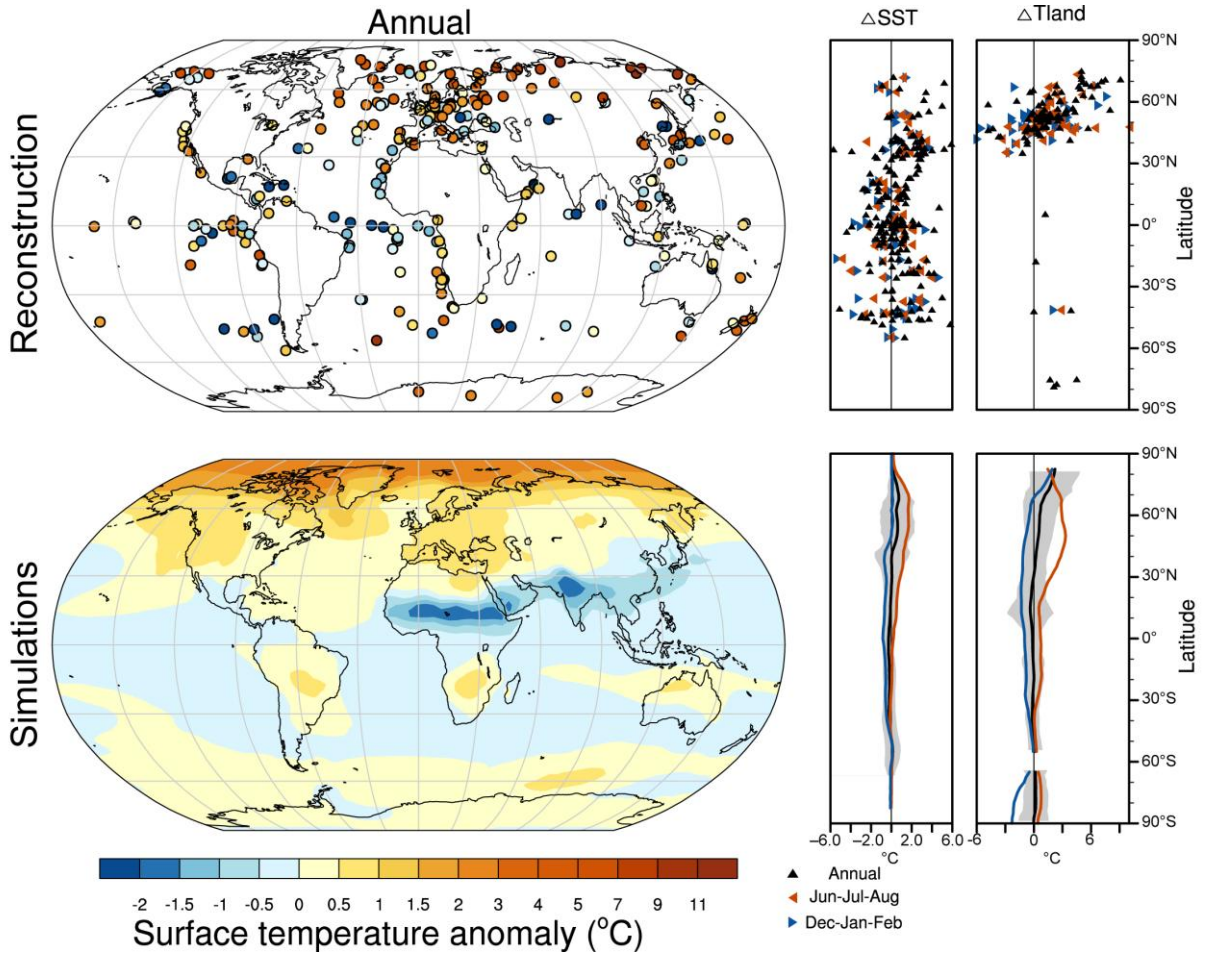

Figure 5.6: Changes in surface temperature for the Last Interglacial as reconstructed from data and simulated by an ensemble of climate model experiments in response to orbital forcing. Top left: Proxy data syntheses of annual surface temperature anomalies as published by Turney and Jones (2010) and McKay et al., (2011) . McKay et al., calculated an annual anomaly for each record as the average SST of the 5-kyr period centered on the warmest temperature between 135 ka and 118 ka and then subtracting the average SST of the late Holocene (5 ka to 0 ka). Turney and Jones calculated the annual temperature anomalies relative to 1961–1990 CE by averaging the LIG temperature estimates across the isotopic plateau in the marine and ice records and the period of maximum warmth in the terrestrial records (assuming globally synchronous terrestrial warmth). Top right: Proxy records of zonal mean anomalies of SST from Turney and Jones (annual) and McKay et al., (annual and seasonal) and terrestrial surface temperature from Turney and Jones (annual) and compiled from published literature by Tarasov and Müller (seasonal). SST anomalies larger than 6°C (two annual in Nordic Sea, two annual in Southern Ocean, one annual in eastern tropical Pacific) and terrestrial anomalies larger than 10°C (four annual in Siberia, one DJF each in Siberia and Finland) or less than –6°C (two DJF in France) are not included in zonal averages. Bottom left: Multi-model average of annual surface air temperature anomalies simulated for the Last Interglacial computed with respect the pre-industrial control simulations. The results for the Last Interglacial are obtained from 18 simulations for 125–130ka conducted by 12 modeling groups (CCSM3_Bremen, CCSM3_LLN, CCSM3_NCAR, CLIMBER_LSCE, COSMOS_AWI, ECHAM5_ZMAW, HadCM3_Bristol, IPSL_LSCE, KCM_Kiehl, LOVECLIM_Amsterdam, LOVECLIM_LLN, and MIROC_Tokyo). Bottom right: Zonal mean anomalies of SST and terrestrial surface temperature from the multi-model mean for annual, June-July-August and December-January-February. Gray-shaded bands indicate the 2 standard deviation uncertainties of the annual mean anomalies.

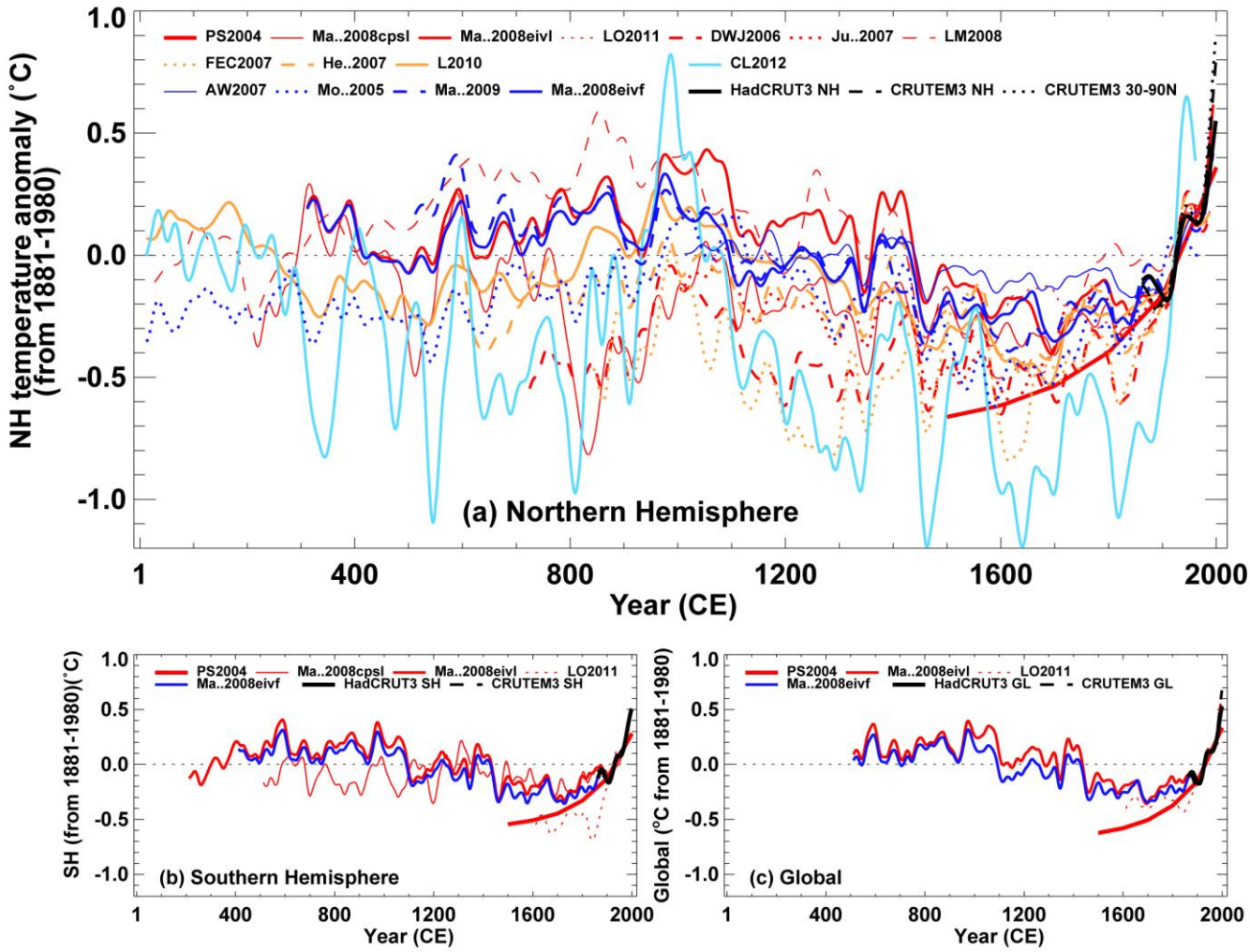

Figure 5.7: Reconstructed (a) Northern and (b) Southern Hemisphere, and (c) global annual temperatures during the last 2000 years. Individual reconstructions (see Appendix 5.A.1 for further information about each one) are shown as indicated in the legends, grouped by colour according to their spatial representation (red: land-only all latitudes; orange: land-only extra-tropical latitudes; light blue: land and sea extra-tropical latitudes; dark blue: land and sea all latitudes) and instrumental temperatures shown in black (HadCRUT3 land and sea, and CRUTEM3 land-only). All series represent anomalies (°C) from the 1881–1980 CE mean (horizontal dashed line) and have been smoothed with a filter that reduces variations on timescales less than ~50 years.

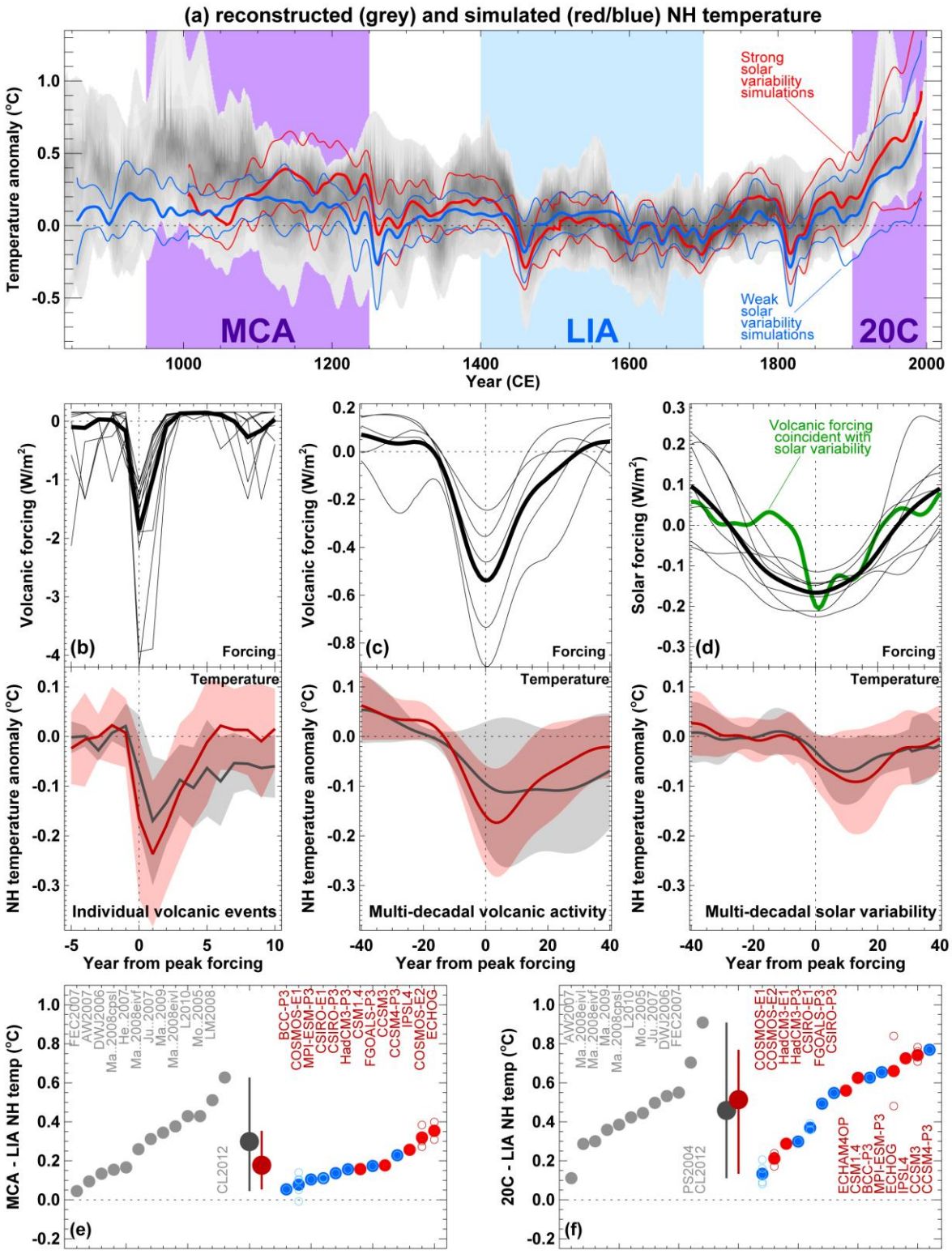

Figure 5.8: Comparisons of simulated and reconstructed NH temperature changes. (a) Changes over the last millennium. (b) Response to individual volcanic events. (c) Response to multi-decadal periods of volcanic activity. (d) Response to multi-decadal variations in solar activity. (e) Mean change from MCA to LIA. (f) Mean change from 20th century to LIA. Note that some reconstructions represent a smaller spatial domain than the full NH or a specific season, while annual temperatures for the full NH mean are shown for the simulations. (a) Simulations shown by coloured lines (thick lines: multi-model-mean; thin lines: multi-model 90% range; red/blue lines: models forced by stronger/weaker solar variability, though other forcings and model sensitivities also differ between the red and blue groups); overlap of reconstructed temperatures shown by grey shading; all data are expressed as anomalies from their 1500–1850 CE mean and smoothed. Superposed composites (time segments from selected periods positioned so that the years with peak

negative forcing are aligned) of the forcing and temperature response to (b) the 13 strongest individual volcanic forcing events after 1400 CE (the data shown are not smoothed); (c) multi-decadal changes in volcanic activity; (d) multi-decadal changes in solar irradiance. Upper panels show the volcanic or solar forcing for the individual selected periods together with the composite mean (thick); in (d), the composite mean of the volcanic forcing (green) during the solar composite is also shown. Lower panels show the NH temperature composite means and 90% range of spread between simulations (red line, pink shading) or reconstructions (grey line and shading), with overlap indicated by darker shading. Mean NH temperature difference between (e) MCA (950–1250 CE) and LIA (1400–1700 CE) and (f) 20th century (1900-2000) and LIA, from reconstructions (grey), multi-reconstruction mean and range (dark grey), multi-model mean and range (brown), and simulations (red/blue for models forced by stronger/weaker solar variability). Where an ensemble of simulations is available from one model, the ensemble mean is shown in solid and the individual ensemble members by open circles. Results are sorted into ascending order and labelled. Reconstructions, models and further details are given in Appendix 5.A.1 and Appendix 5.A.2.

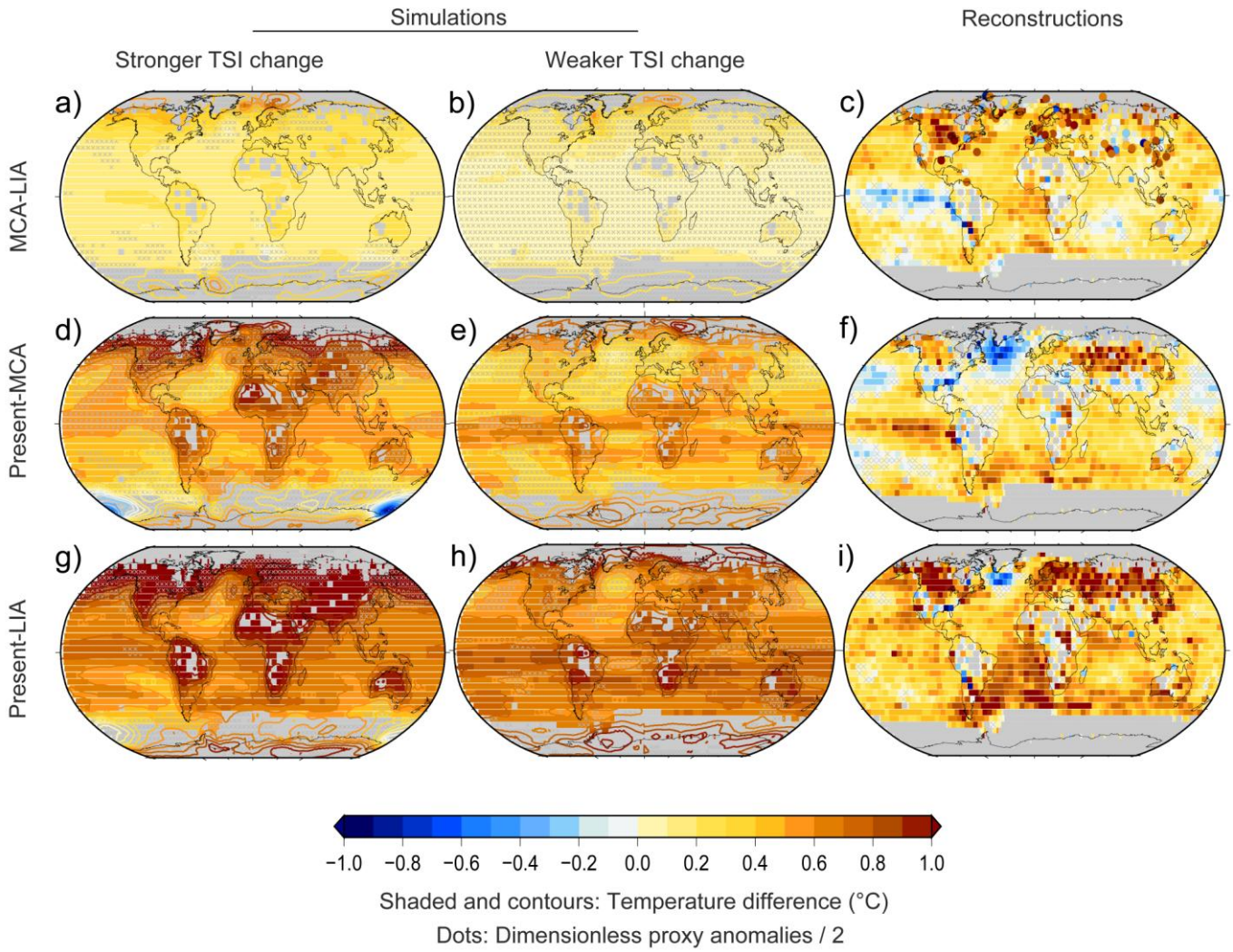

Figure 5.9: Simulated and reconstructed temperature changes for key periods in the last millennium. Annual temperature differences for: (a) to (c) MCA (950–1250 CE) minus LIA (1400–1700 CE); (d) to (f) present (1950–2000 CE) minus MCA; (g) to (i) present minus LIA. Model temperature differences (left and middle columns) are average temperature changes in the ensemble of available model simulations of the last millennium (see Appendix 5.A.2), grouped into those using stronger solar forcing changes (TSI change from the LMM to present >0.23 %; left column) and those weaker changes (TSI change from the LMM to present < 0.1%; middle column). Right column shows differences in the Mann et al., (2009) field reconstruction, and in (c), dots represent proxy anomalies from Ljungqvist et al., (2012) scaled by 0.5 for display purposes. Unhatched grid-cells indicate significant differences (<0.05 level) in reconstructed fields (right) or that ≥80% of the simulations agreed in showing significant changes of the same sign (left and middle). For simulations starting after 950 CE, the period 1000–1250 was used to estimate MCA values. Grid-cells outside the domain of the Mann et al., (2009) reconstruction are shaded grey in the model panels to enable easier comparison, though contours illustrate model output over the complete global domain. Simulations have been weighted by the number of experiments used from each model: BCC-csm1-1 (1), CSM1.4 (1), CCSM3 (5), CSIRO-mk3L-1-2 (7), ECHAM5-MPIOM (8), MPI-ESM-P (1), ECHO-G (3), FGOALS-gl (1), GISS-E2-R (4), HadCM3 (2), IPSLCM4 (1).

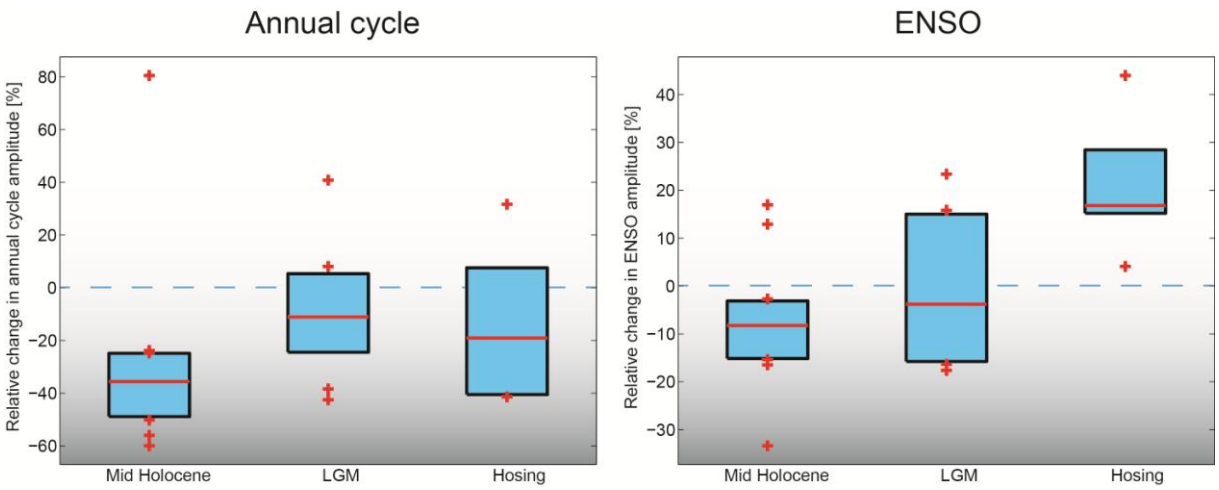

Figure 5.10: Relative changes in amplitude of the annual cycle of SST in Niño 3 region (average over 5°S–5°N and 150°W–90°W) (left) and changes in amplitude of interannual SST anomalies in the Niño 3.4 region (average over 5°S–5°N and 170°W–120°W) (right) simulated by an ensemble of climate model experiments in response to external forcing. Left: Multi-model average of relative changes (%) in amplitude of the mean seasonal cycle of Niño 3 SST for mid-Holocene and LGM time-slice experiments and for freshwater perturbation experiments (Hosing) that lead to a weakening of the AMOC by more than 50%. Bars encompass the 25 and 75 percentiles, with the red horizontal lines indicating the median in the respective multi-model ensemble, red crosses are values in the upper and lower quartile of the distribution; Right: same as left, but for the SST anomalies in the Niño 3.4 region, representing ENSO variability. The MH and LGM experiments were coordinated by the Paleoclimate Modelling Intercomparison Project Phase II (PMIP2) or III (PMIP3). The MH ensemble includes 4 experiments (6k) performed by models participating in PMIP2 (FGOALS1.0g, IPSL-CM4, MIROC3.2 medres, CCSM3.0) and *7* experiments (mid-Holocene) performed by models participating in PMIP3 (CCSM4.0, CSIRO-Mk3-6-0, HadGEM2-CC, HadGEM2-ES, MIROC-ESM, MPI-ESM-P, MRI-CGCM3). The LGM ensemble includes 5 experiments (21 ka) performed by models participating in PMIP2 (FGOALS1.0g, IPSL-CM4, MIROC3.2 medres, CCSM3.0, HadCM3) and 5 experiments (LGM) performed by models participating in PMIP3 (CCSM4, GISS-E2-R, IPSL-CM5A-LR, MIROC-ESM, and MPI-ESM-P). The changes in response to MH and LGM forcing are computed with respect the preindustrial control simulations coordinated by PMIP2 (0k experiment) and PMIP3 (piControl experiment). The results for Hosing are obtained from freshwater perturbation experiments conducted with CCSM2.0, CCSM3.0, HadCM3, ECHAM5-MPIOM, GFDL-CM2.1 (Timmermann et al., 2007), CSM1.4 (Bozbiyik et al., 2011) for pre-industrial or present-day conditions and with CCSM3 for glacial conditions (Merkel et al., 2010). The changes in response to fresh water forcing are computed with respect the portion of simulations when the AMOC is high.

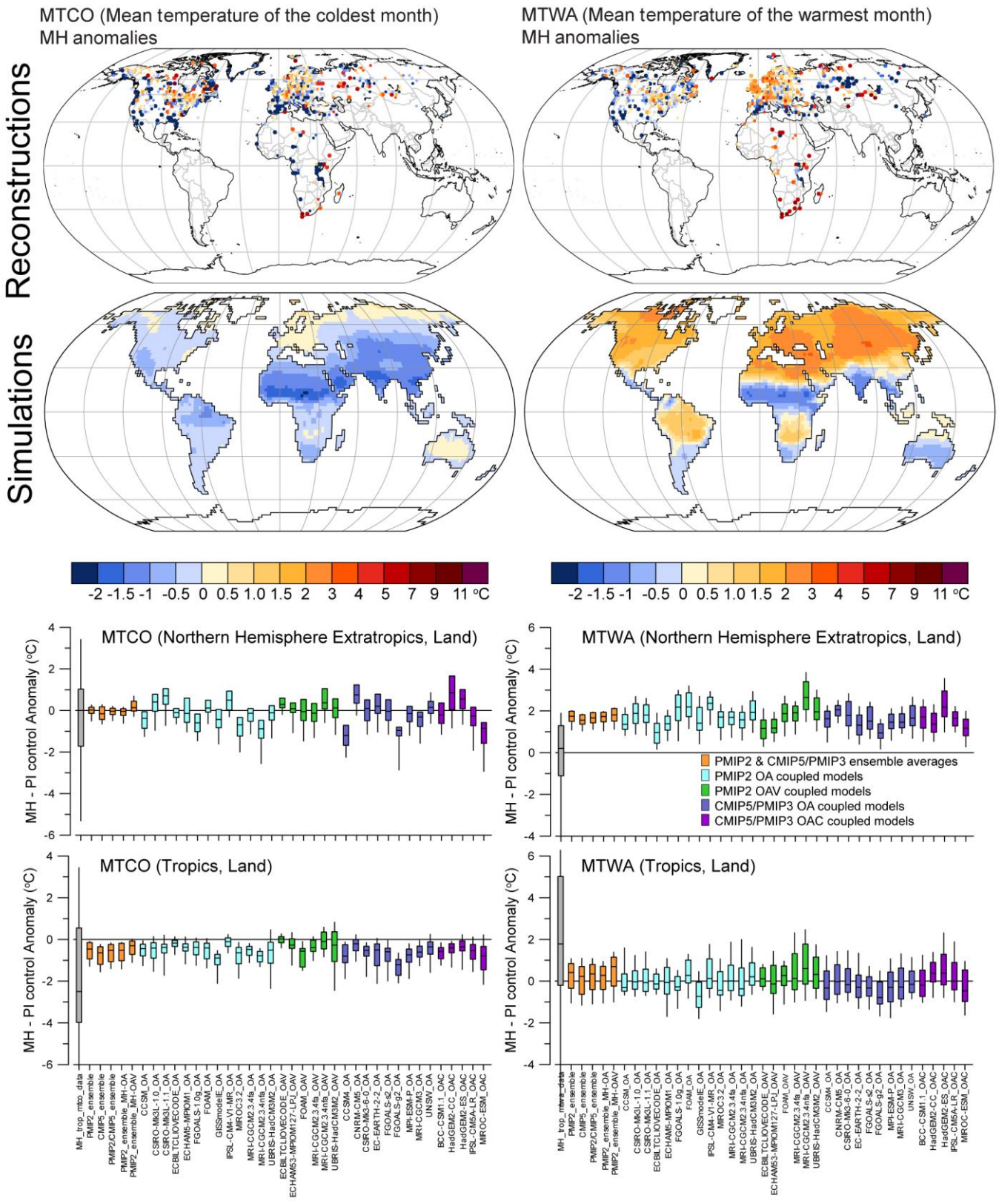

Figure 5.11: Model-data comparison of surface temperature anomalies for the mid-Holocene (6 ka). MTCO is the mean temperature of the coldest month; MTWA is the mean temperature of the warmest month. Top panels are pollen-based reconstructions of Bartlein et al., (2011). Middle panels are corresponding surface temperature anomalies simulated by the PMIP2 and PMIP3 models. Bottom panels contain boxplots for reconstructions (grey), for model ensembles (orange) and for the individual models interpolated to the locations of the reconstructions. The boxes are drawn using the 25th, 50th and 75th percentiles (bottom, middle and top of the box, respectively), and whiskers extend to the 5th and 95th percentiles of data or model results within each area. The northern extratropics are defined as 30-90ºN and the tropics as

30ºS-30ºN. Thirty-three models are assessed, PMIP2 OA: CCSM3, CSIRO-Mk3L-1.0, CSIRO-Mk3L-1.1, ECBILTCLIOVECODE, ECHAM5-MPIOM1, FGOALS-1.0g, FOAM, GISSmodelE, IPSL-CM4-V1-MR, MIROC3.2, MRI-CGCM2.3.4fa, MRI-CGCM2.3.4nfa, UBRIS-HadCM3M2; PMIP2 OAV: ECBILTCLIOVECODE, ECHAM53-MPIOM127-LPJ, FOAM, MRI-CGCM2.3.4fa, MRI-CGCM2.3.4nfa, UBRIS-HadCM3M2; CMIP5/PMIP3 OA: CCSM4, CNRM-CM5, CSIRO-Mk3-6-0, EC-EARTH-2-2, FGOALS-s2, FGOALS-g2, MPI-ESM-P, MRI-CGCM3, UNSW; CMIP5/PMIP3 BCC-CSM1.1, HadGEM2-CC, HadGEM2-ES, IPSL-CM5A-LR, MIROC-ESM.

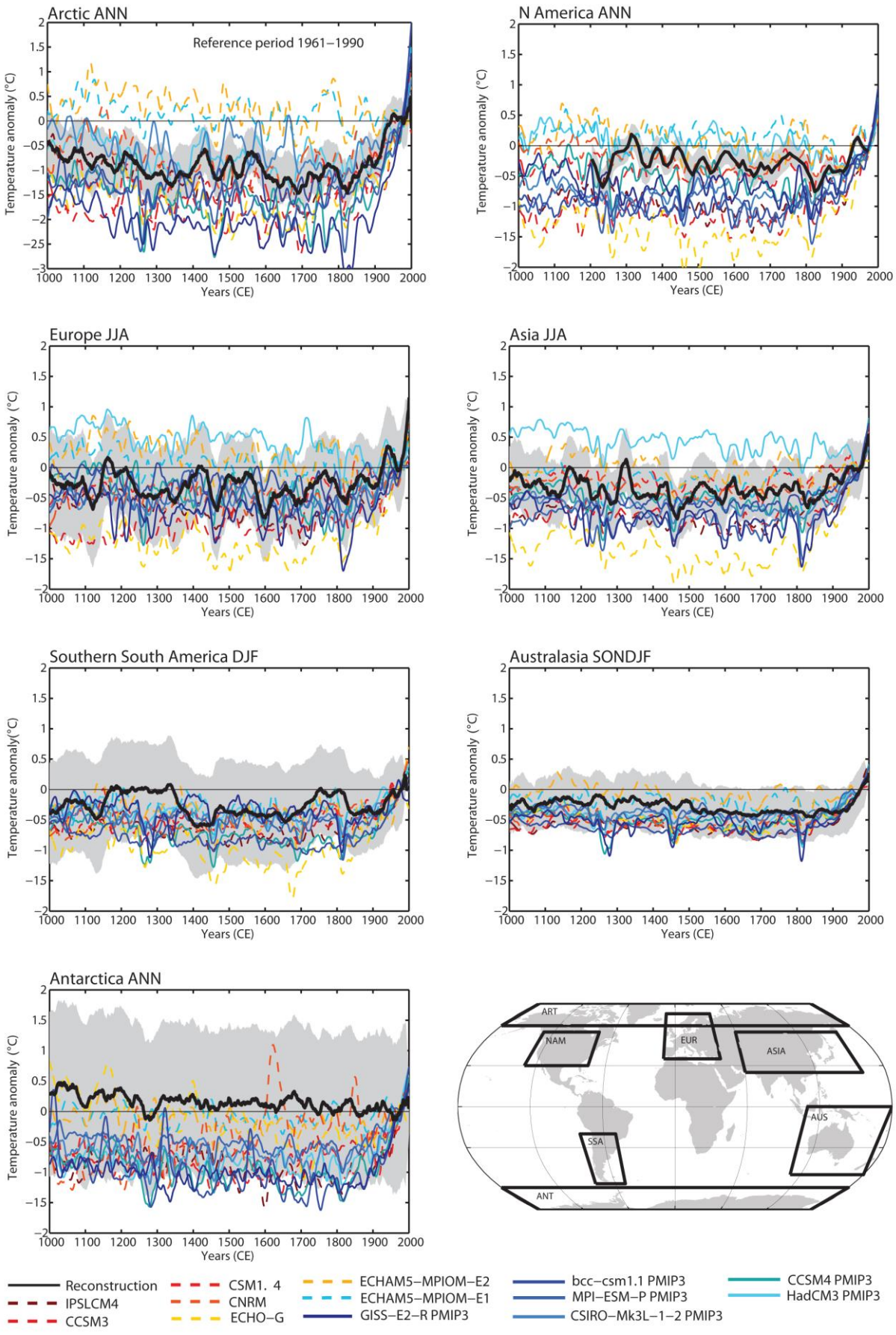

Figure 5.12: Regional temperature reconstructions and simulations over the past millennium (1001–1999 CE). Temperature anomalies are calculated with respect to the 1961–1990 CE reference period, for annual (ANN) or selected

seasons (December to February [DJF], June to August [JJA] or September to February [SONDJF]) in regions indicated in the lower right panel. Reconstructions (PAGES 2k Consortium, submitted, thick black line) and simulated (coloured lines) temperature anomalies are for land only, with the exception of the Arctic and Australasian regions which combine land and ocean. Grey shading indicates uncertainty ranges of reconstructions, as defined for each region (PAGES 2k Consortium, submitted). Model results from Last Millennium simulations are displayed using dashed lines for pre-PMIP3 simulations and solid lines for CMIP5-PMIP3 simulations. Blue/green colours indicate simulations using low solar forcing (see Appendix 5.A, Table 5.A.5) and red/yellow indicate simulations using strong solar forcing (Appendix 5.A, Table 5.A.5). All model time series are smoothed with a 30-year moving average filter. Models used: Pre-PMIP3: ECHO-G (Gonzalez-Rouco et al., 2006), CCSM (Ammann et al., 2007), IPSL (Servonnat et al., 2010), CCSM-Bern (Hofer et al, 2011), ECHAM5/MPIOM (E1, E2) (Jungclaus et al., 2010), and CNRM (Swingedouw et al., 2011). CMIP5-PMIP3: CCSM4 (Landrum et al., submitted), GISS-E2-R (Schmidt et al., 2006), HadCM3 (Schurer et al., submitted), CSIRO-Mk3L-1-2 (Phipps et al., 2011), MPI-ESM-P (Raddatz et al., 2007), and BCC-CSM1-1 (Wu et al., submitted).

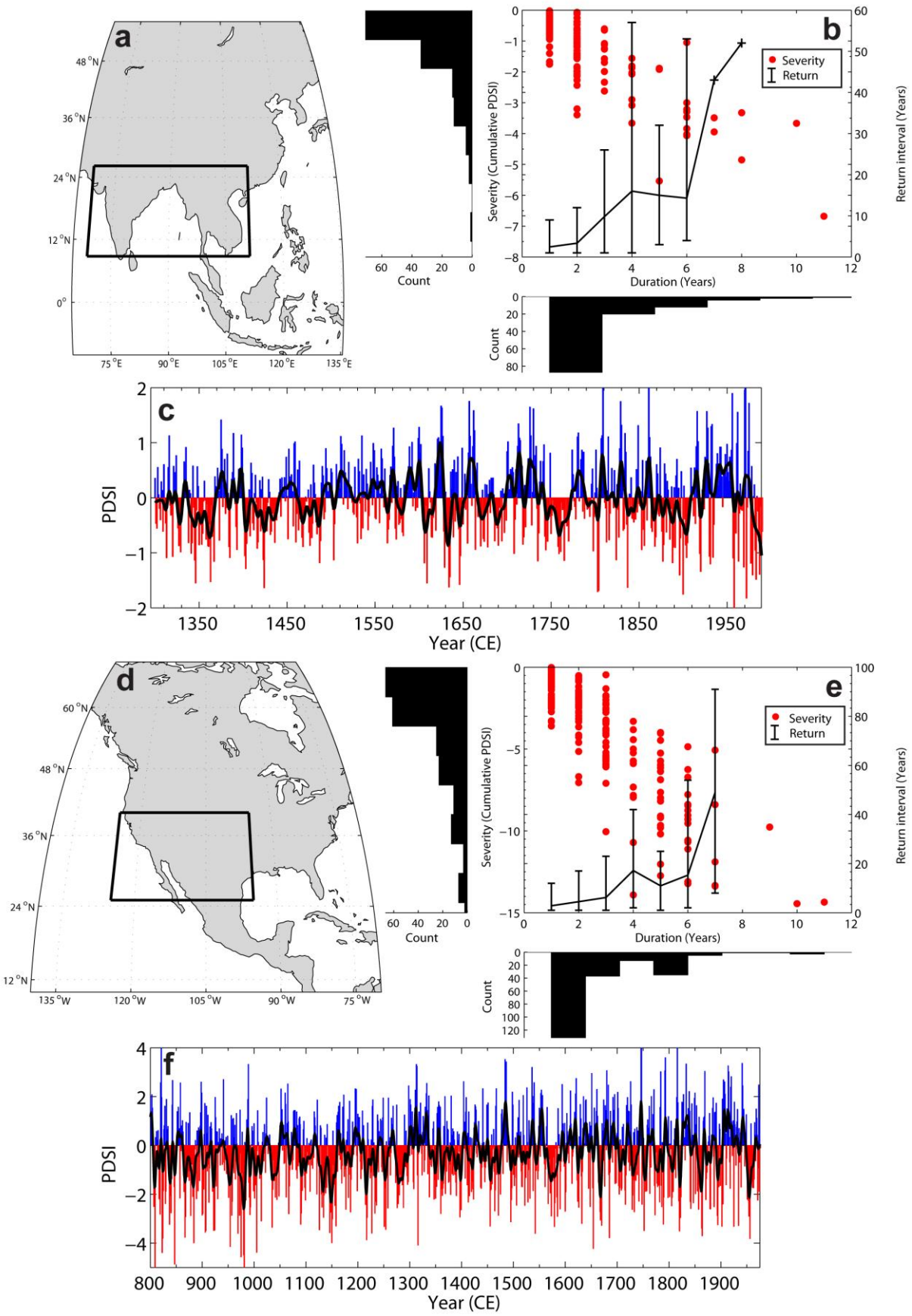

Figure 5.13: Severity, duration, and frequency of droughts in the Monsoon Asia (Cook et al., 2010b) and North American (Cook et al., 2004) Drought Atlases. The box in a) and d) indicates the region over which the tree ring reconstructed Palmer Drought Severity Index (PDSI) values have been averaged to form the regional mean time series

shown in c) and f), respectively. Solid black lines in c) and f) are a 9 year Gaussian smooth on the annual data shown by the red and blue bars. The covariance of drought (PDSI < 0) duration and cumulative severity for each region is shown in panels b) and e) by the red circles (corresponding to the left x-axis), along with the respective marginal frequency histograms for each quantity. Not shown in b) is an outlier with an apparent duration of 24 years, corresponding to the 'Strange Parallels' drought identified in Cook et al., (2010b). Return intervals for droughts of given durations (shown as connected lines and their error bars and corresponding to the right x-axes in the same panels) are estimated as the mean interval between their occurrence, with the minimum and maximum reconstructed intervals indicated. No error bars are present if there is only a single observation of a drought of that duration. The period of analysis is restricted by the availability of tree-ring data to the period 1300 CE to 1989 CE for Monsoon Asia, following Cook et al., (2010), and from 800 CE to 1978 CE for North America, following Cook et al., (2004).

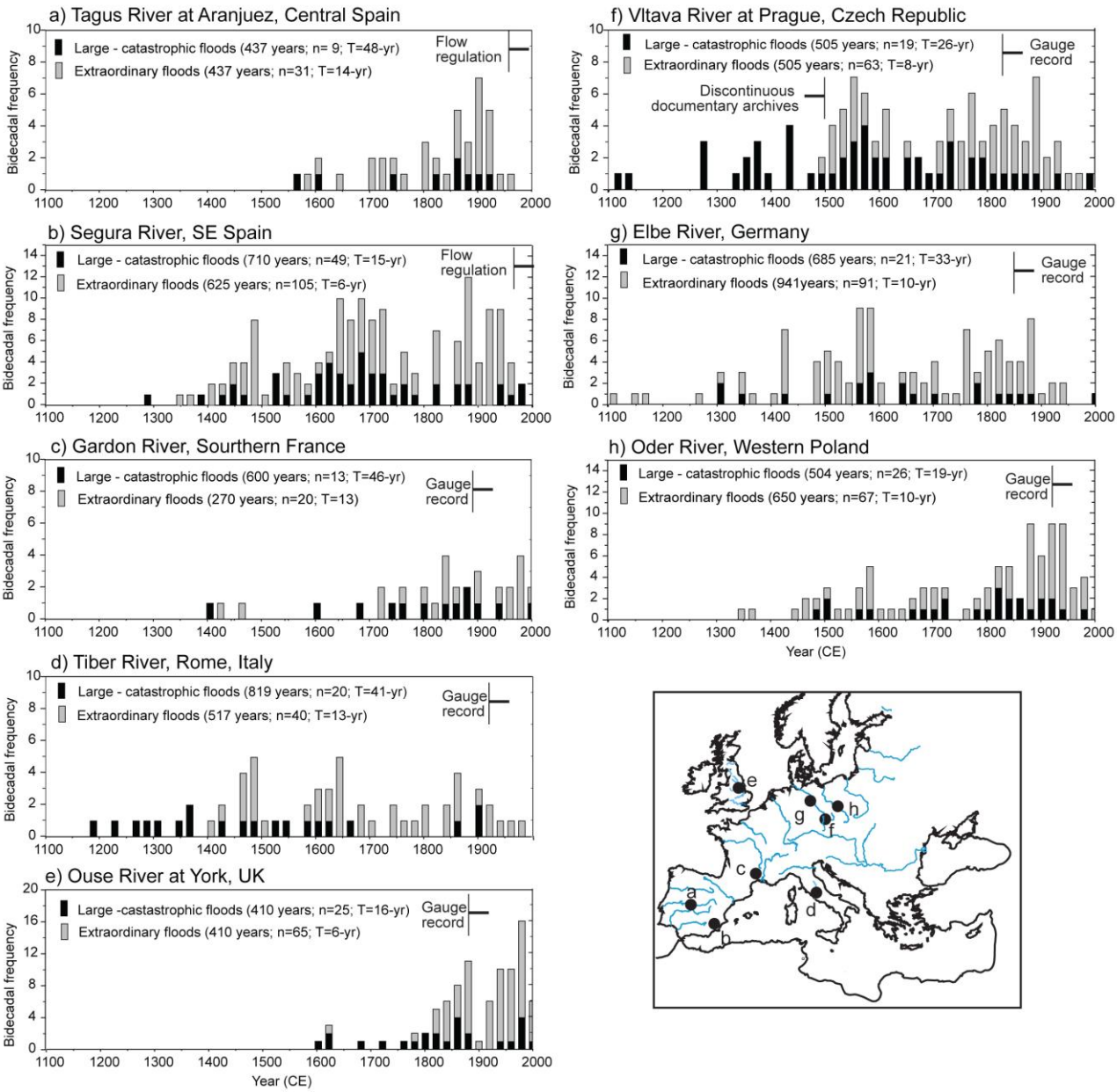

Figure 5.14: Flood frequency from palaeofloods, historical and instrumental records in selected European rivers. Depicted is the number of floods that exceeded a particular discharge threshold or flood level over periods of 20-years (bidecadal). Flood categories include large-catastrophic floods (CAT) associated with high flood discharge or severe damages, and extraordinary floods (EXT) causing inundation of the floodplain with moderate to minor damages. Legend at each panel indicates for each category the period of record in years, number of flood over the period, and the average occurrence interval (in years). A: Tagus River combined paleoflood, historical and instrumental flood records from Aranjuez and Toledo with thresholds of 100–400 $m^3 s^{-1}$ (EXT) and >400 $m^3 s^{-1}$ (CAT) (data from (Benito et al., 2003; Benito et al., 2003b). B: Segura River Basin (SE Spain) documentary and instrumental records at Murcia (Barriendos and Rodrigo, 2006; Machado et al., 2011). C: Gardon River combined discharges from paleofloods at La Baume (Sheffer et al., 2008), documented floods (since the 15th century and historical and daily water stage readings at Anduze (1741–2005; (Neppel et al., 2010). Discharge thresholds referred to Anduze are 1000–3000 $m^3 s^{-1}$ (EXT), >3000 $m^3 s^{-1}$ (CAT). At least five floods larger than the 2002-flood (the largest in the gauged record) occurred in the period AD 1400–1800 (Sheffer et al., 2008). D: Tiber River floods in Rome from observed historical stages (since AD 1100; (Calenda et al., 2005; Camuffo and Enzi, 1996) and continuous stage readings (1870 to present) at the Ripetta landing (Calenda et al., 2005). Discharge thresholds set at 2300–2900 $m^3 s^{-1}$ (EXT) and >2900 $m^3 s^{-1}$ (CAT; >17 m stage at Ripetta). Recent flooding is difficult to evaluate in context due to river regulation structures. F: Vltava River combined documentary and instrumental flood record at Prague (Brázdil et al., 2005) discharge thresholds: CAT, flood index 2 and 3 or discharge >2900 $m^3 s^{-1}$; EXT flood index 1 or discharge 2000–2900 $m^3 s^{-1}$. G: Elbe River combined documentary and instrumental flood record (Mudelsee et al., 2003). Classes refer to Mudelsee et al., (2003) strong

(EXT) and exceptionally strong (CAT) flooding. H: Oder River combined documentary and instrumental flood record (Mudelsee et al., 2003). I: River Ouse at York combined documentary and instrumental flood record (Macdonald and Black, 2010). Discharge thresholds for large floods was set at 500 $m^3 s^{-1}$ (CAT) and for ordinary floods at 350–500 $m^3 s^{-1}$ (EXT). The map shows the location of rivers used in the flood frequency plots.

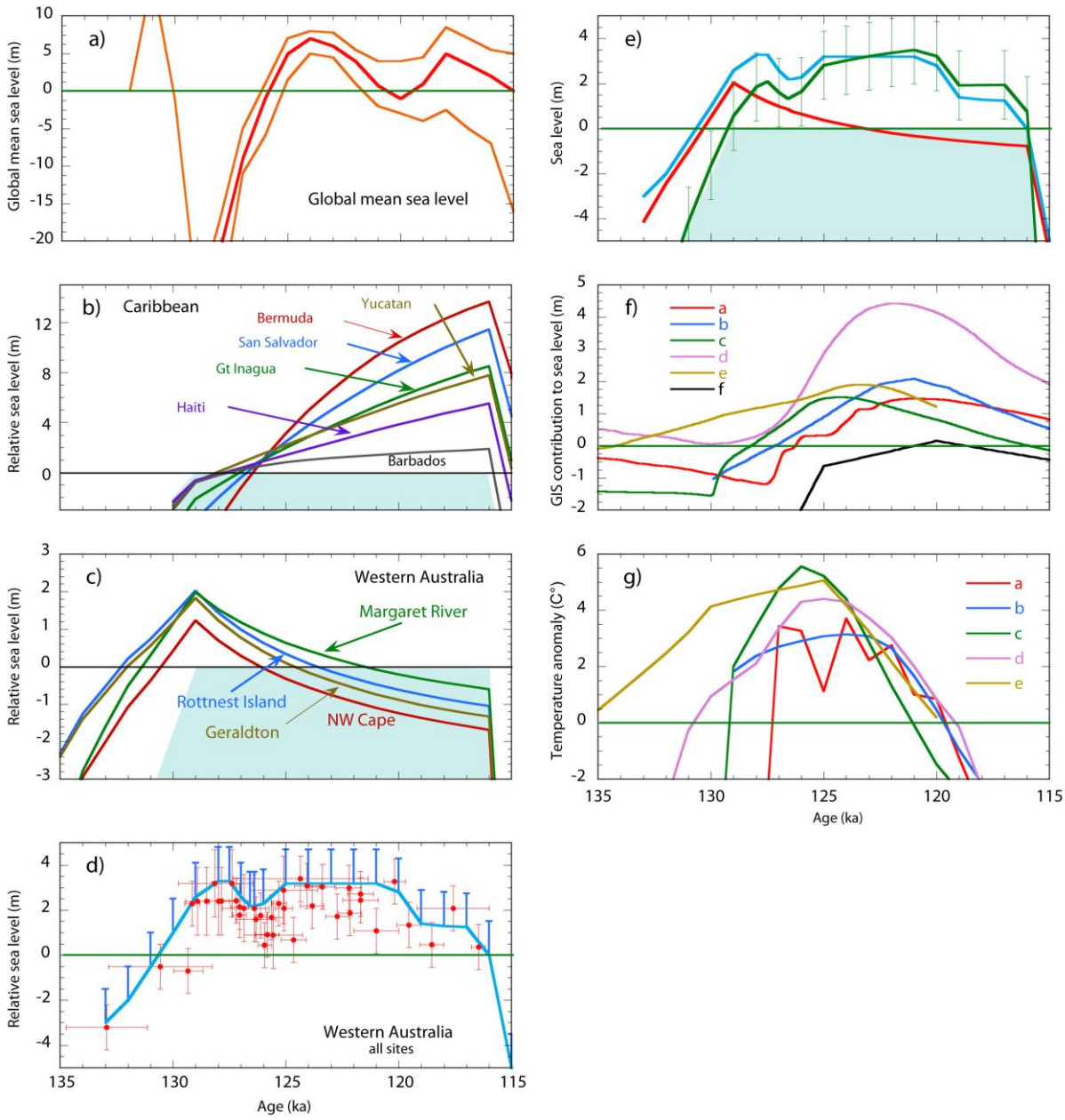

Figure 5.15: Sea level during the Last Interglaciation. (**a**) Proxy-derived estimate of global mean sea level anomaly (Kopp et al., (2009). Median (red line) and 16th and 84th percentiles (orange lines). Due to scale, only the 84th percentile is displayed prior to 130 ka. (**b**) Predicted sea levels for selected sites in the Caribbean and North Atlantic on the assumption that ice volumes during the interval from 129–116 ka are equal to those of today (Lambeck et al., 2012), displaying the spatial variability that can be expected across the region due to isostatic effects. The reference ice-volume model for the LIG interval (shaded), Earth rheology and ice sheet parameters are based on rebound analyses from different regions spanning the interval from Marine Isotope Stage 6 to the present (c.f. Lambeck et al., 2006).These predictions are strongly dependent on the ice load over North America, both, before and after the interglacial period, as well as on mantle rheology. Observations from these sites provide more information on ice histories than on global sea level function. (**c**) Same as (b) but for different sites along the Western Australia coast. The dependence on details of the ice sheet and on Earth-model parameters is less important at these sites than for those in (b). Thus data from these locations, assuming tectonic stability, is more appropriate for estimating LIG sea level. (**d**) Local LIG relative sea level reconstructions from Western Australia based on coral elevations (red) that pass diagenetic screening (Dutton and Lambeck, 2012). All results are for *in-situ* samples. Age error bars correspond to 2 standard deviation uncertainties. All elevations have been normalised to the upper growth limit of corals corresponding to mean low water spring or mean low sea level. The blue line indicates the simplest interpretation of local sea level consistent with reef stratigraphy and should be considered as lower limits by an amount indicated by the blue upper limit error bars. The differences from (a) in the timing of the start and end of the interglacial interval, as well as in the timing of the lowstand in the middle of the interval may be a consequence of different assumptions used in deriving the model ages.

(**e**) The Western Australian reconstructed evidence (blue) from (d) compared with the model-predicted result (red) as in (c) for a reference site midway between the northern and southern most localities. The difference between the reconstructed and predicted functions provides an estimate of the global mean sea level (green). Uncertainties in this estimate include the observational uncertainties from (d) and the model uncertainties. Reference ice-volume model (shaded) as in (c). (**f**) Contribution of ice sheets to sea level change derived from transient ice sheet model simulations for the Greenland ice sheet (red, a: Quiquet et al., submitted; blue, b: Helsen et al., submitted; green, c: Abe-Ouchi et al., 2007 and Greve et al, 2011; pink, d:Robinson et al., 2011; light green, e: Stone et al., submitted, (a)–(e) correspond to the labels in Figure 5.16) and for the Antarctic ice sheet (black, f: Pollard and DeConto, 2009). (**g**) Central Greenland surface-air temperature anomalies for summer (June–August, JJA) used for ice sheet simulations displayed in panel (f) and in Figure 5.16. Anomalies in all panels are calculated relative to present.

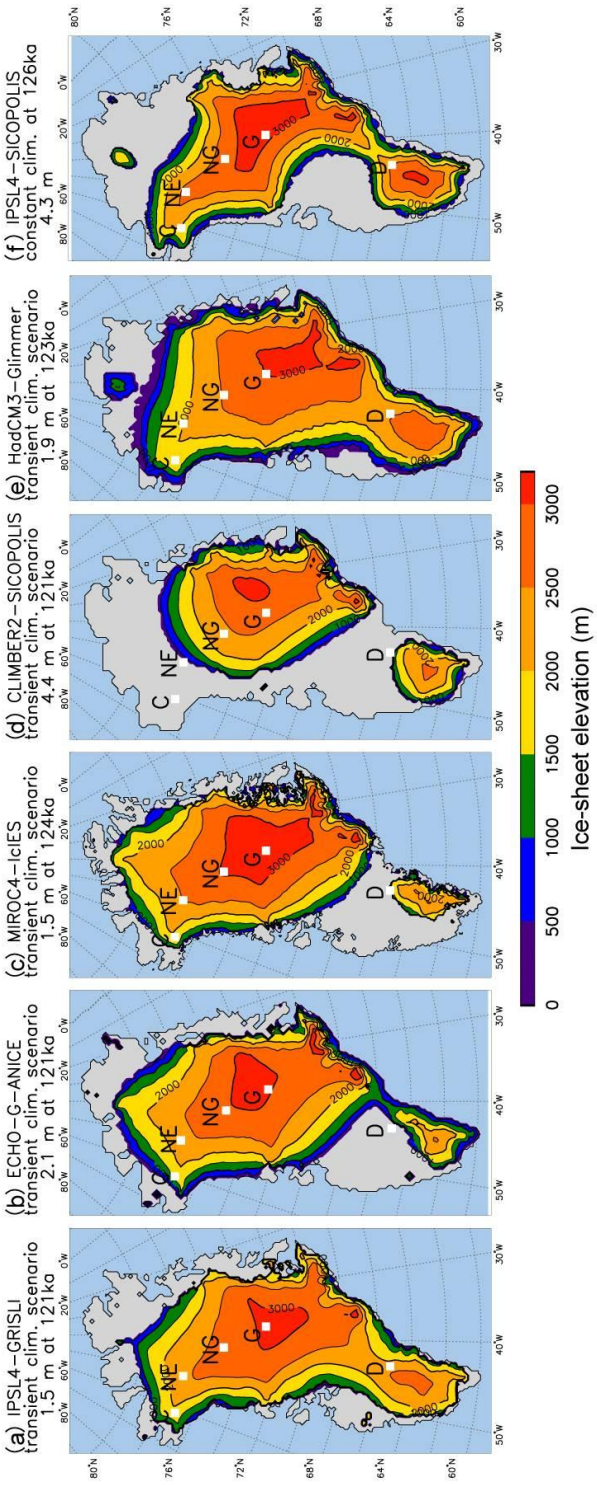

Figure 5.16: Simulated Greenland ice-sheet elevation at the LIG in transient (a–e) and constant-forcing experiments (f). (a) GRISLI ice-sheet model with transient climate forcing derived from IPSL simulations and paleoclimate reconstructions (Quiquet et al., 2012). (b) ANICE ice-sheet model asynchronously two-way coupled with the regional climate model RACMO2 forced with ECHO-G simulated climate from 130–115ka (Helsen et al., submitted). (c) IcIES ice-sheet model with transient climate forcing from 135–115 ka from MIROC GCM (Abe-Ouchi et al., 2007; Greve et al., 2011). (d) "Best-guess" simulation from ensemble runs with the SICOPOLIS ice-sheet model driven by transient LIG climate simulations downscaled from CLIMBER2 with the regional model REMBO (Robinson et al., 2011). (e) "Best guess" simulation from ensemble simulations with the Glimmer ice-sheet model forced with transient climate forcing from 135–120 ka with HadCM3 (Stone et al., submitted). (f) SICOPOLIS ice model forced with a constant Eemian climate simulation of IPSL (at 126 ka), running for 6000 years starting from fully glaciated present-day GIS, as in Otto-Bliesner et al, (2006) in AR4 (Born and Nisancioglu, submitted). White squares in each panel show the locations of ice core sites at which ice from the LIG has been found (Dahl-Jensen et al., submitted; Dansgaard et al.,

1985; North Greenland Ice Core Project members, 2004) : GRIP/GISP (G), NGRIP (NG), NEEM (NE), Camp Century (C), and possibly Dye3 (D). For ice sheet simulations using transient climate forcing, the minimum in ice volume is illustrated. The discrepancy of model outputs regarding timing and topography for minimum ice volume results from differences in climate forcings (cf. Figure 5.15g), ice-sheet models including their melt schemes (van de Berg et al., 2011), as well as differences in present-day climate (Quiquet et al., 2012). Compared to present-day, the average Greenland ice sheet volume of the 4 transient ice sheet models in panels a–e, which depict ice at the NEEM location, corresponds to 1.8 m sea level change. All panels use original model resolution and grids.

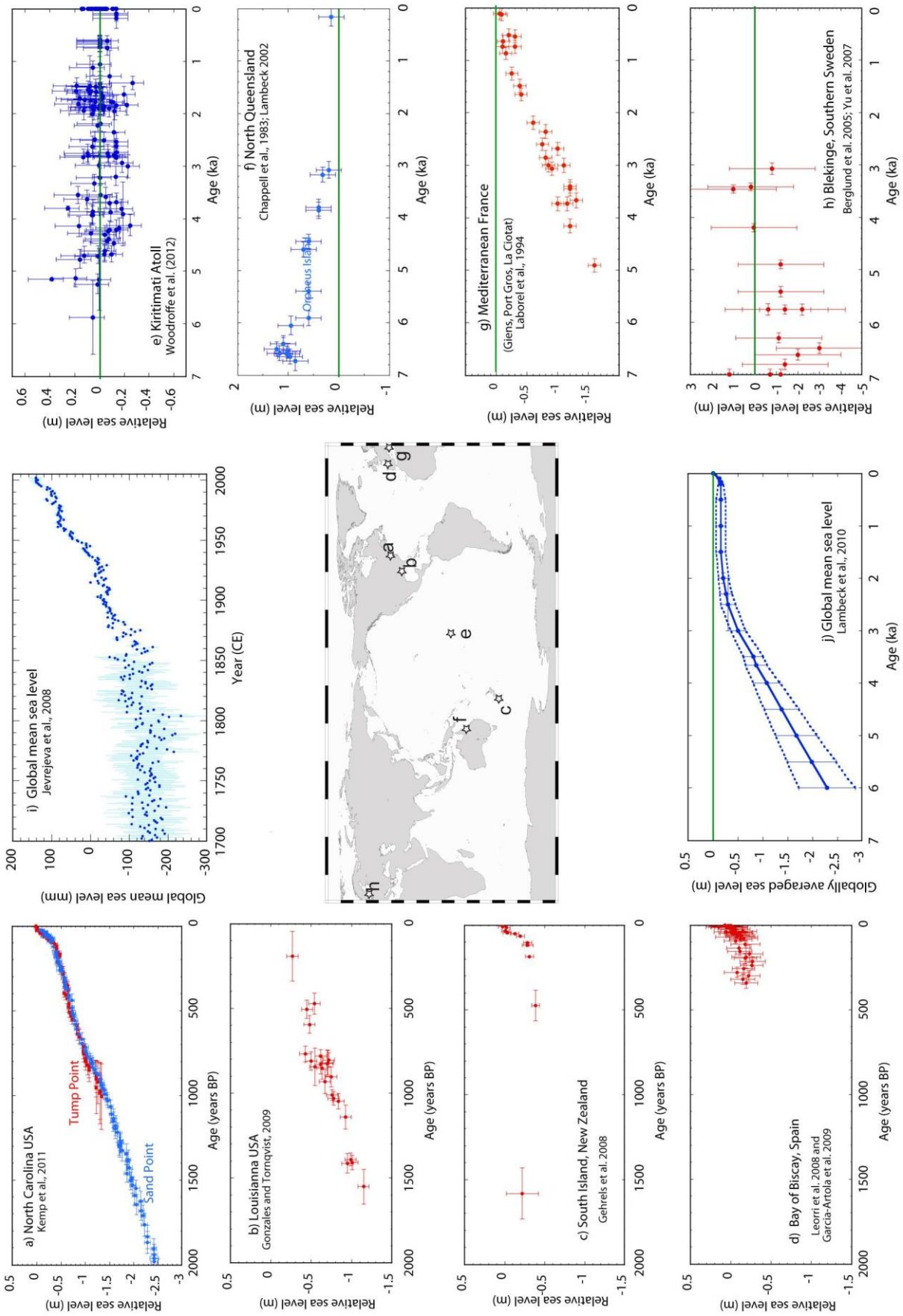

Figure 5.17: Observational evidence for sea level change in recent and late Holocene time. Left panels (a-d): High resolution relative sea level results from saltmarsh data at representative sites, without corrections for glacial isostatic

movement of land and sea surfaces. Locations are given on the map. The North Carolina (a) result is representative of other North American Atlantic coast locations (Kemp et al., 2011). The rate of change occurring late in the 19th century are seen in all high resolution saltmarsh records – e.g., (c) Gehrels et al., (2008) (see also Gehrels and Woodworth, submitted); (d) Garcia-Artola et al., (2009); Leorri et al., (2008) –that extend into modern time and is consistent with Roman archaeological evidence (Lambeck et al., 2004). The oscillation in sea level at about 1000 CE seen in the North Carolina record occurs in some (González and Törnqvist, 2009; van de Plassche et al., 1998) but not all records (c.f., Gehrels et al., 2011; Kemp et al., 2011). Right hand side panels (e-h) Observational evidence for sea level change from lower resolution but longer period records. All records, except for Blekinge (h) where the isostatic signal dominates the observed sea level change (Yu et al., 2007), are uncorrected for isostatic effects. The Kiritimati record (Christmas Island) consists of coral microatoll elevations whose fossil elevations are with respect to the growth position of living microatolls (Woodroffe et al., 2012). The Orpheus Island record (f) is also based on microatoll evidence (Chappell, 1983; Lambeck et al., 2002b). The data from Mediterranean France (g) is based on biological indicators (Laborel et al., 1994) restricted to three nearby locations between which differential isostatic effects are less than the observational errors (Lambeck and Bard, 2000). The Blekinge result (h), corrected for isostatic rebound, is based on the analysis of transgression and regression sequences in marginal basins (Yu et al., 2007). The two global records are estimates of change in global mean sea level from (i) the instrumental record (Jevrejeva et al., 2008), and (j) from a range of geological and archaeological indicators (Lambeck et al., 2010b), with the contributing records corrected for the isostatic effects at each location.

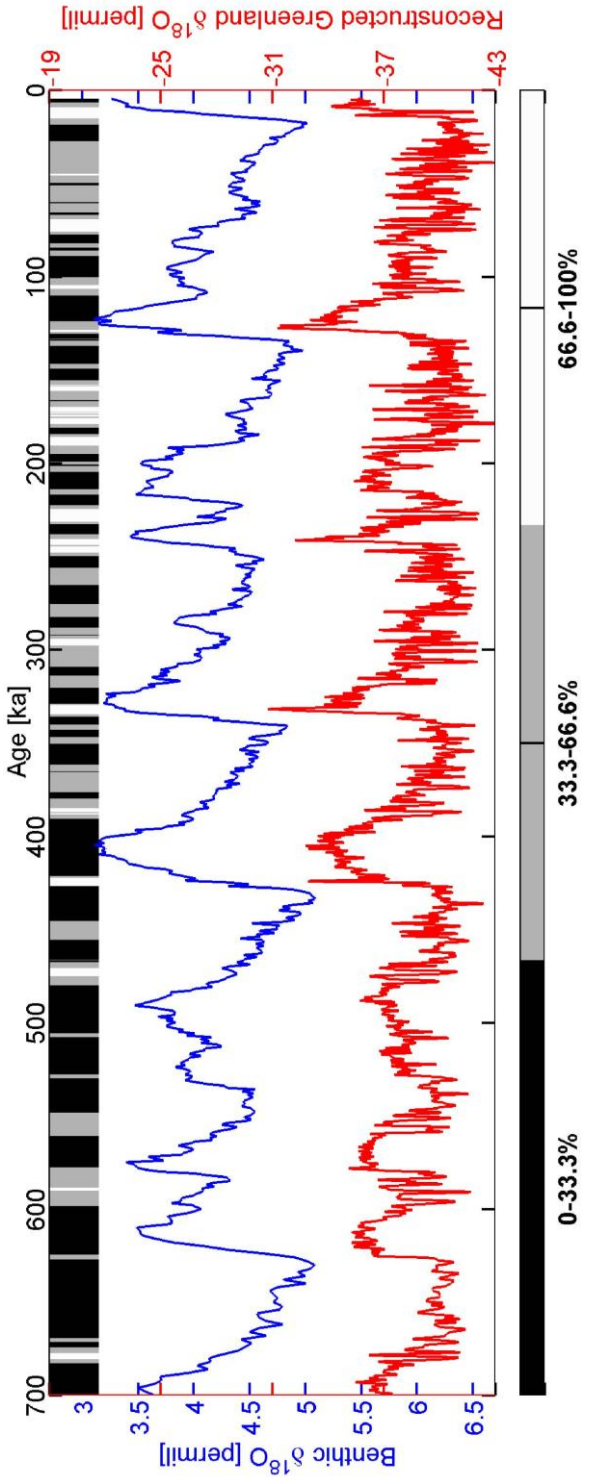

Figure 5.18: Dependence of millennial-scale bipolar seesaw activity (a measure of DO variability) on climate background state: Benthic $\delta^{18}O$ stack (blue) (Lisiecki and Raymo, 2005) representing a combination of global ice-volume, deep ocean temperature and hydrography, terciles of millennial-scale bipolar seesaw activity index (gray shading, showing periods with low frequency of events in black and high frequency in white) (Barker et al., 2011), and $\delta^{18}O$ analogue for Greenland (red) empirically derived from Antarctic ice core data using bipolar seesaw methods and assumptions on orbital lags (Barker et al., 2011).

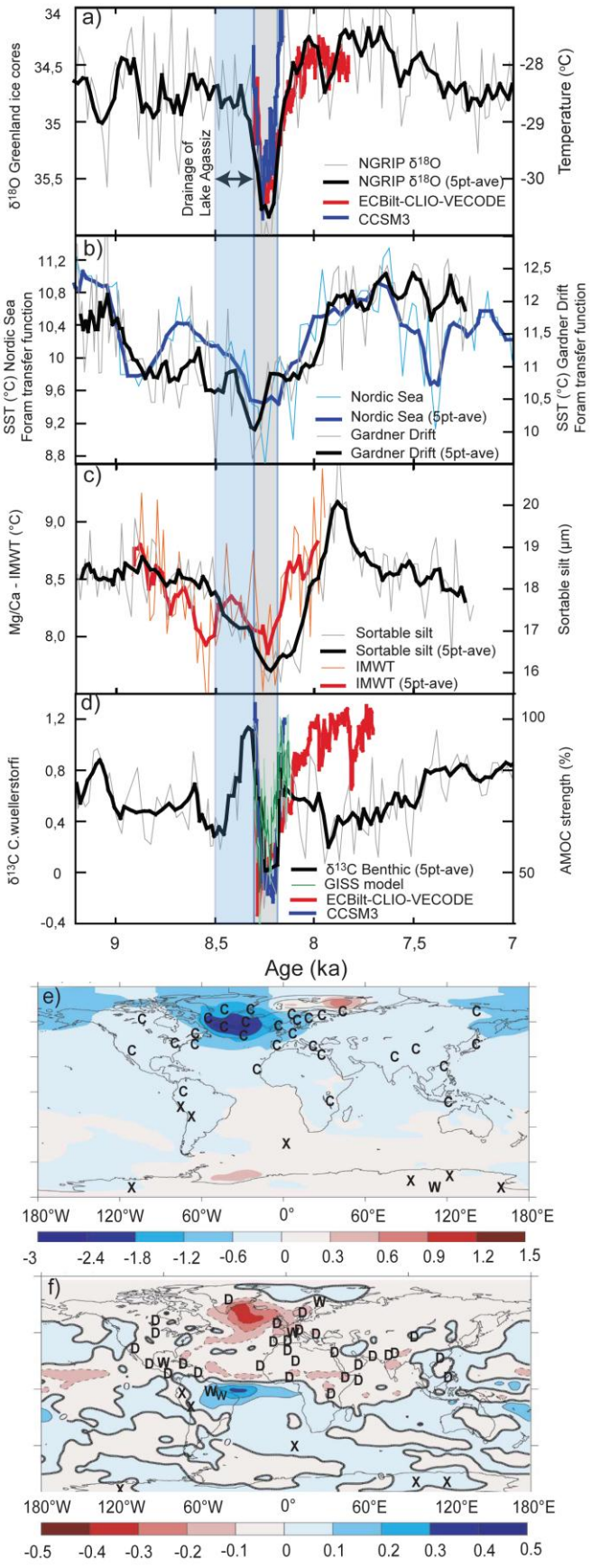

Figure 5.19: Compilation of selected paleoenvironmental and climate model data for the abrupt Holocene cold event at ca. 8.2 ka, documenting temperature and ocean circulation changes around the event and the spatial extent of climate anomalies following the event. Published age constraints for the period of release of freshwater from glacier Lakes

Agassiz and Ojibway are bracketed inside the vertical blue bar. Vertical grey bar denotes the time of the main cold event as found in Greenland Ice core records (Thomas et al., 2007). **a)** Black curve: NGrip $\delta^{18}O$ (temperature proxy) from Greenland Summit (North Greenland Ice Core project members (2004). Red curve: Simulated Greenland temperature in an 8.2-ka event simulation with the ECBilt-CLIO-VECODE model (Wiersma et al., 2011). Blue curve: Simulated Greenland temperature in an 8.2-ka event simulation with the CCSM3 model (Morrill et al., 2011). **b)** North Atlantic/Nordic Seas SST-reconstructions, age models are aligned on the peak of the cold-event (less than 100-year adjustment). Blue curve: Nordic Seas (Risebrobakken et al., 2011). Black curve: Gardar Drift south of Iceland (Ellison et al., 2006). **c)** Deep- and intermediate water records. Black curve: Sortable silt record (overflow strength proxy) from Gardar Drift south of Iceland (Ellison et al., 2006), Atlantic intermediate water temperature reconstruction (Bamberg et al., 2010). **d)** Black curve: $\delta^{13}C$ (deep water ventilation proxy) at 3.4 km water depth south of Greenland (Kleiven et al., 2008). Age model is aligned on the minimum overflow strength in c) (less than 100-year adjustment). Modelled change in the strength of the AMOC: Green curve: An 8.2-ka event simulation with the GISS model (LeGrande et al., 2006). Red curve: An 8.2-ka event simulation with the ECBilt-CLIO-VECODE (v. 3) model (Wiersma et al., 2011). Blue curve: An 8.2-ka event simulation with the CCSM3 model (Morrill et al., 2011). **e)** Spatial distribution of the ensemble mean annual mean surface temperature anomaly (°C) from a multi-model water hosing experiment with 0.1 Sv freshwater forcing in the NW Atlantic (Stouffer et al., 2006). Paleoclimate data from records resolving the 8.2-ka event are plotted with symbols: C=cold anomaly, W=warm anomaly, X=No significant anomaly. Main data sources: (Wiersma et al., 2011); (Morrill et al., 2011) **f)** Spatial distribution of the ensemble mean annual mean precipitation anomaly (mm day^{-1}) from a multi-model water hosing experiment with 0.1 Sv freshwater forcing in the NW Atlantic (Stouffer et al., 2006). Paleoclimate data from records resolving the 8.2-ka event are plotted with symbols: D=dry anomaly, W=wet anomaly, X=No significant anomaly. Main data sources: (Wiersma et al., 2011); (Morrill et al., 2011).

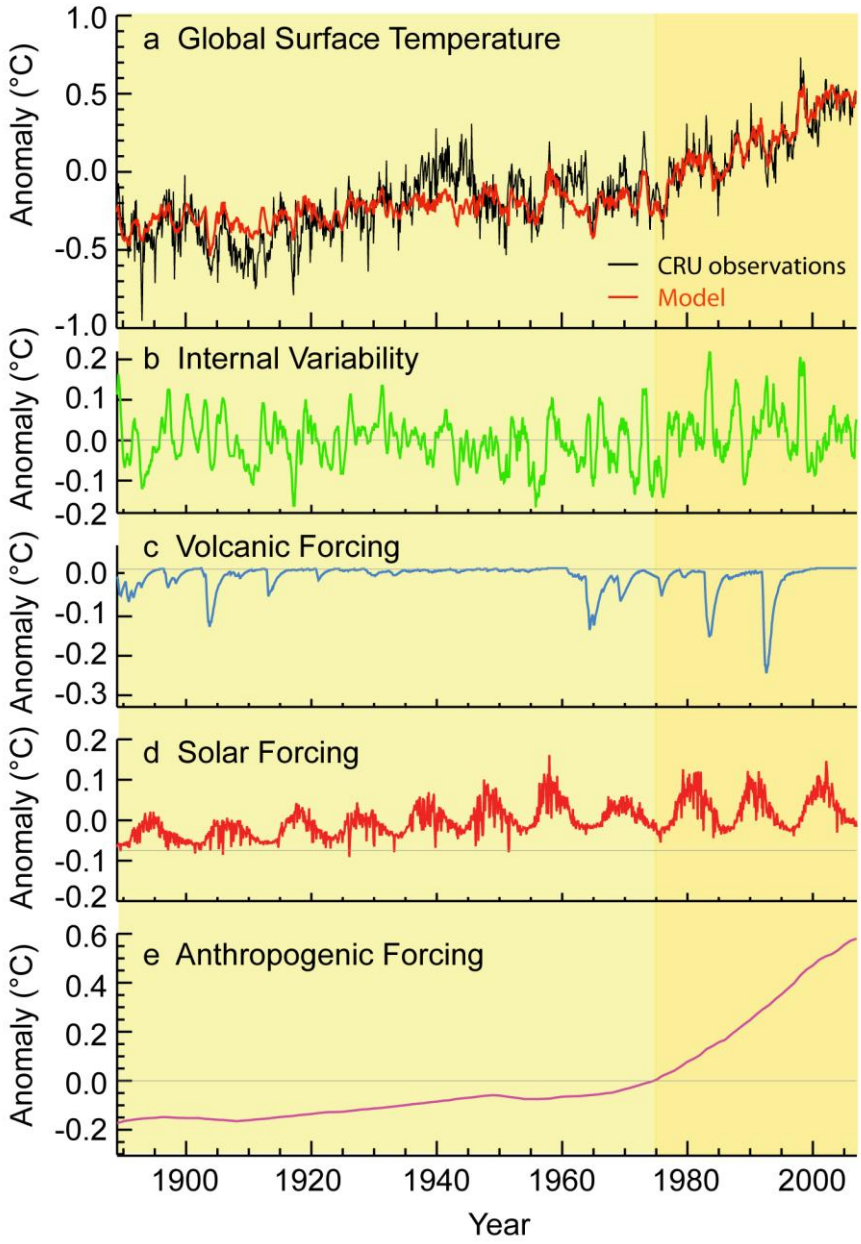

FAQ 5.1, Figure 1: Global surface temperature variations from 1899 to 2006 and natural (internal, volcanic, and solar) and anthropogenic factors that influence surface temperatures (modified from Lean, 2010). a) Observed (black line) and model (red line) composed from the monthly mean global surface temperature time series in panels b to e. b) The El Niño Southern Ocean index, used as an indicator of short-term internal variability that cannot be directly attributed to an external forcing. c) Short-lived, but strong, cooling effects of volcanic eruptions, d) Solar forcing which consists of the 11-year sunspot cycle, superimposed on a steadily increasing trend during the first half of the 20th century. e) Anthropogenic forcing, consisting of a warming component due to greenhouse gases, and a cooling component due to aerosols.

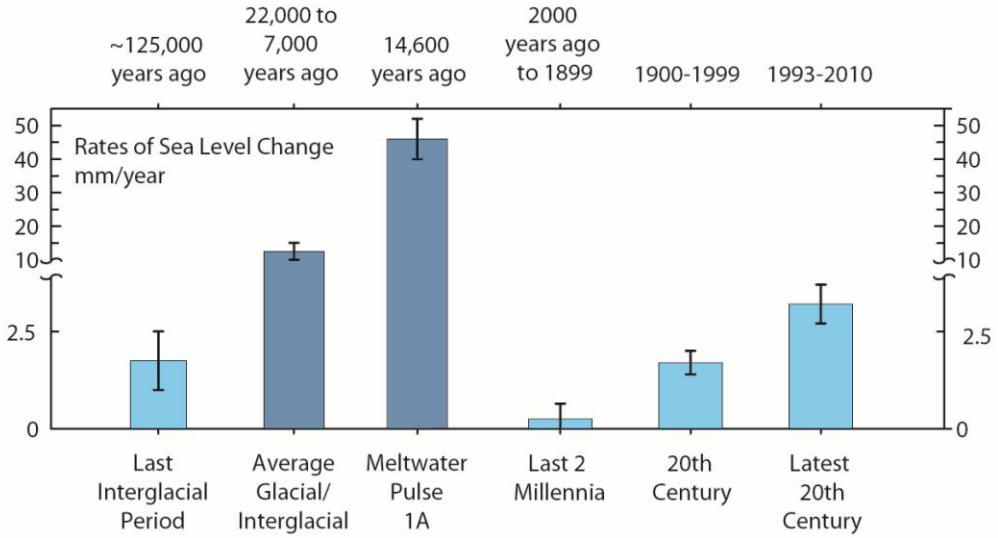

FAQ 5.2, Figure 1: Estimates of the average rate of sea level change (mm yr^{-1}) for 4 select time intervals: last 5 glacial/interglacial transitions; last 2 millennia; 20th century; satellite altimetry era (1993–2010).